# Turbo-Coded MIMO Systems:
# Receiver Design and Performance Analysis

*Naveen Mysore*

Department of Electrical and Computer Engineering
McGill University
Montreal, Canada

February 2006

---

A thesis submitted to McGill University in partial fulfillment of the requirements for the degree of Doctor of Philosophy.

Library and
Archives Canada

Published Heritage
Branch

395 Wellington Street
Ottawa ON K1A 0N4
Canada

Bibliothèque et
Archives Canada

Direction du
Patrimoine de l'édition

395, rue Wellington
Ottawa ON K1A 0N4
Canada

*Your file Votre référence*
*ISBN: 978-0-494-25218-5*
*Our file Notre référence*
*ISBN: 978-0-494-25218-5*

NOTICE:
The author has granted a non-exclusive license allowing Library and Archives Canada to reproduce, publish, archive, preserve, conserve, communicate to the public by telecommunication or on the Internet, loan, distribute and sell theses worldwide, for commercial or non-commercial purposes, in microform, paper, electronic and/or any other formats.

The author retains copyright ownership and moral rights in this thesis. Neither the thesis nor substantial extracts from it may be printed or otherwise reproduced without the author's permission.

AVIS:
L'auteur a accordé une licence non exclusive permettant à la Bibliothèque et Archives Canada de reproduire, publier, archiver, sauvegarder, conserver, transmettre au public par télécommunication ou par l'Internet, prêter, distribuer et vendre des thèses partout dans le monde, à des fins commerciales ou autres, sur support microforme, papier, électronique et/ou autres formats.

L'auteur conserve la propriété du droit d'auteur et des droits moraux qui protège cette thèse. Ni la thèse ni des extraits substantiels de celle-ci ne doivent être imprimés ou autrement reproduits sans son autorisation.

In compliance with the Canadian Privacy Act some supporting forms may have been removed from this thesis.

While these forms may be included in the document page count, their removal does not represent any loss of content from the thesis.

Conformément à la loi canadienne sur la protection de la vie privée, quelques formulaires secondaires ont été enlevés de cette thèse.

Bien que ces formulaires aient inclus dans la pagination, il n'y aura aucun contenu manquant.

Canada

# Abstract

Future wireless communication systems will have to support large uplink / downlink data rates within the allocated frequency spectrum in order to support emerging multimedia applications. Recently explored multiple antenna or multi-input multi-output (MIMO) systems have the potential of achieving large increases in wireless channel capacities and spectral efficiencies. However, powerful channel codes and sophisticated signal processing techniques are required to achieve these increases for low signal-to-noise ratios and in the presence of multipath fading. Motivated by the third generation wireless standard and efforts towards fourth generation systems, this dissertation explores turbo-coded uplink transmission over Rayleigh faded MIMO channels, when channel state information is available only at the receiver (base-station). In this context, unlike previously proposed MIMO signal detection techniques of exponential or polynomial complexity, we first derive a novel soft-decision MIMO signal detector, which is of linear complexity in the number of transmit antennas, receive antennas and users.

The proposed detector is integrated into a new iterative receiver for turbo-coded MIMO systems and simulation results are presented for various antenna configurations on slow, frequency non-selective Rayleigh fading channels. The explored MIMO systems achieve target bit error rate (BER) performance of $10^{-5}$ within 1.5 to 2.9 dB of the ergodic capacity limit in single and multi-user scenarios. Furthermore, system performance is shown to be robust to the effects of spatial correlation, channel estimation errors and imperfect power control. In addition, turbo-coded digital recording systems with multiple heads and tracks were considered as a further application of the proposed detector and iterative receiver. Good BER performance is achieved in these systems despite strong intertrack and intersymbol interference.

Finally, we extend the union bound based method from turbo codes on the Gaussian noise channel to the proposed turbo-coded systems on wireless MIMO channels. Calculated bounds on BER performance are within 0.5 to 0.8 dB of the simulated results in the error floor region. In addition, a new performance analysis technique is proposed, which provides BER performance bounds within 0.1 to 0.5 dB of the simulated performance in the waterfall region. Furthermore, the latter technique can also provide accurate bounds for selected coded digital recording systems.

# Sommaire

Dans le but de répondre aux applications multimédia émergentes, les systèmes de communication sans fil du futur auront à supporter de grandes quantités de données sortantes/entrantes à l'intérieur du spectre de fréquence qui leur est alloué. Il a récemment été démontré que les systèmes à antennes multiples et les systèmes d'entrée-multiple/sortie-multiple (MIMO) peuvent mener à une large augmentation de la capacité des canaux sans fil et de l'efficacité spectrale qui leur est associée. Toutefois, de puissants codes correcteurs d'erreur et des techniques sophistiquées de traîtement de signal sont requises afin d'obtenir ces augmentations pour des ratios bruits-signaux faibles ou lors de la présence d'évanouissement sur trajets multiples. Inspirée par les standards sans-fil de troisième génération et les efforts fournis envers les systèmes de quatrième génération, cette dissertation explore l'application des turbo-codes aux signaux transmis sur les canaux MIMO à évanouissement de Rayleigh, lorsque l'état du canal n'est disponible qu'à la station réceptrice. Dans ce contexte, nous dérivons un nouveau détecteur de signaux MIMO à décisions pondérées qui possède une complexité linéaire quant au nombre d'antennes émettrices, réceptrices et d'utilisateurs, contrairement aux techniques de détection de signal MIMO précédemment proposées, qui affichent une complexité exponentielle ou polynomiale.

Le détecteur proposé est intégré dans un nouveau récepteur itératif pour les systèmes MIMO à turbo-codes et des résultats de simulation sont présentés pour plusieurs configurations d'antennes sur canaux à évanouissement de Rayleigh lents et sans évanouissement progressif de fréquence. Le système MIMO étudié obtient un taux d'erreurs sur les bits de $10^{-5}$ à $1.5 - 2.9$ dB de la capacité ergodique, pour différents scénarios à utilisateurs simple et multiples. De plus, la performance du système démontre une certaine robustesse quant aux effets de corrélation spatiale, des erreurs d'estimation de canal et du control de puissance. Les systèmes d'enregistrement digital à turbo-codes possédant plusieurs têtes lectrices et pistes d'enregistrement sont considérés à titre d'application additionnelle pour le détecteur proposé. Un bon taux d'erreur sur les bits est obtenu pour ces systèmes en dépit de l'interférence importante entre le pistes et les symboles.

Finalement, nous étendons la technique de la probabilité d'union pour les turbo-codes sur les canaux-bruits Gaussian au système proposé pour les canaux MIMO. Les limites calculées pour le taux d'erreur sur les bits se trouvent à $0.5 - 0.8$ dB des résultats de simulation dans la région du plancher d'erreur. De plus, une nouvelle technique d'évaluation de performance est proposée par laquelle nous obtenons une borne sur le taux d'erreur sur les bites (TEB) qui se trouve à $0.1 - 0.5$ dB des performance simulées dans la région de chute. Finalement, cette dernière technique permet de déterminer des bornes précises pour les systèmes d'enregistrement digital.

# Acknowledgements

Mere words are insufficient to express the appreciation and gratitude I have for my advisor, Prof. Jan Bajcsy. Over the last five years, I have benefited immensely from his guidance, patience, insight and enthusiasm. He has contributed significantly to my personal as well as professional development and will always remain an important person in my life.

I would like to acknowledge the financial support of the National Science and Engineering Research Council (NSERC) and my advisor, Prof. Bajcsy. Furthermore, the computing infrastructure provided through the financial support of the Canadian Foundation for Innovation and Québec Fonds pour la Formation de Chercheurs et l'Aide à la Recherche are duly acknowledged.

I would like to thank the members of my Ph.D. committee, Prof. Peter Kabal and Prof. David Plant for their feedback and suggestions to define the scope and breadth of my doctoral research. Special thanks to Prof. Michael Kaplan who sparked my interest in wireless systems and to Prof. Kabal who first encouraged me to pursue my research with Prof. Bajcsy.

I would also like to thank my external examiner, Prof. Vijay K. Bhargava of University of British Columbia, and the members of my Ph.D. defense committee, namely, Prof. Masad Damha, Prof. Benoît Champagne, Prof. Peter Kabal, Prof. Fabrice Labeau, Prof. Jan Bajcsy and Prof. M. Reza Soleyamani (Concordia University), for their useful comments and suggestions.

Special thanks to my lab colleagues and friends, Aminata Amadou Garba, Martin Irman, Isabel Deslauriers, Phillip Sawbridge and Mehmet Akçakaya for making our lab (Mc 820) intellectually stimulating and enjoyable. Also, I would like to thank Bobby Girouard for the French translation of the abstract. I express my sincere gratitude to Jana and Daniela Bajcsy for their patience while completing the conference and journal papers.

Above all, I am deeply indebted to my parents, Latha and Mohan and to my sister Navya for their love, support and unwavering belief in me. They constantly enrich my life and help me to realize my dreams. It is to them that I dedicate this thesis.

*"Learn from yesterday,*
*live for today,*
*hope for tomorrow.*
*The important thing is not to stop questioning."*

Albert Einstein (1879 – 1955)

# Contents

# List of Figures

# Chapter 1

# Introduction

Future wireless cellular systems will be required to support increased user data rates for multimedia applications based on images, video and data. Beyond third generation (3G) wireless systems will be expected to offer seamless user access to the backbone communication network and integrate multiple services, such as,

- Uploading personal photos and video clips
- Downloading movies, sporting events and television news
- Accessing electronic library resources
- Multi-point video conferencing
- Increased surveillance for business, police and security purposes
- Interactive 3-D gaming, telemedicine, telerobotics, etc.

Intensive research is currently underway to develop technologies that will meet the data rate requirements of these services. A combination of powerful error control codes and multiple antenna systems appears to be the most promising approach to enabling the above applications.

## 1.1 A Brief Overview of Personal Wireless Communication

Wireless transmission of information, demonstrated first by Marconi over a hundred years ago, has had a significant impact on the mode and extent of personal communication [11]. Compared to wireline and fibre optic communication systems, wireless transmission has many benefits including:

- Access flexibility (users can use network services anytime/anywhere)
- Easy and quick setup (no physical lines have to be installed)
- Low maintenance costs (no physical lines have to be fixed or replaced)
- Low cost of access rights (limited property acquisition for facilities).

In 1947, AT&T developed the concept of cellular telephony, in its proposal to the Federal Communications Commission [3]. In 1983, the first such system, known as the Advanced Mobile Phone System (AMPS), was set-up by Ameritech in Chicago [3]. By the late 1980's, the first generation analog mobile phone systems were in widespread use. Fig. 1.1 illustrates a typical cellular network connected to the public switched telephone network through the mobile telephone switching office. Advances in integrated circuit technology enabled digital wireless communication to be more practical and economical than the corresponding analog counterpart.

By the early 1990s, the second generation (2G) digital wireless systems, supporting voice and low data rate applications, have emerged in the United States, Europe and Japan. These systems rely on data compression and errorcontrol coding to achieve noise robustness, increased fidelity, higher spectral effici ency and enhanced security [53], [76]. In uplink transmission, these standards relied on Time Division Multiple Access (IS-54, IS-136 and GSM) or Code Division

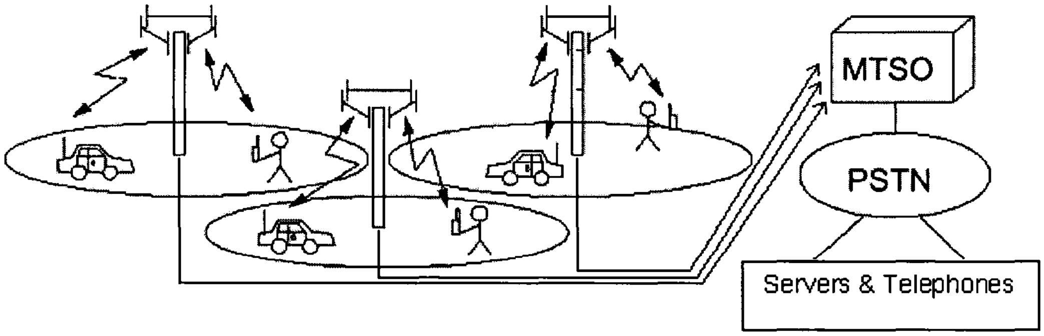

**Fig. 1.1. A typical cellular telephone network (PSTN stands for Public Switched Telephone Network and MTSO is Mobile Telephone Switching Office).**

Multiple Access (IS-95) [49]. The explosive growth rate in the mobile communication market in recent years is illustrated in Fig. 1.2. The number of mobile phone subscribers increased almost threefold from 1997 to 2001 and is predicted to reach 1.7 billion users by 2010 [45]. This figure also shows the growth in (low rate) mobile internet subscribers, which in turn, illustrates the potential increase in demand for high-rate wireless multimedia services.

Research and development of the third generation (3G) wireless communication systems started in the early 1990's with the objective of enabling fast mobile access to internet services for wireless phones, notebook personal computers, personal digital assistants (PDAs), etc. Unlike the second generation, the 3G standard was developed through a partnership of many standardization organizations (ARIB, CCSA, ETSI, ATIS, TTA and TTC) [95] and is solely based on CDMA technology for uplink transmission. Even though 3G uses very powerful error control codes (convolutional and turbo), its first commercial deployment, attempted in 2000, was delayed until 2005 [22] due to technical difficulties (e.g.,

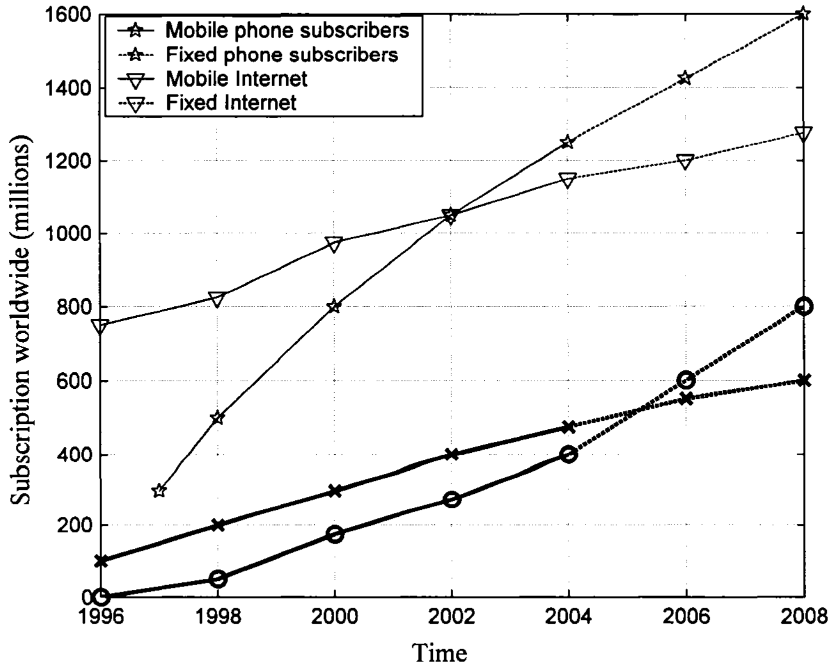

Fig. 1.2. Actual (solid) and predicted (dashed) growth in mobile and fixed phone subscribers [45].

challenges in supporting the target data rates, call reliability problems, short battery life). In addition, current target download and upload data rates for 3G systems (380 kbits/sec and 2.4 Mbits/sec) are only sufficient for brief news clips or small personal video sequences of low resolution [94]. To upload or download a high resolution archived video on 3G systems would require hours. (For instance, downloading a 4 GB movie file would take about four hours at the maximum 3G data rate of 2.4 Mbps.) Consequently, further improvements / developments of wireless CDMA technology are needed.

In line with the typical ten year development period between initial planning stages and full commercial roll out, the fourth generation (4G) wireless systems are expected to be first deployed around the year 2010 [45]. These systems are projected to increase data rates to 20 Mbps for upload and 100 Mbps for download scenarios, as illustrated in Fig. 1.3. Initial field tests related to 4G have been conducted by NTT DoCoMo in June 2004 [13], in order to demonstrate feasibility of high data rate communication beyond the 3G standard and to invest-

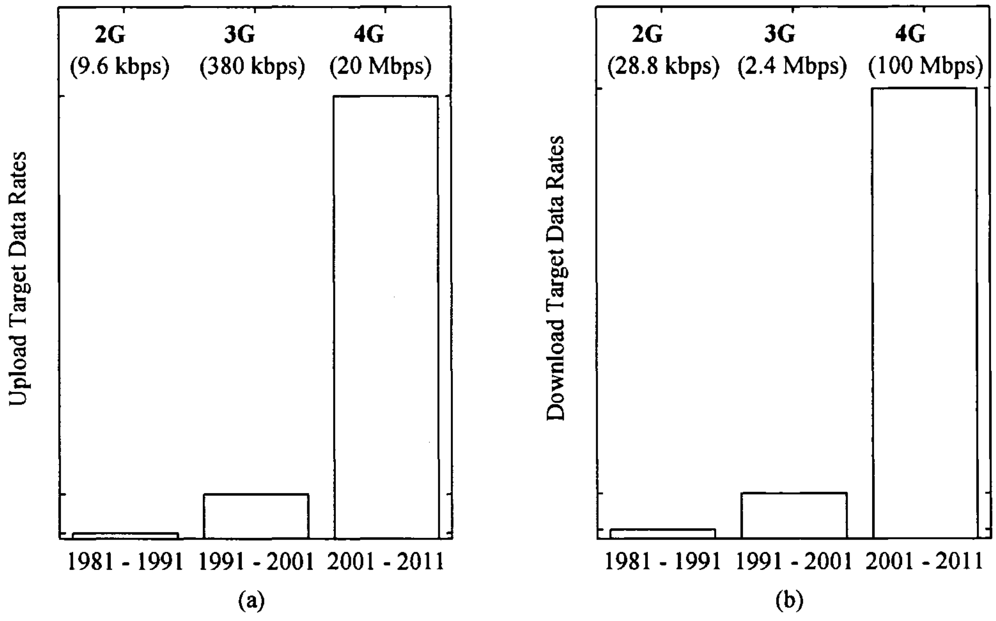

**Fig. 1.3. Target uplink and downlink data rates of digital wireless systems [36].**

igate potentially enabling technologies for this standard. In 4G systems, for instance, digital broadcasting and commercial wireless services are expected to be integrated to create new value-added services for end users [45]. To achieve high data rate requirements and efficient handling of multimedia services, future wireless systems have to be more spectrally efficient than current standards technology. Multi-input multi-output (MIMO) wireless communication systems based on multiple antennas are considered to be a key technology in achieving high spectral efficiencies [45] and have also been considered as a means to improve the 3G system performance [13].

## 1.2 Capacity Potential of MIMO Systems

The radio spectrum is a premium resource, as it has to be leased from a government agency and is divided among different wireless applications and service providers. It is interesting to remark that the high cost of leasing the radio - spectrum, for instance, the wireless spectrum for 3G services in Britain was auctioned for 22.5 billion pounds in 2000 [12]. Hence, there exists a clear incentive to maximize the revenue generation by using the allocated spectrum efficiently, i.e., transmitting as much data as possible within a given frequency band. However, wireless data transmission is subject to the detrimental effects of time-varying multipath fading channels, thermal noise from receiver's electronics and multi-user / multi-path interference. Fading can reduce the amplitude of the transmitted signal by as much as 20 dB [76], while interference from antennas of the same user or other users can result in a poor rendition of the transmitted signal.

Traditionally, frequency and time diversity methods, i.e., multiple transmissions of data, have been used for several decades as a means to counter the impact of fading channels. However, the time and frequency diversity methods reduce the overall system efficiency by requiring additional time slots and/or frequency spectrum. In contrast, MIMO spatial diversity techniques based on multiple transmit and receive antennas can re-use both allocated frequency spectrum and time slots. Through appropriate utilization of coding, signal processing techniques and spatial antenna separation, MIMO spatial diversity techniques can improve signal transmission over wireless channels in terms of both reliability and spectral efficiency.

Recently, MIMO systems have been theoretically shown to provide an order of magnitude increase in capacity / spectral efficiency, when compared to traditional single-input single-output (SISO) wireless systems [92]. This is shown in Fig. 1.4, for selected antenna configurations in an uncorrelated Rayleigh fading channel. This potential for high rates and spectral efficiencies was experimentally confirmed by the Bell Labs layered space-time (BLAST) system, which demonstrated a spectral efficiency of 25.9 bits/s/Hz at SNR = 27 dB using 8 transmit and 12 receive antennas [33]. Since channel coding was not employed in the BLAST system, high wireless SNRs were required to achieve target bit-error rates. Consequently, system performance was far from the channel capacity limit, i.e., the exploited MIMO channel could support even higher spectral efficiencies if error control coding were used.

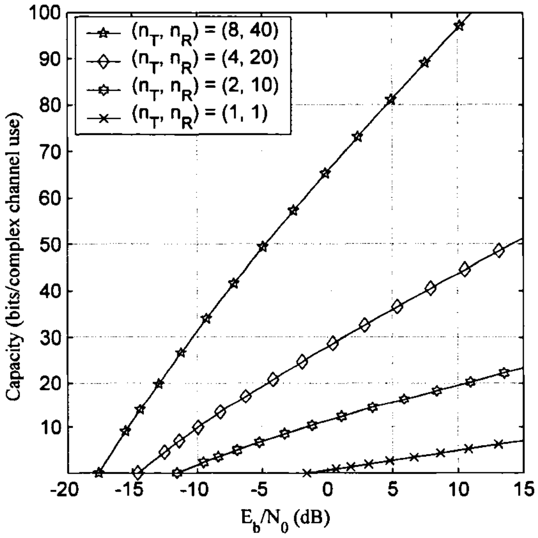

**Fig. 1.4. A plot of ergodic capacity for various transmit and receive antenna configurations in an uncorrelated Rayleigh fading channel.**

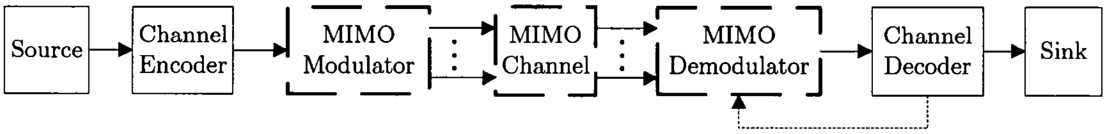

**Fig. 1.5. Schematic block diagram of a coded MIMO system.**

## 1.3 Channel Coding for Multiple Antenna Systems

Fig. 1.5 illustrates the schematic block diagram of a coded MIMO system. The channel encoder introduces redundancy into the message bits and this redundancy is used by the channel decoder to correct the effects of channel noise, interference, fading, etc. The channel encoder may be based on the serial concatenation of component encoders to achieve target bit error rate (BER) values. For instance, a Reed Solomon code [104] can be concatenated with an inner turbo code to provide a further reduction of achieved BER values to levels required for data, image or video communication (e.g., below $10^{-12}$ to $10^{-14}$). The MIMO modulator performs a similar function as a SISO modulator for every transmit antenna. However, the MIMO demodulator has to mitigate the negative effects of the channel and produce soft decisions on the coded bits. To improve performance, the coded MIMO system can employ an iterative processing loop between the MIMO demodulator and channel decoder, as will be discussed in detail in Chapter 4.

Exploiting the full capacity potential of wireless MIMO channels requires a shift from traditional diversity schemes, such as antenna selection, equal gain combining and/or maximum ratio combining. Furthermore, achieving near MIMO capacity[1] performance requires the use of powerful channel codes in order to combat the effects of fading, interference and noise. Initial attempts at coded transmission over MIMO channels included the design of space-time block codes

---

[1] Channel capacity represents the highest rate at which reliable data transmission is possible [81].

and linear dispersion codes [1], [40], [91]. These codes use simple encoding methods and maximum likelihood (or sphere-based) decoding at the receiver. However, due to their short block lengths, these codes operate at very high signal-to-noise ratios (SNRs), usually greater than 20 dB. Consequently, space-time trellis codes [89] were the first scheme to combine trellis-based channel coding and symbol mapping onto multiple transmit antennas. These codes achieve better performance than space-time block codes, but their decoding complexity becomes impractical for systems with many transmit antennas.

Due to their near-capacity performance on the additive white Gaussian noise (AWGN) channel [9], turbo-codes have become a part of the 3G wireless standard [96] and have also been successfully applied in other areas, e.g., space applications such as the European SMART-1 probe, the Mars Reconnaissance Orbiter and Messenger [35] and the DVB-RCS standard [27]. Because of their excellent performance and incorporation into existing standards, turbo codes are a natural candidate for efficient data communication over wireless MIMO channels. However, employing turbo codes in MIMO systems requires soft decision front-end signal detection in the receiver architecture. The computation of soft decisions on the transmitted MIMO symbols at the receiver in a low complexity manner is non-trivial, as the number of signal space points increase exponentially with the number of transmit antennas.

Prior work on (turbo-) coded MIMO systems can be classified based on the complexity of the MIMO signal detection technique being employed. In general, these schemes achieve better performance than the space-time trellis coded systems due to the use of turbo codes and/or iterative processing at the receiver. The coded MIMO systems of [55], [87], [98] use variations of the exponentially complex optimal soft decision MIMO signal detector and thus can only be used for a small number of antennas. Consequently, lower (polynomial) complexity signal detection schemes have been recently proposed, e.g., the modified sphere detection in [42] and MIMO signal detection in Turbo-BLAST [80].

Given that the 3G standard is CDMA based [97] and that the 4G standard may be based on the multi-carrier CDMA scheme [45], multi-user detection is an attractive tool to improve performance of these systems. However, the presence of multiple users further increases the complexity of (multi-user) MIMO signal detection and thus there is a need for even lower complexity soft decision signal detection for coded MIMO systems.

## 1.4 Thesis Contributions and Structure

We focus on the problem of uplink communication on a wireless MIMO channel, where the number of receive antennas at the base-station exceeds the number of transmit antennas at the mobile and the channel state information (CSI) is available at the receiver only. The main objectives of this research is to propose a low complexity turbo-coded MIMO transceiver architecture that achieves near capacity performance for various antenna configurations, present corresponding simulation results and develop two performance analysis techniques for the considered MIMO systems. The proposed techniques provide accurate bounds on BER performance in the waterfall and error floor regions for the proposed turbo-coded MIMO systems.

Chapter 2 reviews the turbo encoder and decoder structures and performance evaluation techniques for turbo codes on Gaussian noise channels. In addition, this chapter provides a review of MIMO wireless channel models, their corresponding ergodic capacity results and a brief overview of previously proposed coded MIMO systems.

Chapters 3, 4 and 5 discuss the research contributions of this dissertation, which have been presented in [57] – [70]:

- A new soft decision MIMO signal detector is proposed, which is of linear complexity in the number of transmit antennas, receive antennas and users.
- Symbol error rate performance of the proposed MIMO signal detector is analyzed in correlated and uncorrelated Rayleigh fading channels when channel state information (perfect and imperfect) is available at the receiver only.
- Three iterative receiver architectures for turbo-coded MIMO systems are presented that incorporate the proposed front-end signal detector. The first two architectures rely on single pass detection with turbo decoding or turbo demodulation. The third architecture includes a novel low complexity iterative processing loop between the signal detector and turbo decoder.
- Turbo-coded MIMO systems employing the three receiver architectures are simulated under correlated Rayleigh fading and single / multiple user scenarios for various antenna configurations. MIMO systems using the proposed iterative receiver architecture performed near the capacity limit in all cases.
- As an additional application, multi-head, multi-track digital recording systems are considered for the proposed detector and iterative MIMO receiver architecture, where the latter is modified appropriately to accommodate strong intertrack and intersymbol interference.
- The union bound based method for turbo codes on the AWGN channel [8] is extended to MIMO channels with correlated and uncorrelated fading to provide bounds on the BER performance of the turbo-coded MIMO system in the *error floor region.*
- A new performance analysis technique is developed to provide accurate (approximate) bounds on BER performance of the proposed turbo-coded MIMO system in the *waterfall region.* When compared to prior analysis techniques for turbo-coded SISO and MIMO systems, the technique is novel in its approach and results and can also provide accurate BER bounds for the considered digital magnetic recording systems.

The first two research contributions are discussed in Chapter 3, while the following three contributions are presented in Chapter 4. Chapter 5 elaborates on the last two contributions and Chapter 6 concludes with a summary of research achievements and directions for future work.

# Chapter 2

# Preliminaries

In this chapter, we review the multi-antenna (MIMO) wireless channel models under consideration and present recently derived MIMO channel capacity formulas. Encoding and decoding of turbo codes is described along with the performance analysis techniques of these codes on the additive white Gaussian noise channel. We conclude this chapter with a review of recent work on coded MIMO systems.

## 2.1 MIMO Channel Models

### 2.1.1 Slow Frequency Non-selective Raleigh Fading

Fig. 2.1 shows a schematic representation of a MIMO channel. This dissertation focuses on uplink transmission, where there are $n_T$ transmit antennas at the mobile and $n_R$ receive antennas at the base-station, $n_T < n_R$. The base-station is assumed to possess channel state information (CSI), whereas this information is unknown at the mobile transmitter due to the time varying nature of the channel. Consequently, the transmitter cannot pre-compensate for the effects of the MIMO channel. We considered a typical urban environment, which is highly detrimental to transmitted signals as no line of sight communication is assumed to be possible between the mobile and the base-station. The antennas at both ends of the com-

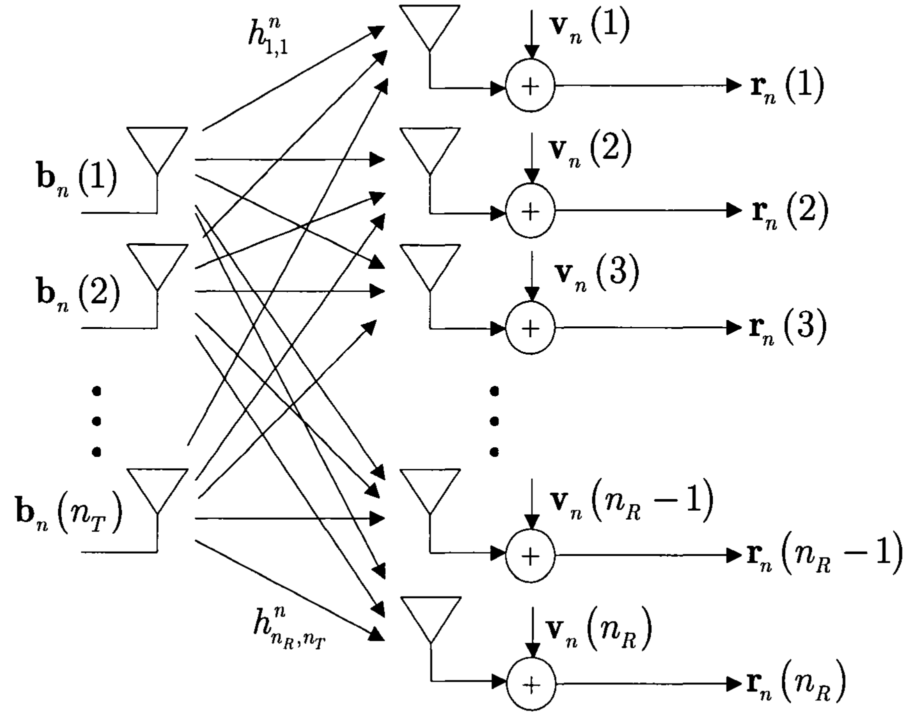

**Fig. 2.1. Schematic diagram of the MIMO wireless channel.**

munication link are spaced uniformly on a linear array and are omni directional, i.e., they radiate and receive from all directions in space.

The signals reaching the receive antennas can be modeled as arriving from a number of equivalent point sources or scatterers. Multipath fading is a process, where by the received signal is a sum of many reflections of the transmitted signal, each with different propagation time, phase and attenuation. The fading coefficients $h_n^{i,j}$, shown in Fig. 2.1, are typically described by the Rayleigh fading model, where the process is modeled as a sum of infinitely many (in practice it is enough with only a few) reflections from all angles uniformly distributed around the receiver [43].

The discrete-time representation of the MIMO channel at time instant $n$ is given by the $n_R$-by-$n_T$ channel matrix

$$\mathbf{H}_n = \begin{bmatrix} h_n^{1,1} & h_n^{1,2} & \cdots & h_n^{1,n_T} \\ h_n^{2,1} & h_n^{2,2} & \cdots & h_n^{2,n_T} \\ \vdots & \vdots & \ddots & \vdots \\ h_n^{n_R,1} & h_n^{n_R,1} & \cdots & h_n^{n_R,n_T} \end{bmatrix}, \tag{2.1}$$

where coefficient $h_n^{i,j}$ is the path gain from the $j$-th transmit to the $i$-th receive antenna, $1 \le j \le n_T$, $1 \le i \le n_R$. The MIMO channel is assumed to be frequency non-selective, i.e., the transmission bandwidth is smaller than the channel coherence bandwidth and the channel's frequency response is flat over the signal bandwidth, i.e., there is no intersymbol interference. We assume that the mobile transmitters are either moving at slow speeds or are almost stationary and thus, the channel is slowly changing, i.e., $\mathbf{H}_n$ is constant for a finite duration and then changes to a new independent realization.

The received signal at each of the $n_R$ antennas is a sum of Rayleigh faded transmitted signals and complex additive white Gaussian noise. The received vector $\mathbf{r}_n$ at the $n$-th time instant is given by

$$\mathbf{r}_n = \mathbf{H}_n \mathbf{b}_n + \mathbf{v}_n, \tag{2.2}$$

where $\mathbf{b}_n$ is the vector of transmitted modulation symbols and the elements of the complex Gaussian noise vector $\mathbf{v}_n$ are assumed to be independent and identically distributed (i.i.d.) with zero mean and variance of $\sigma^2 = N_0/2$ in the real and imaginary dimensions. If the antennas are spaced sufficiently apart and there exists a rich scattering environment between the transmitter and receiver, then an *uncorrelated* Rayleigh fading model can be assumed, i.e., the channel coefficients $h_n^{i,j}$ are i.i.d. realizations of a zero mean complex Gaussian random variable with variance 0.5 in the real and imaginary dimensions.

### 2.1.2 Correlated Rayleigh Fading

Spatial correlation can exist between antennas due to small antenna separations and/or due to presence of few scatterers around the transmitter and receiver. The MIMO channel matrix can be appropriately modified to incorporate spatial correlation [18] through the following expression

$$\mathbf{H}_n = \mathbf{C}_{RX}^{1/2}\mathbf{G}_n\mathbf{C}_{TX}^{1/2}. \tag{2.3}$$

The elements of $\mathbf{G}_n$ are assumed to be realizations of a zero mean complex Gaussian random variable with variance of 0.5 in the real and imaginary dimensions, while the real and symmetric matrices $\mathbf{C}_{TX}$ (of size $n_T$-by-$n_T$) and $\mathbf{C}_{RX}$ (of size $n_R$-by-$n_R$) represent the correlation between antennas.

We use Jakes' model [43] to describe the correlation between the $i$-th and $j$-th transmit antennas, which is given by

$$\mathbf{C}_{TX}(i,j) = J_0\left(2\pi\frac{d_{i,j}^{TX}}{\lambda}\right). \tag{2.4}$$

The transmission wavelength is $\lambda$, $d_{i,j}^{TX}$ is the distance between the $i$-th and $j$-th transmit antennas and $J_0(\bullet)$ is the Bessel function of the first kind and zero-th order. Fig. 2.2 (a) illustrates the plot of the power correlation between the transmit antennas (the square of the elements of $\mathbf{C}_{TX}$).

Spatial correlation at the base-station is determined by the distance between antenna elements, angular spread of the arrival incident waves and mean angle of arrival. Fig. 2.3 shows the MIMO scattering scenario illustrating the effect of the cluster of scatterers on the angular spread value. The angular spread is the average angular region over which all paths corresponding to the received signal are located [15]. The Pedersen et *al.* [74] correlation model for the base-station antennas is used throughout this dissertation[2]. Assuming the mean angle of arrival is zero (i.e., the received signals impinge from broadside), the correlation between the $i$-th receive antenna and $j$-th receive antenna is given by

$$\mathbf{C}_{RX}(i,j) = J_0\left(2\pi\frac{d_{i,j}^{RX}}{\lambda}\right) + \frac{2}{\beta^2}\left(1 - e^{-\frac{\sqrt{2}\pi}{\beta}}\right)\sum_{m=1}^{\infty}\frac{1}{\beta^{-2}+2m^2}J_{2m}\left(2\pi\frac{d_{i,j}^{RX}}{\lambda}\right), \tag{2.5}$$

where $\beta$ is the angular spread, $\lambda$ is the wavelength corresponding to the trans-

---

[2] The Pedersen et *al.* correlation model was developed as part of the METRA (Multi-Element Transmit and Receive Antennas) project, which was partially sponsored by the European Commission under the Information Society Technologies Programme.

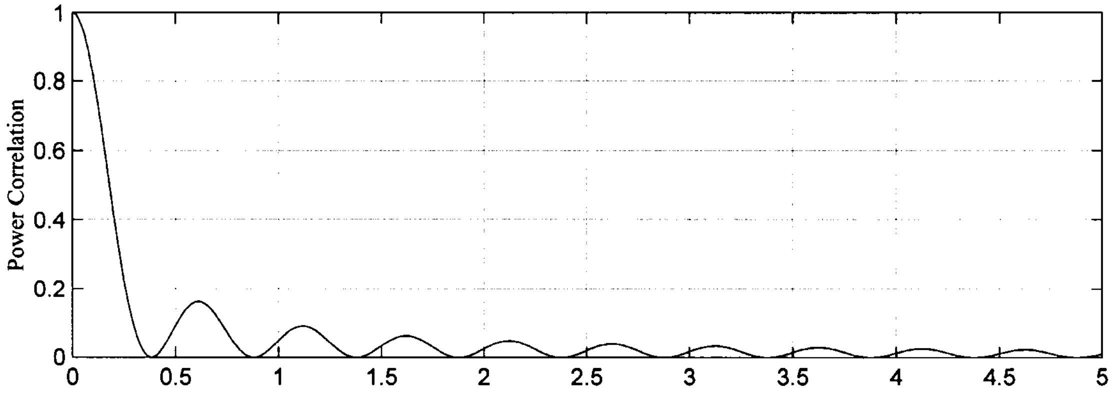

(a) Normalized Distance d/λ

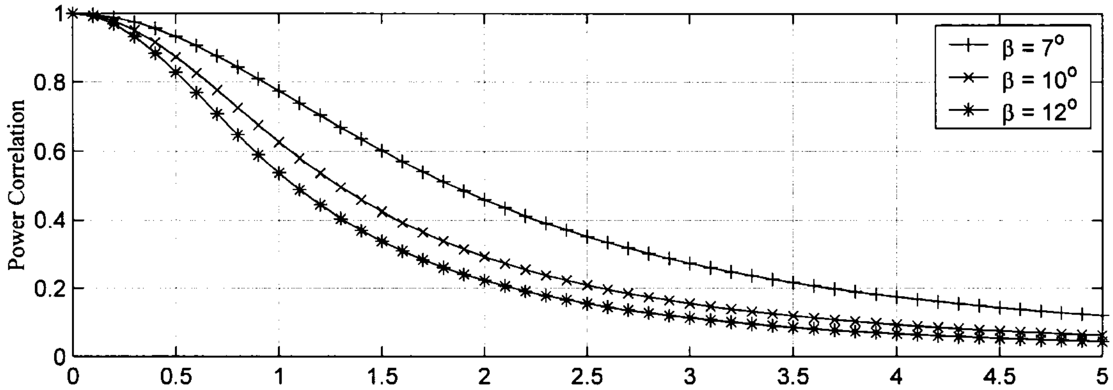

(b) Normalized Distance d/λ

**Fig. 2.2. An illustration of the power correlation models: (a) Jakes' model used at the mobile transmitter [43] and (b) Pedersen et *al.* model used at the base-station receiver [74].**

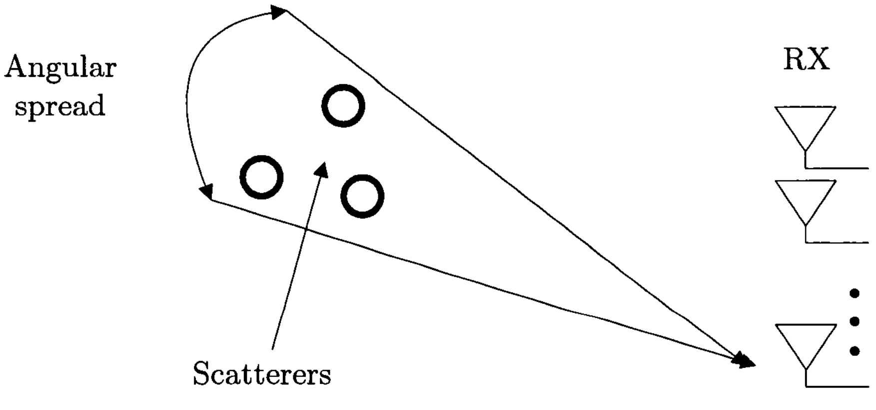

**Fig. 2.3. Illustration of the MIMO scattering scenario.**

mission frequency and $J_{2m}(\bullet)$ is the Bessel function of the first kind and $2m$-th order.

### 2.1.3 Physical Setup of an Urban Environment

In a typical urban environment, the mobile is surrounded by many scatterers and this fact usually results in the antennas being uncorrelated, i.e., $\mathbf{C}_{TX} = \mathbf{I}$ in (2.3). On the other hand, the base-station is placed at large heights and, as such, there are few nearby scatterers, which results in correlated antennas. Usually, an urban environment has values of angular spread $\beta$ between 7 and 12 degrees [75]. Fig. 2.2 (b) illustrates the power correlation between receive antennas (the square of the elements of $\mathbf{C}_{RX}$) versus antenna spacing for $\beta = 7$, 10 and 12 degrees.

### 2.1.4 Channel Models with Imperfect CSI and Multiple Users

The channel coefficients are usually estimated at the receiver using known training sequences transmitted by the mobile. Since the estimated parameters may not accurately represent the actual channel coefficients, (coded or uncoded) MIMO systems should be robust in accommodating channel estimation errors. At each time instant $n$, the receiver usually performs an (minimum mean squared error or MMSE) estimate of the channel and the corresponding estimated channel matrix $\hat{\mathbf{H}}_n$ is given by

$$\mathbf{H}_n = \hat{\mathbf{H}}_n + \varepsilon_n, \tag{2.6}$$

where $\varepsilon_n$ is an $n_R$-by-$n_T$ matrix due to estimation errors [106]. The estimated channel matrix $\hat{\mathbf{H}}_n$ and $\varepsilon_n$ are assumed to be uncorrelated and the entries of $\varepsilon_n$ are i.i.d. complex Gaussian random variables with zero mean and variance $\sigma_\varepsilon^2/2$ in each dimension [106], where $\sigma_\varepsilon^2 = E\left[\left(\mathbf{H}_n(i,j)\right)^2\right] - E\left[\left(\hat{\mathbf{H}}_n(i,j)\right)^2\right]$ for all $i = 1, 2, \ldots, n_R$ and $j = 1, 2, \ldots, n_T$. The variance $\sigma_\varepsilon^2$ indicates the quality of channel estimation and is assumed to be known at the receiver.

In Chapter 4, we will consider a synchronous multi-user CDMA system, where the mobiles and base-station employ multiple antennas as shown in

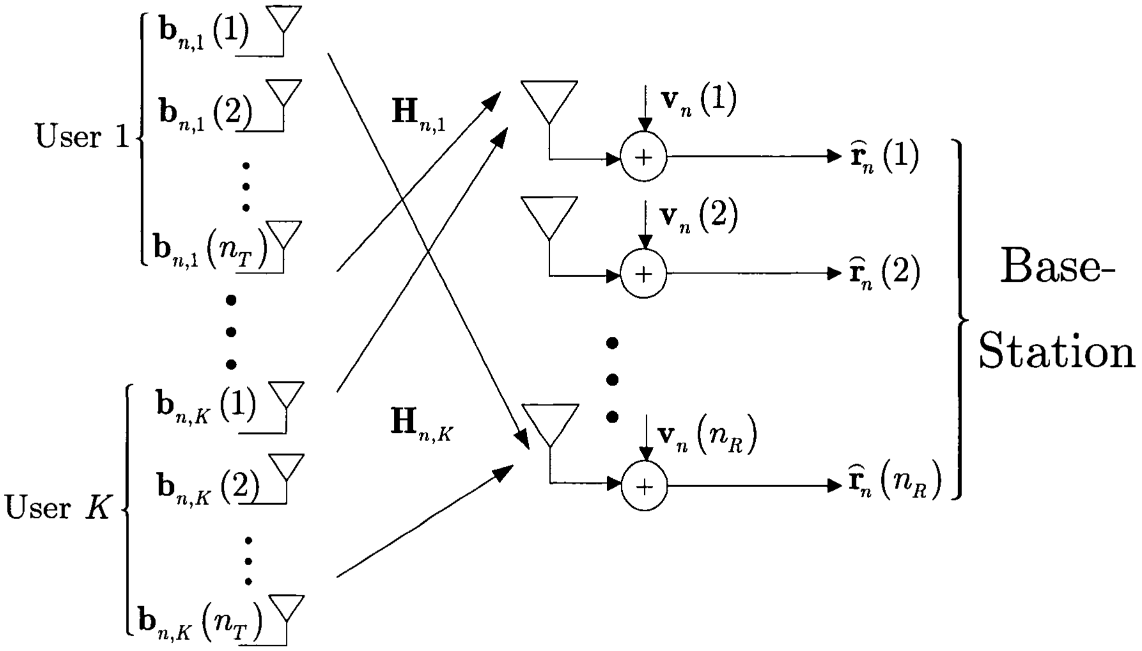

**Fig. 2.4. Schematic diagram of a multi-user MIMO wireless channel.**

Fig. 2.4. In this case, the received discrete-time signal vector at the base-station becomes

$$\hat{\mathbf{r}}_n = \sum_{l=1}^{K} \mathbf{H}_{n,l}\mathbf{b}_{n,l} + \mathbf{v}_n, \tag{2.7}$$

where $K$ is the number of active CDMA users, $\mathbf{b}_{n,l}$ and $\mathbf{H}_{n,l}$ are the $l$-th user's transmitted vector and channel matrix, respectively.

Due to their location, nearer users to the base-station would strongly interfere with signals transmitted by mobile users who are further away. To avoid this problem (known as the near-far effect), the base-station controls the power of individual mobile transmitters. Power control has been successfully implemented in existing DS-CDMA systems, such as the IS-95 based system. If perfect power control is employed then each user's channel matrix is given by (2.3). Imperfect power control can be incorporated into the channel model by modifying (2.3) as

$$\bar{\mathbf{H}}_{n,l} = \rho_{n,l}\mathbf{C}_{RX}^{1/2}\mathbf{G}_{n,l}\mathbf{C}_{TX}^{1/2}, \tag{2.8}$$

where $\rho_{n,l}$ is modeled as a realization of an i.i.d. random variable with log-normal distribution. The standard deviation of $20\log_{10}(\rho_{n,l})$ is the power control error and is typically about 1.5 to 2.5 dB [105].

## 2.2 Ergodic Capacity Results for Multi-Antenna Systems

Recently, Telatar has shown that MIMO systems could theoretically lead to large capacity gains over single antenna systems [92]. The ergodic capacity for MIMO fading channels represents the highest rate at which reliable transmission can be achieved for a given SNR and will be used as a benchmark to compare the simulated performance of coded MIMO systems considered in Chapter 4. The objective of this section is to summarize the capacity results for MIMO channels with uncorrelated and correlated fading, perfect and imperfect CSI at the receiver and for single and multi-user scenarios. In addition, we compare the capacity of MIMO channels, where different symbols are sent from each transmit antenna, to the capacity of traditional multi-antenna diversity schemes, such as antenna selection, equal gain and maximum ratio combining. This comparison highlights that the latter schemes cannot achieve the same capacity gains. (Details on the derivation of these capacity expressions are provided in Appendix A.)

### 2.2.1 Transmission Rate and SNR Definitions

For a MIMO system that employs $n_T$ transmit antennas, the transmission rate (in bits per MIMO channel use) is given by

$$R = n_T R_m R_c\,, \tag{2.9}$$

where $R_m$ is the modulation rate and $R_c = N_m/N_c$ is the channel coding rate (an $N_m$ bit message sequence is represented as an $N_c$ coded bit sequence). We consider a communication system that has a rate of transmission $R$, average received power (per channel use) $P$ and a noise variance of $\sigma^2 = N_0/2$ (in the real and imaginary dimensions). For such systems, then the SNR per (message) bit is given by

$$\frac{E_b}{N_0} = \frac{P}{2R\sigma^2}. \tag{2.10}$$

The SNR per bit allows comparison of systems with different antenna configurations, modulations and coding rates. (Since $E_b/N_0$ is employed throughout this thesis, we simply denote it as SNR.)

In a multi-user scenario, we assume that $K$ users are symmetric in terms of power and transmitted rates, i.e., each user transmits with power $P/K$. The corresponding transmission rate for each user is $R = n_T R_m R_s R_c$ bits per MIMO channel use, where $R_s$ is the rate due to the use of spreading sequences. Thus, the SNR for each user is given by $E_b/N_0 = P/(2RK\sigma^2)$.

## 2.2.2 Discussion of Ergodic MIMO Capacity Results

The ergodic capacity expression for a slow frequency non-selective Rayleigh fading channel with channel state information available at the receiver only [92] is given by

$$C_{MIMO} = E\left[\log_2\left(\det\left(\mathbf{I} + \frac{P}{2n_T\sigma^2}\mathbf{H}_n^H\mathbf{H}_n\right)\right)\right]. \tag{2.11}$$

The details of this derivation are provided in Appendix A.1. In [92], the expectation in (2.11) has been evaluated as an integral involving Laguerre polynomials. Instead, since the channel is assumed to be stationary and ergodic, we can approximate the expectation in (2.11) as an average over a large number of realizations of the channel matrix $\mathbf{H}_n$, i.e.,

$$C_N = \frac{1}{N}\sum_{n=1}^{N}\log_2\left(\det\left(\mathbf{I} + \frac{P}{2n_T\sigma^2}\mathbf{H}_n^H\mathbf{H}_n\right)\right) \xrightarrow[N\to\infty]{} C_{MIMO}. \tag{2.12}$$

For large values of $N$, the approximation of $C_N$ is close to $C_{MIMO}$. Equation (2.12) can also be used to determine the capacity of a correlated MIMO fading channel.

Fig. 2.5 shows the MIMO capacity for $(n_T, n_R) = (2,10)$, (4, 20) and (8, 40) antenna systems on an uncorrelated and correlated Rayleigh fading channel, respectively. The capacity values were calculated using (2.12) for $N =$ 100,000 and the correlation model assumes an angular spread $\beta$ of 10 degrees, an antenna

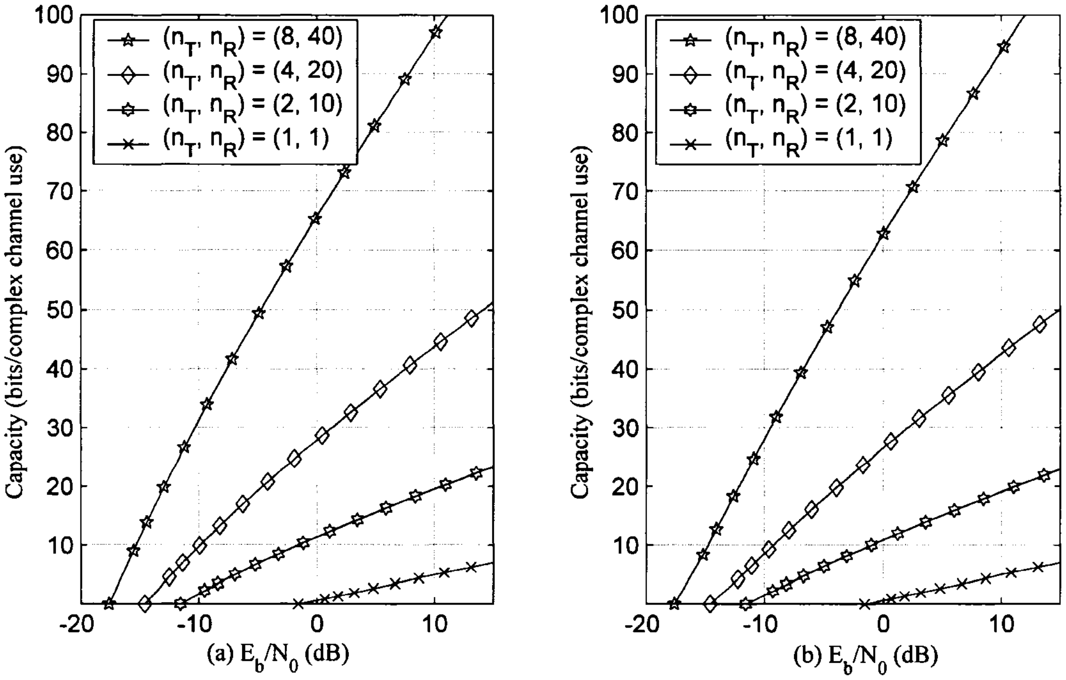

**Fig. 2.5. A plot of ergodic capacity for various antenna configurations on an (a) uncorrelated and (b) correlated slow frequency non-selective Rayleigh fading channel.**

spacing of $\lambda/2$ at the transmitter and $\lambda$ at the receiver. The plots illustrate the fast increase in MIMO capacity (in bits per channel use) with the number of antennas. They also show a 3 dB shift to the left for the MIMO capacity curves with doubling of the number of receive antennas. This shift is a result of collecting more power at the receiver due to having additional observations on the transmitted symbols. It is also interesting to observe that the effects of spatial correlation slightly reduce (i.e., by less than one dB) the capacity values from the uncorrelated case. At an $E_b/N_0$ of 10 dB, the SISO system has a capacity of 5 bits per channel use, while the (8, 40) system has a capacity of 100 bits per channel use. Thus, MIMO systems can potentially achieve higher transmission rates or, conversely, for the same rate, the required SNR is much lower.

### 2.2.3 Benefits of MIMO Systems over Traditional Diversity Schemes

The potential capacity gains of MIMO systems, shown in Fig. 2.5, rely on the fact that different symbols are sent from every transmit antenna. On the other hand, traditional diversity schemes, such as antenna selection, equal gain or maximum ratio combining, rely on transmitting the same symbol from every transmit antenna. It is important to note that the latter three techniques do not have the potential of high transmission rates, which are possible with MIMO systems on a slow, frequency non-selective Rayleigh fading channel when perfect CSI is available at the receiver only. In this section, we summarize the main results and compare them to the MIMO capacity and in Appendix A.2, we derive the capacity expressions for these three techniques.

In antenna selection systems, the same symbol is sent from all transmit antennas. At the receiver, the antenna that experiences the least fading (which corresponds to the row vector of $\mathbf{H}_n$ having the highest norm) is selected. Let the $i$-th receive antenna be selected ($i = 1, 2, \ldots, n_R$),

$$\mathbf{r}_n(i) = \sum_{j=1}^{n_T} \mathbf{H}_n(i,j) b_n + \mathbf{v}_n(i). \tag{2.13}$$

The corresponding ergodic channel capacity expression with antenna selection can be written as

$$C_{AS} = E\left[\log_2\left(1 + \frac{P}{2n_T\sigma^2}\left\|\sum_{j=1}^{n_T}\mathbf{H}_n(i,j)\right\|^2\right)\right]. \tag{2.14}$$

In equal gain combining systems, the receiver utilizes the observations from all receive antennas by correcting for the phase introduced by the channel and adding the receive antenna outputs. The channel capacity using this technique is given by

$$C_{EGC} = E\left[\log_2\left(1 + \frac{P}{2n_T\sigma^2}\sum_{i=1}^{n_R}\left\|\boldsymbol{\xi}_n(i)\right\|\right)\right], \tag{2.15}$$

where $\boldsymbol{\xi}_n(i) = \sum_{j=1}^{n_T}\mathbf{H}_n(i,j)$, $i = 1, 2, \ldots, n_R$, is the sum of the $i$-th row channel coefficients.

Maximum ratio combining is similar to equal gain combining, however, instead of correcting only for the phase introduced by the channel, each component of the received vector is weighted to maximize the post combining SNR [26].

In this case, the channel capacity using this technique is given by

$$C_{MRC} = E\left[\log_2\left(1+\frac{P}{2n_T\sigma^2}\sum_{i=1}^{n_R}\left\|\xi_n(i)\right\|^2\right)\right], \tag{2.16}$$

where $\xi_n(i) = \sum_{j=1}^{n_T} \mathbf{H}_n(i,j)$, $i = 1, 2, \ldots, n_R$.

Since the channel is stationary and ergodic, the expectations in (2.14), (2.15) and (2.16) can be numerically approximated by an average over many channel realizations. Fig. 2.6 compares the ergodic capacity results of traditional diversity schemes to corresponding MIMO system capacity for $(n_T, n_R)$ = (2, 10), (4, 20) and (8, 40) antenna configurations. (Note that the capacity values were evaluated as an average over 100,000 channel realizations.) Due to the benefits of spatial diversity, all the multiple antenna systems have higher channel capacities than equivalent SISO systems. The antenna selection technique provides the smallest capacity gain, as the receiver does not take into account observations from all antennas and this results in a loss of received power. Equal gain and maximum ratio combining systems have similar capacity limits that are about 4/3 times higher than the capacity of corresponding antenna selection systems. In all cases, antenna selection, equal gain and maximum ratio combining techniques saturate to a maximum of about 15 bits per complex channel use, while the corresponding MIMO systems exhibit a growth in capacity with increasing numbers of antennas, reaching over 100 bits per channel use for equivalent SNRs.

However, to achieve the capacity benefits of MIMO systems, sophisticated coded architectures are required to suppress co-antenna interference (which is non-existent in traditional diversity schemes) and noise. A review of prior coded MIMO systems is provided in Section 2.5. In Chapter 3 and Chapter 4, we propose a new MIMO signal detector and a corresponding turbo-coded architecture, which operates near the capacity limit in various scenarios.

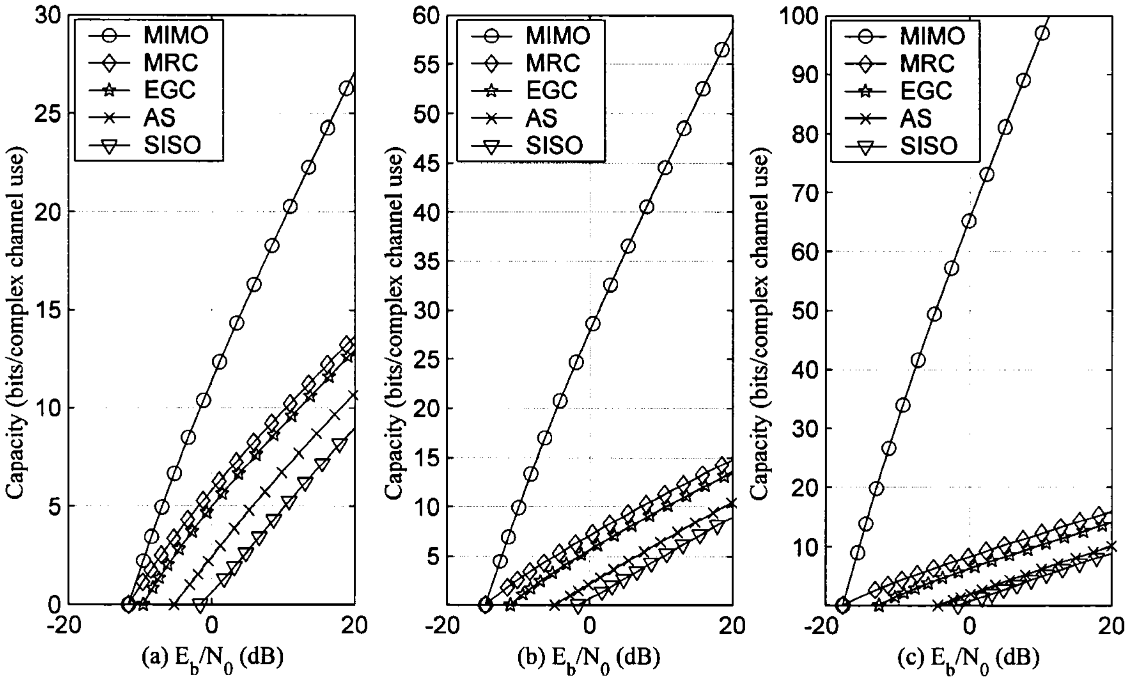

**Fig. 2.6. A plot illustrating the ergodic capacities for an uncorrelated Rayleigh fading channel using antenna selection (AS), equal gain combining (EGC), maximum ratio combining (MRC) and MIMO systems (different symbols transmitted from every antenna) for $(n_T, n_R)$ = (a) (2, 10), (b) (4, 20) and (c) (8, 40) antenna configurations.**

## 2.2.4 Ergodic Capacity for the Imperfect CSI Scenario

Using the channel model from (2.6), Yoo and Goldsmith [106] derived the following MIMO capacity expression for the case of imperfect CSI at the receiver

$$\hat{C} = E\left[\log_2\left(\det\left(\mathbf{I} + \frac{P}{2n_T\sigma^2}\hat{\mathbf{H}}_n^H\hat{\mathbf{H}}_n\frac{2\sigma^2}{2\sigma^2+\sigma_\varepsilon^2 P}\right)\right)\right]. \qquad (2.17)$$

The details regarding its derivation are provided in Appendix A.3. The channel estimation error impacts the capacity of the MIMO channel in two separate ways. The estimation error increases the effective noise power from $2\sigma^2$ to $2\sigma^2 + \sigma_\varepsilon^2 P$ and it reduces the average channel power gain from $E\left(\mathbf{H}_n^H\mathbf{H}_n\right) = n_R\mathbf{I}$ to $E\left(\hat{\mathbf{H}}_n^H\hat{\mathbf{H}}_n\right) = n_R\left(1-\sigma_\varepsilon^2\right)\mathbf{I}$ [106]. As before, the expectation in (2.17) is numerically approximated by averaging over many channel realizations of $\hat{\mathbf{H}}_n$, i.e.,

$$\hat{C}_N = \frac{1}{N}\sum_{n=1}^{N}\log_2\left(\det\left(\mathbf{I} + \frac{P}{2n_T\sigma^2}\hat{\mathbf{H}}_n^H\hat{\mathbf{H}}_n\frac{2\sigma^2}{2\sigma^2+\sigma_\varepsilon^2 P}\right)\right)\xrightarrow[N\to\infty]{}\hat{C}. \qquad (2.18)$$

This approximation is valid in both uncorrelated and correlated fading scenarios.

Fig. 2.7 illustrates the impact of channel estimation errors on the ergodic MIMO capacity for $(n_T, n_R)$ = (2, 10) and (4, 20) antenna configurations for a slow frequency non-selective uncorrelated and correlated Rayleigh fading channels. (We used an angular spread $\beta$ of 10 degrees, an antenna spacing of $\lambda/2$ at the transmitter and $\lambda$ at the receiver.) Fig. 2.7 also illustrates that the capacity curves for imperfect CSI saturate in the high SNR region, while the capacity for perfect CSI continues to increase. Conversely, at lower SNRs (our region of interest), the presence of channel estimation errors only slightly reduces the MIMO capacity. Nonetheless, the performance of specific coded MIMO systems can be significantly reduced by channel estimation errors.

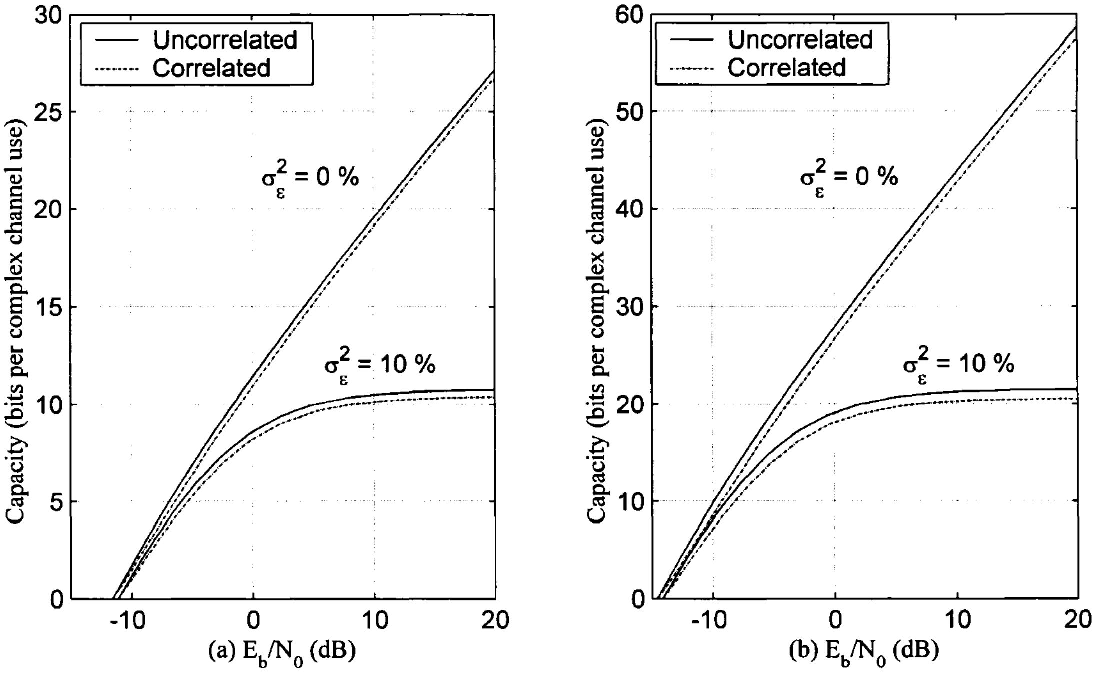

**Fig. 2.7. The comparison of the ergodic MIMO capacity curves for an (a) $(n_T, n_R)$ = (2, 10) and (b) $(n_T, n_R)$ = (4, 20) antenna configurations on an uncorrelated and correlated slow frequency non-selective Rayleigh fading with perfect channel state information and 10 % channel estimation errors.**

### 2.2.5 Multi-user MIMO Capacity

Rhee and Cioffi extended the work by Telatar for multi-user MIMO systems [78] using the channel model from (2.7). Expressing (2.7) in block matrix notation, one can observe the multi-user MIMO scenario as a single user case, where the vector and matrix dimensions have been scaled by the number of users $K$. Hence, assuming joint multi-user decoding at the receiver, the ergodic sum capacity is expressed as

$$C_{sum} = E\left[\log_2\left(\det\left(\mathbf{I} + \sum_{l=1}^{K} \frac{P_l}{2n_T\sigma^2}\mathbf{H}_{n,l}\mathbf{H}_{n,l}^H\right)\right)\right]. \tag{2.19}$$

where the capacity for each user is $C_{sum}/K$. In case of imperfect power control, the channel matrix of each user is given by (2.8). Assuming the power control error $\rho_{n,l}$ changes independently for each channel realization, we can still evaluate the ergodic capacity using (2.19), where $\bar{\mathbf{H}}_{n,l}$ replaces $\mathbf{H}_{n,l}$. (Recall that $\rho_{n,l}$ is a realization of a log-normal random variable [105].)

Fig. 2.8 illustrates the SNR per bit required to maintain rates of 2, 1 and 0.2 bits per MIMO channel use (for each user) on a symmetric $K$ user MIMO fading channel with $(n_T, n_R) = (2,10)$. It is interesting to observe the significant increase in the required user SNR, when more active users are present. For example, the SNR has to increase from -10 dB to about 10 dB for a corresponding increase of 0.2 to 2 bits per MIMO channel use on a 50 user system. The reason is that higher transmission rates for each user on the channel increases the "effective" multi-user interference due to more information being sent. Consequently, the SNR has to be significantly higher to compensate for this increased interference.

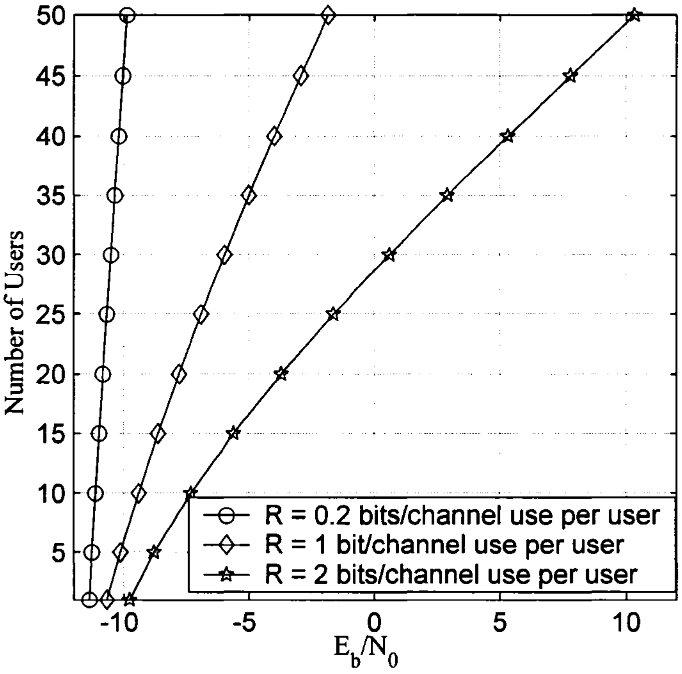

**Fig. 2.8. A plot illustrating the increase in SNR per user required to support a rate of 0.2, 1 and 2 bits per channel use per user on an uncorrelated Rayleigh fading channel with $n_T = 2$ transmit antennas and $n_R = 10$ receive antennas.**

## 2.3 Turbo Encoding and Decoding

In this section, we review the structure and process of turbo encoding and decoding. Turbo codes, proposed in [9], were shown to operate within a fraction of one dB of the capacity limit on Gaussian noise channels. Thus, over the last ten years, turbo codes have become parts of the 3G wireless and DVB-RCS standards [27], [96].

### 2.3.1 Parallel and Serial Turbo Encoding

A turbo encoder consists of parallel or serial concatenation of simpler component codes [9]. These component codes are usually recursive convolutional codes. A parallel concatenated (turbo) code is shown in Fig. 2.9, where the message sequence $\mathbf{m} \in \mathcal{M}$ ($\mathcal{M}$ is the set of message sequences of length $N_m$ bits) is encoded

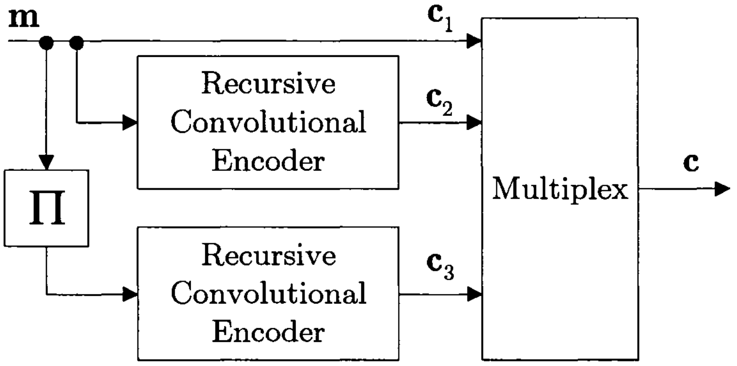

**Fig. 2.9. Schematic block diagram of a general turbo encoder using recursive convolutional codes.**

by the first component or constituent encoder, while the interleaver Π reorders the message symbols before they enter the second constituent encoder. The interleaver can be based on a pseudorandom permutation or a designed permutation, such as the $\mathcal{S}$-random interleaver [41]. The $\mathcal{S}$-random interleaver ensures that neighbouring bits in the original sequence are mapped to a certain sequence length ($\mathcal{S}$) apart.

The three outputs of the turbo encoder are the systematic bits $\mathbf{c}_1$ and the two streams of party bits $\mathbf{c}_2$ and $\mathbf{c}_3$, which are multiplexed into a single codeword $\mathbf{c}$ (of length $N_c$ bits). (The systematic stream can sometimes be combined with the parity stream at the output of the first encoder.) The recursive encoders can be represented by the feedforward and feedback generator polynomials, $(g_{ff}, g_{fb})$. Fig. 2.10 (a), (b) and (c) illustrate respectively the block diagram of the four state recursive convolutional encoder from [9] ($g_{ff} = 1 \oplus D^2$ and $g_{fb} = 1 \oplus D \oplus D^2$, where $\oplus$ denotes the binary XOR function), the eight state component code used in the 3G standard [96] ($g_{ff} = 1 \oplus D \oplus D^3$ and $g_{fb} = 1 \oplus D^2 \oplus D^3$) and the eight state two-bit-in-one-bit-out code from [10], which is related to the one used in the DVB-RCS standard [27] ($g_{ff} = 1 \oplus D^2 \oplus D^3$ and $g_{fb} = 1 + D + D^3$). (In Fig. 2.10 (c), $A$ and $B$ represent adjacent bits in the message stream.) The overall rate of the turbo code depends on the constituent encoders being used, e.g., if the component codes from Fig.

2.10 (a) or (b) are used, the overall rate is 1/3, while if the component code from Fig. 2.10 (c) is used, the overall rate is 1/2.

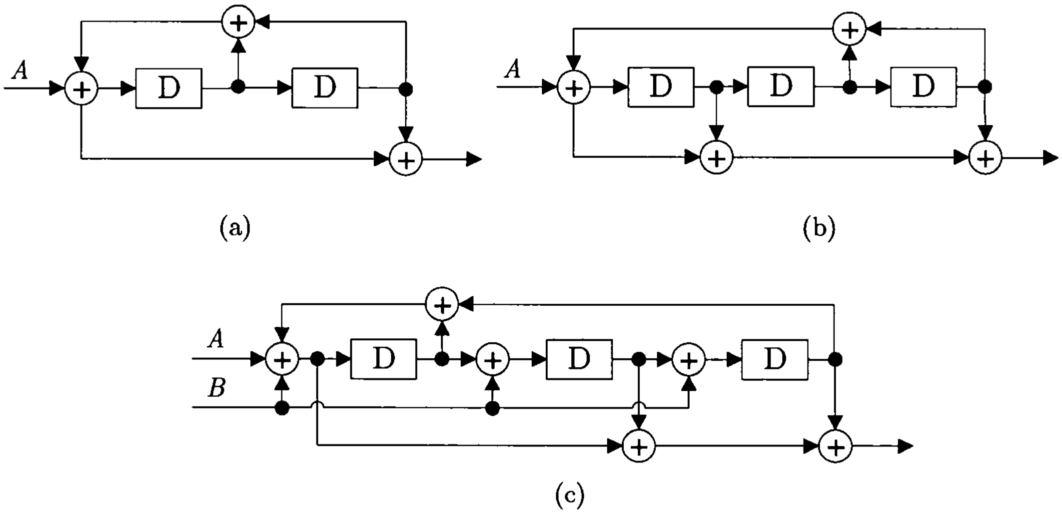

**Fig. 2.10. Schematic block diagram of (a) recursive convolutional code from Berrou and Glavieux [9], (b) recursive convolutional code from the 3G standard [96], (c) two-bit-in-one-bit-out recursive convolutional code from [10] related to the DVB-RCS standard [27].**

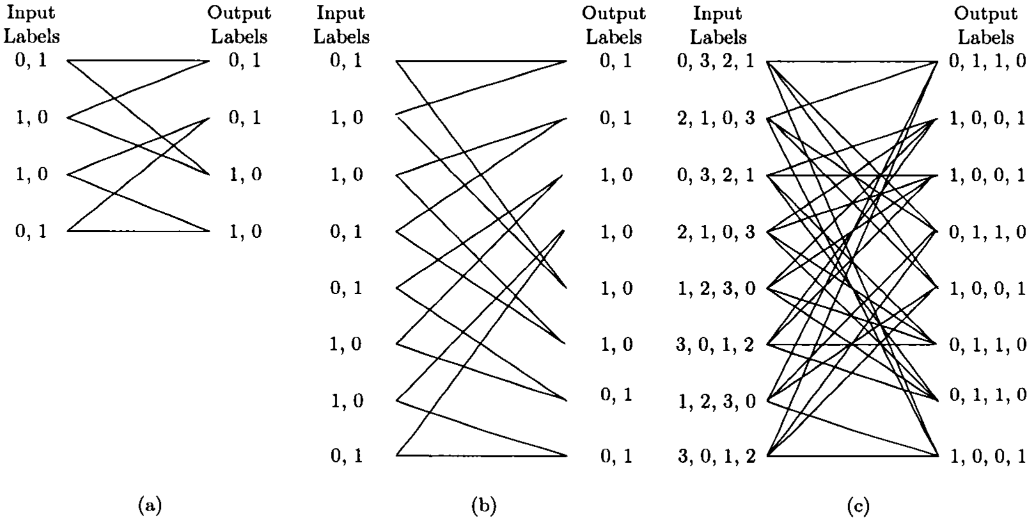

**Fig. 2.11. The corresponding complete trellis diagrams for one stage of the recursive convolutional codes from Fig. 2.10. (The input labels for (c) are in octal notation.)**

After the last message bit arrives at the constituent encoder, the corresponding trellis is terminated by forcing it to the all-zero state and generating corresponding parity bits in the process. This is to ensure that the last message bit is protected by several coded bits and that the encoder starts and finishes in the all-zero state. The constituent trellis termination is designed in such a way that the smallest number of forced state transitions is employed to reach the all-zero state from any particular state.

Recursive systematic convolutional codes can also be described using a trellis representation. A trellis is a layered directed graph, where the vertices are partitioned into sets $V_1, V_2, \ldots, V_N$, so that edges can only go from $V_\tau$ to $V_{\tau+1}$ in the $\tau$-th time instant. In a trellis, states corresponding to the convolutional encoder are depicted as a column of vertices and are repeated at each time instant. A *trellis stage* corresponds to proceeding from one column to the next and a *trellis path* is a series of states that an encoder has visited based on the input bit sequence. The complete trellises for one stage corresponding to each of the encoders in Fig. 2.10 are shown in Fig. 2.11.

Serially concatenated codes were proposed by Forney in 1966 [29] and were used in deep space exploration. However, these codes did not employ an interleaver between the two concatenated codes and iterative decoding was not used. A serial concatenated (turbo) code, shown in Fig. 2.12, consists of the message sequence being encoded by an outer encoder (Encoder 2) producing a coded bit sequence **p**, which is then reordered by an interleaver and passed to an inner encoder (Encoder 1). For instance, in a coded magnetic system, the inner constituent encoder is a precoded ISI channel, while the outer encoder can be based on a convolutional code. The discrete-time representation of an ISI recording channel is known as the partial response channel model [47] and has been classified by

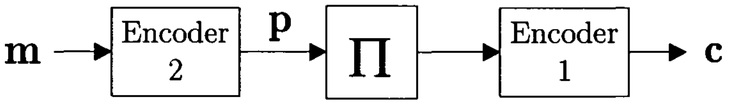

**Fig. 2.12. Schematic block diagram of a serially concatenated (turbo) code.**

Kabal and Pasupathy in [44] and channel equalization through maximum likelihood sequence detection was proposed by Kobayashi and Tang [46]. For example, the Class 4 partial response channel is given by $h_{PR4}(D) = 1 - D^2$ and its extended version is given by $h_{EPR4}(D) = (1-D)(1+D)^2$.

### 2.3.2 The BCJR Algorithm

We consider the probabilistic decoding of single trellis-based encoder. The notation and methodology of this section are adopted from [5]. A message sequence **m** is encoded using a trellis encoder (e.g., a convolutional encoder) into a coded sequence **c**, which is then mapped to modulated symbols and is transmitted over a noisy channel. The channel randomly maps the modulated symbols to a received sequence **r**. From the received sequence, the de-mapper generates likelihood estimates (conditional probabilities) on the received sequence given the coded bits are a zero or a one. If the channel were a MIMO fading channel, then a front-end signal detector would try to compensate for the effects of co-antenna interference. The probability of a particular $N_m$ bit message sequence **m** given the received sequence **r**, can be expressed as,

$$P(\mathbf{m}|\mathbf{r}) = P(\mathbf{c}|\mathbf{r}), \tag{2.20}$$

as the encoder is a one to one mapping. Using Bayes' rule, the right hand side of (2.20) can be further expanded as

$$\begin{aligned} P(\mathbf{m}|\mathbf{r}) &= \frac{P(\mathbf{r}|\mathbf{c})P(\mathbf{c})}{P(\mathbf{r})} \\ &= \frac{P(\mathbf{r}|\mathbf{c})P(\mathbf{m})}{P(\mathbf{r})}, \\ &= \frac{\left(\prod_{j=1}^{N_c} P\left(\mathbf{r}_j \middle| \mathbf{c}_j\right)\right)\left(\prod_{i=1}^{N_m} P(\mathbf{m}_i)\right)}{P(\mathbf{r})}. \end{aligned} \tag{2.21}$$

Every message sequence $\mathbf{m} \in \mathcal{M}$ ($\mathcal{M}$ is the set of messages) corresponds to a particular path $Q$ in the trellis. Hence, re-indexing the probabilities that form the product in the numerator of (2.21) to edge weights on the trellis, we get

$$P(\mathbf{m}|\mathbf{r}) = \frac{1}{P(\mathbf{r})} \prod_{e \in E(Q)} \gamma(e), \tag{2.22}$$

where $\gamma(e) = P\left(\mathbf{r}_j \middle| \mathbf{c}_j = l_O(e)\right) P\left(\mathbf{m}_i = l_I(e)\right)$ ($l_I(e)$ and $l_O(e)$ are the input and output labels of edge $e$). Note that the de-mapper for the demodulator would provide $P\left(\mathbf{r}_j \middle| \mathbf{c}_j = l_O(e)\right)$, and $P\left(\mathbf{m}_i = l_I(e)\right)$ is given by the *a priori* distribution of the source.

In order to evaluate $P(\mathbf{m}|\mathbf{r})$ efficiently, we use the BCJR algorithm [4], which is a special case of the path counting algorithm and can be formulated using matrix notation [5]. Let $N$ be the number of stages in the trellis and let $\blacklozenge_n$ be the edge weight matrix for the $n$-th stage, $n$ = 1, 2, ..., $N$. Let edge $e_{n,p,q}$ connect states $p$ and $q$ in the $n$-th stage, and $\mathbf{\Gamma}_n(p,q)$ is given by $\gamma\left(e_{n,p,q}\right) = P\left(\mathbf{r}_j \middle| \mathbf{c}_j = l_O\left(e_{n,p,q}\right)\right) P\left(\mathbf{m}_i = l_I\left(e_{n,p,q}\right)\right)$. The arrays $\mathbf{\Gamma}_1$ and $\mathbf{\Gamma}_N$ are row and column vectors, respectively as all paths through the trellis are assumed to start and end in the zero state. In addition, the decoder calculates two support quantities: the forward and backward metrics for each stage. For $n$ = 1, 2, ..., $N$, the forward metric, $\boldsymbol{\alpha}_n$, of size one-by-$L$ ($L$ is the number of states), is the sum of all weighted paths from 0-th state in the first stage to each state at the $n$-th stage,

$$\boldsymbol{\alpha}_n = \boldsymbol{\alpha}_0 \mathbf{\Gamma}_1 \mathbf{\Gamma}_2 \cdots \mathbf{\Gamma}_n, \tag{2.23}$$

where $\boldsymbol{\alpha}_0 = 1$. Similarly, the backward metric is the sum of all weighted paths from the 0-th state in the $N$-th stage to each state at the $n$-th stage and is defined as,

$$\boldsymbol{\beta}_n = \mathbf{\Gamma}_{n+1} \mathbf{\Gamma}_{n+2} \cdots \mathbf{\Gamma}_N \boldsymbol{\beta}_N, \tag{2.24}$$

where $\boldsymbol{\beta}_N = 1$ and $\boldsymbol{\beta}_n$ is a $L$-by-one matrix. Conceptually, the backward metric is the same as the forward metric, except that it is evaluated starting from the end of the trellis. Therefore, the total number of distinct paths from the 0-th state in the first stage to the 0-th state in the $N$-th stage is given by $\boldsymbol{\alpha}_N$ and $\boldsymbol{\beta}_0$ as well as by the product $\boldsymbol{\alpha}_n \boldsymbol{\beta}_n$ in the $n$-th stage of the trellis, $n$ = 1, 2, ..., N.

The probability, $P\left(\mathbf{m}_i = 0 \middle| \mathbf{r}\right)$ is equivalent to finding the number of paths passing through the edge, where the $i$-th bit of the message sequence is zero,

$\mathbf{m}_i = 0$, over the total number of paths. For example, let $\mathbf{m}_i$ correspond to the $n$-th trellis stage and the *a posteriori* probability on $\mathbf{m}_i = 0$ can be written as

$$P\left(\mathbf{m}_i = 0 \middle| \mathbf{r}\right) = \frac{\boldsymbol{\alpha}_{n-1}\boldsymbol{\Gamma}^*_n\boldsymbol{\beta}_n}{\boldsymbol{\alpha}_n\boldsymbol{\beta}_n}, \tag{2.25}$$

where $*$ indicates that $\boldsymbol{\Gamma}_n$ has been modified such that the edges corresponding to $\mathbf{m}_i = 1$ are set to zero. Using the same forward, backward metrics and edge weight matrix, an analogous operation as shown in (2.25) can be performed to generate the *a posteriori* probabilities on the coded bits. The BCJR decoder can output either an array of *a posteriori* probabilities:

$$\begin{bmatrix} P\left(\mathbf{m}_1 = 0 \middle| \mathbf{r}\right) & P\left(\mathbf{m}_2 = 0 \middle| \mathbf{r}\right) & & P\left(\mathbf{m}_{N_m} = 0 \middle| \mathbf{r}\right) \\ P\left(\mathbf{m}_1 = 1 \middle| \mathbf{r}\right) & P\left(\mathbf{m}_2 = 1 \middle| \mathbf{r}\right) & ,\ldots, & P\left(\mathbf{m}_{N_m} = 1 \middle| \mathbf{r}\right) \end{bmatrix} \tag{2.26}$$

or in the case of binary encoders, an array of logarithmic ratios of *a posteriori* probabilities:

$$\boldsymbol{\Lambda}(\mathbf{m}|\mathbf{r}) = \left[\log\left(\frac{P\left(\mathbf{m}_1 = 1 \middle| \mathbf{r}\right)}{P\left(\mathbf{m}_1 = 0 \middle| \mathbf{r}\right)}\right) \log\left(\frac{P\left(\mathbf{m}_2 = 1 \middle| \mathbf{r}\right)}{P\left(\mathbf{m}_2 = 0 \middle| \mathbf{r}\right)}\right), \ldots, \log\left(\frac{P\left(\mathbf{m}_{N_m} = 1 \middle| \mathbf{r}\right)}{P\left(\mathbf{m}_{N_m} = 0 \middle| \mathbf{r}\right)}\right)\right]. \tag{2.27}$$

The BCJR algorithm can be implemented using log-ratios of the corresponding likelihood estimates and probabilities. The advantages of the log domain are that the dynamic range improves, memory savings (e.g., in (2.26), we have a 2-by-$N_m$ array, while in (2.27), we only need to store a 1-by-$N_m$ vector) and renormalization of the probabilities is not required. However, when the message and / or codeword alphabets have more than two elements (e.g., equalization on an ISI channel), it is advantageous to use probabilities. The probabilities and their corresponding log-ratios for the binary case are interchangeable. For instance, let $p_1$ and $p_0$ be the probability that a bit is 1 and 0, respectively and $\Lambda = \log\left(p_1/p_0\right)$. We can define the following relation for $p_1$ and $p_0$:

$$p_1 = \frac{e^{\Lambda}}{1+e^{\Lambda}}, p_0 = \frac{1}{1+e^{\Lambda}}. \tag{2.28}$$

As a final note, the addition operations in the matrix multiplication of (2.25) can be performed using a lookup table.

### 2.3.3 Iterative Turbo Decoding

The notation and methodology of this section are adopted from [6]. Given the turbo encoder structure in Fig. 2.9, optimal decoding that minimizes the bit error probability would be too complex, as the number of states of the joint trellis (of both encoders) would increase exponentially with message block length. A sub-optimal structure was proposed in [9], which consists of two separate decoders connected in a loop. One constituent decoder operates on the first encoder's output and the systematic stream. The other constituent decoder operates on the second encoder's output. In the iterative decoding loop, the two decoders exchange information on the message bits or the first encoder's coded bits in case of parallel or serial turbo codes, respectively.

Fig. 2.13 illustrates the turbo decoder structure for a parallel concatenated code. The two BCJR decoders are represented as $\varphi_1$ and $\varphi_2$. The turbo decoder, in the $i$-th iteration can be described as

$$\begin{aligned} \mathbf{x}_1^i &= \varphi_1\left(\mathbf{d}_1, \mathbf{x}_2^{i-1}\right) - \mathbf{x}_2^{i-1} \\ \mathbf{x}_2^i &= \varphi_2\left(\mathbf{d}_2, \mathbf{x}_1^i\right) - \mathbf{x}_1^i, \end{aligned} \tag{2.29}$$

where $\mathbf{d}_1$ and $\mathbf{d}_2$ are log-likelihood ratio (LLR) vectors on the coded bits from the two encoders produced by the de-mapper for the demodulator ($\mathbf{d}_1$ also includes LLRs on the systematic bits) and $\mathbf{x}_2^0 = [0,0,\ldots,0]$. We assume that appropriate interleaving, de-interleaving is performed at the front, and back ends of the BCJR decoders. The outputs of the decoding functions are logarithmic ratios on

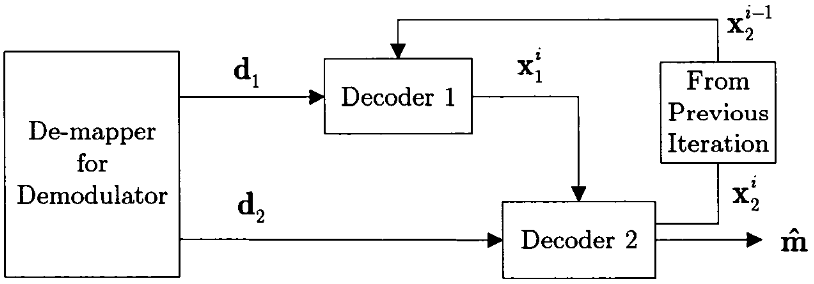

**Fig. 2.13. Schematic block diagram of the turbo decoder for a parallel concatenated code.**

the *a posteriori* probabilities,

$$\begin{aligned}\varphi_1\left(\mathbf{d}_1,\mathbf{x}_2^{i-1}\right) &= \Lambda\left(\mathbf{m}\,|\,\mathbf{d}_1,\mathbf{x}_2=\mathbf{x}_2^{i-1}\right)\\ \varphi_2\left(\mathbf{d}_2,\mathbf{x}_1^{i}\right) &= \Lambda\left(\mathbf{m}\,|\,\mathbf{d}_2,\mathbf{x}_1=\mathbf{x}_1^{i}\right),\end{aligned} \tag{2.30}$$

where vectors $\mathbf{x}_1$ and $\mathbf{x}_2$ are known as extrinsic information. The elements of these vectors are treated as if they contain independent log-ratios on the message bits and are fed as *a priori* information to the next decoder. The subtraction that is performed in (2.29) ensures that the next decoder only receives new information (innovation) on the message bits. Finally, hard decisions on the message bits can be determined by thresholding the output of decoder 2, i.e.,

$$\hat{\mathbf{m}} = u\left(\Lambda\left(\mathbf{m}\,|\,\mathbf{d}_2,\mathbf{x}_1^{i}\right)\right), \tag{2.31}$$

where $u(x)=1$ if $x>0$ and $u(x)=0$ if $x<0$.

Fig. 2.14 illustrates the schematic block diagram of the turbo decoder for a serially concatenated code. The turbo decoder, in the $i$-th iteration can be described as

$$\begin{aligned}\mathbf{x}_1^{i} &= \varphi_1\left(\mathbf{d},\mathbf{x}_2^{i-1}\right)-\mathbf{x}_2^{i-1}\\ \mathbf{x}_2^{i} &= \varphi_2\left(\mathbf{x}_1^{i}\right)-\mathbf{x}_1^{i},\end{aligned} \tag{2.32}$$

where $\mathbf{d}$ is the log-likelihood ratio vector on the coded bits from the outer encoder produced by the de-mapper for the demodulator and $\mathbf{x}_2^0=[0,0,\ldots,0]$. The decoding functions $\varphi_1$ and $\varphi_2$ produce logarithmic ratios on the outer encoder's coded bits and message bits, respectively:

$$\begin{aligned}\varphi_1\left(\mathbf{d},\mathbf{x}_2^{i-1}\right) &= \Lambda\left(\mathbf{p}\,|\,\mathbf{d},\mathbf{x}_2=\mathbf{x}_2^{i-1}\right)\\ \varphi_2\left(\mathbf{x}_1^{i}\right) &= \Lambda\left(\mathbf{m}\,|\,\mathbf{x}_1=\mathbf{x}_1^{i}\right).\end{aligned} \tag{2.33}$$

The extrinsic information vectors $\mathbf{x}_1$ and $\mathbf{x}_2$ are treated as if they contain independent log-ratios on the coded bit sequence $\mathbf{p}$ from the outer encoder. The decisions on the message bits are once again determined by making hard decisions at the output of decoder 2,

$$\hat{\mathbf{m}} = u\left(\Lambda\left(\mathbf{m}\,|\,\mathbf{x}_1^{i}\right)\right). \tag{2.34}$$

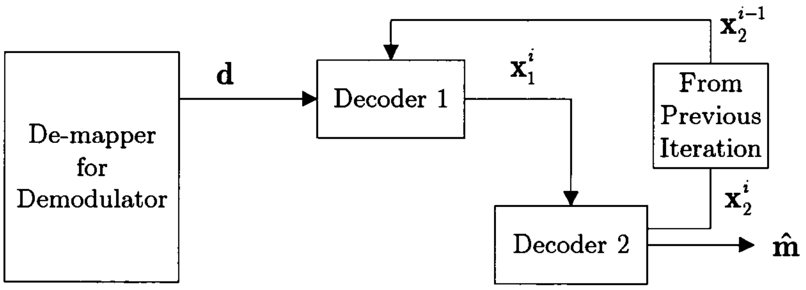

**Fig. 2.14. Schematic block diagram of the turbo decoder for a serially concatenated code.**

## 2.4 Performance Analysis Techniques for Turbo Codes

### 2.4.1 Motivation

In addition to Monte Carlo simulations, performance analysis techniques provide faster evaluation of bit error rate (BER) curves and permit parametric sensitivity analysis. In the high SNR region, reliable simulations of turbo codes to estimate BER can be extremely long and is usually not feasible without dedicated hardware. As an alternative, analytical or approximate methods such as the union bound based method [8], [23] may be used. The union bound based method uses the input-output weight enumerating functions of the code to establish the BER performance. Recently, the EXIT chart technique [16] has been proposed as a semi-analytical method to determine the SNR threshold when the turbo decoder starts to converge, i.e., the start of the waterfall region. This technique enables speedy evaluation of the effects of design parameters, such as the use of different types of constituent encoders, on system performance.

We focus on the analysis of the rate 1/3 turbo code from [9] using the component code shown in Fig. 2.10 (a), over an AWGN channel. We consider the union bound based results and describe the methodology of constructing EXIT charts for this code.

### 2.4.2 The Union Bound Based Method

The union bound establishes turbo code performance in the region where Monte Carlo simulation techniques require lengthy simulation time, i.e., the high SNR region. The bound is evaluated assuming maximum likelihood decoding of turbo codes and is independent of the interleaver being used. The evaluation of the union bound for turbo codes differs with respect to the union bound for convolutional codes in four different ways.

- The bounds require a term-by-term joint enumeration of all possible combinations of input weights and output weights of error events.
- Since turbo codes are block codes, we need to enumerate compound error events, which include more than one excursion from the all-zero state.
- Evaluation of the bound is intractable for any particular interleaver.
- The bounds are developed assuming maximum likelihood (ML) decoding. However, in practice, ML decoding of turbo codes is impractical even for small interleaver sizes. The iterative decoding structure is sub-optimal, i.e., it is possible in certain scenarios that the ML decoder will converge to the correct codeword but the turbo decoder may not. Hence, the simulated performance may not correspond exactly to the bound.

To evaluate the bound requires knowledge of the input-output weight enumerating function, which is the number of message sequences with a particular Hamming weight and a corresponding codeword Hamming weight. However, this is intractable even for small massage block lengths, as it would require the encoding of $2^{N_m}$ message sequences, where $N_m$ is the number of message bits. To overcome this difficulty, Benedetto and Montorsi developed the concept of the uniform interleaver, which is defined as follows [8].

*Definition*: A uniform interleaver of length $N_m$ is a probabilistic device, which maps a given message sequence of Hamming weight $w$ into all distinct $\binom{N_m}{w}$ permutations with equal probability $1\Big/\binom{N_m}{w}$.

The use of the uniform interleaver permits evaluation of the bound in terms of input-output weight enumerating functions of the two constituent encoders. The resulting bound represents the BER performance averaged over all possible interleavers. The bound on the probability of bit error, assuming BPSK signalling, is approximately evaluated as

$$P_b \leq \sum_{w=1}^{N_m} \frac{w}{N_m} \binom{N_m}{w} E_{d|w}\left[ Q\left( \sqrt{\frac{2dE_s}{N_0}} \right) \right], \tag{2.35}$$

where the average power per BPSK symbol is $E_s$ and $\sigma^2 = N_0/2$ is the variance of the additive noise [23]. (Equation (2.35) is derived in Chapter 5.) The expectation $E_{d|w}[\bullet]$ is based on $p(d|w)$, which is the conditional probability of producing an overall codeword of weight $d$ given an input sequence $\mathbf{m}$ of weight $w$. Using the uniform interleaver definition, we can decompose $p(d|w)$ as

$$p(d|w) = p(d_1, d_2, d_3|w) = p_1(d_1|w) p_2(d_2|w) p_3(d_3|w), \tag{2.36}$$

where $d = d_1 + d_2 + d_3$ and $d_1, d_2, d_3$ correspond to the weights of the codeword fragments $\mathbf{c}_1$, $\mathbf{c}_2$ and $\mathbf{c}_3$, shown in Fig. 2.9. The conditional probability $p_1(d_1|w)$ = 1 when $d_1 = w$ and zero otherwise (as $\mathbf{c}_1$ corresponds to the systematic stream). The probabilities $p_2(d_2|w)$ and $p_3(d_3|w)$ are expressed as

$$p_2(d_2|w) = \frac{t(N_m, w, d_2)}{\binom{N_m}{w}} \text{ and } p_3(d_3|w) = \frac{t(N_m, w, d_3)}{\binom{N_m}{w}}, \tag{2.37}$$

where $\binom{N_m}{w}$ is the number of codewords corresponding to a message sequence $\mathbf{m}$ with Hamming weight $w$. The input-output weight enumerating functions of the constituent encoders are given by $t(N_m, w, d_2)$, $t(N_m, w, d_3)$ and can be evaluated using the method described in [23].

The union bound and corresponding simulation results are shown in Fig. 2.15 for a message block length of 100 and 1,000 bits. Due to time and memory restrictions, the bound for $N_m$ = 1,000 bits was only calculated until an input and output Hamming weight of 100. The bound closely approximates the simulated performance in the error floor region, but abruptly diverges for SNR values

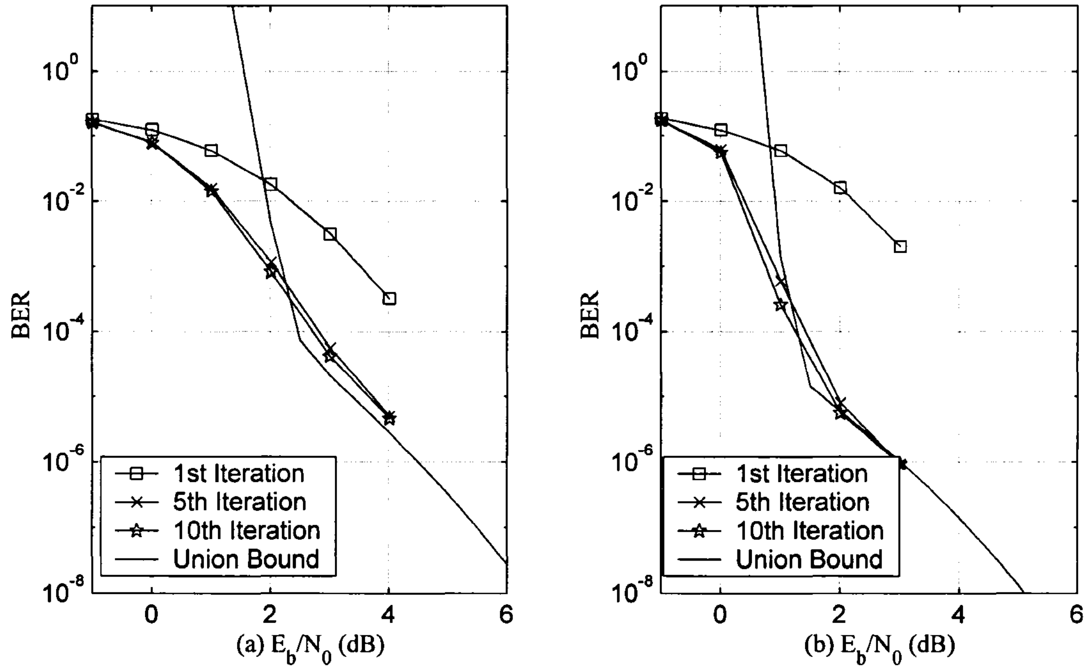

**Fig. 2.15. Comparison of the union bound versus simulated bit error rates for a rate 1/3 turbo code and a message block size of (a) 100 and (b) 1,000 bits.**

below the cutoff rate, given by $E_b/N_0 = 10\log_{10}\left(-\ln\left(2^{1-R_c}-1\right)/R_c\right) \approx 2$ dB for $R_c = 1/3$ [7].

## 2.4.3 The EXIT Chart Technique

Extrinsic information on the message bits are new estimates that are exchanged between the two constituent decoders. As described in Section 2.3.3, they are computed using the *a posteriori* probabilities by one of the constituent decoders and fed as *a priori* estimates on the message bits to the next one. Ten Brink proposed a semi-analytical technique to describe the flow of extrinsic information between the two constituent decoders [16]. The technique relies on calculating the mutual information of the extrinsic and *a priori* knowledge (with respect to the message bits) and plotting the extrinsic information transfer (EXIT) chart. These charts provide a graphical description of the turbo decoding process and are used to predict the SNR value corresponding to the start of the waterfall region.

The idea behind EXIT charts is to analyze the constituent decoders separately and thus predict the performance of the overall turbo decoder. The message sequences are encoded using the component code and the *a priori* input to the channel decoder is assumed to be Gaussian distributed. Using channel observations on the component code and the randomly generated *a priori* information, a *single* BCJR decoder is used to generate extrinsic information. The mutual information on the message sequence is calculated using the *a priori* and extrinsic information. However, the extrinsic information is not assumed to be Gaussian distributed, but instead, the mutual information is given by an average over many message sequences [99]. The extrinsic information transfer characteristics for the recursive convolutional code from [9] ($g_{ff} = 1 \oplus D^2$ and $g_{fb} = 1 \oplus D \oplus D^2$) is shown in Fig. 2.16 (a) for various values of $E_b/N_0$. The function is monotonically increasing with a maximum value of 1. At larger values of SNR, the curve begins at a higher mutual information value.

The transfer characteristics of both decoders are used to construct the EXIT chart for the turbo decoder (the axes are swapped for the second decoder). This is shown in Fig. 2.16 (b) for the turbo code from [9] for various values of $E_b/N_0$. Since the two constituent encoders are identical, the transfer characteristics are symmetrical about the $y = x$ line. The EXIT chart describes a tunnel through which the decoding trajectory must pass. If the transfer characteristics of the two decoders intersect, then the tunnel closes and the turbo decoder does not converge. Conversely, if the tunnel is wide, then the turbo decoder will converge within a small number of iterations. Hence, the SNR value, where the two transfer characteristics are just touching each other corresponds tothe start of the waterfall region. Fig. 2.16 (b) indicates that the decoder should converge at SNR values slightly higher than 0 dB.

For a particular SNR value, the average decoding trajectory can be superimposed on the EXIT chart. To determine the points on the trajectory, a codeword generated by a turbo encoder is mapped to a BPSK symbol vector and

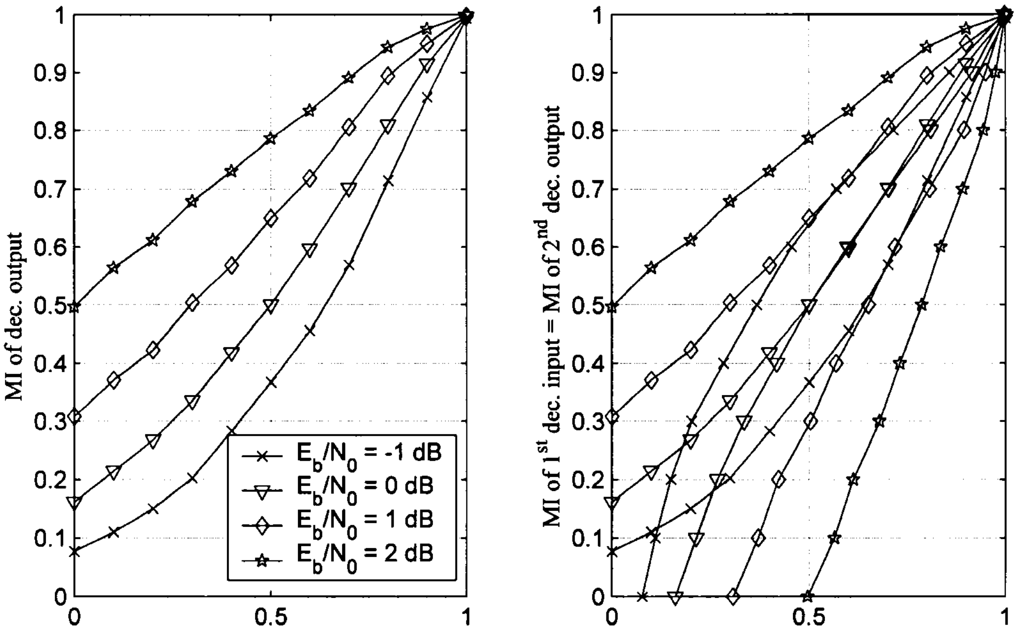

(a) MI of dec. input

(b) MI of 2nd dec. input = MI of 1st dec. output

**Fig. 2.16. (a) Extrinsic information characteristics of decoder for the convolutional code from [9] ($g_{ff} = 1 + D^2$ and $g_{fb} = 1 + D + D^2$); (b) the EXIT chart for the rate 1/3 turbo code from [9] (MI stands for mutual information and dec. stands for decoder).**

corrupted by additive white Gaussian noise. Prior to decoding, the trajectory starts at a mutual information of zero and subsequently rises to a new value based on the extrinsic information produced by the first constituent decoder, which is equal to the mutual information on the *a priori* knowledge of the second decoder. The second constituent decoder decodes the second parity stream and the resulting mutual information computed on the extrinsic information increases to a new value. This process is repeated for all iterations.

For the considered code and a message block length of 1,000 bits, we illustrate the decoding trajectory (averaged over one million message bits) for SNR values before and after the start of convergence. Fig. 2.17 shows the decoding trajectory and the corresponding EXIT chart at $E_b/N_0 = 0$ dB, 0.2 dB and 1 dB. Below the start of convergence, there is no decoding tunnel (i.e., the transfer characteristics intersect) and hence, the trajectory never reaches the maximum

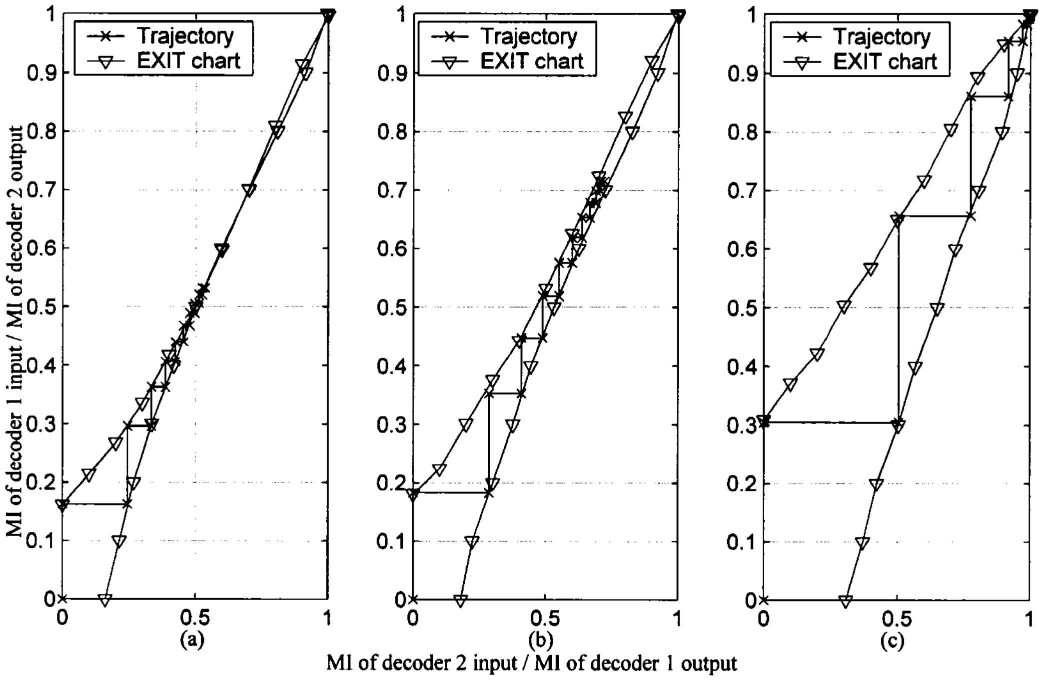

**Fig. 2.17. Decoding trajectory for a message block length of 1 000 bits at (a)** $E_b/N_0 = 0$ dB **(b)** $E_b/N_0 = 0.2$ dB **(c)** $E_b/N_0 = 1$ dB **for the considered rate 1/3 turbo code.**

value of 1 (correctly decoded message block). At an SNR of 0.2 dB, there exists a narrow decoding tunnel and as such the turbo decoder performs many decoding iterations (corresponding to small steps in the trajectory) to correctly decode the message block. Finally, at high SNR values, the turbo decoder proceeds with large decoding steps, which corresponds to knowing many of the bits with high confidence. In all cases, the trajectory is well defined by the transfer characteristics for the first few iterations. However, for $E_b/N_0 = 0.2$ dB , the trajectory "dies out" before reaching a maximum value of 1, due to breakdown of the i.i.d. assumption on the *a priori* knowledge and extrinsic information of the message bits after many iterations.

## 2.5 Prior Coded MIMO Systems

Fig. 2.18 illustrates the block diagram of a single user coded MIMO system. At the transmitter, channel coded bits are mapped to modulation symbols and de-

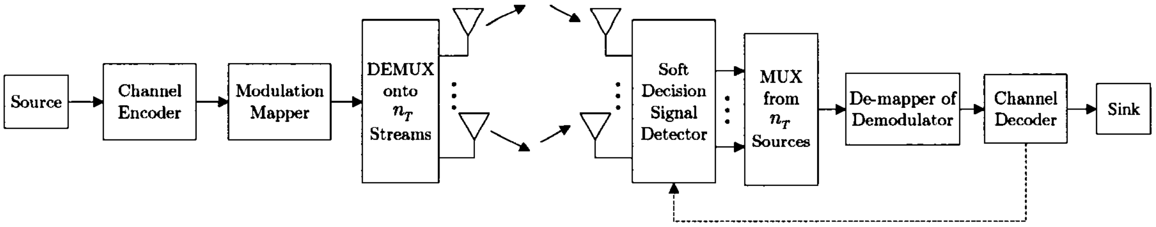

**Fig. 2.18. A schematic block diagram of a single user coded MIMO transceiver with iterative processing.**

multiplexed onto $n_T$ streams and transmitted over the MIMO channel. The receiver operations consist of front-end signal detection, channel decoding and possibly iterative processing. In this section, we review recently proposed signal detection techniques for coded MIMO systems to highlight complexity and performance issues.

## 2.5.1 Existing Single Pass MIMO Signal Detection Techniques

Decoding of powerful channel codes, such as turbo codes, necessitates soft decision outputs from the front-end signal detector. Generating soft decisions on the transmitted symbol vectors is difficult as the number of signal space points increase as $M^{n_T}$, where $M$ is the modulation order and $n_T$ is the number of transmit antennas. In the multi-user scenario, the number of signal space points also increase exponentially with the number of users $K$, i.e., $M^{Kn_T}$. Thus, the optimal MIMO signal detector is limited to a small number of antennas (reduced data rates) in the single-user scenario and is impractical for a large number of users.

Space-time trellis codes [89] combined channel encoding with symbol mapping onto multiple transmit antennas, i.e., a form of trellis-coded modulation modified for multi-antenna systems. At the receiver, joint detection and channel decoding was accomplished through maximum likelihood sequence estimation using the Viterbi algorithm [76]. However, the number of states in the trellis increase exponentially with the rate of transmission and / or number of transmit antennas. A further disadvantage of these codes is that they cannot be designed algorithmically.

Lower complexity signal detection alternatives included the Bell Labs layered space-time (BLAST) detector, space-time block codes and linear dispersion codes. In all these systems, channel coding in the strict sense is not employed. The BLAST decoder possess cubic complexity in the number of receive antennas as it involves MMSE or zero forcing based nulling operations and hard decisions are used to cancel the co-antenna interference [30], [33]. As a result, the BLAST system operates at high SNRs. Alamouti proposed a simple transmit diversity scheme [1], which was later generalized by Tarokh et *al.* [91] to form the class of space-time block codes. These codes create orthogonal sequences that are sent from different transmit antennas. The block length of these codes are small (e.g., two or three symbols) and hence, maximum likelihood detection is performed on a symbol-by-symbol basis. Linear dispersion codes [40] subsume BLAST and space-time block codes as special cases. These codes are defined by mapping matrices to create space and time interrelationships and use sphere decoding (originally developed by Fincke and Pohst [28]) to recover the transmitted symbols. As in space-time block codes, the encoding mapping is simple and the block lengths are short resulting in good system performance only at high SNRs (e.g., around 20 dB) [40].

### 2.5.2 Iterative Detection / Decoding Systems

Reliable data transmission at low SNRs, requires sophisticated channel codes with large block lengths and low complexity soft decision signal detection methods that can scale up to larger numbers of antennas. Joint detection and decoding would require processing over the entire coded sequence and as such would not be computationally feasible even for moderate size block lengths. Instead, iterative processing is employed wherein new information on the transmitted symbols from the channel decoder is fed back to the soft decision signal detector. In this section, we review coded MIMO systems that employ convolutional codes, turbo codes and some form of iterative processing to achieve better performance than the single pass detection systems.

Variations on the optimal signal detector have been proposed in systems that employ convolutional or turbo codes [55], [87], [98]. In these systems, a front-end channel equalizer based on the maximum *a posteriori* algorithm generates soft decisions on the transmitted symbol vector. Subsequent to convolutional or turbo decoding, soft decisions on the coded bits are mapped into soft decisions on the transmitted symbol vector, which is fed back to the equalizer in the form of *a priori* information. As in the case of the optimal detector, these systems are limited to small numbers of antennas (e.g., two to four) and the detection complexity becomes prohibitively complex in the multi-user case.

Lower complexity signal detection techniques include the modified sphere detector [21], [42], [102] and the layered space-time architectures [2], [80]. Instead of an exhaustive search in $\mathbb{C}^{n_R}$ space to determine the transmitted symbol vector, the sphere detector restricts its attention to a sphere of a particular radius. The complexity of the algorithm is closely related to the choice of the radius. A larger radius will result in too many candidates (symbol vector possibilities) to search over and a small radius may result in an empty sphere. The coded MIMO system proposed by Hochwald and ten Brink [42] is particularly interesting as they achieve medium to high data rates (36 bits per channel use) within 4 dB of the ergodic capacity limit. The sphere detector, which they considered, was in an iterative detection / decoding loop with a turbo decoder. The authors claim that for the values of radii that were considered, the complexity can be roughly cubic in the number of transmit antennas [42].

The layered space-time (LST) architecture [2] and Turbo-BLAST [80] architecture employ convolutional codes and iterative processing in addition to the nulling and cancelling techniques of the BLAST system. In both systems, message bits are demultiplexed and independently coded on each antenna and the front-end of the receiver consists of a bank of equalizers. In case of LST systems, the soft decision output of the first transmit antenna's equalizer is convolutionally decoded and the decoder's output is used to generate hard decisions on the modulation symbols, which is subtracted from the received vector. This process is repeated for all receive antennas. In the Turbo-BLAST system, the $n_T$ equalizers use the MMSE criterion to generate channel observations on the transmitted symbols. After the decoding of all $n_T$ streams, improved estimates on the modulation symbols are used in updating the MMSE filter coefficients and are also used to cancel the co-antenna interference. This process is repeated for a desired number of iterations. Since the equalizer coefficients of both systems rely on the inversion of a $n_R$-by-$n_R$ matrix for each transmitted stream, the detection complexity is $O(n_T n_R^3)$ ($n_R$ is the number of receive antennas). Although both systems operate at lower SNRs than the BLAST system, the use of hard decisions in interference cancellation results in system performance that is far from the ergodic capacity limit.

### 2.5.3 Multi-user Coded MIMO Systems

In contrast to single-user MIMO systems, fewer coded multi-user MIMO architectures have been explored and simulated [50], [82]. For these systems, iterative multi-user detection/decoding at the receiver consists of first stage (typically MMSE based) filtering followed by channel decoders for $K$ users. However, results of these systems indicate that more effort is needed to achieve performance closer to the ergodic capacity limit and to lower MIMO signal detection complexity (from cubic in the number of users and/or number of transmit / receive antennas).

## 2.6 Chapter Summary

In this chapter, we have reviewed prior results and techniques from literature, which are relevant to the work presented in this dissertation. In particular, Section 2.1 has presented Rayleigh-faded MIMO channel models, including the cases of spatially correlated fading, imperfect channel state information at the receiver and presence of multiple users. Section 2.2 has summarized the relevant ergodic capacity results for these channels and since these results are used as performance benchmarks for coded wireless systems in Chapter 4. We have also used the MIMO capacity results to illustrate system-level benefits of MIMO transmission as opposed to the traditional diversity techniques, e.g., antenna selection, equal gain combining and maximum ratio combining. Section 2.3 has focused on the process of turbo encoding and iterative decoding, including the BCJR algorithm as a special case of the path counting algorithm in matrix notation. Section 2.4 has reviewed the two existing performance analysis techniques for turbo codes, i.e., the union bound based method (for approximating the BER performance in high SNR regions) and the EXIT chart method (for graphically estimating the SNR value corresponding to the start of the waterfall region). Finally, Section 2.5 has covered recently proposed coded MIMO systems and their potential limitations due to implementation complexity.

# Chapter 3

# Proposed MIMO Signal Detector

In this chapter, we describe the proposed soft decision MIMO signal detector, which is first developed for the single user scenario with perfect channel state information (CSI) available at the receiver. Subsequently, appropriate modifications to the detector are made to accommodate imperfect CSI and interference due to the presence of multiple users. Finally, the symbol error rate performance of the proposed detector is analyzed and is compared to the performance of the (exponentially complex) optimal MIMO signal detector.

## 3.1 Development of the Proposed MIMO Signal Detector

As shown in Fig. 3.1, the channel matrix can be thought of as spatially spreading the symbols from each transmit antenna across all the receive antennas. The proposed MIMO signal detector combines the transmitted energy from the receive antennas based on a channel dependent transformation. Using the resulting channel observations on the transmitted symbols, the detector produces soft decisions on these symbols using the Gaussian approximation for the co-antenna interference, filtered noise and channel estimation errors. The proposed detector is not based on a MMSE filter realization nor is it a variation of prior signal detection schemes [2], [21], [42], [55], [80], [87], [89], [90], [98], [102]. In this section, the structure of the detector is formulated for various settings.

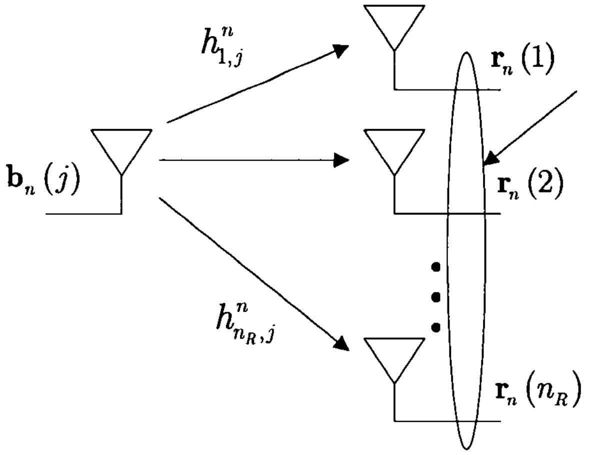

The MIMO signal
detector transforms
the received vector
into a channel
observation on
$\mathbf{b}_n(j)$

**Fig. 3.1. An illustration of the spatial spreading performed by the channel for the *j*-th transmitted symbol $\mathbf{b}_n(j)$.**

### 3.1.1 Single User Transmission and Perfect CSI at the Receiver

We focus first on the uncoded uplink transmission over a slow frequency non-selective MIMO fading channel. Recall from (2.2) that the received vector at the $n$-th time instant is given by $\mathbf{r}_n = \mathbf{H}_n\mathbf{b}_n + \mathbf{v}_n$. If perfect CSI is available at the receiver, the proposed detector decomposes the channel matrix $\mathbf{H}_n$ into two matrices, $\mathbf{H}_n = \mathbf{S}_n\mathbf{A}_n$, where $\mathbf{S}_n$ is given by

$$\mathbf{S}_n = \left[\frac{\mathbf{h}_{n,1}}{\left\|\mathbf{h}_{n,1}\right\|}, \frac{\mathbf{h}_{n,2}}{\left\|\mathbf{h}_{n,2}\right\|}, \ldots, \frac{\mathbf{h}_{n,n_T}}{\left\|\mathbf{h}_{n,n_T}\right\|}\right], \tag{3.1}$$

where $\mathbf{h}_{n,1}$, $\mathbf{h}_{n,2}$, …, $\mathbf{h}_{n,n_T}$ are the columns of $\mathbf{H}_n$ and $\mathbf{A}_n$ is a diagonal matrix composed of the column norms of $\mathbf{H}_n$, $\mathbf{A}_n = diag\left(\left\|\mathbf{h}_{n,1}\right\|, \left\|\mathbf{h}_{n,2}\right\|, \ldots, \left\|\mathbf{h}_{n,n_T}\right\|\right)$. The complexity of this decomposition increases as $O(n_T n_R)$ (as the calculation of the column norm requires $O(n_R)$ operation and there are $n_T$ columns in the channel matrix). Furthermore, this decomposition is not related to any of the traditional matrix decompositions used in signal processing, e.g., Cholesky, QR, LU or SVD [34].

Using the matrix $\mathbf{S}_n$, the received vector $\mathbf{r}_n$ is transformed into an $n_T$-by-1 channel observation vector $\mathbf{y}_n$, i.e.,

$$\begin{aligned}\mathbf{y}_n &= \mathbf{S}_n^H \mathbf{r}_n = \mathbf{S}_n^H \mathbf{H}_n \mathbf{b}_n + \mathbf{S}_n^H \mathbf{v}_n \\ &= \mathbf{S}_n^H \mathbf{H}_n \mathbf{b}_n + \overline{\mathbf{v}}_n \\ &= \mathbf{R}_n \mathbf{A}_n \mathbf{b}_n + \overline{\mathbf{v}}_n,\end{aligned} \tag{3.2}$$

where the antenna correlation matrix $\mathbf{R}_n$ is given by $\mathbf{S}_n^H \mathbf{S}_n$ and the vector $\mathbf{y}_n$ contains observations on modulation symbols (e.g., QPSK or 16-QAM), corrupted by co-antenna interference and filtered noise $\overline{\mathbf{v}}_n$. The elements of the vector $\overline{\mathbf{v}}_n$ in (3.2) are correlated across transmit antennas and are realizations of a zero mean complex Gaussian random variable with variance $\sigma^2$ in the real and imaginary dimensions. We do not need to consider the correlation effects as the detector processes each element of the channel observation vector $\mathbf{y}_n$ individually. The potential negative effects of time correlation can be avoided if the matrix $\mathbf{H}_n$ changes with each channel use. This is made possible through the use of perfect channel interleaving and deinterleaving at the transmit and receive ends, respectively. The $j$-th element of the channel observation vector $\mathbf{y}_n$ is given by

$$\mathbf{y}_n(j) = \mathbf{A}_n(j,j)\mathbf{b}_n(j) + \sum_{\substack{k=1 \\ k \neq j}}^{n_T} \mathbf{A}_n(k,k)\mathbf{R}_n(j,k)\mathbf{b}_n(k) + \overline{\mathbf{v}}_n(j), \tag{3.3}$$

where $\mathbf{R}_n(j,k) = \mathbf{s}_{n,j}^H \mathbf{s}_{n,k}$ (where $\mathbf{s}_{n,1}$, $\mathbf{s}_{n,2}$, …, $\mathbf{s}_{n,n_T}$ are columns of $\mathbf{S}_n$) and $\mathbf{R}_n(j,j) = 1$.

To compute soft decisions on the transmitted symbols, the sum of the co-antenna interference and filtered noise $\overline{\mathbf{v}}_n(j)$ in (3.3) is approximated as a two-dimensional real Gaussian random vector. The mean $\boldsymbol{\mu}_n(j)$ of this two-dimensional Gaussian random vector is given by

$$\boldsymbol{\mu}_n(j) = \left[ \Re\left\{ \sum_{\substack{k=1 \\ k \neq j}}^{n_T} E\left[\mathbf{A}_n(k,k)\mathbf{R}_n(j,k)Q\right] \right\}, \Im\left\{ \sum_{\substack{k=1 \\ k \neq j}}^{n_T} E\left[\mathbf{A}_n(k,k)\mathbf{R}_n(j,k)Q\right] \right\} \right]^T, \tag{3.4}$$

because the mean of the filtered noise is zero as $E[\overline{\mathbf{v}}_n] = \mathbf{S}_n^H E[\mathbf{v}_n] = \mathbf{0}$, $[\bullet]^T$ represents the transpose operation, $\Re\{\bullet\}$ and $\Im\{\bullet\}$ denote the real and imaginary components and $E$ is the expectation on the discrete random variable $Q$, which can be one of $M$ possible complex modulation symbols. The diagonal terms of the covariance matrix of the Gaussian random vector are

$$\begin{aligned}\mathbf{K}_{n,j}(1,1) &= \sum_{\substack{k=1\\k\neq j}}^{n_T} E\left[\left(\mathbf{A}_n(k,k)\Re\{\mathbf{R}_n(j,k)Q\}\right)^2\right] - \left(E\left[\mathbf{A}_n(k,k)\Re\{\mathbf{R}_n(j,k)Q\}\right]\right)^2 + \sigma^2,\\ \mathbf{K}_{n,j}(2,2) &= \sum_{\substack{k=1\\k\neq j}}^{n_T} E\left[\left(\mathbf{A}_n(k,k)\Im\{\mathbf{R}_n(j,k)Q\}\right)^2\right] - \left(E\left[\mathbf{A}_n(k,k)\Im\{\mathbf{R}_n(j,k)Q\}\right]\right)^2 + \sigma^2,\end{aligned} \tag{3.5}$$

and the cross covariance terms can be expressed as

$$\begin{aligned}\mathbf{K}_{n,j}(1,2) = \mathbf{K}_{n,j}(2,1) = \sum_{\substack{k=1\\k\neq j}}^{n_T} \Big( & E\left[\left(\mathbf{A}_n(k,k)\right)^2 \Re\{\mathbf{R}_n(j,k)Q\}\Im\{\mathbf{R}_n(j,k)Q\}\right]\\ & - \left(E\left[\mathbf{A}_n(k,k)\Re\{\mathbf{R}_n(j,k)Q\}\right]\right)\left(E\left[\mathbf{A}_n(k,k)\Im\{\mathbf{R}_n(j,k)Q\}\right]\right)\Big).\end{aligned} \tag{3.6}$$

For the case of QPSK transmission, $\mathbf{K}_{n,j}(1,2)$ and $\mathbf{K}_{n,j}(2,1)$ are approximately zero due to the independence of the inphase and quadrature components of the QPSK symbol. On the other hand, for 16-QAM, the cross covariance terms can be non-zero if the random variable $Q$ has a non-uniform distribution. In (3.5) and (3.6), we have used the fact that the transmitted symbols from each antenna are independent, so that the variance operation can be applied on each term of the summation. The above calculations are repeated for transmitted symbols from all transmit antennas. Finally, we express the likelihood for the transmitted symbol from the $j$-th antenna $\mathbf{b}_n(j)$ being the $p$-th modulation symbol $q_p$ as

$$P\left(\mathbf{y}_n(j)\middle|\mathbf{b}_n(j) = q_p\right) = \frac{\exp\left(-\frac{1}{2}\left(\boldsymbol{y} - \boldsymbol{\mu}_n(j) - \mathbf{A}_n(j,j)\boldsymbol{q}\right)\mathbf{K}_{n,j}^{-1}\left(\boldsymbol{y} - \boldsymbol{\mu}_n(j) - \mathbf{A}_n(j,j)\boldsymbol{q}\right)^T\right)}{2\pi\sqrt{\det\left(\mathbf{K}_{n,j}\right)}}, \tag{3.7}$$

where $\boldsymbol{y} = \left[\Re\{\mathbf{y}_n(j)\}, \Im\{\mathbf{y}_n(j)\}\right]^T$ and $\boldsymbol{q} = \left[\Re\{q_p\}, \Im\{q_p\}\right]^T$.

### 3.1.2 Single User Transmission and Imperfect CSI at the Receiver

Channel state information (CSI) available at the receiver can be imperfect due to effects of user mobility and estimation errors. This is particularly the case in uplink wireless systems due to power limitations at the mobile, as the precision of channel estimation tends to decrease for lower SNRs. Hence, it is desirable that the front-end MIMO signal detector is robust to the effect of imperfect CSI.

Recall from Section 2.1.4 that the channel matrix $\mathbf{H}_n$ and the estimated channel matrix $\hat{\mathbf{H}}_n$ are related by $\mathbf{H}_n = \hat{\mathbf{H}}_n + \varepsilon_n$, where elements of $\varepsilon_n$ are i.i.d. zero mean complex Gaussian random variables with variance $\sigma_\varepsilon^2/2$ in each dimension. The estimated channel matrix $\hat{\mathbf{H}}_n$ is decomposed into two sub-matrices $\hat{\mathbf{S}}_n$ and $\hat{\mathbf{A}}_n$, where $\hat{\mathbf{S}}_n$ contains the normalized columns of $\hat{\mathbf{H}}_n$ and $\hat{\mathbf{A}}_n$ is a diagonal matrix with the column norms of $\hat{\mathbf{H}}_n$ along the main diagonal. Transforming the received vector $\mathbf{r}_n$ by $\hat{\mathbf{S}}_n$, we have

$$\begin{aligned} \hat{\mathbf{y}}_n &= \hat{\mathbf{S}}_n^H \mathbf{r}_n \\ &= \hat{\mathbf{S}}_n^H \left(\hat{\mathbf{H}}_n + \varepsilon_n\right)\mathbf{b}_n + \hat{\mathbf{S}}_n^H \mathbf{v}_n \\ &= \hat{\mathbf{R}}_n \hat{\mathbf{A}}_n \mathbf{b}_n + \hat{\mathbf{S}}_n^H \varepsilon_n \mathbf{b}_n + \hat{\mathbf{v}}_n, \end{aligned} \tag{3.8}$$

where $\hat{\mathbf{R}}_n = \hat{\mathbf{S}}_n^H \hat{\mathbf{S}}_n$. Thus, the channel observations of the transmitted symbols are corrupted by an additional term $\hat{\mathbf{S}}_n^H \varepsilon_n \mathbf{b}_n$ due to channel estimation error. In scalar format, the $j$-th element of $\hat{\mathbf{y}}_n$ is given by

$$\hat{\mathbf{y}}_n(j) = \hat{\mathbf{A}}_n(j,j)\mathbf{b}_n(j) + \sum_{\substack{k=1 \\ k\neq j}}^{n_T} \hat{\mathbf{R}}_n(j,k)\hat{\mathbf{A}}_n(k,k)\mathbf{b}_n(k) + \left(\hat{\mathbf{S}}_n^H \varepsilon_n \mathbf{b}_n\right)_j + \hat{\mathbf{v}}_n(j) \tag{3.9}$$

where $\left(\hat{\mathbf{S}}_n^H \varepsilon_n \mathbf{b}_n\right)_j$ is the $j$-th element of the vector $\hat{\mathbf{S}}_n^H \varepsilon_n \mathbf{b}_n$.

In order to compute soft decisions on the transmitted symbols, we approximate the sum of the co-antenna interference, term due to channel estimation errors and filtered noise in (3.9) with a two dimensional Gaussian random vector. The mean of this Gaussian vector is given by

$$\hat{\boldsymbol{\mu}}_n(j) = \left[\Re\left\{\sum_{\substack{k=1 \\ k\neq j}}^{n_T} E\left[\hat{\mathbf{R}}_n(j,k)\hat{\mathbf{A}}_n(k,k)Q\right]\right\}, \Im\left\{\sum_{\substack{k=1 \\ k\neq j}}^{n_T} E\left[\hat{\mathbf{R}}_n(j,k)\hat{\mathbf{A}}_n(k,k)Q\right]\right\}\right]^T, \tag{3.10}$$

where we used $E[\hat{\mathbf{v}}_n] = \hat{\mathbf{S}}_n^H E[\mathbf{v}_n] = \mathbf{0}$ and $E\left[\hat{\mathbf{S}}_n^H \varepsilon_n \mathbf{b}_n\right] = \hat{\mathbf{S}}_n^H E[\varepsilon_n] E[\mathbf{b}_n] = \mathbf{0}$ as $\hat{\mathbf{S}}_n$, $\varepsilon_n$ and $\mathbf{b}_n$ are independent.

The corresponding covariance matrix elements of the two-dimensional Gaussian random vector are expressed as

$$\begin{aligned}
\hat{\mathbf{K}}_{n,j}(1,1) &= \sum_{\substack{k=1\\k\neq j}}^{n_T} E\left[\left(\Re\left\{\hat{\mathbf{R}}_n(j,k)\hat{\mathbf{A}}_n(k,k)Q\right\}\right)^2\right]-\left(E\left[\Re\left\{\hat{\mathbf{R}}_n(j,k)\hat{\mathbf{A}}_n(k,k)Q\right\}\right]\right)^2+\sigma^2+\frac{\sigma_\varepsilon^2}{2},\\
\hat{\mathbf{K}}_j(2,2) &= \sum_{\substack{k=1\\k\neq j}}^{n_T} E\left[\left(\Im\left\{\hat{\mathbf{R}}_n(j,k)\hat{\mathbf{A}}_n(k,k)Q\right\}\right)^2\right]-\left(E\left[\Im\left\{\hat{\mathbf{R}}_n(j,k)\hat{\mathbf{A}}_n(k,k)Q\right\}\right]\right)^2+\sigma^2+\frac{\sigma_\varepsilon^2}{2},\\
\hat{\mathbf{K}}_{n,j}(1,2) = \hat{\mathbf{K}}_{n,j}(2,1) &= \sum_{\substack{k=1\\k\neq j}}^{n_T}\Bigg(E\left[\left(\Re\left(\hat{\mathbf{R}}_n(j,k)\hat{\mathbf{A}}_n(k,k)Q\right)\Im\left(\hat{\mathbf{R}}_n(j,k)\hat{\mathbf{A}}_n(k,k)Q\right)\right)\right]\\
&\quad -\left(E\left[\Re\left(\hat{\mathbf{R}}_n(j,k)\hat{\mathbf{A}}_n(k,k)Q\right)\right]\right)\left(E\left[\Im\left(\hat{\mathbf{R}}_n(j,k)\hat{\mathbf{A}}_n(k,k)Q\right)\right]\right)\Bigg),
\end{aligned} \tag{3.11}$$

where the variance of $\left(\hat{\mathbf{S}}_n^H \varepsilon_n \mathbf{b}_n\right)_j$ is $\sigma_\varepsilon^2/2$ as the covariance matrix of $\hat{\mathbf{S}}_n^H \varepsilon_n \mathbf{b}_n$ is given by

$$E\left[\hat{\mathbf{S}}_n^H \varepsilon_n \mathbf{b}_n \mathbf{b}_n^H \varepsilon_n^{\mathbf{H}} \hat{\mathbf{S}}_n\right] = \hat{\mathbf{S}}_n^H E\left[E\left[\varepsilon_n \mathbf{b}_n \mathbf{b}_n^H \varepsilon_n^H \middle| \varepsilon_n\right]\right]\hat{\mathbf{S}}_n = \hat{\mathbf{S}}_n^H E\left[\frac{\varepsilon_n \varepsilon_n^H}{n_T}\right]\hat{\mathbf{S}}_n = \sigma_\varepsilon^2 \hat{\mathbf{R}}_n. \tag{3.12}$$

In the second step, we used $E\left[\mathbf{b}_n \mathbf{b}_n^H\right] = 1/n_T\,\mathbf{I}$ and the elements of the random product matrix $\varepsilon_n \varepsilon_n^H$ have a mean of $n_T\sigma_\varepsilon^2$ along the main diagonal and zero for the off-diagonal terms [103]. Since the main diagonal of $\hat{\mathbf{R}}_n$ is composed of ones, the variance of the $j$-th element of $\hat{\mathbf{S}}_n^H \varepsilon_n \mathbf{b}_n$ remains the same as the variance of the elements of $\varepsilon_n$, i.e., $\sigma_\varepsilon^2/2$ in each dimension. The off-diagonal entries $\hat{\mathbf{K}}_{n,j}(1,2)$ and $\hat{\mathbf{K}}_{n,j}(2,1)$ in (3.11) do not include terms from the filtered noise and channel estimation error, as the real and imaginary dimensions of $\hat{\mathbf{v}}_n(j)$ and $\left(\hat{\mathbf{S}}_n^H \varepsilon_n \mathbf{b}_n\right)_j$ are independent of each other and their corresponding means are zero.

The likelihood for the transmitted symbol from the $j$-th antenna, $\mathbf{b}_n(j)$ being the $p$-th modulation symbol $q_p$, can be computed through

$$P\left(\hat{\mathbf{y}}_n(j)\middle|\mathbf{b}_n(j)=q_p\right) = \frac{\exp\left(-\frac{1}{2}\left(\hat{\boldsymbol{y}}-\hat{\boldsymbol{\mu}}_n(j)-\hat{\mathbf{A}}_n(j,j)\boldsymbol{q}\right)\hat{\mathbf{K}}_{n,j}^{-1}\left(\hat{\boldsymbol{y}}-\hat{\boldsymbol{\mu}}_n(j)-\hat{\mathbf{A}}_n(j,j)\boldsymbol{q}\right)^T\right)}{2\pi\sqrt{\det\left(\hat{\mathbf{K}}_{n,j}\right)}}, \tag{3.13}$$

where $\hat{\boldsymbol{y}} = \left[\Re\left\{\hat{\mathbf{y}}_n(j)\right\},\Im\left\{\hat{\mathbf{y}}_n(j)\right\}\right]^T$ and $\boldsymbol{q} = \left[\Re\left\{q_p\right\},\Im\left\{q_p\right\}\right]^T$. The signal detector can produce a hard decision corresponding to the $j$-th transmitted symbol $\mathbf{b}_n(j)$, by choosing an element from the alphabet $\left\{q_1,q_2,\ldots,q_M\right\}$ that maximizes the likelihood $P\left(\hat{\mathbf{y}}_n(j)\middle|\mathbf{b}_n(j)=q_p\right)$ for $p$ = 1, 2, …, $M$. The following example illust-rates the operation of the proposed detector in a specific case.

**Example 1:**

Consider an $(n_T, n_R)$ = (2, 4) MIMO system, where the transmitter sends a BPSK symbol vector $\mathbf{b}_1=[1,-1]$, the Gaussian noise variance in each dimension is assumed to be $\sigma^2 = 1$ and the channel estimation error is $\sigma_\varepsilon^2 = 0.1$. The specific channel matrix $\mathbf{H}_1$ is given by

$$\mathbf{H}_1 = \begin{bmatrix} 0.5 + 0.5i, & 0.5 - 0.5i \\ 1 + 1i, & 1 - 1i \\ -1, & 1 \\ -1i, & -1i \end{bmatrix},$$

where $i = \sqrt{-1}$ and the corresponding estimated channel matrix $\hat{\mathbf{H}}_1$ is

$$\hat{\mathbf{H}}_1 = \begin{bmatrix} 0.70 + 0.42i, & 0.28 - 0.64i \\ 0.97 + 0.68i, & 1.09 + 0.73i \\ -0.84 + 0.10i, & 0.96 - 0.47i \\ -0.31 - 1.30i, & 0.30 - 0.80i \end{bmatrix}$$

Let the received vector $\mathbf{r}_1 = \mathbf{H}_1\mathbf{b}_1 + \mathbf{v}_1$, be given by

$$\mathbf{r}_1 = \begin{bmatrix} -0.28 + 0.45i \\ -1.14 - 0.67i \\ -1.66 - 0.10i \\ -1.32 - 0.04i \end{bmatrix}.$$

*Step 1: Matrix Decomposition*

The detector first decomposes the channel matrix into the two sub-matrices, $\hat{\mathbf{H}}_1 = \hat{\mathbf{S}}_1\hat{\mathbf{A}}_1$,

$$\hat{\mathbf{A}}_1 = \begin{bmatrix} 2.13 & 0 \\ 0 & 2.02 \end{bmatrix},$$

$$\hat{\mathbf{S}}_1 = \begin{bmatrix} 0.33 + 0.20i, & 0.14 - 0.32i \\ 0.46 + 0.32i, & 0.54 + 0.36i \\ -0.39 + 0.05i, & 0.47 - 0.23i \\ -0.14 - 0.61i, & 0.15 - 0.40i \end{bmatrix}.$$

*Step 2: Estimating Transmitted Symbols*

We transform the received vector $\mathbf{r}_1$ by the matrix $\hat{\mathbf{S}}_1$ to acquire the channel observation vector $\hat{\mathbf{y}}_1$ about the transmitted symbols contained in $\mathbf{b}_1$ and to lower the dimensionality of the problem (from $n_R = 4$ to $n_T = 2$),

$$\hat{\mathbf{y}}_1 = \begin{bmatrix} 0.13 \text{ - } 0.42i \\ \text{-}1.97 \text{ - } 0.94i \end{bmatrix}.$$

Note that this reduction in dimensionality is interesting for the case of large number of receive antennas (at the base-station), when compared to the number of transmit antennas (at the mobile). The use of large numbers of receive antennas (up to $n_R = 60$) in practical prototypes have been explored in [14].

*Step 3: Computing Statistics for the Gaussian Approximation*

Using the antenna correlation matrix $\hat{\mathbf{R}}_1 = \hat{\mathbf{S}}_1^H \hat{\mathbf{S}}_1 = \begin{bmatrix} 1 & 0.37 + 0.08i \\ 0.37 \text{ - } 0.08i & 1 \end{bmatrix}$, the statistics of the Gaussian approximation from (3.10) and (3.11) for the first transmit antenna are determined to be

$$\hat{\boldsymbol{\mu}}_{1,1} = \mathbf{0},$$

$$\hat{\mathbf{K}}_{1,1} = \begin{bmatrix} 1.65 & 0 \\ 0 & 1.13 \end{bmatrix}.$$

Note that the mean vector $\hat{\boldsymbol{\mu}}_{1,1}$ and cross covariance terms $\hat{\mathbf{K}}_{1,1}(1,2), \hat{\mathbf{K}}_{1,1}(2,1)$ are zero, as the BPSK constellation is symmetric around zero and its points are equiprobable.

*Step 4: Calculating the Soft Decisions*

Using (3.13), the likelihood values for the symbol from the first transmit antenna are given by $P\left(\hat{\mathbf{y}}_1(1)\middle|\mathbf{b}_1(1) = -1\right) = 0.022$ and $P\left(\hat{\mathbf{y}}_1(1)\middle|\mathbf{b}_1(1) = 1\right) = 0.033$. By repeating the above calculation for the second transmit antenna, we get, $P\left(\hat{\mathbf{y}}_1(2)\middle|\mathbf{b}_1(2) = -1\right) = 0.077$ and $P\left(\hat{\mathbf{y}}_1(2)\middle|\mathbf{b}_1(2) = 1\right) = 0.006$. (Again, note that these likelihood values are not normalized, as *a posteriori* probabilities would be.)

### 3.1.3 Multi-user Scenario with Perfect CSI at the Receiver

In this section, we extend the proposed MIMO signal detector from Section 3.1.1 to the multi-user case. The two main modifications from the single user scenario include a change in notation (consistent with Section 2.1.4) and accommodating multi-user interference in the calculation of the soft decisions. The detector again decomposes each user's channel matrix into sub-matrices, e.g., for the $l$-th user,

$$\mathbf{H}_{n,l} = \mathbf{S}_{n,l}\mathbf{A}_{n,l}, \quad l = 1, 2, \ldots, K,, \tag{3.14}$$

where $\mathbf{S}_{n,l} = \left[\mathbf{h}_{n,l,1}/\left\|\mathbf{h}_{n,l,1}\right\|, \mathbf{h}_{n,l,2}/\left\|\mathbf{h}_{n,l,2}\right\|, \ldots, \mathbf{h}_{n,l,n_T}/\left\|\mathbf{h}_{n,l,n_T}\right\|\right]$, $\mathbf{A}_{n,l} = diag\left(\left\|\mathbf{h}_{n,l,1}\right\|, \left\|\mathbf{h}_{n,l,2}\right\|, \ldots, \left\|\mathbf{h}_{n,l,n_T}\right\|\right)$ and $\mathbf{h}_{n,l,j}$ is the $j$-th column of $\mathbf{H}_{n,l}$, $j = 1, 2, \ldots, n_T$.

We consider the detector's operations for user 1 $(l = 1)$. The received vector $\widehat{\mathbf{r}}_n$ from (2.7) is transformed using $\mathbf{S}_{n,1}$ resulting in the channel observation vector $\widehat{\mathbf{y}}_{n,1} = \mathbf{S}_{n,1}^H \widehat{\mathbf{r}}_n$, whose $j$-th element is given by

$$\begin{aligned}\widehat{\mathbf{y}}_{n,1}(j) = {} & \underbrace{\mathbf{A}_{n,1}(j,j)\,\mathbf{b}_{n,1}(j)}_{\text{desired signal}} + \underbrace{\sum_{\substack{u=1\\u\neq j}}^{n_T} \mathbf{R}_{n,1,1}(j,u)\,\mathbf{A}_{n,1}(u,u)\,\mathbf{b}_{n,1}(u)}_{\text{co-antenna interference}} \\ & + \underbrace{\sum_{m=2}^{K}\sum_{u=1}^{n_T} \mathbf{R}_{n,1,m}(j,u)\,\mathbf{A}_{n,m}(u,u)\,\mathbf{b}_{n,m}(u)}_{\text{multi-user interference}} + \widehat{\mathbf{v}}_{n,1}(j),\end{aligned} \tag{3.15}$$

where $\mathbf{R}_{n,1,m}(j,u) = \left(\mathbf{h}_{n,1,j}/\left\|\mathbf{h}_{n,1,j}\right\|\right)^H \left(\mathbf{h}_{n,m,u}/\left\|\mathbf{h}_{n,m,u}\right\|\right)$ and $\widehat{\mathbf{v}}_{n,1}(j)$ is a realization of a zero mean complex Gaussian random variable with variance $\sigma^2$ in the real and imaginary dimensions. As noted in (3.15), multi-user interference as well as co-antenna interference and filtered noise corrupts the channel observation of $\mathbf{b}_{n,1}(j)$.

In the multi-user scenario, we shall assume that users employ QPSK modulation in addition to CDMA spreading sequences. To determine the likelihood of the transmitted symbol $\mathbf{b}_{n,1}(j)$ being the $p$-th symbol in the QPSK alphabet $\{q_1, q_2, q_3, q_4\}$, i.e., $P\left(\widehat{\mathbf{y}}_{n,1}(j) \middle| \mathbf{b}_{n,1}(j) = q_p\right)$, we approximate in (3.15), the sum of the co-antenna interference of the first user, the multi-user interference and filtered noise $\widehat{\mathbf{v}}_{n,1}(j)$ as a two-dimensional Gaussian random vector. The mean $\widehat{\boldsymbol{\mu}}_{n,1,j}$ of this random vector is given by

$$\widehat{\boldsymbol{\mu}}_{n,1,j} = \begin{bmatrix} \Re\left\{ \sum_{\substack{u=1 \\ u\neq j}}^{n_T} E\left[\mathbf{R}_{n,1,1}(j,u)\mathbf{A}_{n,1}(u,u)Q\right] + \sum_{m=2}^{K}\sum_{u=1}^{n_T} E\left[\mathbf{R}_{n,1,m}(j,u)\mathbf{A}_{n,m}(u,u)Q\right] \right\} \\ \Im\left\{ \sum_{\substack{u=1 \\ u\neq j}}^{n_T} E\left[\mathbf{R}_{n,1,1}(j,u)\mathbf{A}_{n,1}(u,u)Q\right] + \sum_{m=2}^{K}\sum_{u=1}^{n_T} E\left[\mathbf{R}_{n,1,m}(j,u)\mathbf{A}_{n,m}(u,u)Q\right] \right\} \end{bmatrix}. \tag{3.16}$$

The diagonal terms of the covariance matrix $\widehat{\mathbf{K}}_{n,1,j}$ of this Gaussian vector are

$$\begin{aligned} \widehat{\mathbf{K}}_{n,1,j}(1,1) &= \sigma^2 + \sum_{\substack{u=1 \\ u\neq j}}^{n_T}\left(E\left[\left(\Re\left\{\mathbf{R}_{n,1,1}(j,u)\mathbf{A}_{n,1}(u,u)Q\right\}\right)^2\right] - \left(E\left[\Re\left\{\mathbf{R}_{n,1,1}(j,u)\mathbf{A}_{n,1}(u,u)Q\right\}\right]\right)^2\right) \\ &\quad + \sum_{m=2}^{K}\sum_{u=1}^{n_T}\left(E\left[\left(\Re\left\{\mathbf{R}_{n,1,m}(j,u)\mathbf{A}_{n,m}(u,u)Q\right\}\right)^2\right] - \left(E\left[\Re\left\{\mathbf{R}_{n,1,m}(j,u)\mathbf{A}_{n,m}(u,u)Q\right\}\right]\right)^2\right), \\ \widehat{\mathbf{K}}_{n,1,j}(2,2) &= \sigma^2 + \sum_{\substack{u=1 \\ u\neq j}}^{n_T}\left(E\left[\left(\Im\left\{\mathbf{R}_{n,1,1}(j,u)\mathbf{A}_{n,1}(u,u)Q\right\}\right)^2\right] - \left(E\left[\Im\left\{\mathbf{R}_{n,1,1}(j,u)\mathbf{A}_{n,1}(u,u)Q\right\}\right]\right)^2\right) \\ &\quad + \sum_{m=2}^{K}\sum_{u=1}^{n_T}\left(E\left[\left(\Im\left\{\mathbf{R}_{n,1,m}(j,u)\mathbf{A}_{n,m}(u,u)Q\right\}\right)^2\right] - \left(E\left[\Im\left\{\mathbf{R}_{n,1,m}(j,u)\mathbf{A}_{n,m}(u,u)Q\right\}\right]\right)^2\right). \end{aligned} \tag{3.17}$$

Recall that the cross covariance terms $\widehat{\mathbf{K}}_{n,1,j}(1,2)$, $\widehat{\mathbf{K}}_{n,1,j}(2,1)$ are approximately zero for the case of QPSK modulation. In (3.17), we use the fact that the filtered noise has zero mean and variance of $\sigma^2$ in each dimension and that the symbols transmitted from the $K$ users' antennas are independent.

Finally, the likelihood of the transmitted symbol from the $j$-th antenna of the first user at the $n$-th time instant $\mathbf{b}_{n,1}(j)$ being the $p$-th modulation symbol $q_p$, $p = 1, 2, 3, 4$ can be expressed as

$$P\left(\widehat{\mathbf{y}}_{n,1}(j) \middle| \mathbf{b}_{n,1}(j) = q_p\right) = \frac{\exp\left(-\frac{1}{2}\left(\widehat{\boldsymbol{y}} - \widehat{\boldsymbol{\mu}}_{n,1,j} - \mathbf{A}_{n,1}(j,j)\boldsymbol{q}\right)\widehat{\mathbf{K}}_{n,1,j}^{-1}\left(\widehat{\boldsymbol{y}} - \widehat{\boldsymbol{\mu}}_{n,1,j} - \mathbf{A}_{n,1}(j,j)\boldsymbol{q}\right)^T\right)}{2\pi\sqrt{\det\left(\widehat{\mathbf{K}}_{n,1,j}\right)}}, \tag{3.18}$$

where $\widehat{\boldsymbol{y}} = \left[\Re\left\{\widehat{\mathbf{y}}_{n,1}(j)\right\}, \Im\left\{\widehat{\mathbf{y}}_{n,1}(j)\right\}\right]^T$ and $\boldsymbol{q} = \left[\Re\left\{q_p\right\}, \Im\left\{q_p\right\}\right]^T$.

## 3.2 Moments of Selected Quantities at the Signal Detector

In this section, we characterize the moments of column norms of the channel matrix and moments of the antenna correlation matrix. These quantities are used in the subsequent symbol error rate analysis of the signal detector and are also used in the analysis of the overall turbo-coded MIMO systems in Chapter 5. We consider the single user case and assume that perfect CSI is available at the receiver only.

### 3.2.1 Moments of the Column Norms in the Channel Matrix

In (3.2), the entries of the diagonal matrix $\mathbf{A}_n$ multiply the transmitted symbols in $\mathbf{b}_n$ and are a part of the co-antenna interference contained in the elements of the channel observation vector $\mathbf{y}_n$. In this section, we determine the mean and variance of $\mathbf{A}_n(j,j)$, $j = 1, 2, \ldots, n_T$, which will be used in the performance analysis techniques described in Section 3.3 and Chapter 5.

The square of the $j$-th column norm of the channel matrix can be expressed as

$$\left|\mathbf{A}_n(j,j)\right|^2 = \left\|\mathbf{h}_{n,j}\right\|^2 = \mathbf{h}_{n,j}^H \mathbf{h}_{n,j} = \mathbf{g}_{n,j}^H \left(\mathbf{C}_{RX}^{1/2}\right)^H \mathbf{C}_{RX}^{1/2} \mathbf{g}_{n,j} = \mathbf{g}_{n,j}^H \mathbf{C}_{RX} \mathbf{g}_{n,j}, \tag{3.19}$$

where $\mathbf{g}_{n,j}$ is the $j$-th column of $\mathbf{G}_n$, $j = 1, 2, \ldots, n_T$. Recall that the elements of $\mathbf{G}_n$ are i.i.d. zero mean complex Gaussian random variables with variance ½ in the real and imaginary dimensions and that for uncorrelated Rayleigh fading, $\mathbf{C}_{TX} = \mathbf{I}$ and $\mathbf{C}_{RX} = \mathbf{I}$. Consequently, $\left|\mathbf{A}_n(j,j)\right|^2$ is a sum of $2n_R$ squared i.i.d. zero mean Gaussian random variables and $\mathbf{A}_n(j,j)$ is a *chi* random variable whose density function is given by

$$p_A(\varsigma) = \frac{2\varsigma^{2n_R-1} e^{-\varsigma^2}}{\Gamma(n_R)}, \quad \varsigma > 0, \tag{3.20}$$

where the gamma function is defined by $\Gamma(\tau) = \int_0^\infty x^{\tau-1} e^{-x} dx$. Using this density function [103], the corresponding expressions for the mean and variance of $\mathbf{A}_n(j,j)$ are given by

$$\begin{aligned} M_A &= \frac{\Gamma(n_R + 0.5)}{\Gamma(n_R)}, \\ V_A &= \frac{\Gamma(n_R + 1)}{\Gamma(n_R)} - M_A^2. \end{aligned} \tag{3.21}$$

For the correlated MIMO channel model, described in Section 2.1.3, the density of $\left|\mathbf{A}_n(j,j)\right|^2$ depends on the correlation matrix $\mathbf{C}_{RX}$ in (3.19), which is in turn parameterized by the angular spread $\beta$ (measured at the receiver) and antenna spacing. By performing the eigenvalue decomposition on the real and symmetric matrix $\mathbf{C}_{RX}$, we obtain

$$\left|\mathbf{A}_n(j,j)\right|^2 = \mathbf{g}_{n,j}^H \mathbf{V}_{\mathbf{C}_{RX}} \mathbf{\Lambda}_{\mathbf{C}_{RX}} \mathbf{V}_{\mathbf{C}_{RX}}^T \mathbf{g}_{n,j} = \mathbf{e}_{n,j}^H \mathbf{e}_{n,j}, \tag{3.22}$$

where $\mathbf{V}_{\mathbf{C}_{RX}}$ is a real orthogonal matrix containing the eigenvectors of $\mathbf{C}_{RX}$ and the real diagonal matrix $\mathbf{\Lambda}_{\mathbf{C}_{RX}}$ has eigenvalues of $\mathbf{C}_{RX}$ along its main diagonal. The random vector $\mathbf{e}_{n,j}$ is given by $\mathbf{\Lambda}_{\mathbf{C}_{RX}}^{1/2} \mathbf{V}_{\mathbf{C}_{RX}}^T \mathbf{g}_{n,j}$. Thus, $\mathbf{e}_{n,j}(l)$ is a realization of a zero mean complex Gaussian random variable with variance $\mathbf{\Lambda}_{\mathbf{C}_{RX}}(l,l)/2$ in the real and imaginary dimensions, $\left|\mathbf{A}_n(j,j)\right|^2$ is a sum of $2n_R$ independent (but not identically distributed) squared zero-mean Gaussian random variables. Consequently, the probability density function of $\left|\mathbf{A}_n(j,j)\right|^2$ could be expressed in a closed form involving Laguerre polynomials [37], but instead, we approximate this density by the *gamma* density function

$$p_{A^2}(\varsigma) = \frac{\varsigma^{a-1} e^{-\varsigma/t}}{\Gamma(a) t^a}, \ \varsigma>0, \tag{3.23}$$

where the parameters $a$ and $t$ can be determined using histogram analysis and goodness of fit. In particular, we determine the histogram of $\left|\mathbf{A}_n(j,j)\right|^2$ through many channel realizations and match it to the corresponding density function, shown in (3.23). The matching is "optimized" by minimizing the mean squared error between the histogram and the approximate density function. Fig. 3.2 illustrates the accuracy of such an approximation for $(n_T, n_R)$ = (2, 10) using a histogram of $\left|\mathbf{A}_n(j,j)\right|^2$ obtained through two million samples for three different values of $\beta$ and antenna spacing. Consequently, the corresponding (approximate) density function of $\mathbf{A}_n(j,j)$ can be determined by a change of variables to be

$$p_A(\varsigma) = \frac{2\varsigma^{2a-1} e^{-\varsigma^2/t}}{\Gamma(a) t^a}, \ \varsigma>0, \tag{3.24}$$

with $a$ and $t$ being correlation specific parameters. The expressions for the mean and variance of $\mathbf{A}_n(j,j)$ are given by

$$
\begin{aligned}
M_A &= \sqrt{t}\,\frac{\Gamma(a+0.5)}{\Gamma(a)} \\
V_A &= t\,\frac{\Gamma(a+1)}{\Gamma(a)} - M_A^2.
\end{aligned}
\tag{3.25}
$$

It is interesting to observe that for uplink configurations, i.e., when $n_T < n_R$, the variance $V_A$ of $\mathbf{A}_n(j,j)$ is usually several times smaller than the mean $M_A$ of $\mathbf{A}_n(j,j)$ on both uncorrelated and correlated MIMO channels. Fig. 3.3 illustrates the closeness of fit between the histogram and the derived density function of $\mathbf{A}_n(1,1)$ for the uncorrelated and correlated fading scenarios on a $(n_T, n_R) = (4,20)$ antenna configuration with $\beta = 10^\circ$ and antenna spacing of $\lambda$. Spatial correlation has more of an impact on the variance than on the mean of $\mathbf{A}_n(1,1)$, i.e., the mean is approximately equal to 4.5 in both the uncorrelated and

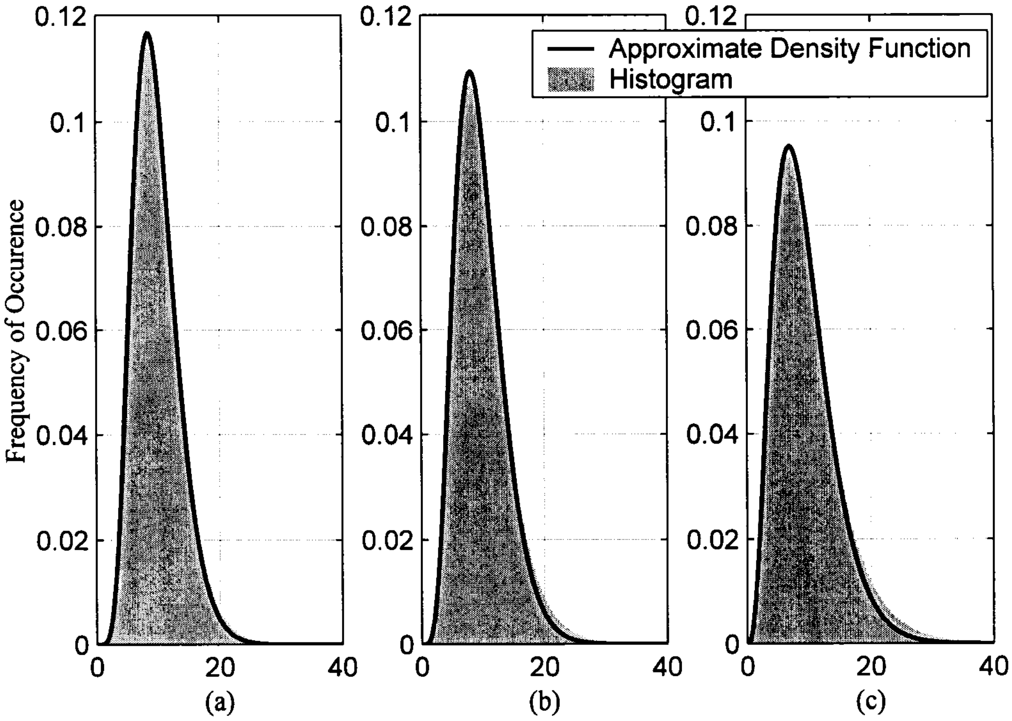

**Fig. 3.2. Histograms of $|\mathbf{A}_n(1,1)|^2$ based on using two million observations and corresponding approximations by a *gamma* density function for $(n_T, n_R) = (2,10)$.**

**(a) $\beta = 7^\circ$ and antenna spacing of $2\lambda$, ($a$ = 7.25, $t$ = 1.35)**

**(b) $\beta = 10^\circ$ and antenna spacing of $\lambda$, ($a$ = 6.03, $t$ = 1.60)**

**(c) $\beta = 12^\circ$ and antenna spacing of $\lambda/2$ ($a$ = 3.90, $t$ = 2.39)**

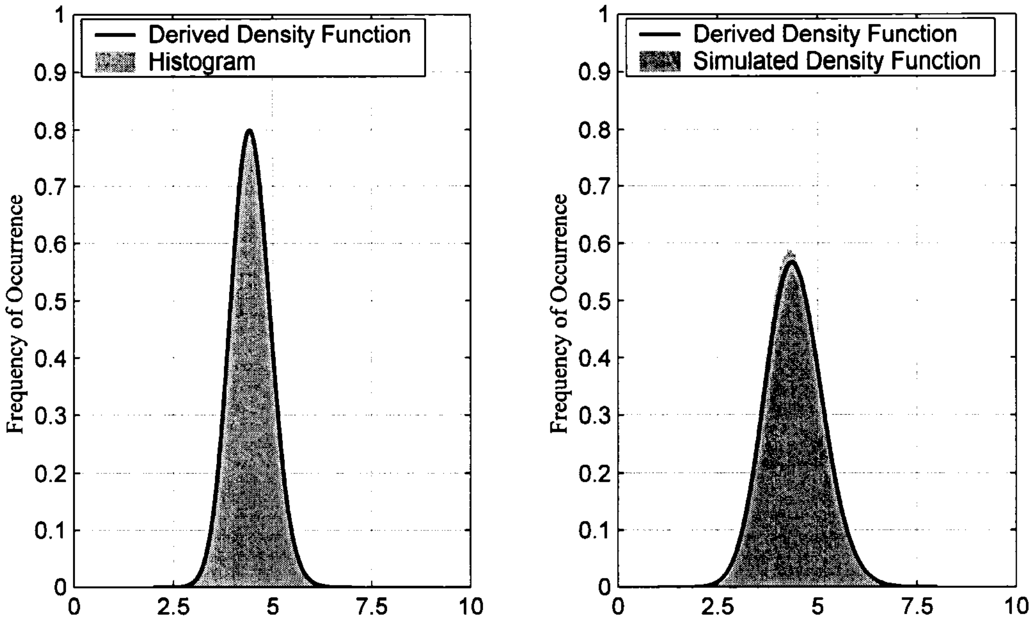

(a) Values of $\mathbf{A}_n(1,1)$ (b) Values of $\mathbf{A}_n(1,1)$

**Fig. 3.3. The derived density functions and histograms of $\mathbf{A}_n(1,1)$ for $(n_T, n_R) = (4, 20)$ antennas in a slow frequency non-selective Rayleigh fading (a) uncorrelated; (b) correlated.**

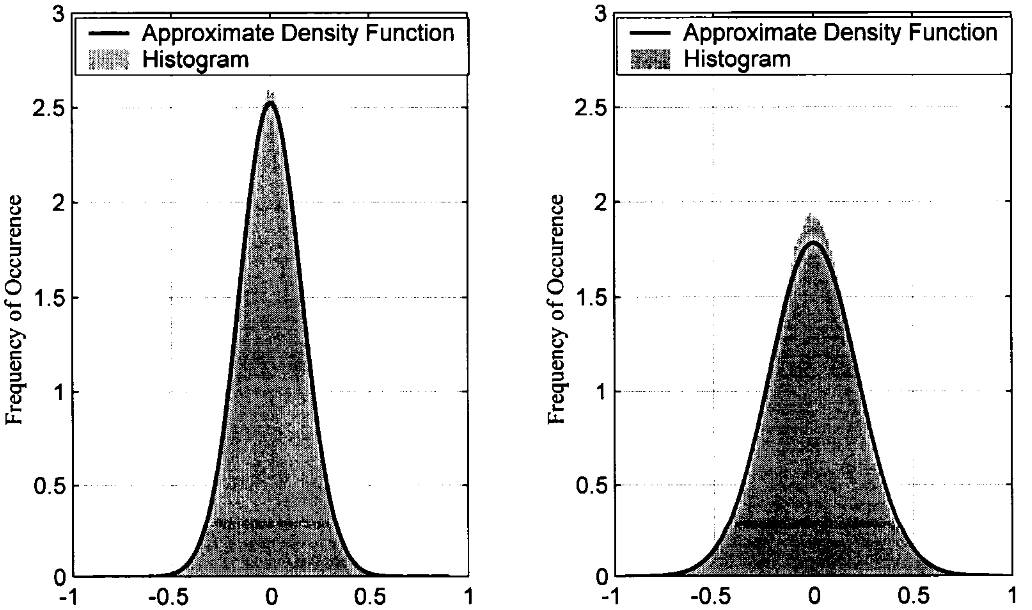

(a) Values of $\Re\{\mathbf{R}_n(1,2)\}$ (b) Values of $\Re\{\mathbf{R}_n(1,2)\}$

**Fig. 3.4. The approximate density functions and histograms of $\Re\{\mathbf{R}_n(1,2)\}$ for $(n_T, n_R) = (4, 20)$ antennas in a slow frequency non-selective Rayleigh fading (a) uncorrelated; (b) correlated.**

correlated scenarios, while the variance increases from 1/4 to 1/2. In the multi-user case, the channel observation on $j$-th transmitted symbol from the $l$-th user is given by (3.15). Since the users' channel matrices are generated independently of each other, the analysis on each user's channel matrix column norms is the same as for the single user case. Thus, the mean and variance of the elements of the diagonal matrix $\mathbf{A}_{n,l}$, for $l = 1, 2, \ldots, K$, is given by (3.21) and (3.25) for the uncorrelated and correlated fading scenario, respectively.

### 3.2.2 Moments of the Antenna Correlation Matrix Elements

In (3.3), the off-diagonal entries of the antenna correlation matrix $\mathbf{R}_n$ give rise to the co-antenna interference corrupting the $j$-th element of the channel observation vector $\mathbf{y}_n$. In this section, we determine the mean and variance of the off-diagonal entries of $\mathbf{R}_n$, which is used in the performance analysis techniques described in Section 3.3 and Chapter 5.

Using the correlated MIMO channel model described in Section 2.1.3, the correlation between the $j$-th and $k$-th normalized columns of the channel matrix $\mathbf{H}_n$, $k \neq j$ can be expressed as

$$\begin{aligned}\mathbf{R}_n(j,k) &= \frac{\mathbf{h}_{n,j}^H \mathbf{h}_{n,k}}{\left\|\mathbf{h}_{n,j}\right\| \left\|\mathbf{h}_{n,k}\right\|} \\ &= \frac{\mathbf{g}_{n,j}^H \left(\mathbf{C}_{RX}^{1/2}\right)^H \mathbf{C}_{RX}^{1/2} \mathbf{g}_{n,k}}{\left\|\mathbf{h}_{n,j}\right\| \left\|\mathbf{h}_{n,k}\right\|} \\ &\approx \frac{\mathbf{g}_{n,j}^H \mathbf{C}_{RX} \mathbf{g}_{n,k}}{M_A^2},\end{aligned} \tag{3.26}$$

where the column norms are approximated by their means $M_A$. This approximation is valid due to the small variance of the column norms when compared to their mean.

In the uncorrelated fading scenario, $\mathbf{C}_{RX} = \mathbf{I}$ is substituted into (3.26) and thus in the real and imaginary dimensions, $\mathbf{R}_n(j,k)$ is the sum of $2n_R$ i.i.d. zero mean *Gaussian product* variables with variance ¼. By the central limit theorem, $\mathbf{R}_n(j,k)$ can be approximated by a zero mean complex Gaussian random variable with variance

$$V_R = n_R \big/ \left(2M_A^4\right). \tag{3.27}$$

in the real and imaginary dimensions.

For the correlated fading scenario, we expand (3.26) using the eigenvalue decomposition on $\mathbf{C}_{RX}$ as

$$\mathbf{R}_n(j,k) \approx \frac{\mathbf{g}_{n,j}^H \mathbf{V}_{\mathbf{C}_{RX}} \mathbf{\Lambda}_{\mathbf{C}_{RX}} \mathbf{V}_{\mathbf{C}_{RX}}^T \mathbf{g}_{n,k}}{M_A^2} = \frac{\mathbf{e}_{n,j}^H \mathbf{e}_{n,k}}{M_A^2}, \tag{3.28}$$

where $\mathbf{e}_{n,j} = \mathbf{\Lambda}_{\mathbf{C}_{RX}}^{1/2} \mathbf{V}_{\mathbf{C}_{RX}}^T \mathbf{g}_{n,j}$, $\mathbf{e}_{n,k} = \mathbf{\Lambda}_{\mathbf{C}_{RX}}^{1/2} \mathbf{V}_{\mathbf{C}_{RX}}^T \mathbf{g}_{n,k}$ and are Gaussian random vectors. The expression for $\mathbf{R}_n(j,k)$ can be written as

$$\begin{aligned} \mathbf{R}_n(j,k) &\approx \frac{1}{M_A^2}\Bigg(\sum_{l=1}^{n_R} \Re\left\{\mathbf{e}_{n,j}(l)\right\}\Re\left\{\mathbf{e}_{n,k}(l)\right\} + \sum_{l=1}^{n_R} \Im\left\{\mathbf{e}_{n,j}(l)\right\}\Im\left\{\mathbf{e}_{n,k}(l)\right\} \\ &\qquad + i\left(\sum_{l=1}^{n_R} \Re\left\{\mathbf{e}_{n,j}(l)\right\}\Im\left\{\mathbf{e}_{n,k}(l)\right\} + \sum_{l=1}^{n_R} \Im\left\{\mathbf{e}_{n,j}^*(l)\right\}\Re\left\{\mathbf{e}_{n,k}(l)\right\}\right)\Bigg) \\ &= \frac{1}{M_A^2}\left(\sum_{l=1}^{n_R} W_l + \sum_{l=1}^{n_R} X_l + i\left(\sum_{l=1}^{n_R} Y_l + \sum_{l=1}^{n_R} Z_l\right)\right). \end{aligned} \tag{3.29}$$

where * represents the conjugate operation. Thus, $W_l, X_l, Y_l$, and $Z_l$ are independent *Gaussian product* variables with zero mean and variance $\left(\mathbf{\Lambda}_{\mathbf{C}_{RX}}(l,l)\right)^2 \big/ 4$ for $l = 1,2,\ldots,n_R$. Applying the central limit theorem to the real and imaginary terms in (3.28), we approximate $\mathbf{R}_n(j,k)$ as a complex Gaussian random variable with zero mean and variance

$$V_R = \frac{1}{2M_A^4} \sum_{l=1}^{n_R} \left(\mathbf{\Lambda}_{\mathbf{C}_{RX}}(l,l)\right)^2 \tag{3.30}$$

in the real and imaginary dimensions for $k = 1, 2, \ldots, n_T$, $k \neq j$. Hence, the variance of $\mathbf{R}_n(j,k)$ is dependent on the eigenvalues of $\mathbf{C}_{RX}$, which in turn is dependent on the angular spread $\beta$.

Fig. 3.4 illustrates the approximate density function and histogram of the real component of $\mathbf{R}_n(1,2)$ based on one million channel realizations in uncorrelated and correlated fading scenarios for the $(n_T, n_R) = (4,20)$ antenna configuration. Note that the histogram is closely approximated by a Gaussian density function. As in Fig. 3.3, spatial correlation does not affect the mean (which is zero) but increases the variance from a value of 0.025 in the uncorrelated fading case to 0.05 in the correlated fading scenario. The higher variance for the correlated fading case translates to an increased co-antenna interference component that is corrupting the channel observations, which in turn reduces the performance of the proposed detector. This is confirmed through simulation results in Section 3.4.

## 3.3 Analysis of the Proposed MIMO Signal Detector

Using the results from the previous section, we analyze the symbol error performance of the proposed detector. We observe that the linearly complex signal detector has slight performance degradation with respect to the exponentially complex optimal signal detector in the operating SNR range of the proposed turbo-coded MIMO systems considered in Chapter 4.

For the proposed detector, we consider the average and approximate symbol error performance in cases of perfect and imperfect CSI at the receiver over a slow frequency non-selective Rayleigh fading channel. The average performance is calculated using the full correlation model shown in (2.3), while the approximate performance uses the channel model described in Section 2.1.3. The transmitter is assumed to use a square QAM constellation, such as 16-QAM, with $M$ points and a minimum distance of $2B$ between signal points. Furthermore, the transmitted symbols from each antenna are assumed to be equiprobable and independent of transmitted symbols from other antennas. Withput loss in generality, we consider the symbol error probability for the first transmit antenna, as similar error expressions follow for the other transmit antennas.

*Claim 1: The probability of error for symbols sent from the first transmit antenna, conditioned on the estimated channel matrix* $\hat{\mathbf{H}}_n$, *is given by*

$$\begin{aligned} P_1^{demod}\left(error \mid \hat{\mathbf{H}}_n\right) &= \frac{4}{M^{n_T}} \sum_{l_2=1}^{M} \sum_{l_3=1}^{M} \cdots \sum_{l_{n_T}=1}^{M} \left[1 - Q\left(\frac{\Re\{D\} - \tilde{\mathbf{R}}_n(1,1)\mathbf{A}_n(1,1)B}{\sigma}\right) Q\left(\frac{\Im\{D\} - \tilde{\mathbf{R}}_n(1,1)\mathbf{A}_n(1,1)B}{\sigma}\right)\right] \\ &+ \frac{\left(\sqrt{M}-2\right)^2}{M^{n_T}} \sum_{l_2=1}^{M} \sum_{l_3=1}^{M} \cdots \sum_{l_{n_T}=1}^{M} \left[1 - \left(1 - 2Q\left(\frac{\Re\{D\} + \tilde{\mathbf{R}}_n(1,1)\mathbf{A}_n(1,1)B}{\sigma}\right)\right)\left(1 - 2Q\left(\frac{\Im\{D\} + \tilde{\mathbf{R}}_n(1,1)\mathbf{A}_n(1,1)B}{\sigma}\right)\right)\right] \\ &+ \frac{4\left(\sqrt{M}-2\right)}{M^{n_T}} \sum_{l_2=1}^{M} \sum_{l_3=1}^{M} \cdots \sum_{l_{n_T}=1}^{M} \left[1 - Q\left(\frac{-\Re\{D\} - \tilde{\mathbf{R}}_n(1,1)\mathbf{A}_n(1,1)B}{\sigma}\right)\left(1 - 2Q\left(\frac{\Im\{D\} + \tilde{\mathbf{R}}_n(1,1)\mathbf{A}_n(1,1)B}{\sigma}\right)\right)\right], \end{aligned} \tag{3.31}$$

*where* $\tilde{\mathbf{R}}_n = \hat{\mathbf{S}}_n^H \mathbf{S}_n$ *and* $D = -\sum_{k=2}^{n_T} \tilde{\mathbf{R}}_n(1,k)\mathbf{A}_n(k,k)Q_{l_k}$ *is the co-antenna interference for the first transmit antenna.*

(Note: In case of perfect CSI at the receiver, $\tilde{\mathbf{R}}_n = \mathbf{S}_n^H \mathbf{S}_n$ and $\tilde{\mathbf{R}}_n(1,1) = 1$. For a time-varying stationary and ergodic channel, the average probability of symbol error can be determined by averaging (3.31) over many channel realizations.)

*Justification of Claim 1:*

From (3.8), the channel observation vector $\hat{\mathbf{y}}_n$ can be re-expressed as

$$\hat{\mathbf{y}}_n = \tilde{\mathbf{R}}_n \mathbf{A}_n \mathbf{b}_n + \hat{\mathbf{v}}_n, \tag{3.32}$$

where $\mathbf{H}_n = \mathbf{S}_n \mathbf{A}_n$, $\tilde{\mathbf{R}}_n = \hat{\mathbf{S}}_n^H \mathbf{S}_n$, $\hat{\mathbf{v}}_n = \hat{\mathbf{S}}_n^H \mathbf{v}_n$. Consequently, $\hat{\mathbf{y}}_n(1)$ is given by

$$\hat{\mathbf{y}}_n(1) = \tilde{\mathbf{R}}_n(1,1)\mathbf{A}_n(1,1)\mathbf{b}_n(1) + \sum_{k=2}^{n_T} \tilde{\mathbf{R}}_n(1,k)\mathbf{A}_n(k,k)\mathbf{b}_n(k) + \hat{\mathbf{v}}_n(1), \tag{3.33}$$

where $\tilde{\mathbf{R}}_n(1,1)$ can be thought of as a loss factor due to imperfect CSI. The probability of symbol error conditioned on the estimated channel matrix is

$$P_1^{demod}\left(error \mid \hat{\mathbf{H}}_n\right) = \sum_{p=1}^{M} P\left[\mathbf{b}_n(1) = q_p\right] P\left[\hat{\mathbf{y}}_n(1) \notin Z_p \middle| \mathbf{b}_n(1) = q_p\right], \tag{3.34}$$

where the minimum distance decision region $Z_p$ corresponds to the $p$-th QAM symbol $q_p$. If $P\left[\hat{\mathbf{y}}_n(1) \notin Z_l \middle| \mathbf{b}_n(1) = q_p\right]$ is further conditioned on the symbols from the remaining transmit antennas, i.e., let $\mathbf{b}_n(k) = q_{p_k}, k = 2,3\ldots,n_T$, then the co-antenna interference term in (3.33) becomes a known deterministic quantity. Therefore, the symbol transmitted from the first antenna $\mathbf{b}_n(1)$ is only corrupted by additive Gaussian noise. Hence, assuming the real and imaginary parts of $\hat{\mathbf{y}}_n(1)$ are independent, the probability of error in (3.34) is given by the weighted sum of the probability of error when $\mathbf{b}_n(1) = q_p$ is a corner, middle or side point of the constellation. These expressions are given by,

$$\begin{aligned} P^{e}_{corner} &= 1 - P\left[\Re\{\hat{\mathbf{v}}_n(1)\} > \Re\{D\} - \tilde{\mathbf{R}}_n(1,1)\mathbf{A}_n(1,1)B\right]\times \\ &\quad P\left[\Im\{\hat{\mathbf{v}}_n(1)\} > \Im\{D\} - \tilde{\mathbf{R}}_n(1,1)\mathbf{A}_n(1,1)B\right], \\ P^{e}_{middle} &= 1 - P\left[\Re\{D\} - \tilde{\mathbf{R}}_n(1,1)\mathbf{A}_n(1,1)B < \Re\{\hat{\mathbf{v}}_n(1)\} < \Re\{D\} + \tilde{\mathbf{R}}_n(1,1)\mathbf{A}_n(1,1)B\right]\times \\ &\quad P\left[\Im\{D\} - \tilde{\mathbf{R}}_n(1,1)\mathbf{A}_n(1,1)B < \Im\{\hat{\mathbf{v}}_n(1)\} < \Im\{D\} + \tilde{\mathbf{R}}_n(1,1)\mathbf{A}_n(1,1)B\right], \\ P^{e}_{side} &= 1 - P\left[\Re\{\hat{\mathbf{v}}_n(1)\} < \Re\{D\} + \tilde{\mathbf{R}}_n(1,1)\mathbf{A}_n(1,1)B\right]\times \\ &\quad P\left[\Im\{D\} - \tilde{\mathbf{R}}_n(1,1)\mathbf{A}_n(1,1)B < \Im\{\hat{\mathbf{v}}_n(1)\} < \Im\{D\} + \tilde{\mathbf{R}}_n(1,1)\mathbf{A}_n(1,1)B\right], \end{aligned} \tag{3.35}$$

where $D = -\sum_{k=2}^{n_T} \tilde{\mathbf{R}}_n(1,k)\mathbf{A}_n(k,k)q_{p_k}$ is the co-antenna interference of the first transmit antenna. By combining (3.34) and (3.35), we obtain the result in (3.31).

*Claim 2: The approximate probability of symbol error for the first transmit antenna is given by*

$$\begin{aligned} P_1^{de\,\mathrm{mod}}(error) \approx{}& \frac{4}{M^{n_T}} \sum_{l_2=1}^{M}\sum_{l_3=1}^{M}\cdots\sum_{l_{n_T}=1}^{M}\left[1 - Q\left(\frac{-\bar{\tilde{\mathbf{R}}}_n(1,1)M_A B}{\sqrt{\sigma_{CAI}^2 + \sigma^2}}\right)^2\right] \\ &+ \frac{\left(\sqrt{M}-2\right)^2}{M^{n_T}} \sum_{l_2=1}^{M}\sum_{l_3=1}^{M}\cdots\sum_{l_{n_T}=1}^{M}\left[1 - \left(1 - 2Q\left(\frac{-\bar{\tilde{\mathbf{R}}}_n(1,1)M_A B}{\sqrt{\sigma_{CAI}^2 + \sigma^2}}\right)\right)^2\right] \\ &+ \frac{4\left(\sqrt{M}-2\right)}{M^{n_T}} \sum_{l_2=1}^{M}\sum_{l_3=1}^{M}\cdots\sum_{l_{n_T}=1}^{M}\left[1 - Q\left(\frac{-\bar{\tilde{\mathbf{R}}}_n(1,1)M_A B}{\sqrt{\sigma_{CAI}^2 + \sigma^2}}\right)\left(1 - 2Q\left(\frac{\bar{\tilde{\mathbf{R}}}_n(1,1)M_A B}{\sqrt{\sigma_{CAI}^2 + \sigma^2}}\right)\right)\right], \end{aligned} \tag{3.36}$$

*where* $\tilde{\mathbf{R}}_n = \hat{\mathbf{S}}_n^H\mathbf{S}_n$ *and the component* $\bar{\tilde{\mathbf{R}}}_n(1,1)$ *is the average loss factor due to imperfect CSI,* $M_A$ *is the mean of the elements of the diagonal matrix* $\mathbf{A}_n$ *and the variance of the co-antenna interference (CAI) in each dimension is given by* $\sigma_{CAI}^2 = \frac{n_R}{2M_A^2}\sum_{k=2}^{n_T}\left\|q_{p_k}\right\|^2$ *and* $\sigma_{CAI}^2 = \frac{1}{2M_A^2}\left(\sum_{l=1}^{n_R}\left(\mathbf{\Lambda}_{\mathbf{C}_{RX}}(l,l)\right)^2\right)\sum_{k=2}^{n_T}\left\|q_{p_k}\right\|^2$ *for the uncorrelated and correlated fading cases respectively.*

(Note: The above expression is in closed form and for the case of perfect CSI at the receiver, $\tilde{\mathbf{R}}_n = \mathbf{S}_n^H\mathbf{S}_n$ and $\bar{\tilde{\mathbf{R}}}_n(1,1) = 1$.)

*Justification of Claim 2:*

For the channel model described in Section 2.1.3, we consider the first transmit antenna without loss of generality, where the channel observation is given in

(3.33) and the corresponding probability of symbol error is given by

$$P_1^{demod}(error) = \sum_{p=1}^{M} P\left[\mathbf{b}_n(1) = q_p\right] P\left[\hat{\mathbf{y}}_n(1) \notin Z_p \middle| \mathbf{b}_n(1) = q_p\right]. \tag{3.37}$$

where the minimum distance decision region $Z_p$ corresponds to the $p$-th QAM symbol $q_p$. If we condition $P\left[\hat{\mathbf{y}}_n(1) \notin Z_p \middle| \mathbf{b}_n(1) = q_p\right]$ on the remaining transmit antennas, i.e., let $\mathbf{b}_n(k) = q_{p_k}$ for $k = 2,3\ldots,n_T$, then the co-antenna interference term in (3.33) is dependent on two random variables, $\mathbf{A}_n(k,k)$ and $\tilde{\mathbf{R}}_n(1,k)$. Using the results from the previous section, $\mathbf{A}_n(k,k)$ can be approximated by its mean $M_A$, as its variance is small. Since the elements of the estimation error matrix $\boldsymbol{\varepsilon}_n$ are usually much smaller than the elements of the channel matrix, the correlation coefficient $\tilde{\mathbf{R}}_n(1,k)$ $(k \neq 1)$ is assumed to be a zero mean complex Gaussian random variable with variance in each dimension given by (3.27) and (3.30) for the uncorrelated and correlated fading scenarios, respectively. Hence, the co-antenna interference term can be approximated by a complex Gaussian random variable with zero mean and variance in each dimension given by $\sigma_{CAI}^2 = \frac{n_R}{2M_A^2}\sum_{k=2}^{n_T}\left\|q_{p_k}\right\|^2$ for the uncorrelated fading case and $\sigma_{CAI}^2 = \frac{1}{2M_A^2}\left(\sum_{l=1}^{n_R}\left(\mathbf{\Lambda}_{C_{RX}}(l,l)\right)^2\right)\sum_{k=2}^{n_T}\left\|q_{p_k}\right\|^2$ for the correlated fading case.

The probability of symbol error in (3.37) is consequently given by the expression for a QAM symbol corrupted by additive Gaussian noise and thus, is the weighted sum of the probability of error for $\mathbf{b}_n(1) = q_p$ is a corner, middle or a side point of the constellation. These expressions are given by

$$\begin{aligned}
P_{corner}^{e} &= 1 - P\left[\Re\{\tilde{\mathbf{v}}_n(1)\} > -\tilde{\mathbf{R}}_n(1,1)\mathbf{A}_n(1,1)B\right]\times \\
&\quad P\left[\Im\{\tilde{\mathbf{v}}_n(1)\} > -\tilde{\mathbf{R}}_n(1,1)\mathbf{A}_n(1,1)B\right], \\
P_{middle}^{e} &= 1 - P\left[-\tilde{\mathbf{R}}_n(1,1)\mathbf{A}_n(1,1)B < \Re\{\tilde{\mathbf{v}}_n(1)\} < \tilde{\mathbf{R}}_n(1,1)\mathbf{A}_n(1,1)B\right]\times \\
&\quad P\left[-\tilde{\mathbf{R}}_n(1,1)\mathbf{A}_n(1,1)B < \Im\{\tilde{\mathbf{v}}_n(1)\} < \tilde{\mathbf{R}}_n(1,1)\mathbf{A}_n(1,1)B\right], \\
P_{side}^{e} &= 1 - P\left[\Re\{\tilde{\mathbf{v}}_n(1)\} < \tilde{\mathbf{R}}_n(1,1)\mathbf{A}_n(1,1)B\right]\times \\
&\quad P\left[-\tilde{\mathbf{R}}_n(1,1)\mathbf{A}_n(1,1)B < \Im\{\tilde{\mathbf{v}}_n(1)\} < \tilde{\mathbf{R}}_n(1,1)\mathbf{A}_n(1,1)B\right],
\end{aligned} \tag{3.38}$$

where the real and imaginary parts of $\hat{\mathbf{y}}_n(1)$ are assumed to be independent and $\tilde{\mathbf{v}}_n(1)$ is the sum of the Gaussian noise $\hat{\mathbf{v}}_n(1)$ and the co-antenna interference. Since $\tilde{\mathbf{R}}_n(1,1)$ is a random variable with an unknown density function, we can approximate it by its value averaged over many channel realizations $\bar{\tilde{\mathbf{R}}}_n(1,1)$, where for instance, $\bar{\tilde{\mathbf{R}}}_n(1,1)$ is equal to 0.95 for an estimation error variance of 10 % (averaged over 100,000 channel realizations). Therefore, the approximate probability of error for the first transmit antenna using (3.38) and the *Q*-function is given in (3.36).

## 3.4 Numerical and Simulated Symbol Error Rate Results

We present the performance of the proposed MIMO signal detector in uncorrelated and correlated Rayleigh fading channels for antenna spacing of $\lambda/2$ at the mobile, $\lambda$ at the base-station and an angular spread $\beta$ of 10 degrees. We consider a specific Gray coded 16-QAM symbol constellation illustrated in Fig. 3.5, which is adopted from [31] with perfect and imperfect channel state information ($\sigma_\varepsilon^2 = 10$ %) being available at the receiver. The expression for the symbol error rate performance given in (3.31) was averaged over 100, 000 channel realizations.

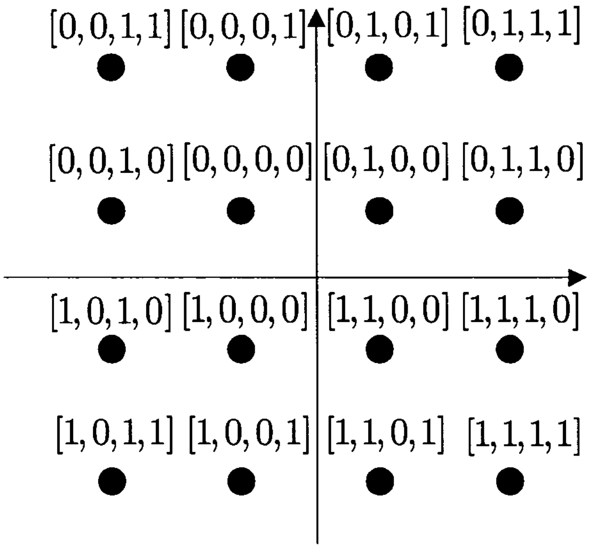

**Fig. 3.5. The Gray coded 16-QAM mapping used in simulations (adopted from [31])**

We also compare the performance of the proposed detector to that of the maximum likelihood or optimal detector. Using channel knowledge at the receiver, the transmit antenna signal space is mapped to the corresponding receive antenna signal space, which has $n_R$ complex dimensions and contains $16^{n_T}$ signal points (for 16 QAM and $n_T$ transmit antennas). Subsequently, the detector generates likelihoods (using the conditional Gaussian density function) on all signal space points, as discussed in detail in Chapter 2 of the author's MEng thesis [56]. By appropriately summing these likelihoods, the soft decision on a particular QAM symbol from each transmit antenna can be generated.

Fig. 3.6 and Fig. 3.7 illustrate the average and approximate symbol error rate (SER) performance of the MIMO signal detector for $(n_T, n_R)$ = (2, 10) and (4, 20) antennas, respectively. In the uncorrelated fading scenarios (Fig. 3.6 (a) and Fig. 3.7 (a)), there is a close match between the approximate and average performance. However, in the correlated fading cases (Fig. 3.6 (b) and Fig. 3.7 (b)), there exists a small difference between the approximate and average symbol error rate as the approximate performance does not include the spatial correlation between transmit antennas. For comparison, the simulated performance of the optimal MIMO signal detector is also shown for the same system parameters.

Although the proposed detector is co-antenna interference limited at high SNRs, it performs only slightly lower than the exponentially complex optimal signal detector at low SNRs, i.e., -5 to -10 dB. As shown in Chapter 4, this region corresponds to the operating SNRs of the turbo-coded MIMO system. Moreover, Fig. 3.6 and Fig. 3.7 illustrate that the performance of the detector is robust to channel estimation errors.

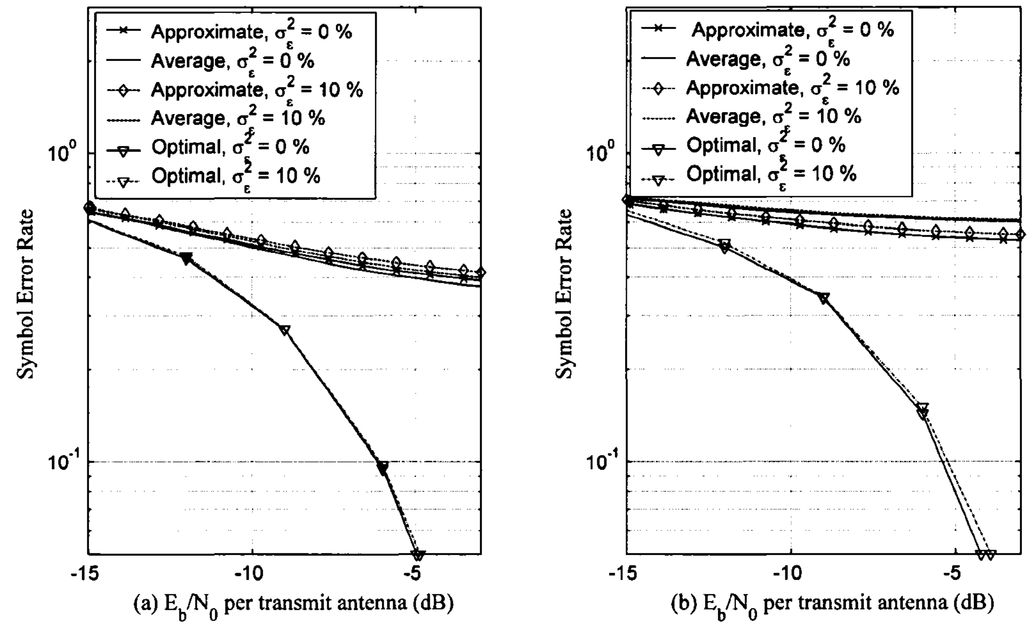

(a) $E_b/N_0$ per transmit antenna (dB) (b) $E_b/N_0$ per transmit antenna (dB)

**Fig. 3.6. Performance analysis of the proposed and optimal MIMO signal detector for $(n_T, n_R)$ = (2, 10) antenna system using 16-QAM signalling in a slow frequency non-selective (a) uncorrelated and (b) correlated Rayleigh fading channel.**

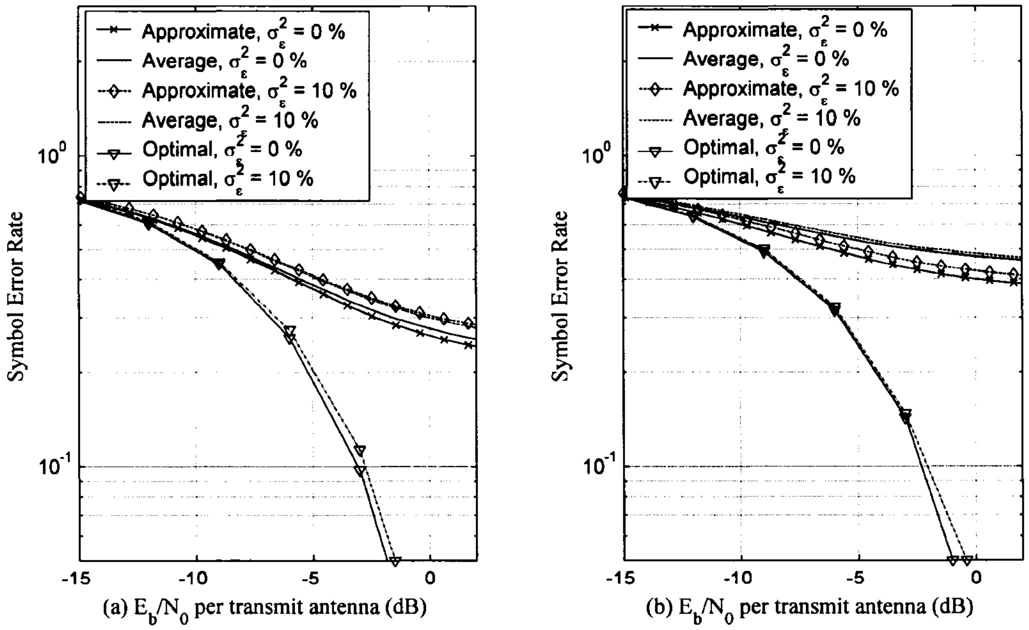

(a) $E_b/N_0$ per transmit antenna (dB) (b) $E_b/N_0$ per transmit antenna (dB)

**Fig. 3.7. Performance analysis of the proposed and optimal MIMO signal detector for $(n_T, n_R)$ = (4, 20) antenna system using 16-QAM signalling in a slow frequency non-selective (a) uncorrelated and (b) correlated Rayleigh fading channel.**

## 3.5 Discussion on the Proposed Signal Detection Method

### 3.5.1 Analogies and Differences between MIMO and DS-CDMA

The discrete-time representation of the MIMO system in (2.2) and further exemplified in (3.2) has parallels to a synchronous DS-CDMA system. The MIMO signal detector uses spatial spreading provided by the channel matrix to distinguish the transmitted symbols, i.e., the $j$-th transmit antenna is analogous to the $j$-th user and the receive antennas correspond to chips of a user's spreading sequence in synchronous DS-CDMA transmission. As seen in (3.3), the other $(n_T - 1)$ transmit antennas result in co-antenna interference, which is similar to multi-user interference. The proposed detector is best suited for an uplink scenario, where it is feasible to have more receive antennas (at the base-station) than transmit antennas (at the mobile), i.e., which corresponds to a typical underloaded CDMA system [101]. Finally, the filtering by the matrix $\mathbf{S}_n$ in (3.2) and the Gaussian approximation for the filtered noise and the co-antenna interference is analogous to that performed by the conventional CDMA detector based on a bank of matched filters.

However, due to the fundamental change in the problem definition, there exist many differences between the two scenarios. One of the differences is that multi-level CDMA modulation has not been studied extensively, e.g., [19], [72], [86]. Another key difference is that elements of the correlation matrix $\mathbf{R}_n$ are functions of random spreading sequences (i.e., the normalized columns of $\mathbf{H}_n$) and as such cannot be designed. Finally, the issue of channel estimation errors has no parallel in synchronous DS-CDMA systems, as the spreading sequences are perfectly known at the receiver.

### 3.5.2 Implementation Complexity Issues

As mentioned in Section 2.5, signal detection complexity determines the scalability of coded MIMO systems to large antenna configurations, which are needed to support higher data rates. The proposed detection complexity increases only linearly with the number of transmit and receive antennas and users, i.e., $O\left(n_T n_R K\right)$. Based on channel observations for each element of the transmitted symbol vector, corresponding soft decisions are generated using the Gaussian approximation for the co-antenna interference and noise. Thus, the computed number of soft decisions is $n_T MK$, where $M$ is the size of the constellation being used, which increases linearly with the number of transmit antennas and users.

Table I compares the implementation complexity of prior MIMO signal detection techniques with the proposed detector. Comparison of the overall receiver architecture is not feasible as each of the schemes presented in Table I uses a slightly different channel coding method. Nonetheless, a comparison of detection complexity provides insight into the scalability potential of the coded MIMO system to many antennas (which corresponds to high spectral efficiencies) and (or) many users.

The proposed detector becomes attractive for uplink systems with a large number of transmit and receive antennas, e.g., 8, 12 or even 30 transmit antennas. In contrast, exponentially complex signal detection methods, such as the one used in space-time trellis codes ([89], [90]) or iterative MAP detection / decoding schemes ([55], [87], [98]) would be too complex to be practical, e.g., for 16-QAM and 30 transmit antennas, space-time trellis codes would have $16^{30} \approx 10^{36}$ states. Similarly, the complexity of sphere detection ([21], [42], [102]) would be excessive in this scenario, as the number of candidates for a given search radius would increase due to the higher co-antenna interference. Furthermore, the impact of imperfect CSI has not been considered in literature for the sphere detector. Due to better interference suppression, the MIMO signal detectors in the layered space-time system [2] and the Turbo-BLAST method [80] may have better performance than the proposed MIMO signal detector at higher SNRs. However, the nulling and cancelling techniques used by the detector, shifts the coded MIMO system performance in [2], [80] to higher SNRs despite the use of channel codes.

**Table I. Comparison of other MIMO signal detection methods to the proposed MIMO signal detector (N. A. refers to not being assessed in literature so far).**

| | **Detection Complexity** | **Imperfect CSI** | **Multi-user** |
|---|---|---|---|
| **Space-Time Trellis Codes** [89], [90] | Exponential | √ | N. A. |
| **Optimal MIMO Detector** [55], [87], [98] | Exponential | N. A. | N. A. |
| **Sphere Detector** [21], [42], [102] | Polynomial (SNR dependent) | N. A. | N. A. |
| **Layered Space-Time; Turbo-BLAST** [2], [80] | Polynomial (cubic) | √ | N. A. |
| **The Proposed Detector** | Linear | √ | √ |

## 3.6 Chapter Summary

In this chapter, we have developed a new linear complexity MIMO soft decision signal detector and analyzed its performance.

In Section 3.1, we have formulated the proposed MIMO signal detector for various settings. This detector produces channel observations on the transmitted symbols and subsequently generates soft decisions on these symbols using the Gaussian approximation for the co-antenna and multi-user interference, filtered noise and channel estimation errors.

In Section 3.2, we have determined expressions for selected moments at the output of the proposed MIMO signal detector. These quantities were used to analyze the average and approximate symbol error performance of the detector in Section 3.3 and are used to analyze the overall turbo-coded MIMO system in Chapter 5. Section 3.4 has showed that at SNRs corresponding to the region of operation of the turbo-coded MIMO system considered in Chapter 4, the proposed linearly complex detector performs only slightly worse than the exponentially complex optimal signal detector.

Finally, in Section 3.5, we have considered the similarities and differences between the proposed MIMO signal detection scheme and the matched filter receivers in DS-CDMA systems. Furthermore, we have compared the complexity of the proposed signal detection method to prior MIMO signal detection schemes to illustrate that the proposed detector is robust and can support large numbers of antennas with many number of users (through a linear complexity increase).

# Chapter 4

# Iterative MIMO Receivers and Simulation Results

In this chapter, we present (iterative) MIMO receiver architectures for the considered turbo-coded MIMO transmitter. Simulation results are shown for scenarios with various antenna configurations. In addition, we illustrate that with appropriate extensions, the proposed coded MIMO system can be successfully applied in multi-head multi-track magnetic recording systems.

## 4.1 Wireless MIMO Transmitter Architecture

Fig. 4.1 illustrates the single user transmitter of a turbo-coded MIMO system in which each antenna transmits a different stream of modulation symbols. The source produces independent equiprobable data bits that are encoded by a rate $N_m/N_c$ turbo encoder. The message sequence $\mathbf{m}$ contains $N_m$ bits and is encoded into a codeword $\mathbf{c}$ of length $N_c$ as

$$\mathbf{c} = \left(g_1(\mathbf{m}), g_2(\Pi(\mathbf{m}))\right), \tag{4.1}$$

where $g_1(\bullet)$, $g_2(\bullet)$ denote the constituent encoders of the turbo code, $\Pi$ represents the interleaver and $g_1(\bullet)$ includes the systematic bits (as discussed in Section 2.3.1). In addition to the interleaver used in the turbo encoder, there is an interleaver at the front-end of the modulation mapper, and a channel interleaver.

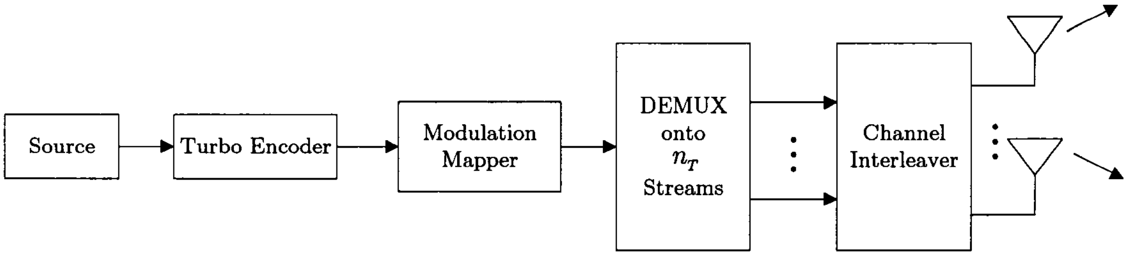

**Fig. 4.1. Schematic block diagram of the single user MIMO transmitter.**

Turbo coded bits are interleaved in order to ensure that consecutive coded bits are not mapped to the same modulation symbol and to disperse blocks of low reliability demodulation data in the iterative processing loop at the receiver. The modulation mapper maps the interleaved coded bits into complex symbols (we consider Gray coded QPSK and 16-QAM signal constellations), which are then de-multiplexed onto $n_T$ streams, channel interleaved and transmitted. The role of the channel interleaver and de-interleaver is to break up channel fades affecting transmitted packets of data.

## 4.2 Single User MIMO Receiver Architectures

### 4.2.1 Overview of the Architectures

Each of the three considered receivers consists of front-end soft decision MIMO signal detection followed by modulation de-mapping and turbo decoding. The proposed MIMO signal detector, presented in Chapter 3, approximates the co-antenna interference as a complex Gaussian random variable in order to produce soft decisions on the transmitted modulation symbols. The de-mapper for the demodulator maps these soft decisions into estimates on the coded bits, which are de-interleaved and fed to the turbo decoder.

The receiver can be implemented either using single pass detection / decoding with optional turbo demodulation (implementation A and B) or by applying overall iterative processing (implementation C), as shown in Fig. 4.2 (a), (b) and (c), respectively. Turbo demodulation is optional as it only provides a gain of less than one dB, when we consider 16-QAM symbols under severe channel conditions (e.g., correlated fading and channel estimation errors). Turbo demodulation turns out to provide little to no gain for QPSK symbols due to independence of the in-phase and quadrature components. In receiver implementation C as shown in Fig. 4.2 (c), extrinsic information on the coded bits from the turbo decoder are used in improving the knowledge of the co-antenna interference structure at the detector. The details of each implementation are described in the following three sections.

### 4.2.2 Single Pass Receiver

Fig. 4.2 (a) illustrates the block diagram of receiver implementation A with single pass detection followed by turbo decoding. The detector generates soft decisions on the transmitted modulation symbols, i.e., $P\left(\mathbf{y}_n(j)\middle|\mathbf{b}_n(j)=q_p\right)$, or $P\left(\hat{\mathbf{y}}_n(j)\middle|\mathbf{b}_n(j)=q_p\right)$, $j = 1, 2, \ldots, n_T$. The exact calculation is shown in (3.7) and (3.13) for the cases of perfect and imperfect channel state information at the receiver, respectively. The de-mapper maps these likelihood values into soft decisions on the turbo-coded bits, for instance the likelihood that the $m$-th coded bit is zero in the perfect CSI scenario is given by

$$P\left(\mathbf{y}_n(j)\middle|\mathbf{c}(m)=0\right)=\sum_{q_p\in\{M\ \mathrm{QAM}|\mathbf{c}(m)=0\}} P\left(\mathbf{y}_n(j)\middle|\mathbf{b}_n(j)=q_p\right)P\left(\mathbf{b}_n(j)=q_p\right) \tag{4.2}$$

and similarly for imperfect CSI,

$$P\left(\hat{\mathbf{y}}_n(j)\middle|\mathbf{c}(m)=0\right)=\sum_{q_p\in\{M\ \mathrm{QAM}|\mathbf{c}(m)=0\}} P\left(\hat{\mathbf{y}}_n(j)\middle|\mathbf{b}_n(j)=q_p\right)P\left(\mathbf{b}_n(j)=q_p\right), \tag{4.3}$$

where the *a priori* probability on the $p$-th modulation symbol $q_p$, $P\left(\mathbf{b}_n(j)=q_p\right)$ is $1/M$ ($M$ is the modulation order), $p = 1, 2, \ldots, M$. Since the turbo decoder operates on log-ratios, the likelihood for $\mathbf{c}(m)=1$ has to be computed and the corresponding log-likelihood ratio is given by

$$\mathbf{\Lambda}_{De-map}(m)=\frac{P\left(\mathbf{y}_n(j)\middle|\mathbf{c}(m)=1\right)}{P\left(\mathbf{y}_n(j)\middle|\mathbf{c}(m)=0\right)} \tag{4.4}$$

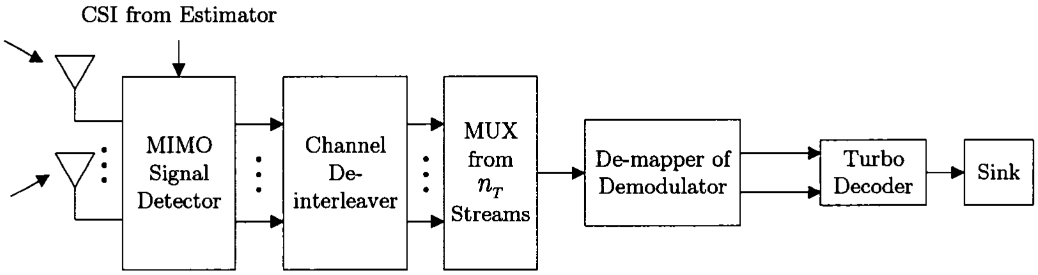

**(a) Implementation A: Single pass Receiver**

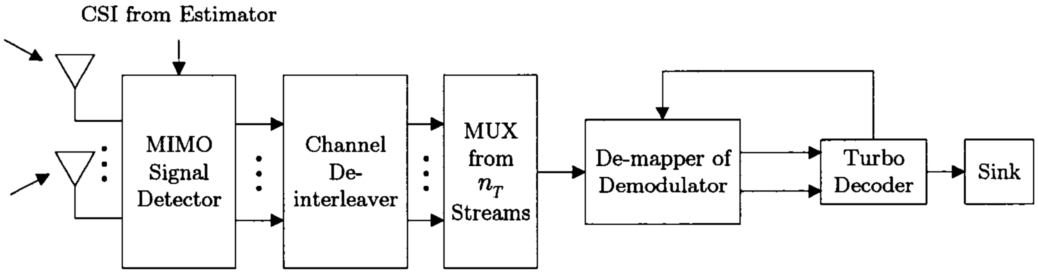

**(b) Implementation B: Single Pass Receiver with Turbo Demodulation**

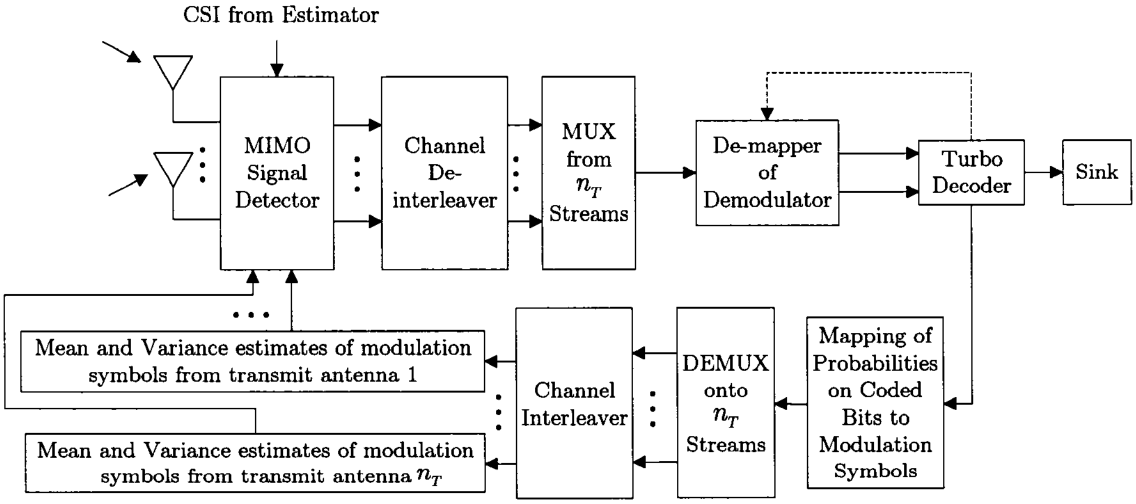

**(c) Implementation C: Fully Iterative Receiver**

**Fig. 4.2. Schematic block diagram of receiver implementations.**

for perfect CSI and

$$\mathbf{\Lambda}_{De-map}(m) = \frac{P\left(\hat{\mathbf{y}}_n(j)\middle|\mathbf{c}(m)=1\right)}{P\left(\hat{\mathbf{y}}_n(j)\middle|\mathbf{c}(m)=0\right)} \tag{4.5}$$

for imperfect CSI at the receiver. The vector of log-ratios $\mathbf{\Lambda}_{De-map}$ are de-interleaved and de-multiplexed into two streams $\mathbf{d}_1$ and $\mathbf{d}_2$, where $\mathbf{d}_1$ are the soft decisions on the coded bits from the first encoder (which includes the systematic bits) and $\mathbf{d}_2$ are the soft decisions on the coded bits from the second encoder. The de-interleaving operation performed on the log-ratio vector $\mathbf{\Lambda}_{De-map}$ is considered to be a part of the de-mapper in all receiver implementations shown in Fig. 4.2.

In receiver implementation A, shown in Fig. 4.2 (a), the turbo decoder in the $i$-th iteration can be described as

$$\begin{aligned} \left[\mathbf{z}_1^i, \mathbf{x}_1^i\right] &= \varphi_1\left(\mathbf{d}_1, \mathbf{x}_2^{i-1}\right) - \mathbf{x}_2^{i-1}, \\ \left[\mathbf{z}_2^i, \mathbf{x}_2^i\right] &= \varphi_2\left(\mathbf{d}_2, \mathbf{x}_1^i\right) - \mathbf{x}_1^i, \end{aligned} \tag{4.6}$$

where $\varphi_1$ and $\varphi_2$ represent the soft decision decoding functions of the constituent decoders. Recall that the decoding functions, $\varphi_1$ and $\varphi_2$ evaluate logarithmic arrays of *a posteriori* probabilities for message and coded bits of the constituent encoders of the turbo code. The vectors $\mathbf{z}_1^i$ and $\mathbf{z}_2^i$ are log-ratios of *a posteriori* probabilities on the coded bits. The extrinsic information vectors on the message bits ($\mathbf{x}_1^i$ and $\mathbf{x}_2^i$) are initially (for $i = 0$) set to zero and are treated as independent coordinate-wise observations of these bits. The decisions on the message bits are formed by thresholding the second decoder output $\varphi_2\left(\mathbf{d}_2, \mathbf{x}_1^i\right)$ after each iteration.

### 4.2.3 Single Pass Receiver with Turbo Demodulation

In receiver implementation B, shown in Fig. 4.2 (b), the iterative loop between the de-mapper and decoder is represented as

$$\begin{aligned}
\left[\mathbf{d}_1^i,\mathbf{d}_2^i\right] &= \phi\left(\mathbf{u},\left[\mathbf{z}_1^{i-1},\mathbf{z}_2^{i-1}\right]\right)-\left[\mathbf{z}_1^{i-1},\mathbf{z}_2^{i-1}\right] \\
\left[\mathbf{z}_1^i,\mathbf{x}_1^i\right] &= \varphi_1\left(\mathbf{d}_1^i,\mathbf{x}_2^{i-1}\right)-\mathbf{x}_2^{i-1} \\
\left[\mathbf{z}_2^i,\mathbf{x}_2^i\right] &= \varphi_2\left(\mathbf{d}_2^i,\mathbf{x}_1^i\right)-\mathbf{x}_1^i.
\end{aligned} \tag{4.7}$$

The de-mapping function is given by $\phi$ and $\mathbf{u}$ is the array of likelihood estimates on the transmitted symbols and is the output of the MIMO signal detector, i.e., $\mathbf{u}\left(p, n_T(n-1)+j\right)=P\left(\mathbf{y}_n(j)\middle|\mathbf{b}_n(j)=q_p\right)$ (or $=P\left(\hat{\mathbf{y}}_n(j)\middle|\mathbf{b}_n(j)=q_p\right)$ for the case of imperfect CSI at the receiver).

### 4.2.4 Fully Iterative Receiver

Turbo equalization for single antenna systems on wireless channels was first proposed in [24] and involved the re-computation of the estimates on the modulation symbols. Extending this approach even to moderately sized antenna arrays is not practically feasible as it involves the re-computation of estimates on $M^{n_T}$ signal space points (assuming $M$-ary modulation). Instead, we propose a lower complexity iterative processing alternative (i.e., receiver implementation C) to effectively cancel the co-antenna interference.

Fig. 4.2 (c) illustrates receiver implementation C, which includes overall iterative processing. Using the log-ratio on coded bits $\mathbf{z}_1^i$ and $\mathbf{z}_2^i$, we compute the corresponding *a* posterori probabilities using (2.28). Since the coded bits and modulation symbols are related through a lookup table with $M$ entries, the *a posteriori* probabilities on the transmitted modulation symbols for all time instants and for all transmitted streams, i.e., $P\left(\mathbf{b}_n(j)=q_p\middle|\mathbf{y}_n(j)\right)$ (or $P\left(\mathbf{b}_n(j)=q_p\middle|\hat{\mathbf{y}}_n(j)\right)$), $n$ = 1, 2, ..., $N_c/(n_T M)$ and $j$ = 1, 2, ..., $n_T$, are determined by an appropriate multiplication of the (interleaved) probabilities on the coded bits. The *a posteriori* probabilities on the modulation symbols correspond to *a priori* probabilities for the detector, i.e., $P\left(\mathbf{b}_n(j)=q_p\right)$, $n$ = 1, 2, ..., $N_c/(n_T M)$ and $j$ = 1, 2, ..., $n_T$ and are subsequently channel interleaved. Consequently, the mean vectors $\boldsymbol{\mu}_n(j)$ and the 2-by-2 covariance matrices $\mathbf{K}_{n,j}$ for $n$ = 1, 2, ..., $N_c/(n_T M)$ and $j$ = 1, 2, ..., $n_T$, are computed for each QPSK symbol on a symbol-by-symbol, antenna-by-antenna fashion using equations (3.4), (3.5) and (3.6). Similarly, $\hat{\boldsymbol{\mu}}_n(j)$ and $\hat{\mathbf{K}}_{n,j}$ are computed using equations (3.10) and (3.11) for the case of imperfect CSI at the receiver.

The computed mean vectors and covariance matrices are used by the MIMO signal detector to form improved soft estimates of the transmitted symbols using (3.7) (or (3.13) for the case of imperfect CSI at the receiver). As the system iterates, the turbo decoder improves the knowledge of the interference structure at the receiver, i.e., the computed mean will approach the actual value of the co-antenna interference and the variance of this interference will tend to zero. This in turn, improves the soft decision output of the detector resulting in an overall increase in performance.

## 4.3 Simulation Results for Wireless MIMO Channels

### 4.3.1 Uncorrelated Rayleigh Fading with Perfect CSI at the Receiver

In this section, we present simulation results for the proposed coded MIMO system in the single user case. The channel code is a rate ½ turbo code based on the two-bit-in-one-bit-out recursive convolutional code from [10] and discussed in Section 2.3.1, with a message block length $N_m$ = 32,000 bits. The turbo code uses an *S*-rand interleaver [41], where the spread value $S$ is set to 80 and we use a specific Gray coded 16-QAM symbol constellation shown in Fig. 3.5, which is adopted from [31]. Since 16-QAM signalling is used, the turbo demodulation loop shown in Fig. 4.2 (b) and (c) is employed for all the simulations presented in this section. We consider a slow frequency non-selective Rayleigh fading channel, where channel state information is available at the receiver only. The ergodic capacity limits are evaluated using (2.12) as an average over 100,000 channel realizations. The turbo decoder in receiver implementation A, the demodulator and turbo decoder in implementation B or the overall receiver in implementation C perform ten iterations.

The BER performance of receiver implementations B and C with respect to the SNR defined in (2.10) is shown in Fig. 4.3, Fig. 4.4 and Fig. 4.5 for $(n_T, n_R)$ = (2, 10), (4, 20), (12, 40) and (30, 120) with corresponding transmission rates of 4, 8, 24 and 60 bits per MIMO channel use, respectively. For the two smaller systems, iterative processing in implementation C provides a 1.6 to 3.1 dB gain when compared to the performance of single pass detection and turbo demodulation (i.e., receiver implementation B) systems. The gain in iterations is about a half a dB when going from the fifth to the $10^{\text{th}}$ iteration. For the 12 and 30 transmit antenna configurations in Fig. 4.5, single pass detection and turbo demodulation do not converge due to increased co-antenna interference. Since progressively improving knowledge of the co-antenna interference is exploited in receiver implementation C, these systems outperform corresponding ones using single pass detection and turbo demodulation (especially for the larger numbers of transmit antennas). All systems with iterative processing are within about 1.5 – 1.6 dB of the ergodic capacity limit at a bit error rate of $10^{-5}$.

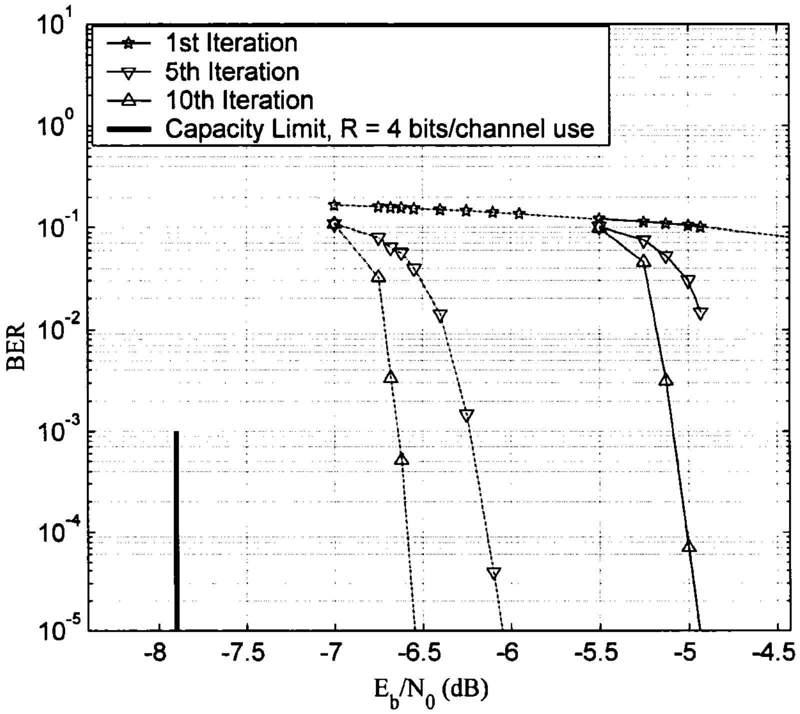

**Fig. 4.3. Comparison of single pass detection and turbo demodulation (solid) and iterative processing (dashed) systems for $(n_T, n_R)$ = (2, 10), $R$ = 4 bits per channel use.**

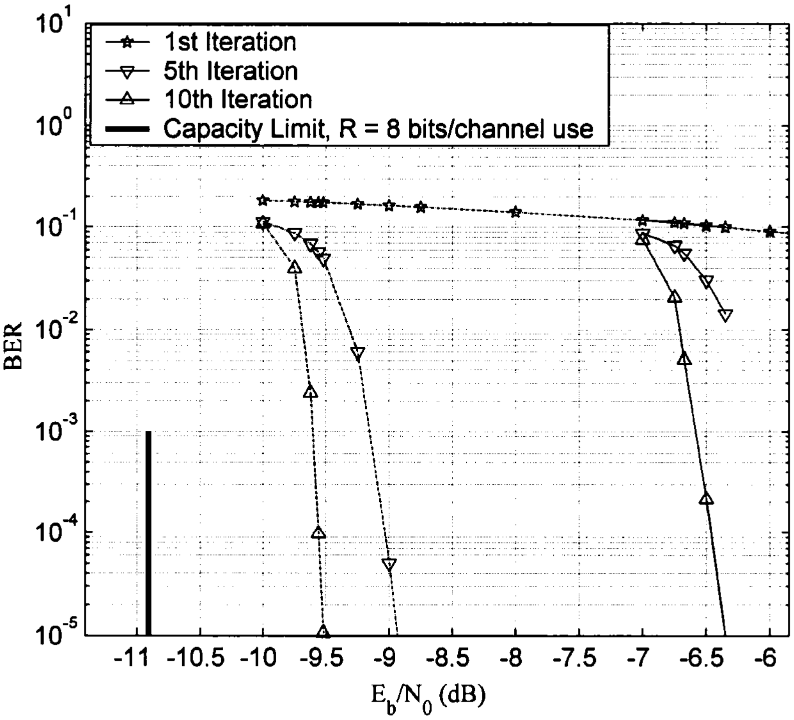

Fig. 4.4. Comparison of single pass detection and turbo demodulation (solid) and iterative processing (dashed) systems for $(n_T, n_R)$ = (4, 20), $R$ = 8 bits per channel use.

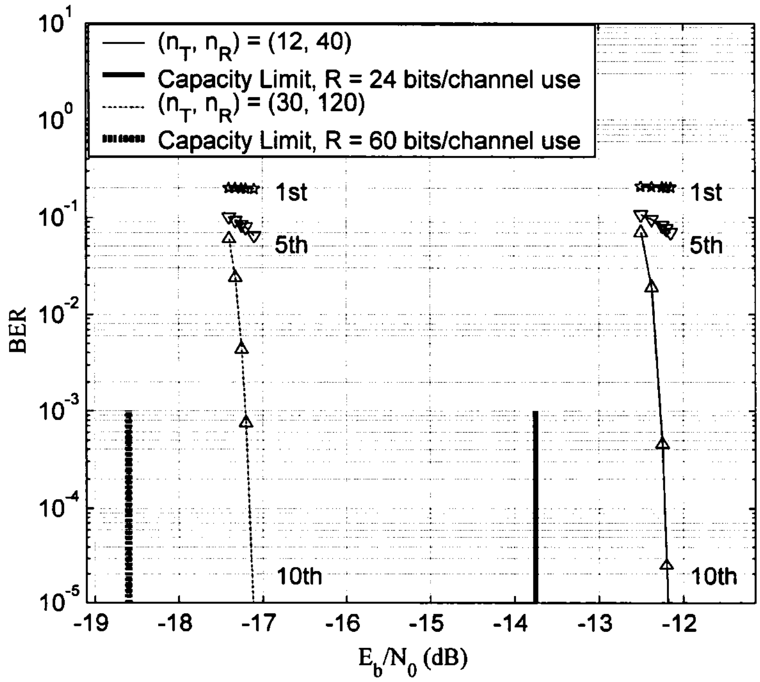

Fig. 4.5. Performance of the iterative processing system for $(n_T, n_R)$ = (12, 40) and (30, 120). (Note that the corresponding single pass detection and turbo demodulation systems do not converge.)

Fig. 4.6 and Fig. 4.7 compare the performance of the coded MIMO system (of linear MIMO signal detection complexity) with iterative processing to the Turbo-BLAST system [80] (of cubic MIMO signal detection complexity) for the (2, 10) and (4, 20) antenna configurations and various interleaver lengths on an uncorrelated Rayleigh fading channel with perfect CSI at the receiver. Both systems have the same transmission rates (the Turbo-BLAST system uses 16-PSK modulation) and perform ten detection / decoding iterations. At the same interleaver length, (i.e., 200 and 400 message bits), the proposed system outperforms the Turbo-BLAST system by about 7.5 dB – 8.5 dB at a bit error rate of $10^{-5}$. Whereas at a larger interleaver length of 32 000 bits, the performance of the proposed system surpasses the Turbo-BLAST system by about 10 dB in both cases.

### 4.3.2 Effects of Imperfect CSI and Spatial Correlation

To illustrate the robustness of the proposed turbo-coded MIMO system, we considered imperfect CSI with an error variance of ten percent ($\sigma_\varepsilon^2 = 0.1$), which is considered to be large as the works in [17], [90], [107] indicate that the error variance is usually lower than one percent. The ergodic capacity limits from (2.17) are evaluated numerically by averaging over 100,000 channel realizations. Fig. 4.8 and Fig. 4.9 illustrate the performance of the coded MIMO system with iterative processing after ten iterations for $(n_T, n_R)$ = (2, 10) and (4, 20) with corresponding transmission rates of 4 and 8 bits per MIMO channel use, respectively in an uncorrelated Rayleigh fading channel. The coded MIMO system with imperfect CSI for both antenna configurations performs within 1.6 dB of the ergodic capacity limit. Comparing to the BER curves for the perfect CSI scenarios (reproduced from Fig. 4.3 and Fig. 4.4), system performance decreases by about 1 dB due to channel estimation errors.

Fig. 4.10 and Fig. 4.11 illustrate the performance of the coded MIMO system with iterative processing for $(n_T, n_R)$ = (2, 10) and (4, 20) antennas on a correlated Rayleigh fading channel. Antenna spacing at the mobile and base-station

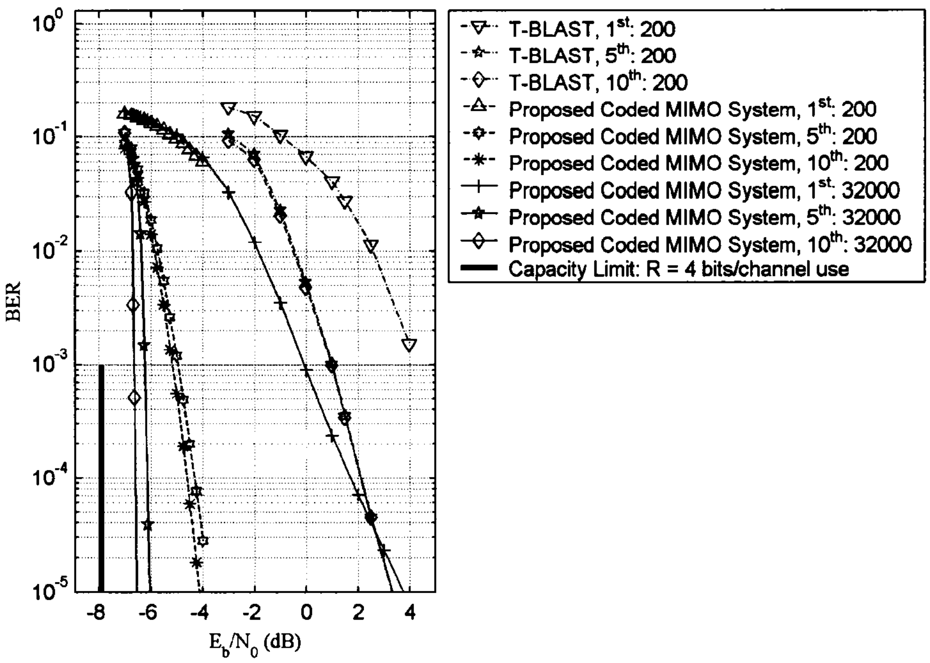

**Fig. 4.6.** **Performance comparison between the proposed coded MIMO system with iterative processing and the Turbo-BLAST architecture [80] for $(n_T, n_R)$ = (2, 10) antennas after 1, 2, 4, 8 and 10 iterations on an uncorrelated Rayleigh fading channel.**

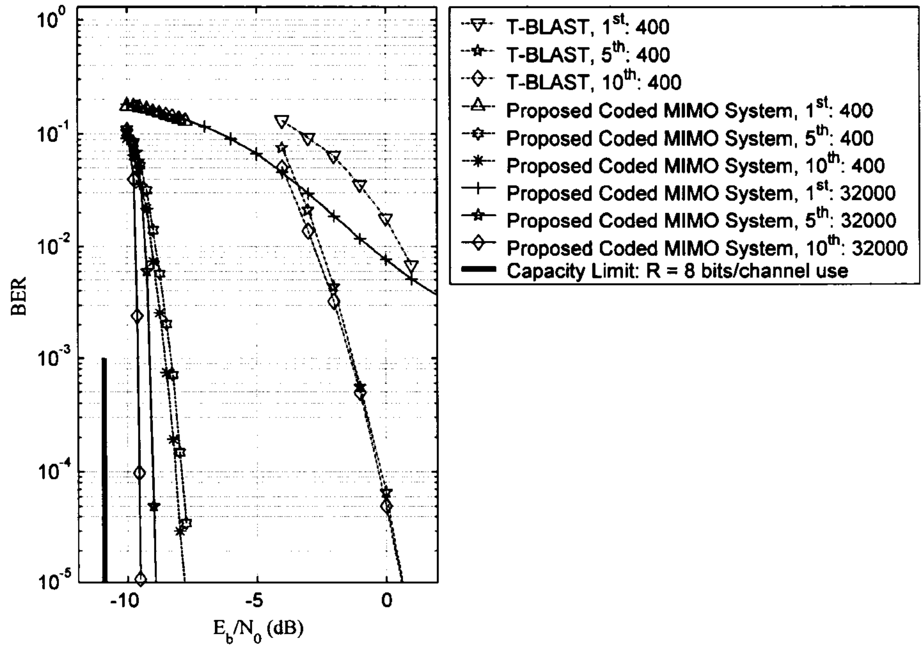

**Fig. 4.7.** **Performance comparison between the proposed coded MIMO system with iterative processing and the Turbo-BLAST architecture [80] for $(n_T, n_R)$ = (4, 20) antennas after 1, 2, 4, 8 and 10 iterations on an uncorrelated Rayleigh fading channel.**

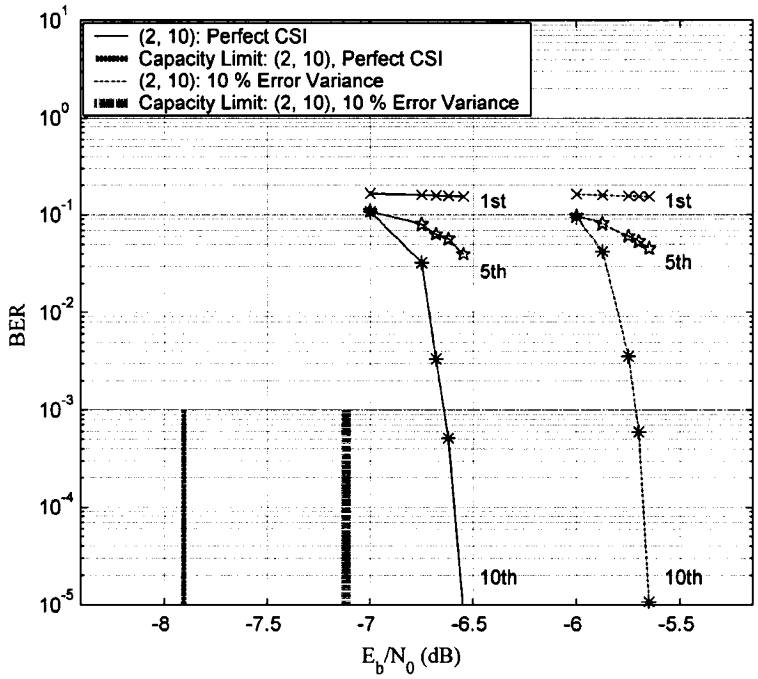

Fig. 4.8. Effects of imperfect CSI on performance of the proposed MIMO system with iterative processing on an uncorrelated Rayleigh fading channel for $(n_T, n_R) = (2, 10)$ antennas.

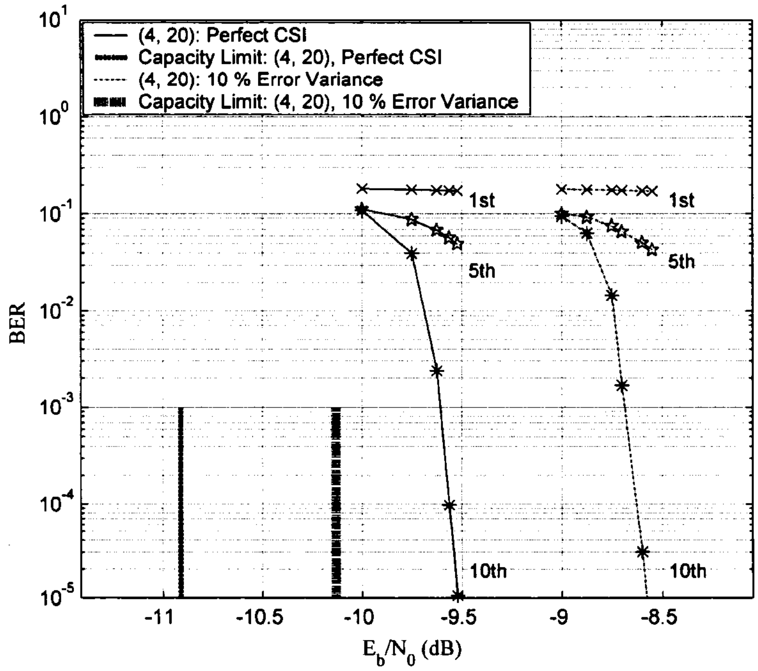

Fig. 4.9. Effects of imperfect CSI on performance of the proposed MIMO system with iterative processing on an uncorrelated Rayleigh fading channel for $(n_T, n_R) = (4, 20)$ antennas.

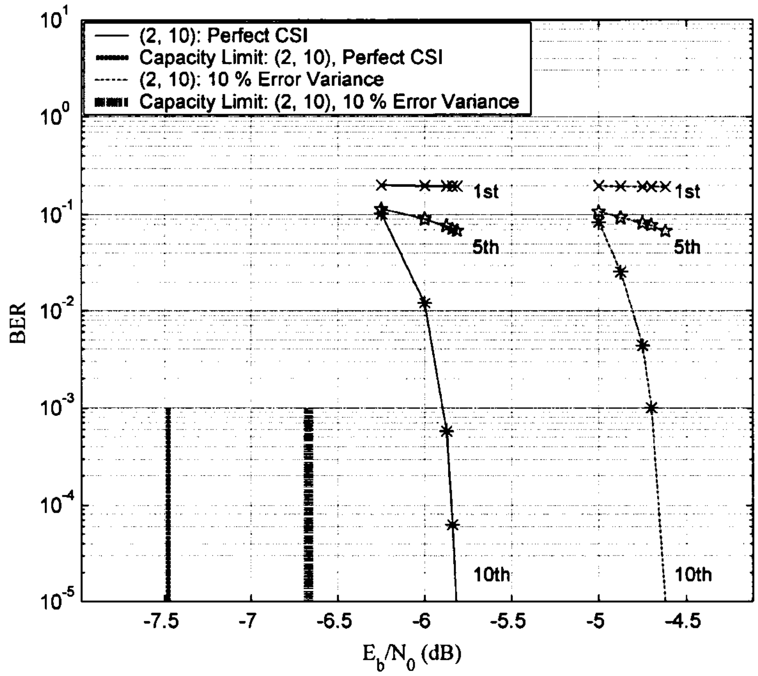

Fig. 4.10. Effects of imperfect CSI on performance of the proposed MIMO system in a correlated Rayleigh fading channel for $(n_T, n_R) = (2, 10)$ antennas.

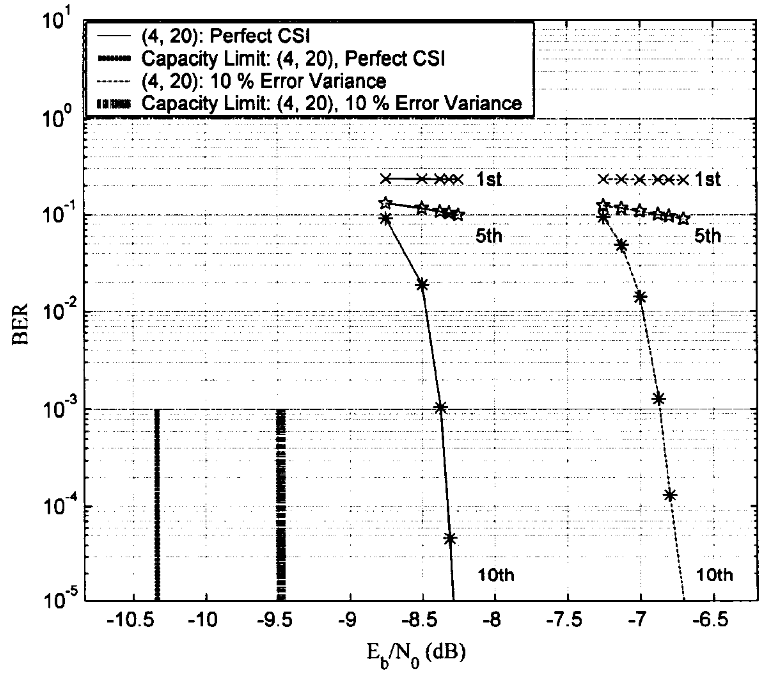

Fig. 4.11. Effects of imperfect CSI on performance of the proposed MIMO system in a correlated Rayleigh fading channel for $(n_T, n_R) = (4, 20)$ antennas.

is assumed to be $\lambda/2$ and $\lambda$, respectively ($\lambda$ is the transmission wavelength). The angular spread $\beta$ is 10 degrees and the estimation error variance is 10 %. Since the antennas are strongly correlated, channel estimation errors have a larger impact on performance than in the uncorrelated case. The coded MIMO systems with $(n_T, n_R)$ = (2, 10) and (4, 20) antennas perform within 2.1 and 2.8 dB of the ergodic capacity limit, respectively and perform 1.2 and 1.6 dB less than the corresponding systems with perfect CSI at the receiver.

### 4.3.3 Discussion of Simulation Results

Overall, the proposed turbo-coded MIMO systems operate near the capacity limit and are robust to the effects of spatial correlation and channel estimation errors. We emphasize that the low complexity of the detector permits scaling to a large number of transmit and receive antennas, e.g., a 30 transmit antenna and 120 receive antenna system with 16-QAM would approximately require 20,370 operations per channel use, while in contrast, the optimal MIMO signal detector would require $16^{30} \approx 10^{136}$ operations per channel use. Thus, the reduction in detection complexity of the proposed scheme translates to low requirements on memory, signal processing, power usage, which reduce implementation cost.

Similar to the setup for the fully iterative MIMO receiver architecture, the T-BLAST system maps the soft decisions on the coded bits from the channel decoder into soft decisions on the modulation symbols. These are used to update the outputs of the T-BLAST signal detector, which requires the inversion of $n_T$ matrices of size $n_R$-by-$n_R$ $(n_T O(n_R^3)$ operations) with each iteration. In contrast, the proposed iterative MIMO receiver architecture uses the soft decisions on the modulation symbols at each iteration to compute mean and variance estimates on the $n_T$ transmitted symbols. As shown in (3.4) – (3.6), these calculations rely on the original channel observation vector $\mathbf{y}_n$ and only require $n_T O(M n_T)$ operations, where $M$ is the size of the modulation scheme.

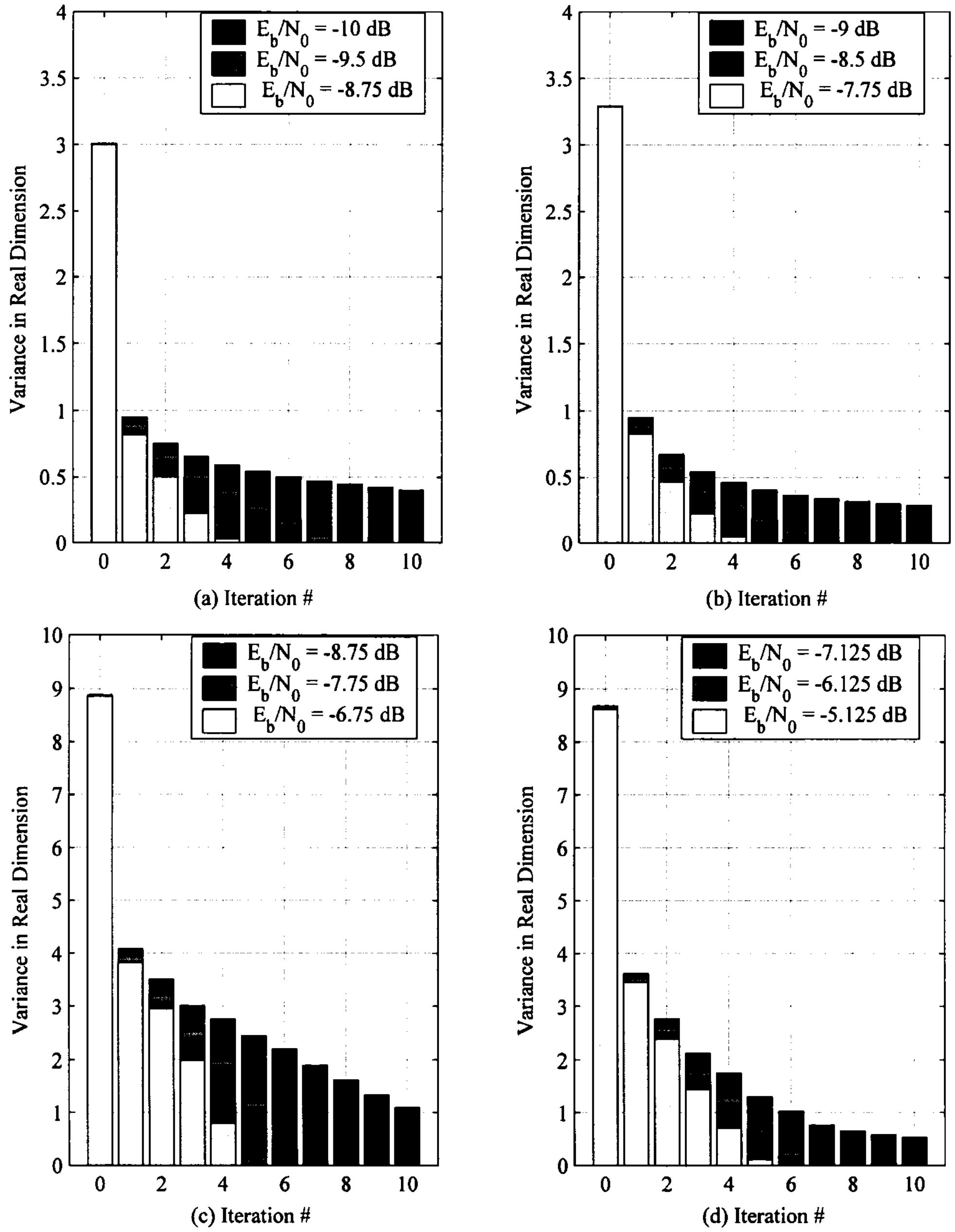

**Fig. 4.12. Reduction of the co-antenna interference during the iterative decoding process for the $(n_T, n_R)$ = (4, 20) antenna coded MIMO system on slow frequency non-selective Rayleigh fading channels:**

**(a) uncorrelated fading and perfect CSI**

**(b) uncorrelated fading and imperfect CSI (10 % error variance)**

**(c) correlated fading and perfect CSI**

**(d) correlated fading and imperfect CSI (10 % error variance)**

The near-capacity performance of the turbo-coded MIMO system is due in part to iterative processing and Fig. 4.12 illustrates reduction in the variance of the co-antenna interference with iterations for different CSI error, correlation and SNR scenarios. In the considered correlated channels, the initial variance of the co-antenna interference at the output of the MIMO signal detector is about three times larger than in the uncorrelated case. For the variance to converge to zero, channel estimation errors require an SNR increase of 1 dB in uncorrelated fading (Fig. 4.12 (a), (b)) and 1.6 dB in correlated fading (Fig. 4.12 (c), (d)).

## 4.4 Multi-user Transceiver Structure

### 4.4.1 The Multi-user MIMO Transmitter Architecture

The multi-user MIMO transmitter structure is shown in Fig. 4.13, where $K$ independent user data sources produce i.i.d. equiprobable bits. Each user's data bits are encoded by a rate $N_m/N_c$ turbo encoder. The $N_m$ message bit sequence of the $l$-th user, $\mathbf{m}_l$, $l = 1, 2, \ldots, K$, is encoded into a codeword $\mathbf{c}_l$ of length $N_c$ as

$$\mathbf{c}_l = (g_1(\mathbf{m}_l), g_2(\Pi(\mathbf{m}_l))), \tag{4.8}$$

where $g_1(\bullet)$, $g_2(\bullet)$ denote the constituent encoders of the turbo code, $\Pi$ represents the interleaver and $g_1(\bullet)$ includes the systematic bits. For the $l$-th user, the coded bits in $\mathbf{c}_l$ are demultiplexed into $2n_T$ streams and each stream is modulated using the user specific CDMA spreading sequence of spreading length $N_s$. The corresponding CDMA chip outputs are assembled into $n_T$ groups of two and each pair is mapped into a complex QPSK symbol. (Thus, each turbo-coded bit will be spread across $N_s$ QPSK symbols.) At the $n$-th time instant, the $n_T$-by-1 QPSK symbol vector $\mathbf{b}_{n,l}$ is transmitted and the corresponding received vector $\hat{\mathbf{r}}_n$ is given in (2.7). User-specific channel interleaving and de-interleaving is performed at the transmitter and receiver to break up channel fades affecting consecutively transmitted packets of data.

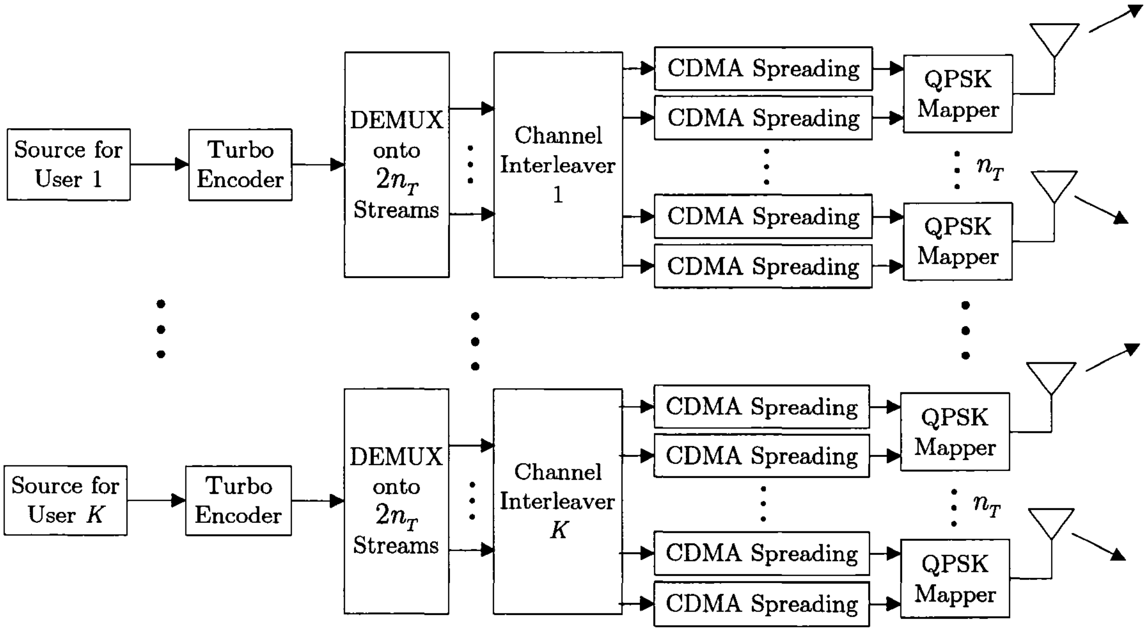

**Fig. 4.13. Transmitter structure of a turbo-coded multi-user MIMO CDMA system.**

## 4.4.2 The Multi-user MIMO Receiver Architecture

The multi-user MIMO receiver architecture is shown in Fig. 4.14. Front-end multi-user MIMO signal detection, described in Section 3.1.3, generates soft decisions on all the users' transmitted QPSK symbols. These estimates correspond to soft decisions on the chips of the spreading sequence in the real and imaginary dimensions. Hence, the estimates on the coded bits are simply given by the appropriate (spreading sequence based) product of the chip likelihood values. The de-spreader corresponding to each transmit antenna produces log-likelihood estimates on the coded bits, which are channel de-interleaved, multiplexed and turbo decoded, as shown in Fig. 4.14. Iterative processing between the multi-user MIMO signal detector and the $K$ turbo decoders, is performed to cancel the co-antenna and multi-user interference. (Note that turbo demodulation is not employed as it provides little benefit.)

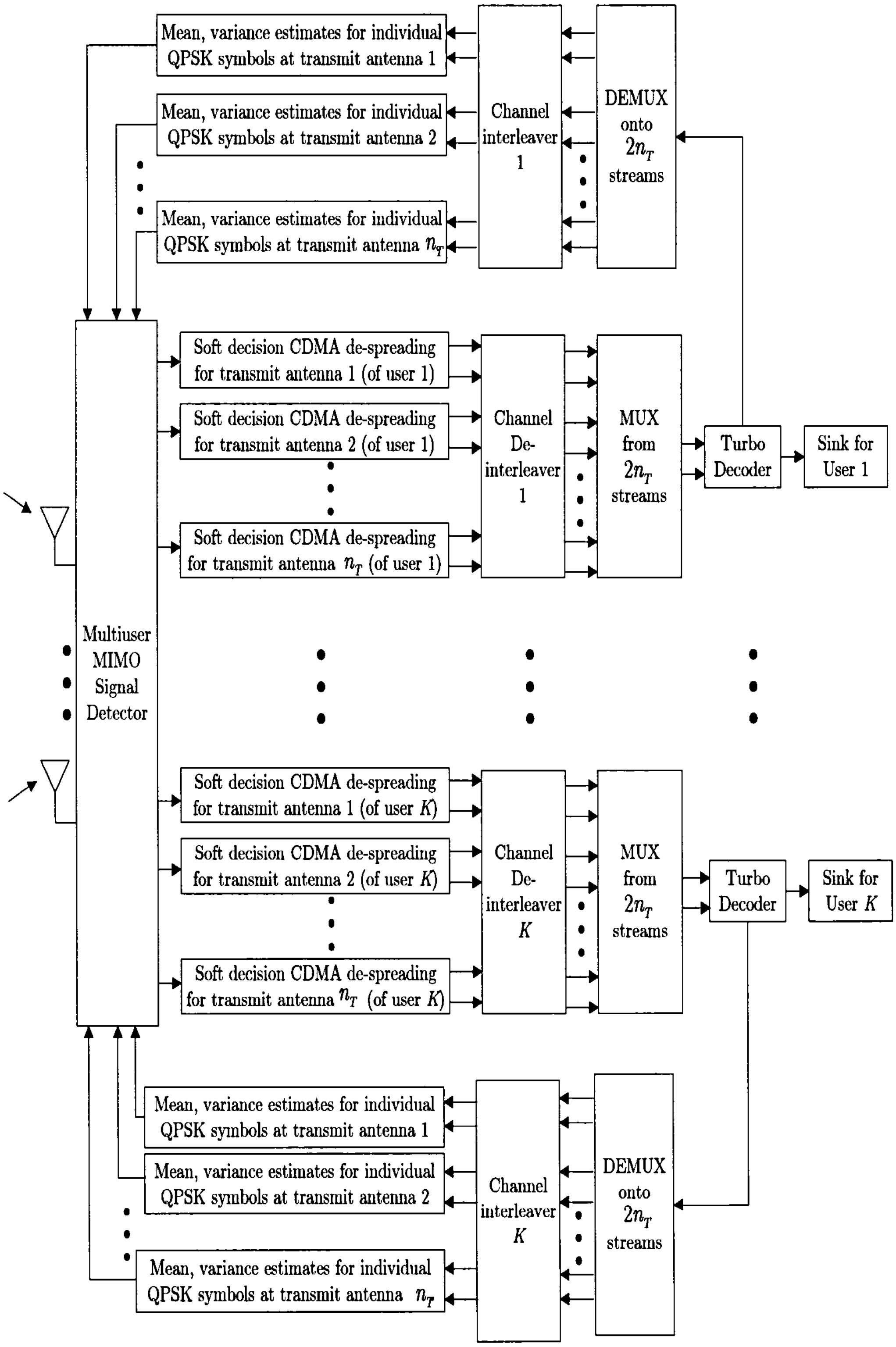

**Fig. 4.14. Schematic block diagram of the considered iterative multi-user MIMO receiver.**

For each user, the multi-user MIMO signal detector generates a channel observation on each transmitted QPSK symbol, as shown in (3.15). The detector subsequently produces likelihood estimates on the transmitted QPSK symbols given in (3.18) by approximating the co-antenna and multi-user interference in each channel observation as a two dimensional Gaussian random vector with mean and co-variance matrix elements given by (3.16) and (3.17), respectively. Soft decisions on turbo-coded bits are obtained by appropriately summing and multiplying the likelihood estimates on QPSK symbols.

For example, let the $\tau$-th coded bit of the first user, $\mathbf{c}_1(\tau)$ be equal to 1 and let this user's spreading sequence be given by $\psi = [+1, -1]$. As described in Section 4.4.1, the chips corresponding to the CDMA modulated outputs are mapped to two different QPSK symbols, which are then assumed to be transmitted from the first antenna. Subsequent to the multi-user MIMO signal detector, the soft decision CDMA despreader for transmit antenna 1, shown in Fig. 4.14, computes the likelihood on $\mathbf{c}_1(\tau) = 1$ as

$$\begin{aligned} P\left(\widehat{\mathbf{y}}_{2\tau-1,1}(1), \widehat{\mathbf{y}}_{2\tau,1}(1) \middle| \mathbf{c}_1(\tau) = 1\right) = {} & \left( \sum_{q_p \in \{\mathrm{QPSK} | \psi(1) = +1\}} P\left(\widehat{\mathbf{y}}_{2\tau-1,1}(1) \middle| \mathbf{b}_{2\tau-1,1}(j) = q_p\right) \right) \times \\ & \left( \sum_{q_p \in \{\mathrm{QPSK} | \psi(1) = -1\}} P\left(\widehat{\mathbf{y}}_{2\tau,1}(1) \middle| \mathbf{b}_{2\tau,1}(j) = q_p\right) \right). \end{aligned} \tag{4.9}$$

This calculation has to be repeated for $\mathbf{c}_1(\tau) = 0$. Subsequently, the soft decisions on the turbo-coded bits from the CDMA de-spreaders of the first user, are channel de-interleaved, multiplexed and converted into two vectors of log-likelihood ratios $\mathbf{d}_{1,1}$, $\mathbf{d}_{1,2}$, which is fed to the turbo decoder.

In the $i$-th iteration, the iterative loop between the constituent decoders in the turbo decoder of the $l$-th user can be represented as

$$\begin{aligned} \left[\mathbf{z}_{l,1}^{i}, \mathbf{x}_{l,1}^{i}\right] &= \varphi_1\left(\mathbf{d}_{l,1}, \mathbf{x}_{l,2}^{i-1}\right) - \mathbf{x}_{l,2}^{i-1}, \\ \left[\mathbf{z}_{l,2}^{i}, \mathbf{x}_{l,2}^{i}\right] &= \varphi_2\left(\mathbf{d}_{l,2}, \mathbf{x}_{l,1}^{i}\right) - \mathbf{x}_{l,1}^{i}, \end{aligned} \tag{4.10}$$

where $\varphi_1$ and $\varphi_2$ denote the soft decision decoding functions of the constituent decoders. The vectors $\mathbf{d}_{l,1}$, $\mathbf{d}_{l,2}$ from the CDMA de-spreaders contain log-likelihood ratios on the coded bits from the turbo encoder of user $l$. After the turbo decoding stage, we compute the *a posteriori* probabilities on the coded bits (using (2.28) and $\mathbf{z}^i_{l,1}$ and $\mathbf{z}^i_{l,2}$), which are then de-multiplexed and channel interleaved for each user as shown in Fig. 4.14. Consequently, the mean and elements of the 2-by-2 covariance matrix are computed using (3.16) and (3.17) for each QPSK symbol on a symbol-by-symbol, antenna-by-antenna, user-by-user fashion. These mean and covariance matrix estimates on individual QPSK symbols are in turn used by the MIMO signal detector to form improved soft decisions on the QPSK symbols using (3.18).

### 4.4.3 Simulation Results

We consider several coded MIMO systems, where each user employs a rate 1/2 turbo code (using the two-bit-in-one-bit-out recursive convolutional codes from [10] and discussed in Section 2.3.1) with a fixed pseudorandom interleaver. The message block length is 2,000 bits and each user is assigned a fixed binary spreading sequence of length seven. The chips of the transmitted sequence are mapped to Gray coded QPSK symbols, as shown in Fig. 4.15, and unless otherwise indicated, the users employ perfect power control. The ergodic sum capacity is evaluated using (2.19) as an average over 100,000 channel realizations. For the correlated fading scenarios, we assume the channel model described in Section 2.1.3, where the angular spread $\beta$ is 10 degrees and base-station antenna spacing is $\lambda$. The overall receiver performs ten iterations and the transmission rate is $n_T/7$ bits per channel use per user.

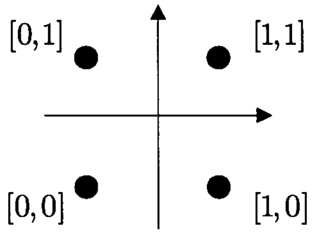

Fig. 4.15. Gray coded QPSK constellation used in presented simulations.

Fig. 4.16 illustrates the performance of the proposed system with respect to the ergodic capacity on an uncorrelated fading channel for $(n_T, n_R) = (2, 10)$ antenna configuration. At a BER of $10^{-5}$, the performance of the five-user coded system is within 2.9 dB of the capacity limit. In addition, we make a comparison to the Turbo-BLAST system from [80] in a similar multi-user setting. Fig. 4.16 illustrates that for $K = 5$ users, the proposed system outperforms the Turbo-BLAST system by 7.7 dB at a BER of $10^{-5}$.

Fig. 4.17 (a) illustrates the performance of user 1 in a five-user coded MIMO system with $(n_T, n_R) = (4, 20)$ antennas on an uncorrelated Rayleigh fading channel. As in the (2, 10) antenna case, system performance at a BER of $10^{-5}$ is within 2.9 dB of the ergodic capacity. Fig. 4.17 (b) illustrates the system performance with four transmit antennas at the mobile and twenty receive antennas at the base-station in a correlated fading environment, where users do not employ perfect power control. We have considered a maximum power control error of 2.5 dB [105] and under these harsh conditions, the system operates within about 4.8 dB from the ergodic capacity limit at a BER of $10^{-5}$.

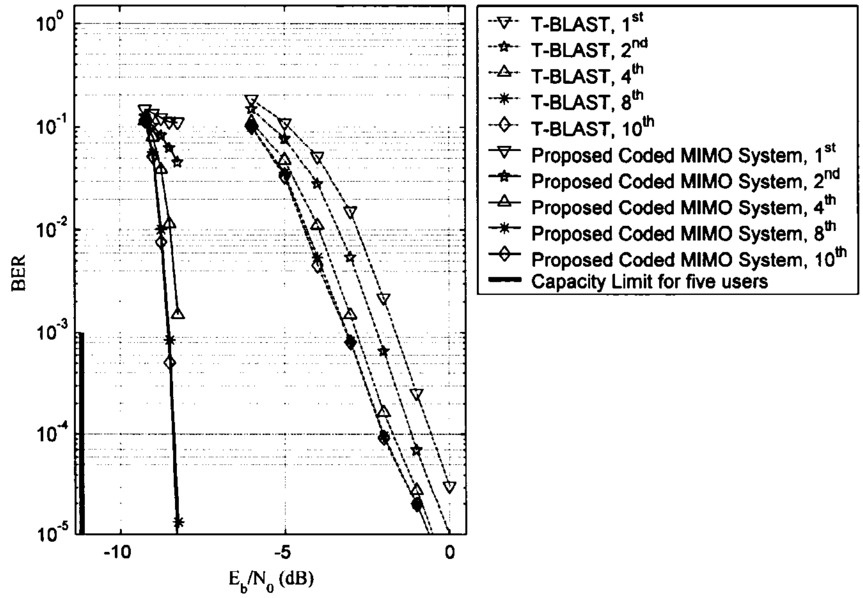

**Fig. 4.16. Performance comparison between the proposed coded MIMO system and the Turbo-BLAST architecture [80] for $(n_T, n_R) = (2, 10)$ antennas, $K = 5$ users and iterative multi-user interference cancellation after 1, 2, 4, 8 and 10 iterations.**

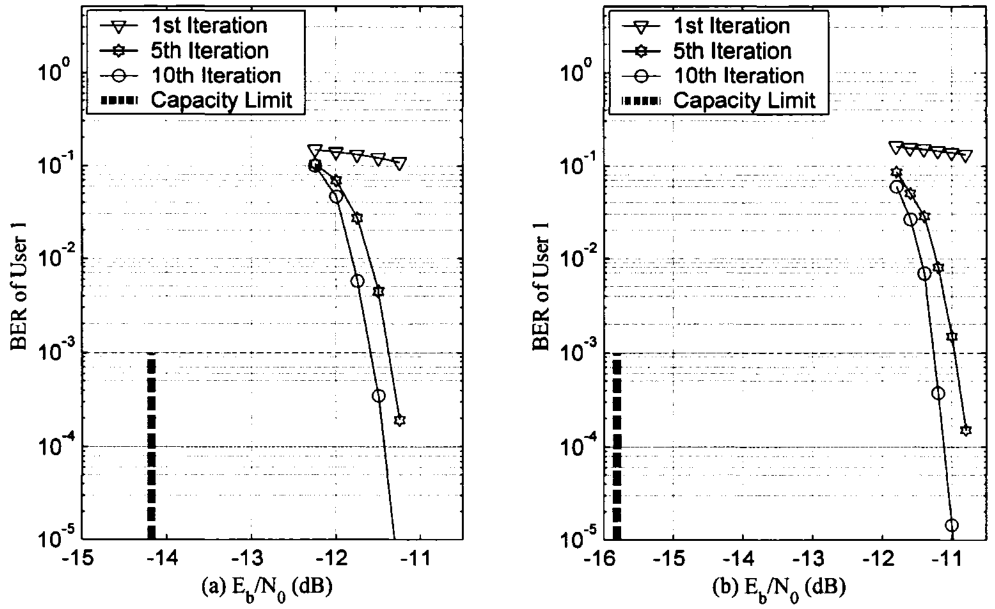

**Fig. 4.17.** (a) Performance of user 1 in a five-user turbo coded MIMO system with $(n_T, n_R) = (4, 20)$ antennas on an

(a) uncorrelated Rayleigh fading channel with perfect power control

(b) a correlated Rayleigh fading channel with a power control error of 2.5 dB.

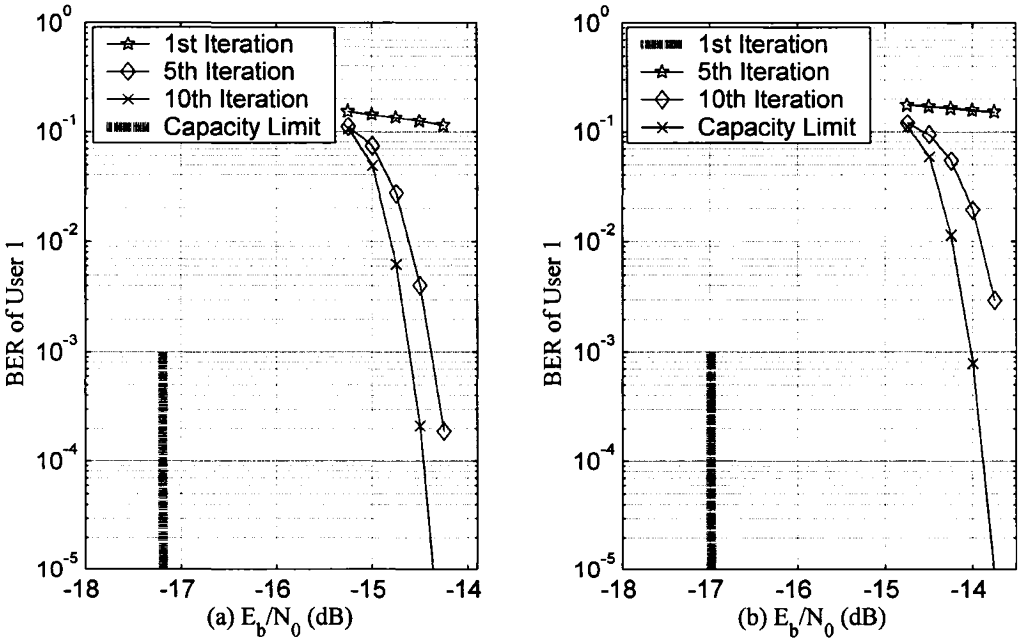

**Fig. 4.18.** Performance of user 1 in a five-user turbo coded MIMO system with $(n_T, n_R) = (8, 40)$, antennas and perfect power control on an (a) uncorrelated and (b) correlated Rayleigh fading channel.

Fig. 4.18 presents simulated BER results for user 1 in a five-user system with $(n_T, n_R)$ = (8, 40) (transmission rate of 8/7 bits per channel use per user) in uncorrelated and correlated fading channels, respectively. In both cases, system performance is within 3.2 dB of the ergodic capacity limit at a BER of $10^{-5}$.

We now consider the sensitivity of the proposed architecture with respect to different parameters in the correlated fading scenario. We assume the channel model described in Section 2.1.3. In particular, we focus on the $(n_T, n_R)$ = (2, 10) system and vary the angular spread $\beta$ between values of 7, 10 and 12 degrees and corresponding antenna spacings $2\lambda$, $\lambda$, and $\lambda/2$ ($\lambda$ is the transmission wavelength). Fig. 4.19 illustrates the performance of the proposed system in the three different correlation scenarios, where the system performance is within 0.5 dB for the various correlated fading situations. Furthermore, the simulated performance is within 3.2 dB of the corresponding ergodic capacity limits.

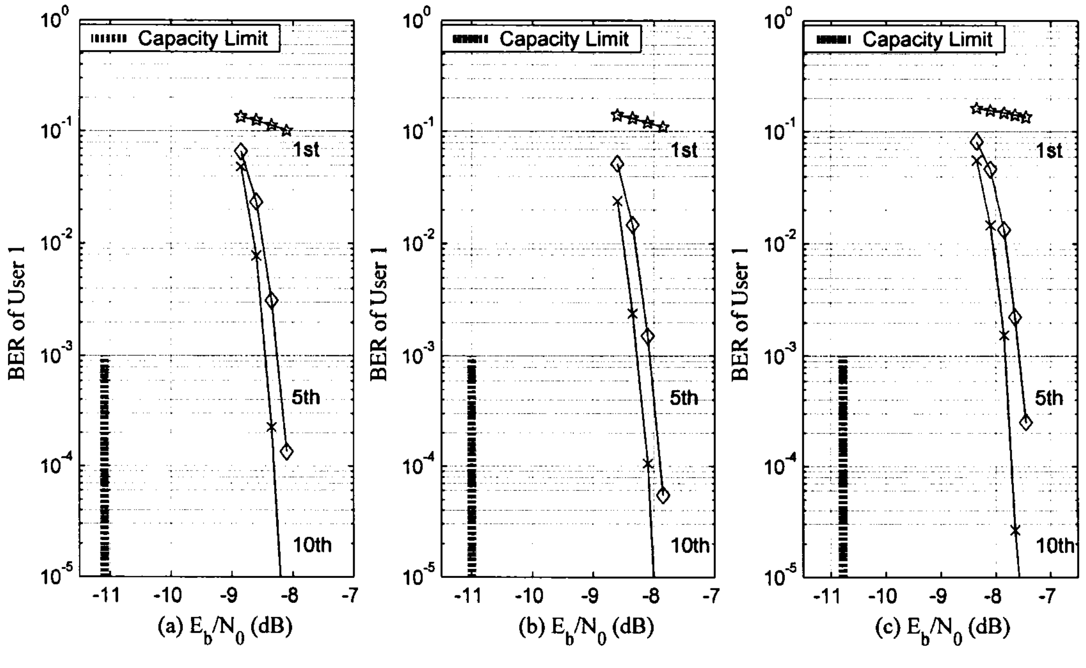

**Fig. 4.19. Performance of user 1 in a five-user turbo coded MIMO system with $(n_T, n_R) = (2,10)$ antennas on a correlated Rayleigh fading channel with perfect power control for**

**(a) $\beta = 7°$ and antenna spacing of $2\lambda$**

**(b) $\beta = 10°$ and antenna spacing of $\lambda$**

**(c) $\beta = 12°$ and antenna spacing of $\lambda/2$.**

## 4.5 Discussion on Implementation Issues

As mentioned in Section 3.5.2, the complexity of the proposed MIMO signal detector increases linearly with the number of transmit antennas $n_T$, number of receive antennas $n_R$ and the number of users $K$. The overall signal detection complexity is $O(n_T n_R K)$ and this is especially attractive in the considered uplink sys tems, where $n_T$ is less than $n_R$. Furthermore, the complexity of the novel iterative processing schemes, shown in Fig. 4.2 (c) and Fig. 4.14, are also linear in the message block length and number of users $K$. The reason for linear complexity is that the processing outside of the turbo decoders is performed on a symbol-by-symbol, antenna-by-antenna and user-by-user fashion.

In contrast, the complexity of the optimal MIMO signal detector is exponential in the number of transmit antennas and users, i.e., $O\left(n_R M^{K n_T}\right)$, which is impractical even for a moderate numbers of users and antennas. Earlier multi-user MIMO signal detectors possess complexity that is significantly higher. For instance, the detector proposed in [82] has complexity that is cubic in the number of users and transmit antennas, $O\left(n_T^3 K^3\right)$, while other proposed MIMO signal detectors, including the ones used in the layered space-time architecture and Turbo-BLAST extended to a multi-user setting, require front end filtering that has cubic complexity in the number of receive antennas $n_T O\left(n_R^3 K\right)$ [2], [50], [80]. Extension of the modified sphere detector in [42] to the multi-user case would lead to high order polynomial complexity in $K$ and $n_R$ (due to the increased multi-user interference).

In the presented simulation results, we considered number of transmit antennas that are practically realisable on a portable hand held transmitter, e.g., $n_T$ = 2, 4 and 8. For instance, two antennas can be placed on opposite ends of the mobile, four antennas can be placed on each of the corners and eight antennas are realizable using four pairs of polarized antennas. Even higher number of antennas can be supported on a laptop (e.g., using the back of the display). Unlike the mobile, many receive antennas can be placed at the base-station as there exists no size and space constraint. Furthermore, the antenna and infrastructure cost of the base-station upgrade can be amortized over many users and over many years. Finally, the proposed coded MIMO system is flexible as it can employ convolutional or turbo codes and any modulation scheme. Hence the proposed MIMO architecture can be applied to existing wireless systems, such as an EDGE system which employs multiple transmit and receive antennas.

In this thesis, we focused on slow frequency non-selective fading channels, which correspond to the use of a mobile at stationary or pedestrian speeds. However, in broadband communication, the channel's frequency response may not be flat in the transmission bandwidth and thus the transmitted symbols undergo frequency selective fading. In this case, the receiver has to combat intersymbol interference as well as co-antenna interference. Channel equalizers based on MMSE criterion can be applied at the output of the MIMO signal detector, i.e., on the elements of the channel observation vector $\mathbf{y}_n$ (in (3.2)).

## 4.6 Multi-head Multi-track Magnetic Recording Systems

So far, we have considered uplink wireless systems and showed that the proposed iterative MIMO receivers are robust, easily scale up to many antennas (and users) and operate near the capacity limit. In this section, the applicability of the proposed MIMO signal detector and iterative receiver (i.e., receiver architecture C illustrated in Fig. 4.2 (c)) is extended to magnetic recording applications. The objective is to demonstrate that this extended MIMO architecture combined with multi-head multi-track recording technology on magnetic hard drives can help realize high recording densities and read-out rates.

### 4.6.1 Motivation and Background

Memory intensive applications, such as storage of multimedia files and video editing, result in a continuous demand for larger and faster hard drives. With increases in linear density, digital recording systems must deal with higher levels of intersymbol interference (ISI) and lower SNRs. Furthermore, higher radial densities (narrower trackwidths) inherently lead to intertrack interference (ITI) and current hard disks rely on using large track widths and guard bands to minimize this effect. Hence, contemporary recording systems have radial densities that are several times smaller than corresponding linear densities. Multi-track recording channels and multi-head detection offer a potential for increasing radial densities and increased readout rates via improved ITI suppression [48], [51], [83].

Turbo codes, LDPC codes and iterative equalization have recently been explored as a means to increase linear recording densities on single track partial response (PR) recording channels, e.g., [5], [79], [84], [100]. In contrast to single-track scenarios, multi-head recording systems must combat ITI and ISI in both the radial and axial directions. Maximum likelihood sequence detection has been considered in [48] and [83] for multi-head systems. Recently, an iterative joint detection and decoding scheme has been proposed for two track systems [51]. Due to the exponential detection complexity in the number of tracks, the schemes in [48], [51], [83] would be limited to a small number of heads and tracks.

### 4.6.2 System Description

Fig. 4.20 shows the block diagram of a turbo-coded PR digital recording system with $n_T$ tracks and $n_H = n_T + 2$ read heads. A group of $n_T$ tracks is separated by a guard track that prevents interference between adjacent groups. Each of the inner $n_T$ reading heads responds to magnetization of its corresponding track and is affected by interference from adjacent tracks, weighted by a parameter $\alpha$. The

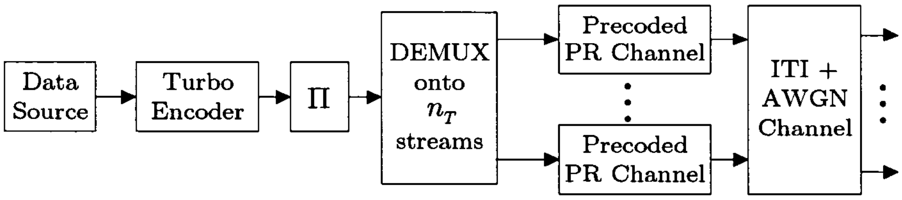

**Fig. 4.20. Schematic block diagram of a turbo-coded $n_T$-track partial response system.**

two outer heads are assumed to be half as wide as the $n_T$ inner heads to ensure that magnetization of neighbouring groups is not picked up [83]. Hence, narrow trackwidth systems with strong ITI can be modeled with a high value of $\alpha$.

The data source in Fig. 4.20 is assumed to produce equiprobable bits, which are fed to a turbo encoder. The coded bits are punctured, interleaved and demultiplexed onto $n_T$ streams, which are then precoded, mapped to a non-return to zero (NRZ) sequence and simultaneously written onto $n_T$ adjacent tracks. (Puncturing involves the removal of selected coded bits from the codeword to increase the coding rate.) At time instant $n$, the discrete-time readback signal $\mathbf{r}_n$ is a real vector of length $n_H$ and is given by

$$\mathbf{r}_n = \mathbf{H}\overline{\mathbf{b}}_n + \mathbf{v}_n, \tag{4.11}$$

where $\overline{\mathbf{b}}_n = I_0\mathbf{b}_n + I_1\mathbf{b}_{n-1} + \ldots + I_d\mathbf{b}_{n-d}$, $I_\ell$ are the ISI terms ($\ell = 0, 1, \ldots, d$), the binary non-return to zero (NRZ) vector is given by $\mathbf{b}_n$. The elements of the noise vector $\mathbf{v}_n$ are i.i.d. zero mean Gaussian random variables with variance $\sigma^2$. The channel matrix $\mathbf{H}$ of size $n_H$-by-$n_T$ does not vary in time and can be expressed as

$$\mathbf{H} = \begin{bmatrix} \alpha & 0 & & \ldots & & 0 \\ 1 & \alpha & 0 & \ldots & & 0 \\ \alpha & 1 & \alpha & 0 & \ldots & 0 \\ \vdots & & & \ddots & & \vdots \\ 0 & & \ldots & 0 & \alpha & 1 \\ 0 & & \ldots & & 0 & \alpha \end{bmatrix}, \tag{4.12}$$

To illustrate the role of $\alpha$, consider for example, read head 3, which corresponds to the third row in $\mathbf{H}$. It is centered on track 2, but picks up magnetization from tracks 1 and 3 weighted by $\alpha$.

### 4.6.3 Iterative Read-back Architecture

The block diagram of the proposed iterative read-back system is shown in Fig. 4.21. The detector first tries to suppress the ITI and provides soft decisions on the noiseless ISI symbols on each track. The $n_T$ PR channel equalizers and turbo decoder subsequently process these decisions.

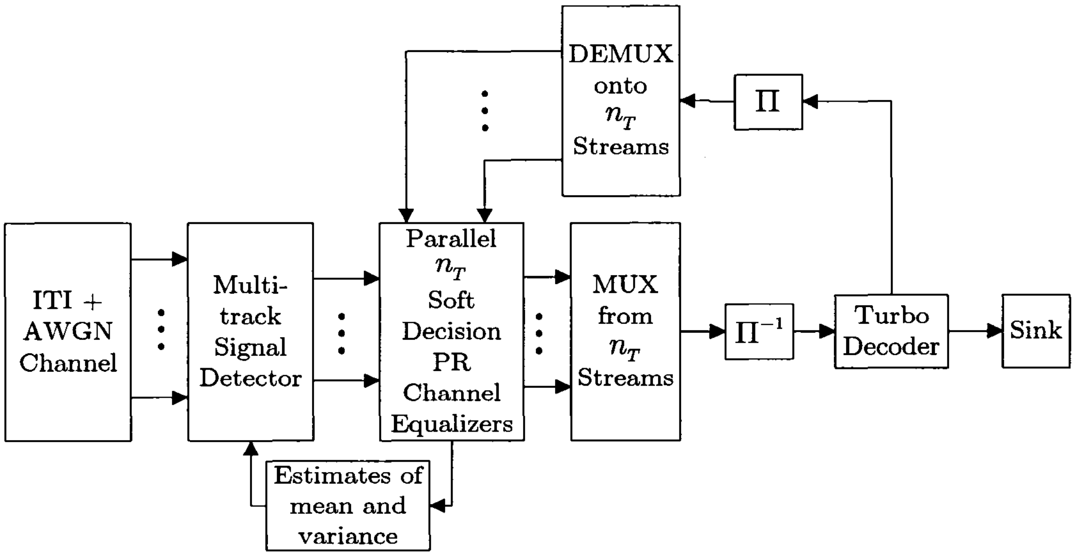

Fig. 4.21. Schematic block diagram of the iterative read-back system.

The detector decomposes the channel matrix $\mathbf{H}$ into two matrices as $\mathbf{H} = \mathbf{SA}$, where $\mathbf{S} = \left[\mathbf{h}_1/\|\mathbf{h}_1\|, \mathbf{h}_2/\|\mathbf{h}_2\|, \cdots, \mathbf{h}_{n_T}/\|\mathbf{h}_{n_T}\|\right]$ and $\mathbf{A} = diag\left(\|\mathbf{h}_1\|, \|\mathbf{h}_2\|, \ldots, \|\mathbf{h}_{n_T}\|\right)$. The received vector $\mathbf{r}_n$ in (4.11) is transformed using $\mathbf{S}$ to obtain channel observations on the ISI symbol vector $\bar{\mathbf{b}}_n$, i.e.,

$$\begin{aligned} \mathbf{y}_n &= \mathbf{S}^T\mathbf{r}_n = \mathbf{S}^T\mathbf{SA}\bar{\mathbf{b}}_n + \mathbf{S}^T\mathbf{v}_n \\ &= \mathbf{RA}\bar{\mathbf{b}}_n + \bar{\mathbf{v}}_n, \end{aligned} \tag{4.13}$$

where $\mathbf{R} = \mathbf{S}^T\mathbf{S}$ and $\bar{\mathbf{v}}_n = \mathbf{S}^T\mathbf{v}_n$ is the filtered noise. To further reduce the residual ITI, $\mathbf{y}_n$ is filtered by the matrix $\mathbf{M}$ whose coefficients are determined through the MMSE criterion: $\mathbf{M} = \arg\min_{\mathbf{M}\in\mathbb{R}^{n_T\times n_T}} E\left[\left\|\mathbf{A}\bar{\mathbf{b}}_n - \mathbf{M}\mathbf{y}_n\right\|^2\right]$ [73]. The resulting MMSE solution is given by

$$\mathbf{M} = \left(\mathbf{R} + \sigma^2\mathbf{P}_I^{-1}\mathbf{A}^{-2}\right)^{-1}, \tag{4.14}$$

where $\mathbf{P}_I$ depends on the sum of the square of the PR channel coefficients, i.e.,

$$\mathbf{P}_I = \left(\sum_{l=0}^{d} I_l^2\right)\mathbf{I}. \tag{4.15}$$

The overall detector is of quadratic complexity in the number of tracks as it only involves multiplication of $\mathbf{r}_n$ by pre-calculated (and stored) matrices $\mathbf{S}$ and $\mathbf{M}$. The MMSE filter output $\bar{\mathbf{y}}_n$ provides channel observations on the ISI symbols in $\overline{\mathbf{b}}_n$ and is given by

$$\begin{aligned}\overline{\mathbf{y}}_n &= \mathbf{M}\mathbf{y}_n = \mathbf{MRA}\overline{\mathbf{b}}_n + \mathbf{M}\overline{\mathbf{v}}_n \\ &= \mathbf{C}\overline{\mathbf{b}}_n + \tilde{\mathbf{v}}_n,\end{aligned} \tag{4.16}$$

where $\mathbf{C} = \mathbf{MRA}$ and the $j$-th element of $\tilde{\mathbf{v}}_n = \mathbf{M}\overline{\mathbf{v}}_n$ is a zero mean Gaussian random variable with variance $\left(\mathbf{MRM}^T\right)_{j,j}\sigma^2$. Expanding the $j$-th element of $\overline{\mathbf{y}}_n$,

$$\overline{\mathbf{y}}_n(j) = \mathbf{C}(j,j)\overline{\mathbf{b}}_n(j) + \sum_{\substack{k=1\\k\neq j}}^{n_T}\mathbf{C}(j,k)\overline{\mathbf{b}}_n(k) + \tilde{\mathbf{v}}_n(j), \tag{4.17}$$

where the desired noiseless ISI symbol $\mathbf{C}(j,j)\overline{\mathbf{b}}_n(j)$ is corrupted by residual interference from other tracks and filtered Gaussian noise.

We approximate the combined effect of the interference and noise for the $j$-th element of $\overline{\mathbf{y}}_n$ in (4.17) as a Gaussian random variable with mean

$$\boldsymbol{\mu}_n(j) = \sum_{\substack{k=1\\k\neq j}}^{n_T} E\left[\mathbf{C}(j,k)Q\right] \tag{4.18}$$

and variance $\mathbf{k}_n(j)$ given by

$$\mathbf{k}_n(j) = \left(\mathbf{MRM}^T\right)_{j,j}\sigma^2 + \sum_{\substack{k=1\\k\neq j}}^{n_T} E\left[\left(\mathbf{C}(j,k)Q\right)^2\right] - \left(E\left[\mathbf{C}(j,k)Q\right]\right)^2, \tag{4.19}$$

where $E$ is the expectation operator on the discrete random variable $Q$, which can take one of $M$ possible ISI symbol values. Due to the independence of the ISI symbols on each track, the variance operation can be applied on each element of the sum as shown in (4.19).

Finally, the likelihood of the $j$-th element of the ISI symbol vector $\overline{\mathbf{b}}_n(j)$ being the $p$-th symbol in the ISI alphabet $\{q_1, q_2, \ldots, q_M\}$ can be expressed as

$$P\left(\overline{\mathbf{y}}_n(j) \middle| \overline{\mathbf{b}}_n(j) = q_p\right) = \frac{1}{\sqrt{2\pi\mathbf{k}_n(j)}}\exp\left(-\frac{\left(\overline{\mathbf{y}}_n(j) - \boldsymbol{\mu}_n(j) - \mathbf{C}(j,j)q_p\right)^2}{2\mathbf{k}_n(j)}\right). \tag{4.20}$$

The array of likelihood estimates for each data stream is subsequently fed to $n_T$ parallel soft decision PR channel equalizers shown in Fig. 4.21.

In a recording system with many read heads, iterative processing shown in Fig. 4.21 can significantly improve performance. During the first iteration, the proposed multi-track signal detector generates soft estimates on the noiseless ISI symbols contained in $\bar{\mathbf{b}}_n$ using the readback vector $\mathbf{r}_n$. These estimates are processed, for each track, by $n_T$ parallel PR channel equalizers based on the BCJR algorithm described in Section 2.3.2. The resulting soft decisions on the coded bits are used by the turbo decoder to produce extrinsic information for the following iteration and hard decision outputs on the message bits.

During each of the following iterations, extrinsic information on coded bits from the turbo decoder are interleaved and demultiplexed onto $n_T$ streams, as shown in Fig. 4.21. These streams are individually fed to $n_T$ PR channel equalizers as *a priori* information and the equalizers generate soft decisions on the noiseless ISI symbols contained in $\bar{\mathbf{b}}_n$. These decisions are used to recompute the mean and variance of the Gaussian approximation for the residual ITI and noise in (4.17) using (4.18) and (4.19). This in turn, will result in improved estimates from the signal detector on the elements of $\bar{\mathbf{b}}_n$, which are consequently processed by the PR channel equalizers followed by the turbo decoder in the same manner as in the first iteration. The turbo decoder at the end of each iteration forms the decisions on the message bits.

### 4.6.4 Simulation Results

We first considered a message block length of 4,000 bits. The rate $R_c = 8/9$ turbo encoder is adopted from [52] and is based on puncturing a rate 1/3 turbo code with feedback and feedforward polynomials given by $1 \oplus D \oplus D^4$ and $1 \oplus D \oplus D^3 \oplus D^4$, respectively. An S-rand interleaver [41] ($S = 22$) is employed in the turbo code and another S-rand interleaver ($S = 25$) is used between the turbo code and the precoded channel. The binary symbols '0', '1' at the output of turbo encoder are mapped to -1, 1, which are demultiplexed and fed to $n_T$ precoded partial response channels. The precoder is $1/\left(1 \oplus D \oplus D^2 \oplus D^4\right)$ and the channel ISI coefficients $I_\ell$ are given by the target response of the modified extended partial response (ME$^2$PR) channel $h(D) = \left(5 + 4D - 3D^2 - 4D^3 - 2D^4\right)$, which has been explored in high density recordings [79]. The SNR can be defined as

$$SNR = 10\log_{10}\left(\frac{\left(1+2\alpha^2\right)\sum_{l=0}^{4}\left\|I_l\right\|^2}{\left(n_T R_c \sigma^2\right)}\right). \tag{4.21}$$

Finally, the overall system performs ten detection and decoding iterations and the $n_T$ PR channel equalizers were implemented using the BCJR algorithm [4].

We considered the performance of a recording system with $n_T = 2$ tracks, $n_H = 4$ read heads and ITI parameter values $\alpha$ being 0.1 and 0.5, respectively. (Note that $\alpha = 0.5$ corresponds to the case of severe ITI.) Simulation results in Fig. 4.22, illustrate that the proposed detector in the read-back system performs well in both considered cases and can allow increased radial storage density and read-out rates. We observe that a five times increase in ITI on the considered ME$^2$PR channel corresponds to only about a 2 dB SNR performance loss.

To demonstrate the scalability potential of the proposed detector, Fig. 4.23 illustrates performance results of an $n_T = 20$ track, $n_H = 22$ read head system for the case of severe ITI ($\alpha = 0.5$). We used a message block size of 40,000 bits and S-rand interleavers ($S = 80$, $S = 83$) in the turbo code and before the ME$^2$PR channel. When compared to the previously considered $\left(n_T, n_H\right) = (2,4)$ system for $\alpha = 0.5$, the SNR required to achieve a BER of $10^{-5}$ increases by about 2.9 dB for a corresponding ten times increase in read-out rates.

As a final note, since the input to the magnetic channels is constrained to -1 or 1, there are no closed form solutions to the Shannon capacity even for SISO magnetic channels [108]. As such, simulated results in this section for multi-head, multi-track recording systems and single head single track recording systems considered in Section 5.4.5 are not compared against the channel capacity limit.

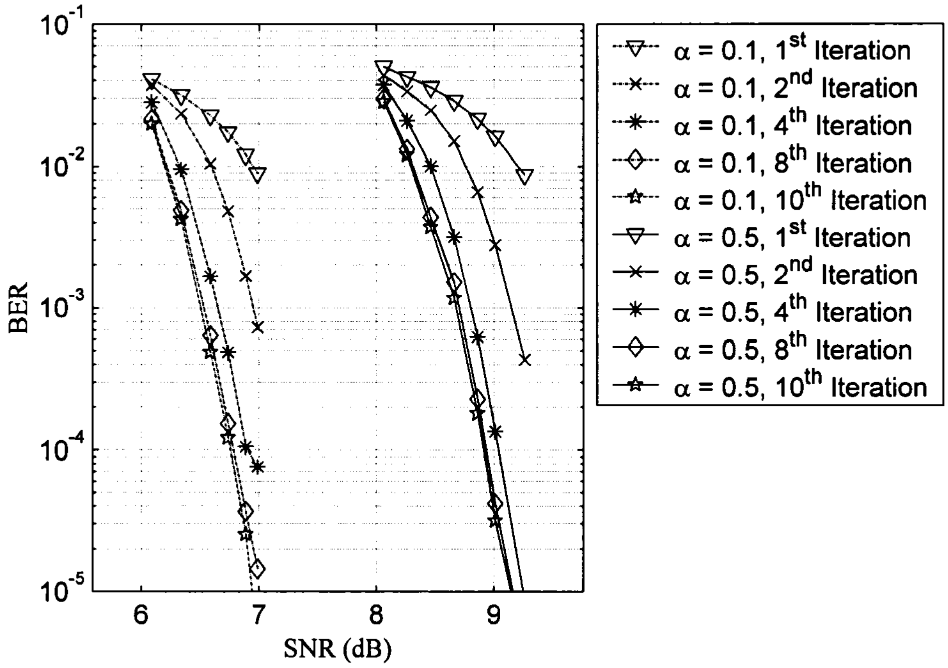

**Fig. 4.22. Bit error rate performance of the proposed multi-track detector with iterative processing for an $(n_T, n_H) = (2,4)$ system with an ITI parameter $\alpha$ being 0.1 and 0.5 after 1, 2, 4, 8, 10 iterations on the ME²PR channel.**

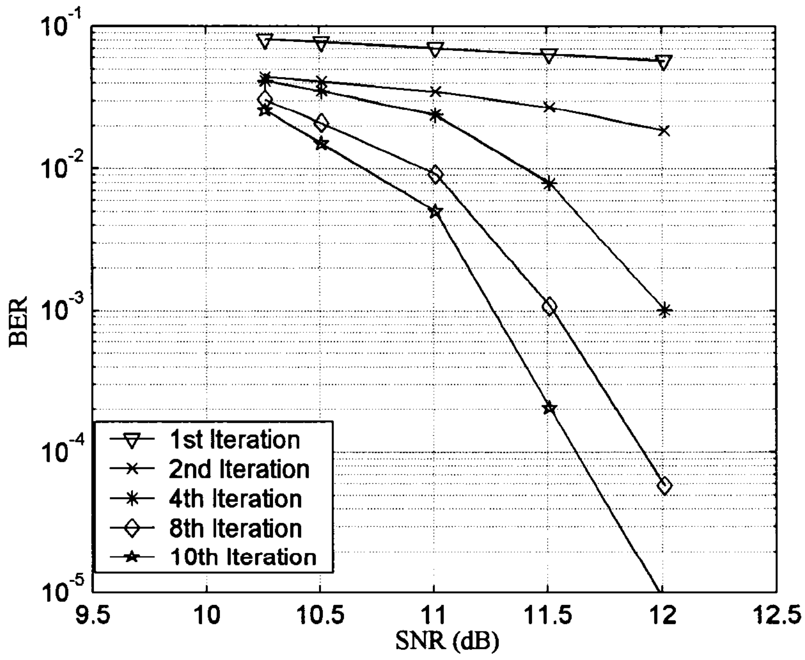

**Fig. 4.23. Bit error rate performance of the proposed multi-track detector with iterative processing for an $(n_T, n_H) = (20,22)$ system in the presence of strong intertrack interference (ITI parameter $\alpha$ = 0.5) on the ME²PR channel.**

## 4.7 Summary and Comments on Extensions

### 4.7.1 Chapter Summary

In this chapter, we have proposed receiver architectures for turbo-coded MIMO systems using the front-end MIMO signal detector proposed in Chapter 3.

In Sections 4.1 and 4.2, we have presented the single user transmitter architecture and three receiver implementations with increasing levels of complexity and performance. In the first two architectures, soft decisions on the transmitted symbols from the proposed detector are passed to the demapper (for the demodulator) and turbo decoder, which can be in an iterative loop. In contrast, the third architecture involves a novel low complexity iterative processing scheme, where soft outputs of the turbo decoder are used to progressively improve the knowledge of the co-antenna interference. In Section 4.3, we have observed through simulation results that only the third receiver architecture (with iterative processing) operates near the capacity limit even up to $\left(n_T, n_R\right) = (30, 120)$. In addition, the turbo-coded MIMO architecture was shown to be robust to spatial correlation and channel estimation errors.

In Section 4.4, we have extended the design of the receiver architecture with iterative processing to the multi-user case. Through effective iterative multi-user interference cancellation, system performance remained close to the capacity limit for various antenna configurations and is robust to the effects of spatial correlation and imperfect power control. In Section 4.5, we have considered benefits of the proposed detector versus previously proposed MIMO signal detectors.

Finally, in Section 4.6, we have considered an extension of the proposed MIMO signal detector and iterative receiver to the area of multi-head multi-track recording systems. Such systems have the potential of providing high read-out rates and increased overall hard drive capacity via increased recording density. Simulation results indicate that the proposed coded MIMO recording architecture has good performance even in the presence of high intersymbol and intertrack interference and is scalable to a large number of heads and tracks.

### 4.7.2 Comments on STBC and Frequency Selective Fading Channels

As shown in this chapter, the proposed coded MIMO system achieves near capacity performance in single and multi-user scenarios. Space-time block codes could be incorporated into the proposed turbo coded MIMO system as a front end to the coded MIMO transmitter (i.e., just prior to antenna transmission in Fig. 4.1.). At the receiver, space-time block decoding can be performed subsequent to MIMO signal detection and prior to turbo decoding. However, due to the short length of the space-time block code [1], [91], only a slight increase in BER performance may be observed. Furthermore, unlike turbo codes, space-time block codes are not used in the 3G standards and may not be employed in next generation wireless systems.

In broadband wireless communication, the wireless MIMO channel will not remain flat over the signal bandwidth and becomes frequency selective. One method to avoid the deleterious effects of intersymbol interference (ISI) is to employ orthogonal frequency division multiplexing. In this case, the allocated frequency spectrum is divided into many small non-overlapping frequency bands. The channel can be assumed to be frequency non-selective in each band and thus the proposed turbo coded MIMO system can be used within each band as described herein. Alternately, if the proposed MIMO system employs CDMA spreading, then a Rake receiver can be used to collect the transmitted symbol energy that is spread across many multipath components. We emphasize that the proposed coded MIMO system with appropriate modifications can minimize the effects of ISI. This ability has been shown in this thesis for multi-head multi-track recording systems (Section 4.6), where good BER performance was achieved despite high intersymbol interference.

# Chapter 5

# Performance Analysis Techniques

This chapter describes two new performance analysis techniques for turbo-coded MIMO systems. The first technique is an extension of the union bound based method [8], [23] from the AWGN channel setting to MIMO fading channels. The proposed technique accurately approximates the error floor performance of turbo-coded MIMO systems from Chapter 4 for various scenarios. In addition, we propose a second performance analysis technique for the considered turbo-coded MIMO systems, which is different in its approach from the union bound based method [8], [23] and EXIT charts [16]. The proposed method approximately evaluates a bound on the BER performance of the turbo-coded MIMO systems in the waterfall region and can also provide accurate bounds for coded digital recording systems.

## 5.1 Motivation and Background

Bit error rate analysis techniques are useful in speedy evaluation of coded MIMO system performance and can provide insights on the role of various design parameters. For instance, such techniques allow a system designer to explore the effects of decreasing or increasing the number of transceiver antennas, e.g., due to loosing antennas through hardware failure or adding antennas in a system upgrade of the base-station. Similarly, one can consider multiple types of correlated fading, e.g., due to different angular spread values at various geographical locations or antenna spacings for several transceiver designs. Finally, one can also explore the impact of turbo code parameters (e.g., block length, constituent encoders, etc.) on system performance for various MIMO setups.

The performance of turbo-coded MIMO systems has generally been obtained using Monte Carlo simulation techniques, as BER performance analysis becomes difficult due to the time-varying nature of the MIMO channel and the use of iterative detection and turbo decoding at the receiver. The EXIT chart technique of ten Brink [16] has not yet been successfully extended beyond fixed MIMO channels [39] and the only attempt at BER analysis of turbo-coded MIMO systems on time-varying channels was that of Stefanov and Duman [88]. The authors provide upper bounds, which are loose by 2 dB for coded MIMO systems that employ the optimal MIMO signal detector on quasi-static Rayleigh fading channels (the channel remains constant for a block of transmissions). Furthermore, their method was limited to systems with few antennas, because the probability of error requires the evaluation of a multi-dimensional integral that is proportional to the number of elements in the channel matrix.

In contrast to the above methods, the two proposed techniques provide bounds on BER performance of the considered turbo-coded MIMO system in the waterfall region (BER $= 10^{-1}$ to $10^{-5}$) and in the error floor region (which corresponds to system performance at high SNRs). In both regions, the performance bounds are within fractions of a dB from the simulated performance on time-varying MIMO channels.

## 5.2 Performance Bounds Based on the Union Bound Method

In this section, we first describe the method for evaluating the union bound in an AWGN channel setting. We subsequently use this result in the evaluation of the performance bound for the proposed turbo-coded MIMO systems. We consider the single user case with QPSK modulation, shown in Fig. 4.15, for single pass detection as well as iterative detection and turbo decoding. Performance bounds for correlated fading scenarios are also presented.

### 5.2.1 Derivation of the Union Bound for the Gaussian Noise Channel

We follow the methodology for evaluating the union bound from [23]. As mentioned in Section 2.4.2, the bound is intractable for a particular interleaver and thus the uniform interleaver construct is used [8]. The use of the uniform interleaver permits evaluation of the bound in terms of input-output weight enumerating functions of the two constituent encoders. Consequently, we first determine the input-output weight enumerating function for the constituent encoder and show how it can be used to determine the bound on BER performance for the overall turbo encoder.

We consider the turbo code from [9] whose constituent encoder is shown in Fig. 2.10 (a). The corresponding state transition diagram for the component encoder is shown in Fig. 5.1. Each edge label is replaced with the monomial $L^l I^w D^d$, where $l$ is always equal to 1, $w$ and $d$ are either 0 or 1 depending on whether the corresponding input or output bits are 0 or 1 respectively. The state transition diagram can be summarized as a state transition matrix

$$\mathbf{X} = \begin{bmatrix} L & LID & 0 & 0 \\ 0 & 0 & LI & LD \\ LID & L & 0 & 0 \\ 0 & 0 & LD & LI \end{bmatrix}. \tag{5.1}$$

We define the transfer function $T(L, I, D)$ as the sum of all paths, which start and end in state zero with all possible input and output Hamming weights

$$T(L,I,D) = \sum_{l \geq 0} \sum_{w \geq 0} \sum_{d \geq 0} t(l,w,d) L^l I^w D^d, \tag{5.2}$$

where $t(l, w, d)$ is the number of paths of length $l$, input weight $w$, and output weight $d$ that start and end in the zero state. We use the transfer-matrix method to determine the transfer function $T(L, I, D)$, which is subsequently used to determine input-output weight enumerator $t(l, w, d)$ [85].

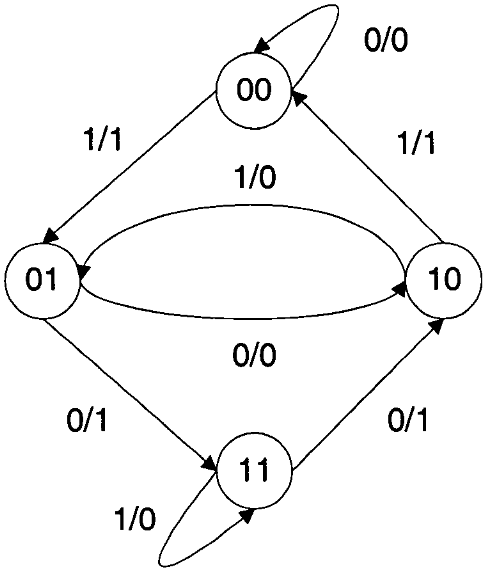

**Fig. 5.1. State diagram corresponding to the recursive convolutional code shown in Fig. 2.10 (a).**

The state transition diagram in Fig. 5.1 can be considered as a directed graph, where we define a walk $W = e_1 e_2 \ldots e_l$ from state $u$ through $l$ edges and arriving in state $v$. The weight of $W$ is defined by $\omega(W) = \omega(e_1)\omega(e_2)\ldots\omega(e_l)$, where the weight of the $i$-th edge $\omega(e_i) \in \{L, LI, LD, LID\}$, $i = 1, 2, \ldots, l$. We define $B_{u,v}(l)$ as the sum of weights of all possible walks $W$ of length $l$ from state $u$ to state $v$,

$$B_{u,v}(l) = \sum_{W} \omega(W), \tag{5.3}$$

where $B_{u,v}(0) = \delta(u - v)$ ($\delta(i) = 1$ for $i = 0$ and $\delta(i) = 0$ otherwise). The $(u, v)$-th entry in the state transition matrix $\mathbf{X}(u,v)$ is given by $B_{u,v}(1)$ and, in order to determine $B_{u,v}(l)$, we need to formulate it as an entry of a certain matrix by using Theorems 4.7.1 and 4.7.2 in [85]. (For the sake of completeness, we prove these theorems in Appendix B.)

*Theorem 4.7.1 in* [85]: The $(u, v)$-th entry of $\mathbf{X}^l$ is equal to $B_{u,v}(l)$, and $\mathbf{X}^0 = \mathbf{I}$, where $\mathbf{X}$ is the state transition matrix.

*Theorem 4.7.2 in* [85]*:* We define the generating function as $F_{u,v} = \sum_{l \geq 0} B_{u,v}(l)$ and it can be expressed as

$$F_{u,v} = \frac{(-1)^{u+v}\det(\mathbf{I}-\mathbf{X}:v,u)}{\det(\mathbf{I}-\mathbf{X})} \tag{5.4}$$

where the notation $(\mathbf{C}:v,u)$ denotes the matrix obtained by removing the $v$-th row and the $u$-th column of $\mathbf{C}$.

Thus, $B_{u,v}(l)$ is the $(u,\ v)$-th entry of $\mathbf{X}^l$ and since the transfer function $T(L,I,D)$ is the sum of all closed walks that originate at state 0 and return to state 0, we get

$$T(L,I,D) = \sum_{l>0} B_{0,0}(l). \tag{5.5}$$

Using the result of Theorem 4.7.2 in [85], the right hand side is the (0, 0)-th entry in the matrix $(\mathbf{I}-\mathbf{X})^{-1}$ and thus, $T(L,\ I,\ D)$ can be expressed as

$$T(L,I,D) = \frac{1-LI-L^2I-L^3\left(D^2-I^2\right)}{1-L(I+D)-L^3\left(D^2-I-I^2+I^3D^2\right)+L^4\left(D^2-I^2-I^2D^4+I^4D^2\right)}. \tag{5.6}$$

Multiplying both sides of (5.6) by the denominator, substituting the expression for $T(L,\ I,\ D)$ from (5.2) and equating the coefficients of the $L^lI^wD^d$, we obtain the following recursive formula for $t(l,\ w,\ d)$:

$$\begin{aligned} t(l,w,d) = {} & t(l-1,w-1,d)+t(l-1,w,d)+t(l-3,w-3,d-2) \\ & -t(l-3,w-2,d)-t(l-3,w-1,d)+t(l-3,w,d-2) \\ & -t(l-4,w-4,d-2)+t(l-4,w-2,d-4) \\ & +t(l-4,w-2,d)-t(l-4,w,d-2)+\delta(l,w,d) \\ & -\delta(l-1,w-1,d)-\delta(l-2,w-1,d)-\delta(l-3,w,d-2) \\ & +\delta(l-3,w-2,d), \end{aligned} \tag{5.7}$$

where $l \geq 0$, $w \geq 0$, $d \geq 0$, $t(l,\ w,\ d) = 0$ if any index is negative and $\delta(l,w,d)=1$ if $l = w = d = 0$ and $\delta(l,w,d)=0$ otherwise.

Since the turbo code has been defined with a message block length of $N_m$, there are $t(N_m,w,d)$ distinct codeword fragments (corresponding to parity streams $\mathbf{c}_2$ and $\mathbf{c}_3$ from Fig. 2.9) of input Hamming weight $w$ and output weight $d$. Let $p(d|w)$ be the conditional probability of producing a codeword fragment of weight $d$ given a randomly selected input sequence of weight $w$, which is given by

$$p(d|w) = \frac{t(N_m, w, d)}{\sum_{d'} t(N_m, w, d')} = \frac{t(N_m, w, d)}{\binom{N_m}{w}}, \tag{5.8}$$

where $\binom{N_m}{w}$ is the number of codewords corresponding to a message sequence of Hamming weight $w$. Using the uniform interleaver definition, the probability $p(d_1, d_2, d_3|w)$ that an input sequence $\mathbf{m}$ of weight $w$ is mapped into codeword fragments $\mathbf{c}_1$, $\mathbf{c}_2$ and $\mathbf{c}_3$ with weights $d_1, d_2$, and $d_3$, respectively, is given by

$$p(d_1, d_2, d_3|w) = p_1(d_1|w)\, p_2(d_2|w)\, p_3(d_3|w), \tag{5.9}$$

where $p_1(d_1|w) = 1$ when $d_1 = w$ and zero otherwise (as $\mathbf{c}_1$ corresponds to a systematic stream).

Since the turbo code is a linear code, we can restrict attention to error events with respect to the all-zero codeword for the calculation of the bound. The conditional probability that the maximum likelihood decoder will decide in favour of a particular codeword $\mathbf{c}$ of total Hamming weight $d = d_1 + d_2 + d_3$ instead of the all-zero codeword (assuming BPSK signalling) is given by

$$P_{error}(d) = Q\left(\frac{d_E}{2\sigma}\right) = Q\left(\sqrt{\frac{2dE_s}{N_0}}\right), \tag{5.10}$$

where $d_E$ is the Euclidean distance between two codewords and $\sigma^2 = N_0/2$. In (5.10), we used the fact that $d_E$ can be expressed in terms of the codeword Hamming weight $d$ and the average power per BPSK symbol $E_s$ as $d_E = 2\sqrt{dE_s}$ [76]. Hence, the bound on the bit error probability is approximately evaluated as

$$P_b = \sum_{w=1}^{N_m} \frac{w}{N_m} \text{Prob}[\text{error event of weight } w] \le \sum_{w=1}^{N_m} \frac{w}{N_m} \binom{N_m}{w} E_{d|w}\left[Q\left(\sqrt{\frac{2dE_s}{N_0}}\right)\right], \tag{5.11}$$

where $E_{d|w}[\bullet]$ is a conditional expectation that uses the probabilities from (5.9). (The inequality in (5.11) is due to error events being counted multiple times.) The result in (5.11) would be the same for the case of Gray coded QPSK modulation shown in Fig. 4.15 as it corresponds to two independent BPSK symbol transmissions.

In Sections 5.2.2 and 5.2.3, we show that under certain conditions, the performance of the considered coded MIMO system is approximated by the performance of a turbo coded system with QPSK modulation on a Gaussian noise channel. Thus, with appropriate modifications, the union bound result in (5.11) can be used to obtain BER performance bounds for various MIMO scenarios.

### 5.2.2 Bounds for Single Pass Detection Systems

For the case of single pass detection and turbo decoding, shown in Fig. 4.2 (a), the mean of the co-antenna interference $\boldsymbol{\mu}_n(j)$ is zero for $n = 1, 2, \ldots, N_c/(2n_T)$ and $j = 1, 2, \ldots, n_T$. The variance of the co-antenna interference in the real dimension can be expressed from (3.5) as

$$\begin{aligned}\mathbf{K}_{n,j}(1,1) &= \sum_{\substack{k=1\\k\neq j}}^{n_T} E\left[\left(\mathbf{A}_n(k,k)\Re\{\mathbf{R}_n(j,k)Q\}\right)^2\right] - \left(E\left[\mathbf{A}_n(k,k)\Re\{\mathbf{R}_n(j,k)Q\}\right]\right)^2 + \sigma^2\\ &= \sum_{\substack{k=1\\k\neq j}}^{n_T} E\left[\left(\mathbf{A}_n(k,k)\Re\{\mathbf{R}_n(j,k)Q\}\right)^2\right] + \sigma^2 \\ &\approx M_A^2 \sum_{\substack{k=1\\k\neq j}}^{n_T} E\left[\left(\Re\{\mathbf{R}_n(j,k)Q\}\right)^2\right] + \sigma^2\end{aligned} \tag{5.12}$$

for $n = 1, 2, \ldots, N_c/(2n_T)$. In (5.12), we have used the fact that the transmitted QPSK symbols are equiprobable and hence, $E\left[\mathbf{A}_n(k,k)\Re\{\mathbf{R}_n(j,k)Q\}\right] = 0$ for all $k = 1, 2, \ldots, n_T$. Since we showed in Section 3.2.1 that the variance of $\mathbf{A}_n(k,k)$ is small in the uncorrelated and correlated fading scenarios, we approximate it by its mean $M_A$ in (5.12). We can further simplify $\mathbf{K}_{n,j}(1,1)$ to

$$\begin{aligned}\mathbf{K}_{n,j}(1,1) &\approx \frac{M_A^2}{4} \sum_{\substack{k=1\\k\neq j}}^{n_T} \sum_{\substack{Q\in\\\{q_1,q_2,q_3,q_4\}}} E\left[\left(\Re\{\mathbf{R}_n(j,k)Q\}\right)^2 \middle| Q\right] + \sigma^2 \\ &= \frac{M_A^2}{4} \sum_{\substack{k=1\\k\neq j}}^{n_T} \sum_{\substack{Q\in\\\{q_1,q_2,q_3,q_4\}}} E\left[(\xi+\eta)^2 \middle| Q\right] + \sigma^2,\end{aligned} \tag{5.13}$$

where the first step follows from conditioning on $Q$ and $\xi$, $\eta$ represent the real terms of the product of $\mathbf{R}_n(j,k)$ and $Q$. Recall from Section 3.2.2, that $\mathbf{R}_n(j,k)$ is a zero mean complex Gaussian random variable with variance $n_R/(2M_A^4)$ and

$\frac{1}{2M_A^4}\sum_{l=1}^{n_R}\left(\mathbf{\Lambda}_{\mathbf{C}_{RX}}(l,l)\right)^2$ in each dimension, where $\mathbf{\Lambda}_{\mathbf{C}_{RX}}(l,l)$ is the $l$-th eigenvalue of the spatial correlation matrix $\mathbf{C}_{RX}$, $l = 1, 2, \ldots, n_R$. Thus, for all QPSK constellation points, $\xi$ and $\eta$ are independent zero mean Gaussian random variables with variance $n_R/(4M_A^4)$ or $\frac{1}{4M_A^4}\sum_{l=1}^{n_R}\left(\mathbf{\Lambda}_{\mathbf{C}_{RX}}(l,l)\right)^2$ corresponding to the uncorrelated and correlated fading scenarios. Simplifying (5.12), we have for uncorrelated fading

$$\mathbf{K}_{n,j}(1,1) \approx \frac{(n_T-1)n_R}{2M_A^2} + \sigma^2, \tag{5.14}$$

while for correlated fading

$$\mathbf{K}_{n,j}(1,1) \approx \frac{(n_T-1)}{2M_A^2}\sum_{l=1}^{n_R}\left(\mathbf{\Lambda}_{\mathbf{C}_{RX}}(l,l)\right)^2 + \sigma^2 \tag{5.15}$$

for $n = 1, 2, \ldots, N_c/(2n_T)$. Due to the symmetry of the setup, $\mathbf{K}_{n,j}(2,2)$ is equal to $\mathbf{K}_{n,j}(1,1)$ and the off-diagonal terms $\mathbf{K}_{n,j}(1,2)$ and $\mathbf{K}_{n,j}(2,1)$ are zero as the in-phase and quadrature components of the QPSK symbol are independent.

Based on (3.3), the $j$-th element of the channel observation vector $\mathbf{y}_n(j)$ is given by

$$\mathbf{y}_n(j) = \mathbf{A}_n(j,j)\mathbf{b}_n(j) + \sum_{\substack{k=1 \\ k\neq j}}^{n_T}\mathbf{A}_n(k,k)\mathbf{R}_n(j,k)\mathbf{b}_n(k) + \overline{\mathbf{v}}_n(j), \tag{5.16}$$

where the desired symbol from the $j$-th transmit antenna $\mathbf{b}_n(j)$ is scaled by $\mathbf{A}_n(j,j)$ and corrupted by complex noise with zero mean and variance approximately given by (5.14) and (5.15) in the real and imaginary dimensions. Since the variance of $\mathbf{A}_n(j,j)$ is small in the uncorrelated and correlated fading scenarios, we approximate it by its mean $M_A$. Thus, the performance of the coded MIMO system can be approximated by the performance of a turbo-coded system using Gray coded QPSK constellation on a Gaussian noise channel (with noise variance $\mathbf{K}_{n,j}(1,1)$ in the real and imaginary dimensions) scaled by a fixed amplitude. Modifying the expression in (5.11), we can approximately evaluate the performance bound of the coded MIMO system with single pass detection as

$$P_b \le \sum_{w=1}^{N_m} \frac{w}{N_m} \binom{N_m}{w} E_{d|w}\left[Q\left(\sqrt{\frac{dM_A^2}{2\mathbf{K}_{n,j}(1,1)}}\right)\right], \tag{5.17}$$

where the probability that the maximum likelihood decoder will decide in favour of a codeword of weight $d$ instead of the all-zero codeword is given by $Q\left(\sqrt{dM_A^2/\left(2\mathbf{K}_{n,j}(1,1)\right)}\right)$.

### 5.2.3 Bounds for the Fully Iterative Receiver

In this section, we approximately evaluate an upper bound on the bit error probability assuming that the co-antenna interference has been perfectly cancelled at the output of the MIMO signal detector. This turns out to be a reasonable assumption in our considered scenarios, as after many iterations, soft decisions on the turbo-coded bits effectively cancel the co-antenna interference, as shown in Fig. 5.2. The presented histogram of the variance of the co-antenna interference approaches zero after seven iterations for a system with four transmit antennas and twenty receive antennas on an uncorrelated Rayleigh fading channel.

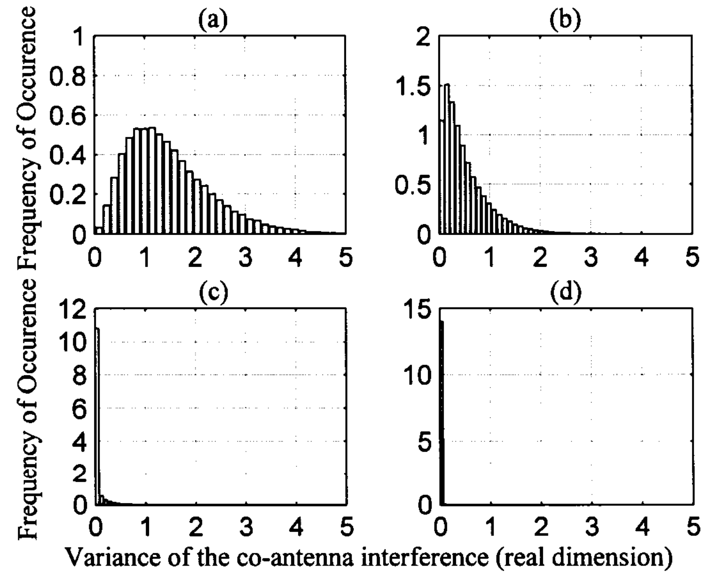

**Fig. 5.2. The reduction in the variance of the co-antenna interference (real dimension) for a coded MIMO system with $(n_T, n_R) = (4, 20)$ antenna configuration at an $E_b/N_0$ = -11.5 dB (a) Prior to decoding, (b) after 1 iteration, (c) after 5 iterations (d) after 7 iterations.**

Using the assumption from the previous paragraph, the channel observation on the modulation symbol transmitted from the $j$-th antenna $\mathbf{y}_n(j)$ from (5.16) simplifies to

$$\mathbf{y}_n(j) = \mathbf{A}_n(j,j)\mathbf{b}_n(j) + \overline{\mathbf{v}}_n(j). \tag{5.18}$$

We again approximate $\mathbf{A}_n(j,j)$ by its mean $M_A$ in both correlated and uncorrelated fading scenarios. Hence, the performance of the turbo-coded MIMO system with iterative processing can be approximated by the performance of a turbo-coded system using Gray coded QPSK constellation on a Gaussian noise channel with variance $\sigma^2$ in the real and imaginary dimensions. Modifying the expression in (5.11), we obtain the following approximately evaluated bound on system performance

$$P_b \le \sum_{w=1}^{N_m} \frac{w}{N_m} \binom{N_m}{w} E_{d|w}\left[Q\left(\sqrt{\frac{dM_A^2}{2\sigma^2}}\right)\right]. \tag{5.19}$$

### 5.2.4 Numerical and Simulation Results

In this section, we compare the simulated performance of several coded MIMO systems to the numerical results obtained using the union bound based method from Sections 5.2.2 and 5.2.3. The rate 1/3 turbo code from [9], with the constituent encoder shown in Fig. 2.10 (a), is used with a pseudorandom interleaver and a message block length of 2,000 bits. The ergodic capacity limits are evaluated using (2.11), where the expectation is approximated as an average over 100,000 channel realizations. For the correlated fading cases, the angular spread $\beta$ is assumed to be 10 degrees, the antenna spacing at the base-station is $\lambda$ and the mobile antennas are uncorrelated. The turbo decoder performs ten iterations in case of single pass detection and decoding, whereas in iterative processing, the overall receiver performs ten iterations.

We first consider the performance of the coded MIMO system with single pass detection on uncorrelated and correlated fading channels. Fig. 5.3 and Fig. 5.4 illustrate the BER performance and the evaluated bounds from (5.17) for $(n_T, n_R)$ = (2, 10) and (4, 20) antenna configurations, respectively. The corres-

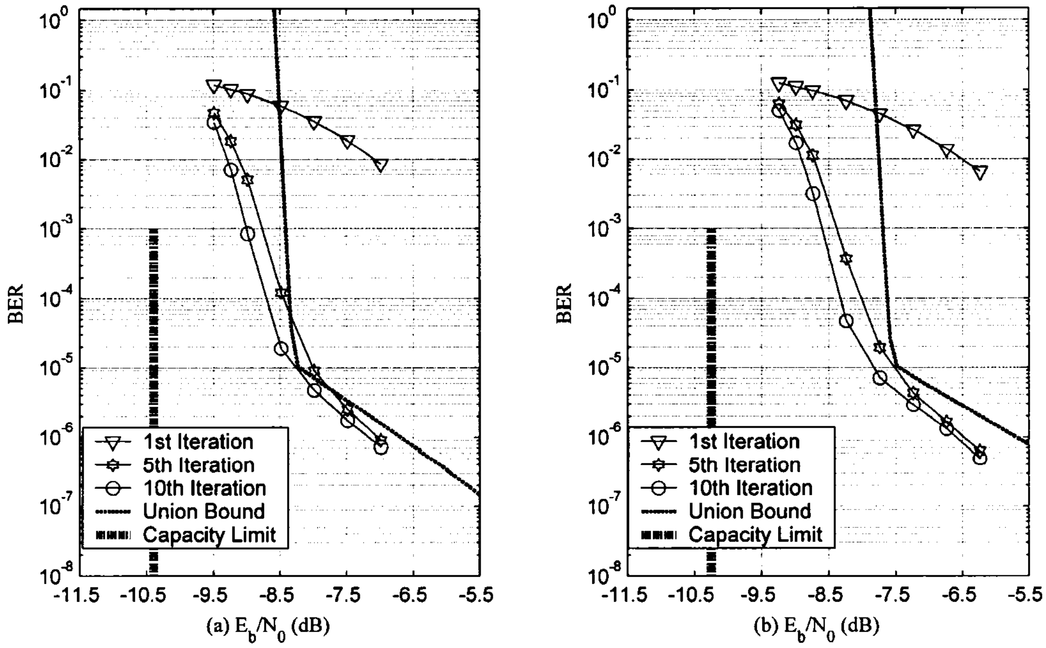

(a) $E_b/N_0$ (dB)

(b) $E_b/N_0$ (dB)

**Fig. 5.3. Simulation and numerical results for $(n_T, n_R)$ = (2, 10) coded MIMO system with single pass detection followed by turbo decoding for (a) uncorrelated Rayleigh fading and (b) correlated Rayleigh fading.**

ponding rates of transmission are 4/3 and 8/3 bits per channel use for the two and four transmit antenna systems, respectively. The bounds are within 0.5 dB of the simulated performance in the error floor region for the uncorrelated cases but the gap increases to 0.8 dB for the correlated fading scenarios.

Next, we consider the performance of the coded MIMO system with iterative processing on uncorrelated and correlated fading channels. Fig. 5.5 and Fig. 5.6 show the BER performance and the evaluated bounds from (5.19) for $(n_T, n_R)$ = (2, 10) and (4, 20) antenna configurations, respectively. The bounds in all four cases are within 0.5 dB of the simulated performance in the error floor region. Furthermore, the simulated performance is within 1.8 dB of the ergodic capacity limit at a BER of $10^{-5}$.

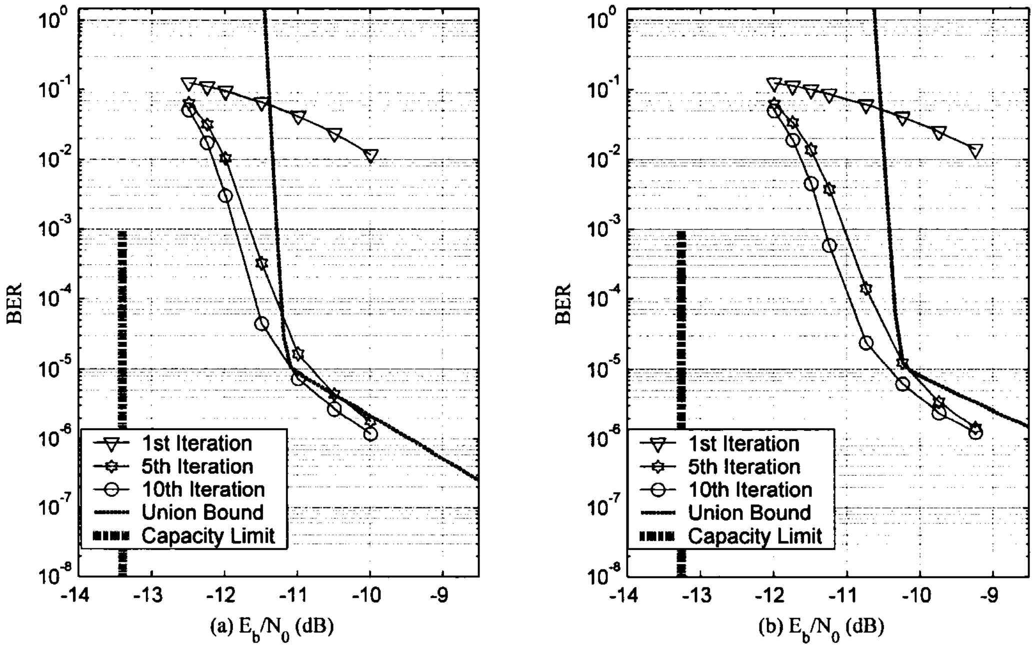

(a) $E_b/N_0$ (dB)

(b) $E_b/N_0$ (dB)

**Fig. 5.4 Simulation and numerical results for $(n_T, n_R)$ = (4, 20) coded MIMO system with single pass detection followed by turbo decoding for (a) uncorrelated Rayleigh fading and (b) correlated Rayleigh fading.**

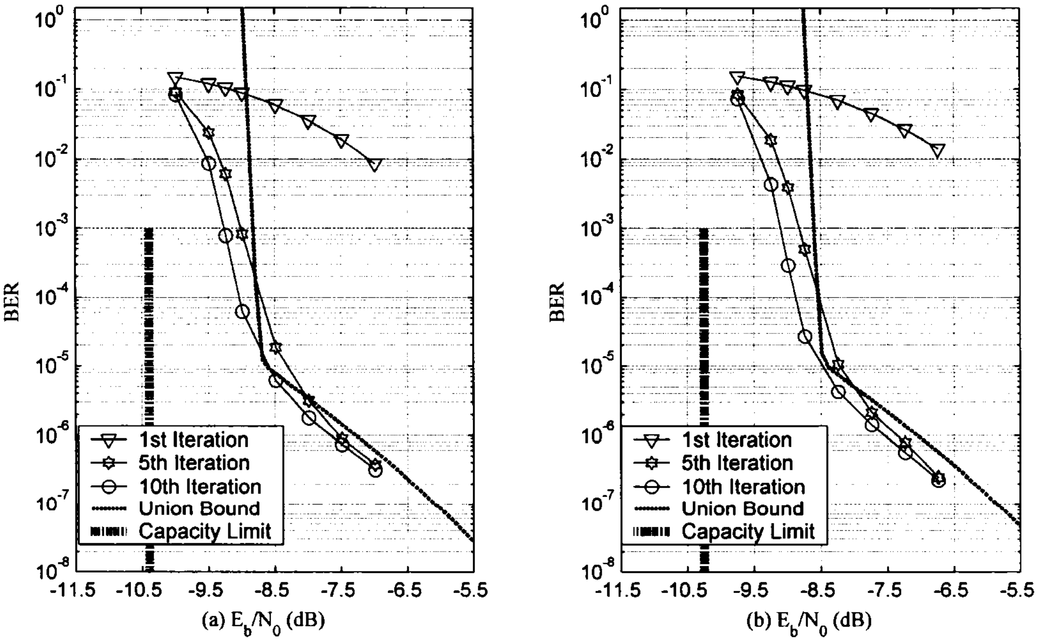

(a) $E_b/N_0$ (dB)

(b) $E_b/N_0$ (dB)

**Fig. 5.5. Simulation and numerical results for $(n_T, n_R)$ = (2, 10) coded MIMO system with iterative processing for (a) uncorrelated Rayleigh fading and (b) correlated Rayleigh fading.**

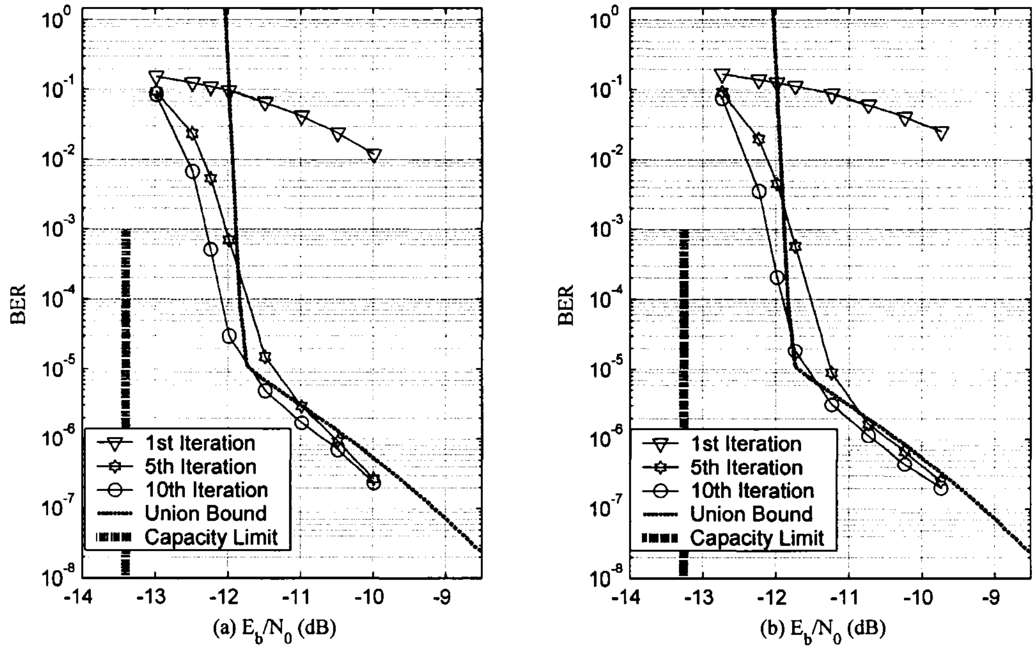

**Fig. 5.6. Simulation and numerical results for $(n_T, n_R)$ = (4, 20) coded MIMO system with iterative processing for (a) uncorrelated Rayleigh fading and (b) correlated Rayleigh fading.**

## 5.3 Proposed S-Curve Method for Coded MIMO Systems

### 5.3.1 Derivation of the Method

We express the bound on BER performance of the considered turbo-coded MIMO system as an integral of a product of two functions. One function has a known, closed form expression and the second function results from the property of the code and can be approximated using sigmoid or cubic spline functions using a small number of simulated sample points.

The considered coded MIMO system employs QPSK modulation and we use the channel model described in Section 2.1.3. Furthermore, perfect channel state information is assumed to be available at the receiver only. We consider the single user case and evaluate a lower bound on the BER performance, i.e., by assuming the co-antenna interference at the output of the proposed detector has been perfectly cancelled. In this case, the channel observation on the transmitted symbol from the $j$-th transmit antenna is given by (5.18) and, as in Section 5.2.3,

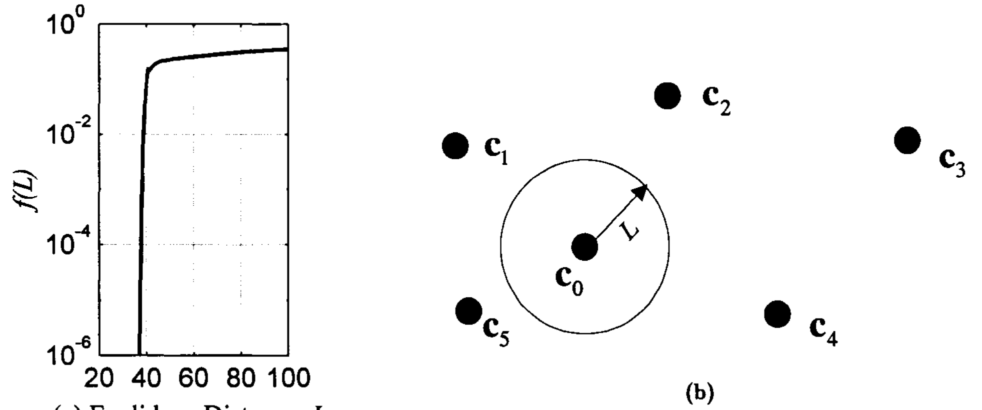

(a) Euclidean Distance $L$

(b)

**Fig. 5.7.(a) A plot of the S-curve for a rate ½ turbo code from [10], which employs the component code from Fig. 2.10 (c) and an $S$-rand interleaver ($S$ = 22) for a message block length of 2,000 bits; (b) An illustration of the codeword space used to provide intuition for equation (5.20).**

we approximate $\mathbf{A}_n(j,j)$ by its mean $M_A$ in uncorrelated and correlated fading scenarios (given by (3.21) and (3.25)). Thus, the evaluation of the lower bound on coded MIMO system performance reduces to the analysis of a turbo-coded system using QPSK modulation on a Gaussian noise channel.

The BER performance bound on the coded MIMO system at the data sink can be expressed as

$$BER(\sigma) = \int_0^\infty f(L)p_\sigma(L)\mathrm{d}L, \tag{5.20}$$

where $p_\sigma(L)\mathrm{d}L$ is the probability that the magnitude of the noise vector has value within $(L, L+\mathrm{d}L)$ and the function $f(L)$ represents the fraction of erroneously decoded message bits when the magnitude of the noise vector is $L$. We call the function $f(L)$ as the S-curve of the turbo code because it is a property of the code (encoder / decoder) and its plot in linear scale is similar to a sigmoid function. Fig. 5.7 (a) illustrates as an example, the S-curve for the rate ½ turbo code from [10], which employs the component code from Fig. 2.10 (c) and an S-rand interleaver ($S = 22$) for a message block length of 2,000 bits.

The function $p_\sigma(L)$ is the density function corresponding to the norm of a complex Gaussian noise vector with $N_c/2$ elements (where $N_c$ is the length of the codeword and the factor of ½ is due to the use of QPSK signalling). Thus, $p_\sigma(L)$

is a *chi* density function with $N_c$ (due to the real and imaginary dimensions) degrees of freedom [103] and is given by

$$p_\sigma(L) = \frac{L^{N_c-1}\,\mathrm{e}^{-L^2M_A^2/2\sigma^2}}{2^{(N_c-2)/2}\left(\sigma^2/M_A^2\right)^{N_c/2}\Gamma\left(N_c/2\right)}. \tag{5.21}$$

The evaluation of the bit error rate in (5.20) (using Riemann sums) is dependent on knowing $f(L)$ for a particular turbo code.

Fig. 5.7 (b) provides the intuition behind the BER decomposition in (5.20). Consider codewords with QPSK symbol mapping in $\mathbb{C}^{N_c/2}$ space. The noise vector, which lies on a sphere of radius $L$, is added to a particular codeword, $\mathbf{c}_0$. (The probability of the noise vector being within ($L$, $L$ + d$L$) is given by $p_\sigma(L)\mathrm{d}L$.) Assuming the turbo decoder can be approximated by the maximum likelihood decoder in the low noise region, then no errors are made by the iterative decoder when $L < d_{\min}/2$, and hence $f\left(d_{\min}/2\right) = 0$. As the magnitude of the noise vector $L$ increases, the iterative decoder can associate the noise corrupted codeword $\mathbf{c}_0$ with one of many possible codewords, which results in $f(L)$ increasing up to a maximum value of ½. Thus, $f(L)$ encapsulates the positions of the codeword vectors, while $p_\sigma(L)$ captures the noise characteristics.

We can approximate $f(L)$ through an interpolation of sample points (or values of $L$). A few message frames (e.g., less than 200) are turbo encoded and the subsequent coded bits are mapped to QPSK symbols. These symbols are corrupted by noise $\upsilon$ that is uniformly distributed on a sphere of radius $L$, centered at the coordinate origin in $N_c/2$-dimensional complex space. Such noise can be generated as

$$\upsilon = \sqrt{L}\frac{\zeta}{\|\zeta\|}, \tag{5.22}$$

where the elements of $\zeta$ are i.i.d. and are realizations of a zero mean complex Gaussian random variable with unit variance in the real and imaginary dimensions [54], [103]. Soft decisions are generated from the noise corrupted QPSK symbols using a standard deviation of 0.4 and the corresponding Gaussian density function. (The standard deviation is used to determine soft decisions and the S-curve method is not very sensitive to variations in its value.) These are subsequently de-mapped and turbo-decoded. The S-curve $f(L)$ can be interpolated between sample points using sigmoid functions [103]

$$g(x) = \gamma\left(1 + e^{-(x-x_0)/w}\right)^{-1}, \tag{5.23}$$

where $x_0$ is the point at which the sigmoid function is centered, $w$ and $\gamma$ are the width and final values of this function, respectively.

An analogous lower bound on turbo-coded MIMO system performance can be computed in the multi-user scenario, i.e., by assuming the co-antenna and multi-user interference has been perfectly cancelled at the output of the detector. In this case, the channel observation on the modulation symbol from the $j$-th antenna of the first user is modified from (3.15) to be

$$\hat{\mathbf{y}}_{n,1}(j) = \mathbf{A}_{n,1}(j,j)\mathbf{b}_{n,1}(j) + \hat{\mathbf{v}}_{n,1}(j), \tag{5.24}$$

which is equivalent to (5.18) for the single user scenario and thus we can apply a similar methodology. Numerical results demonstrating the accuracy of the performance bounds using the S-curve method for the single and multi-user scenarios are provided in the following section.

### 5.3.2 Numerical and Simulation Results

We consider the coded MIMO system with iterative processing in uncorrelated and correlated fading channels for single and multi-user scenarios. A rate ½ turbo code is used, which employs the two-bit-in-one-bit-out component encoder discussed in [10] and shown in Fig. 2.10 (c), with a message block length of 2,000 or 32,000 bits. The turbo code uses a $S$-rand interleaver from [41], where $S = 22$ and 80 for the smaller and larger message block length, respectively. The coded bits are mapped to QPSK symbols (using the mapping described in Fig. 4.15) and transmitted over a slow frequency non-selective Rayleigh fading channel.

Fig. 5.8 (a) and (b) illustrate the sample points and interpolation of the S-curve $f(L)$ for a message block length of 2,000 and 32,000 bits, respectively. The first five of seven points require simulations of less than 50 message packets. Only the last two points need simulations of 100 and 200 message packets. The evaluation of the sample points of the S-curve requires about two hours on a PIII 900 MHz computer. The $f(L)$ curve consists of three different regions. Region 1 corresponds to large values of $L$ and can be approximated by a straight line from 0.5 to 0.2. Region 2 corresponds to error values between 0.2 to 0.01, where the location of the bend in the curve is determined by the characteristics of the code (e.g., interleaver length in the overall coded system). Finally, region 3 corresponds to a rapid decay from 0.01 to 0 (which occurs at approximately $d_{\min}/2$). The last region is especially sensitive to interpolation and determines the slope of the BER curve at high SNR values.

The comparison of simulated results and the corresponding approximately evaluated bounds using the S-curve method is shown for $N_m$ = 2,000 bits for (2, 10), (4, 20) antenna configurations in Fig. 5.9. Similarly, Fig. 5.10 illustrates the

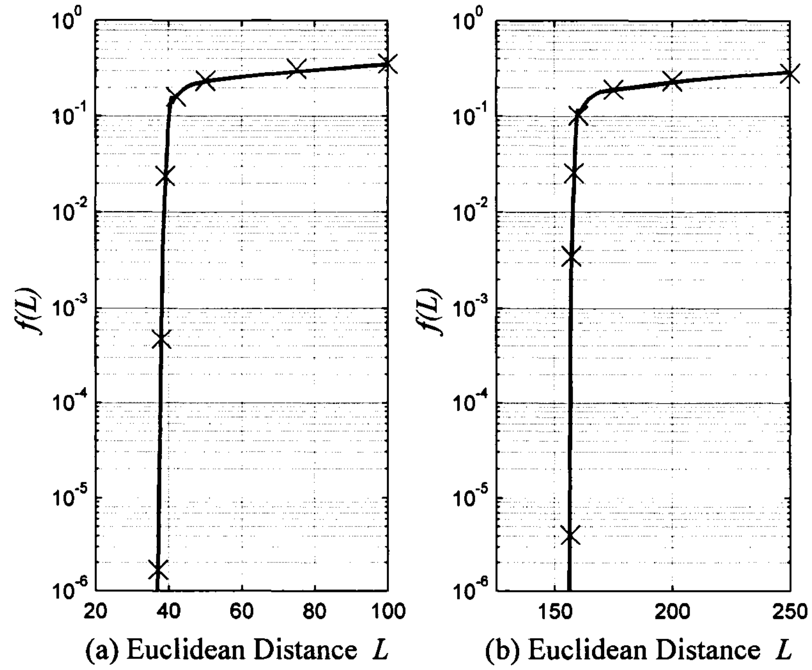

**Fig. 5.8. Sample points and corresponding interpolation of the S-curve for the rate ½ turbo code from [10] with S-rand interleaving and a message block length of (a) 2,000 bits; (b) 32,000 bits.**

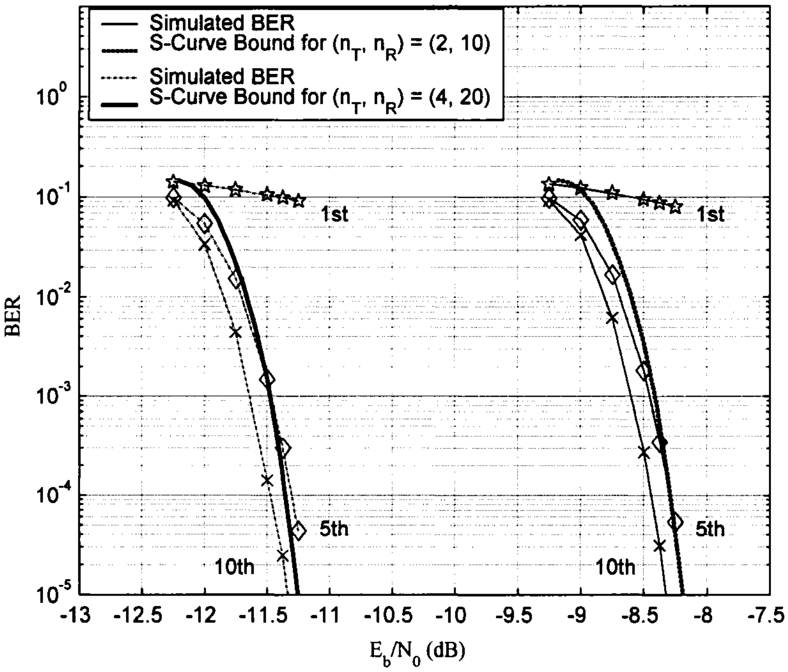

**Fig. 5.9. Comparison of simulated BER performance and the corresponding approximately evaluated bounds for a message block length of 2,000 bits and $(n_T, n_R)$ = (2, 10) and (4, 20) antenna configurations.**

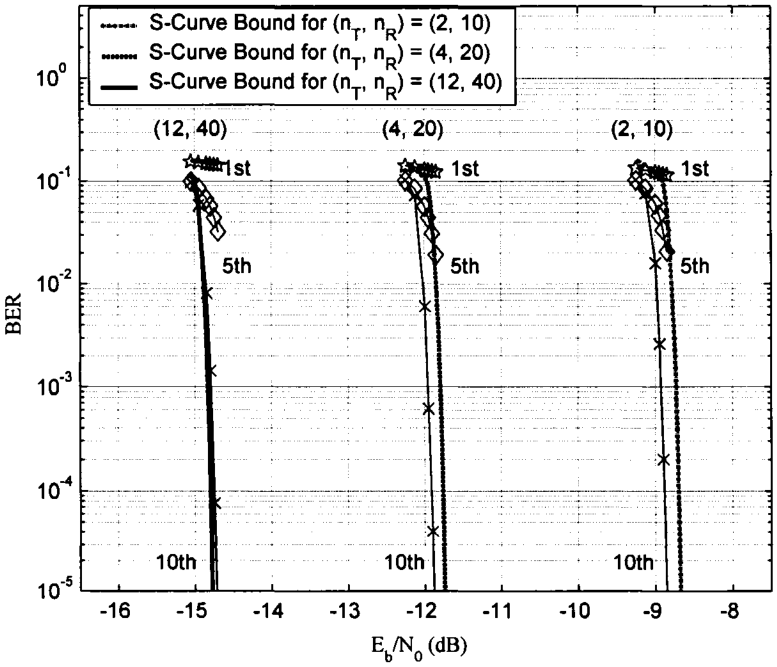

**Fig. 5.10. Comparison of simulated BER performance and the corresponding approximately evaluated bounds for a message block length of 32,000 bits and $(n_T, n_R)$ = (2, 10), (4, 20) and (12, 40) antenna configurations.**

comparison for $N_m$ = 32,000 bits for (2, 10), (4, 20) and (12, 40) antenna configurations. The bounds are evaluated using the interpolated S-curve (from Fig. 5.8 (a) and Fig. 5.8 (b) for $N_m$ = 2,000 and 32,000 bits respectively) and are within 0.2 dB of the simulated performance after ten iterations. The accuracy of the bound is maintained despite the increase in message block length, thus illustrating that the S-curve can capture the properties of the turbo code for different interleaver lengths.

The setup for the multi-user scenario is similar to the single user case, however, we use a pseudorandom interleaver (message block size $N_m$ = 2,000 bits) in the turbo code and spreading sequences (of length 7) in addition to QPSK symbol mapping. Furthermore, we assume $K = 5$ users and perfect power control is employed. Fig. 5.11 (a) illustrates the sample points of the S-curve for the rate 1/2 turbo code (with QPSK symbol mapping and no spreading) and its corresponding interpolation. The *chi* density function of (5.21) is illustrated in

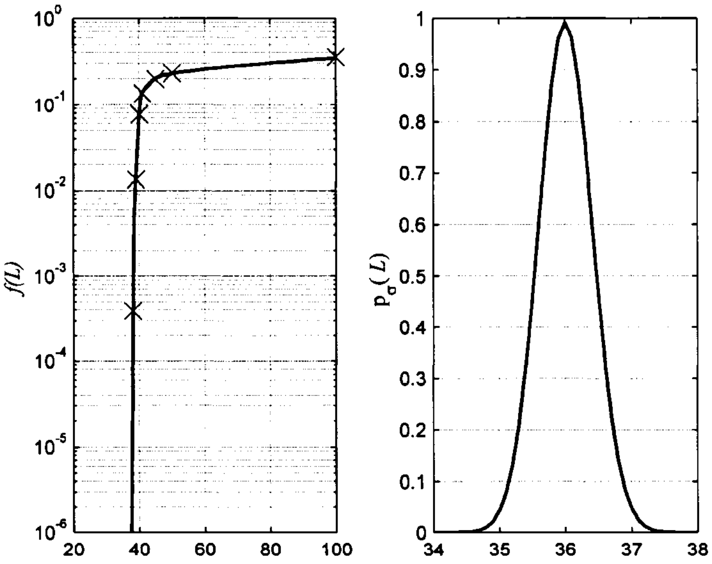

(a) Euclidean Distance $L$ (b) Euclidean Distance $L$

**Fig. 5.11. (a) Sample points and corresponding interpolation of the S-curve for the rate ½ turbo code from [10] with pseudorandom interleaving and message block length of 2,000 bits; (b) *chi* density function $p_\sigma(L)$ for $\sigma^2 = 3.15$, $(n_T, n_R) = (2,10)$ and uncorrelated fading.**

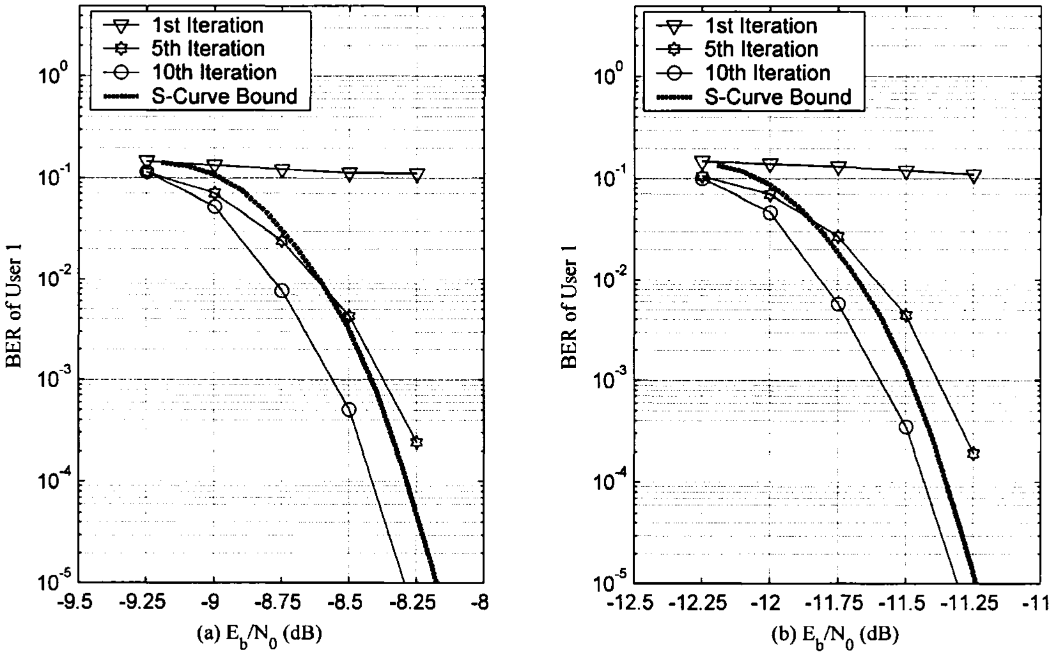

**Fig. 5.12. Performance comparison of a five-user turbo coded system with approximately evaluated bounds for (a) (2, 10) and (b) (4, 20) antenna configurations for an uncorrelated Rayleigh fading channel with perfect power control.**

Fig. 5.11 (b) for the case of $(n_T, n_R) = (2,\ 10)$, $N_c = 4008$ degrees of freedom and noise variance $\sigma^2 = 3.15$ (which corresponds to $E_b/N_0$ of - 8 dB).

In Fig. 5.12, the bound calculated using the S-curve method is compared to the simulated performance of user 1 in an uncorrelated Rayleigh fading channel with $(n_T, n_R) = (2,\ 10)$ and (4, 20) antenna configurations. The difference between the simulated performance after ten iterations (reproduced from Fig. 4.16 and Fig. 4.17 (a)) and the corresponding approximately evaluated bounds are within about 0.15 dB. Fig. 5.13 (a) illustrates the comparison between the bound and the simulated performance of user 1 (reproduced from Fig. 4.18 (a)) with $(n_T, n_R) = (8,\ 40)$ antennas in uncorrelated fading. The gap between the bound and simulated performance is within about 0.1 dB. Fig. 5.13 (b) illustrates the comparison for the same system on a correlated fading channel (reproduced from Fig. 4.18 (b), angular spread $\beta = 10$ degrees and antenna spacing of $\lambda$). In this

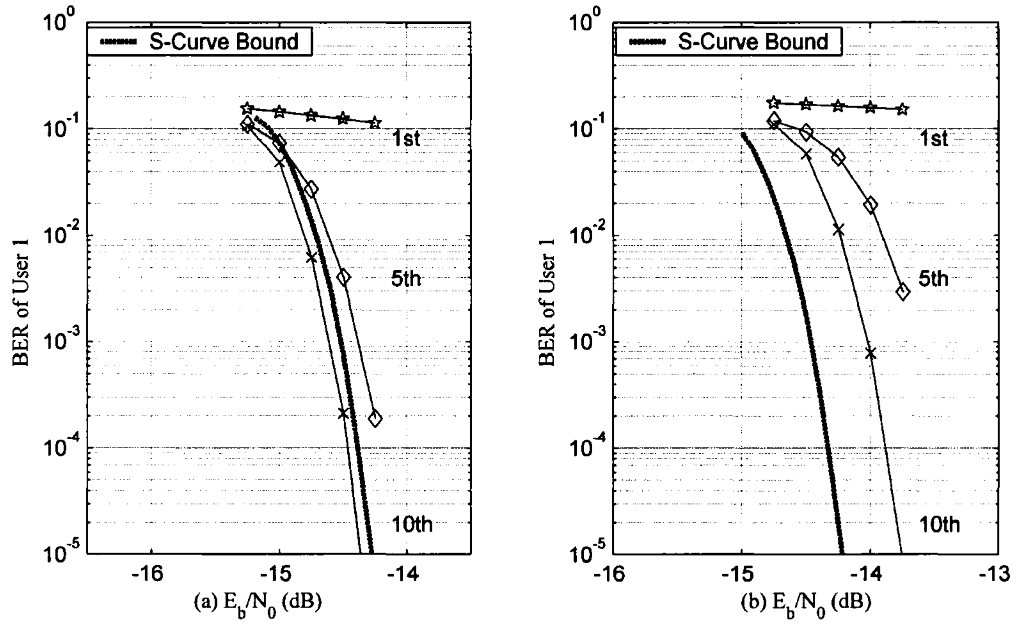

**Fig. 5.13. Performance comparison of a five-user turbo coded system with approximately evaluated bounds for (8, 40) antenna configuration with perfect power control for an (a) uncorrelated Rayleigh fading channel and (b) correlated Rayleigh fading channel.**

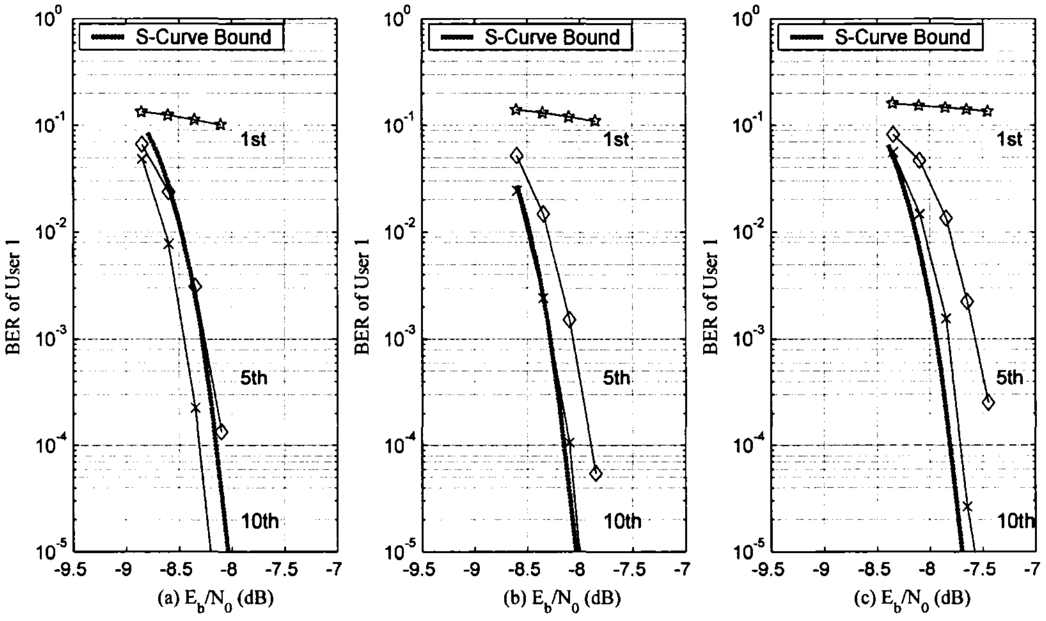

**Fig. 5.14. Comparison of the simulated performance in a five-user turbo coded system with $(n_T, n_R) = (2,10)$ antennas to the approximately evaluated bounds for:**

**(a) $\beta = 7$ degrees and $2\lambda$ antenna spacing**

**(b) $\beta = 10$ degrees and $\lambda$ antenna spacing**

**(c) $\beta = 12$ degrees and $\lambda/2$ antenna spacing.**

case, there is a 0.5 dB difference between the approximately evaluated bound and the simulated performance.

We consider the sensitivity of the proposed S-curve method to different correlation scenarios. As in Section 4.4.3, we focus on the $(n_T, n_R)$ = (2, 10) system and consider three different correlation situations: $\beta$ = 7, 10 and 12 degrees with corresponding $\lambda/2$, $\lambda$ and $2\lambda$ antenna spacing. Fig. 5.14 illustrates the performance of the proposed system for the three scenarios (reproduced from Fig. 4.19) and the corresponding approximately evaluated bounds. The calculated bounds are within 0.15 dB of the simulated results for the low to moderate levels of correlation ($\beta = 10^\circ$ and $\beta = 12^\circ$) and for high level of correlation ($\beta = 7^\circ$) the difference is 0.3 dB.

### 5.3.3 Discussion on the Results of the S-curve Method

We emphasize that there are no exact BER performance evaluation techniques for turbo coded and iteratively decoded MIMO (or even SISO) systems in the literature. The union bound based method for turbo codes [8] uses two approximations. The definition of the uniform interleaver permits an analytical approximation of the simulated performance in the error floor region. However, a turbo code using a particular interleaver can perform better or worse than this approximation. Furthermore, the approximate BER curves are determined assuming the use of the maximum likelihood decoder, when in practice a sub-optimal iterative decoder is employed. Meanwhile, the EXIT chart technique [16] assumes that the extrinsic information on message bits is uncorrelated, however, this approximation is only valid for very large interleaver lengths and the method often fails for intermediate message block lengths (e.g., 1,000 bits). Thus, only for large message block lengths, the EXIT chart technique accurately approximates the decoding trajectory and provides a good SNR estimate for the start of the waterfall region. As a final note, extensions of both the union bound based method and EXIT charts to MIMO fading channels have resulted in bounds, which are loose by 2 dB [88] or have been only (successfully) applied to fixed MIMO channels [39].

The approximately evaluated lower bounds based on the proposed S-curve method are within about 0.5 dB of the simulated performance in all scenarios considered in the previous section. However, due to the approximations used in the derivation of this method, the bound was sometimes slightly above the simulated performance (after ten iterations). One of three reasons can cause this discrepancy. The random variable $\mathbf{A}_n(j,j)$ in the channel observation output of the detector is approximated by its mean $M_A$. Although the variance of $\mathbf{A}_n(j,j)$ is usually several times smaller than the mean (as observed in Section 3.2.1), the small variation in its values could result in a slight shift of the lower bound. Furthermore, the noise at the output of the detector is correlated across channel observations, while the BER decomposition in (5.20) assumes the noise affecting the QPSK symbols is uncorrelated. Finally, the S-curve of the turbo code $f(L)$ is currently being approximated using sigmoid functions, however analytically determining this function could result in a more accurate lower bound.

## 5.4 Coded Magnetic Recording Systems

### 5.4.1 Background Information

Coding and advanced signal processing in (single-head, single-track) data storage systems are used to achieve significant increases in linear recording density. As a result, turbo codes and iterative (turbo) equalization have been considered for magnetic recording channels in [5], [52], [84], [100]. In most cases, Monte Carlo simulations are used to determine system performance of coded recording systems. In this section, we consider a serially concatenated coded system, where the outer code is a convolutional code and the inner code is a precoded partial response (PR) channel. The proposed S-curve method, developed for wireless MIMO channels is modified to determine the approximate BER of this coded magnetic recording system in the waterfall region.

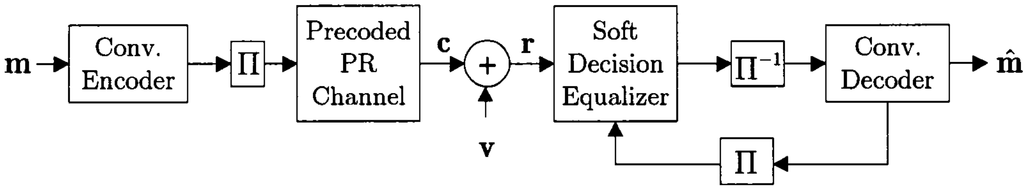

**Fig. 5.15. Schematic block diagram of the considered coded partial response (PR) system.**

### 5.4.2 System Model

Consider a convolutionally coded partial response system depicted in Fig. 5.15. Let vector $\mathbf{c}$ (of length $N_c$) be the output of the precoded PR channel. The "codeword" $\mathbf{c}$ can be expressed as a function of the $N_m$ bit message sequence $\mathbf{m}$

$$\mathbf{c} = g_1(g_2(\mathbf{m})), \tag{5.25}$$

where $g_2$ represents the outer encoder including the interleaver $\Pi$ and $g_1$ represents the precoded PR channel. Recall from Section 2.3.1 that this configuration corresponds to a serially concatenated (turbo) coded system. The sequence $\mathbf{c}$ is corrupted by additive Gaussian noise and the channel output is given by

$$\mathbf{r} = \mathbf{c} + \mathbf{v}, \tag{5.26}$$

where the elements of $\mathbf{v}$ are independent and identically distributed (i.i.d.) zero mean Gaussian random variables with variance $\sigma^2$. The read-back device performs a fixed number of iterations, where extrinsic information on coded bits is exchanged between the soft decision equalizer and the convolutional decoder.

### 5.4.3 Application of the S-curve Method

The bound on BER performance at the output of the convolutional decoder is given by (5.20), where the S-curve $f(L)$ corresponds to the serially concatenated (turbo) code composed of the convolutional encoder and precoded partial response channel. As in the wireless MIMO systems, we approximate the S-curve through sample points (or values of $L$). A few message frames (e.g., less than 300) are convolutionally encoded, interleaved and then 'encoded' using the precoded PR channel. The resulting ISI symbols are corrupted by noise that is uniformly distributed on a sphere of radius $L$, centered at the coordinate origin in $N_c$-

dimensional space. Such noise can be generated as described in [54], [103]. Subsequently, the noise corrupted ISI symbols undergo iterative equalization as shown in Fig. 5.15. (The likelihood calculation on the noise corrupted ISI symbols uses a standard deviation of 0.4.). The S-curve $f(L)$ is then interpolated between sample points using the cubic spline interpolation technique.

### 5.4.4 Determining the Minimum Euclidean Distance

Since we employ the cubic spline interpolation method to approximate the S-curve, we require an additional sample point to accurately approximate $f(L)$. Given that the turbo decoder performs close to the maximum likelihood decoder in the high SNR region [8], we set the fraction of erroneously decoded message bits at $L = d_{\min}/2$ to almost zero, i.e., $f\left(d_{\min}/2\right) = 10^{-300}$. Thus, we need to determine the minimum Euclidean distance $d_{\min}$ of the overall concatenated code. Since the inner encoder (PR4 / EPR4 channel) is a non-linear code, a direct comparison to the all-zero sequence may not necessarily yield $d_{\min}$. Nonetheless, we describe a method to determine $d_{\min}$ for the considered coded magnetic systems.

Consider the state diagram of the precoded PR4 trellis shown in Fig. 5.16 (a) and assume that we start from the zero state. Two ones in the codeword from the outer encoder cause the PR4 trellis to return to the zero state, resulting in a sequence that has the smallest Euclidean distance, $d_{\min} = 2\sqrt{2}$. Given the puncturing pattern of the convolutional code, a message sequence with ones in the 8th and 23rd positions (all other positions are zeros) produces a codeword with Hamming weight of 2.

In addition, we consider the precoded EPR4 channel with state transition diagram shown in Fig. 5.16 (b). The minimum Euclidean distance of this code is $d_{\min} = 4$, which corresponds to an input sequence of [1 0 1 0] with state transitions: 000 → 100 → 010 → 001 → 000. Furthermore, we observe that an odd number of zeros between two ones in the input sequence does not change the

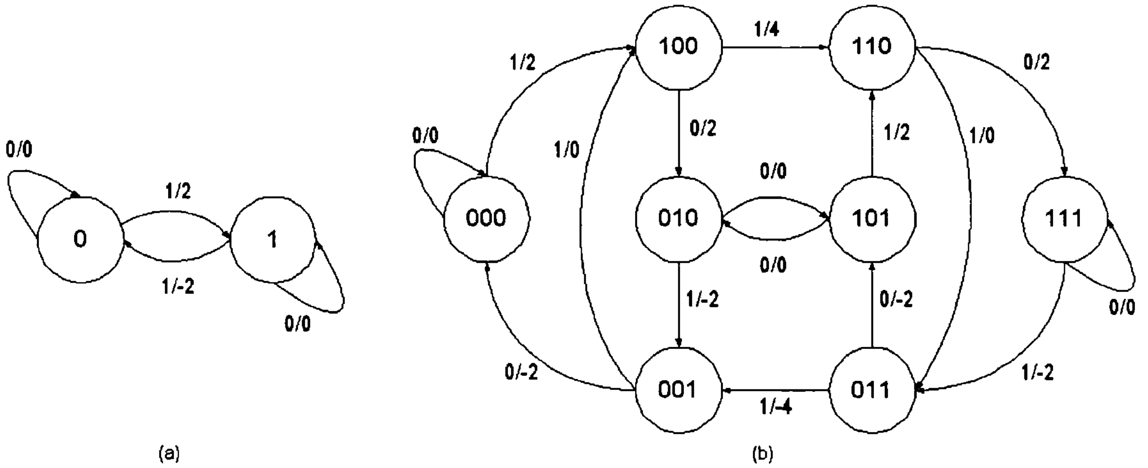

**Fig. 5.16. State diagrams for (a) the precoded PR4 channel; (b) the precoded EPR4 channel.**

minimum Euclidean distance. Hence, the codeword from the outer encoder must have Hamming weight of 2. Using a random interleaver, there exists (with high probability) a message sequence of Hamming weight 2 corresponding to an interleaved codeword (from the outer encoder) of weight 2, where the two ones are separated by an odd number of zeros.

## 5.4.5 Numerical and Simulation Results

We consider a message block length of 4,000 bits and a rate 8/9 outer convolutional code based on puncturing a rate 1/2 recursive systematic convolutional code with feedback and feedforward polynomials given by $1 \oplus D \oplus D^4$ and $1 \oplus D \oplus D^3 \oplus D^4$, respectively. The corresponding trellis for this code is shown in Fig. 5.17. The parity bit streams are punctured so that in consecutive blocks of eight parity bits, we only keep the first ones. The partial response channel under consideration is either the $h_{PR4}(D) = 1 - D^2$ or $h_{EPR4}(D) = (1-D)(1+D)^2$ and the corresponding precoders are $1/(1 \oplus D)$ and $1/\left(1 \oplus D^2\right)$. The SNR is defined as $10\log_{10}\left(\left\|h_{(E)PR4}\right\|^2 / \left(R_c\sigma^2\right)\right)$, where $R_c = 8/9$, $\left\|h_{PR4}\right\|^2 \triangleq 1^2 + 1^2 = 2$ and $\left\|h_{EPR4}\right\|^2 \triangleq 1^2 + 1^2 + 1^2 + 1^2 = 4$. The coded system employs a pseudorandom interleaver and the read-back device performs ten decoding iterations, where the equalizer and the decoder use the BCJR algorithm [4].

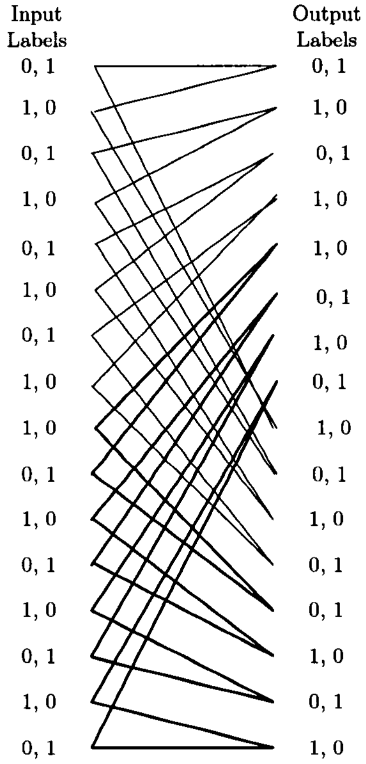

**Fig. 5.17. The trellis diagram of the rate ½ convolutional code, used in the recording systems.**

Fig. 5.18 (a) shows the sample points of the S-curve corresponding to the coded PR4 system. Each sample point of the S-curve is generated by simulating the coded system for a maximum of 300 message frames with noise that is uniformly distributed on an $N_c$ dimensional sphere. (A standard deviation value of $\sigma = 0.4$ is used for soft decision calculations in the evaluation of sample points.) Similarly, Fig. 5.18 (b) shows the sample points of the S-curve $f(L)$ for the coded EPR4 system. The two coded magnetic recording systems have approximately the same S-curve and thus, we expect similar BER performance. The simulated performance for the PR4 and EPR4 channels, after ten iterations, is shown in Fig. 5.19 (a) and (b) respectively. The corresponding approximately evaluated bounds are within about 0.1 dB of the simulated performance in the waterfall region.

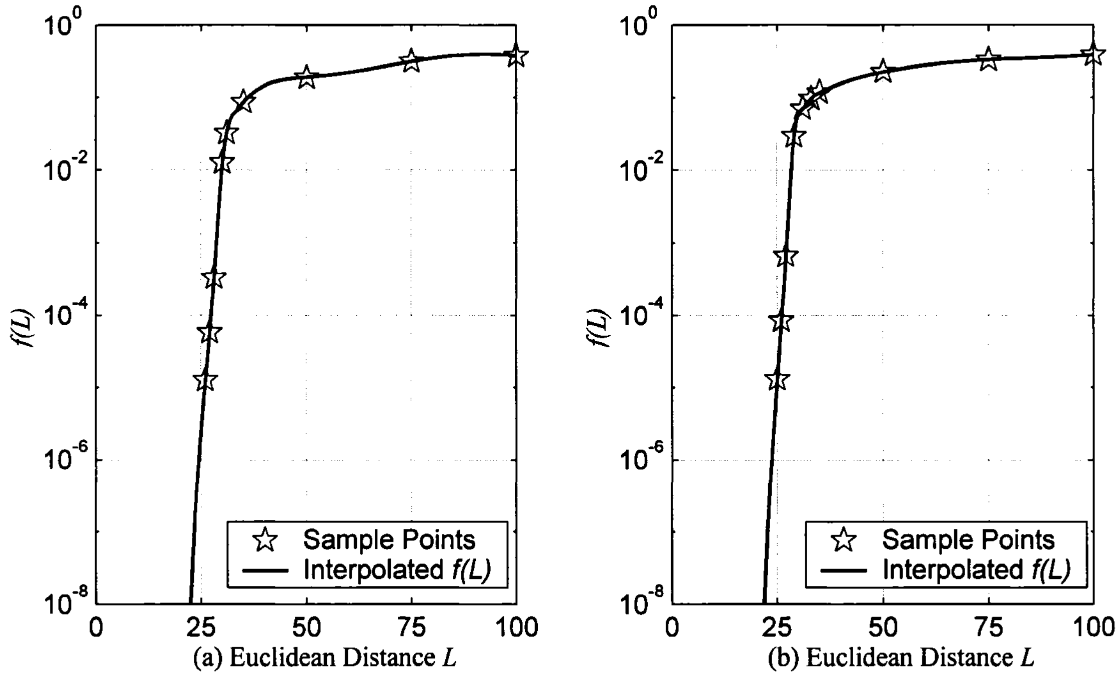

**Fig. 5.18. Interpolation of the S-curve for (a) the PR4 channel; (b) the EPR4 channel.**

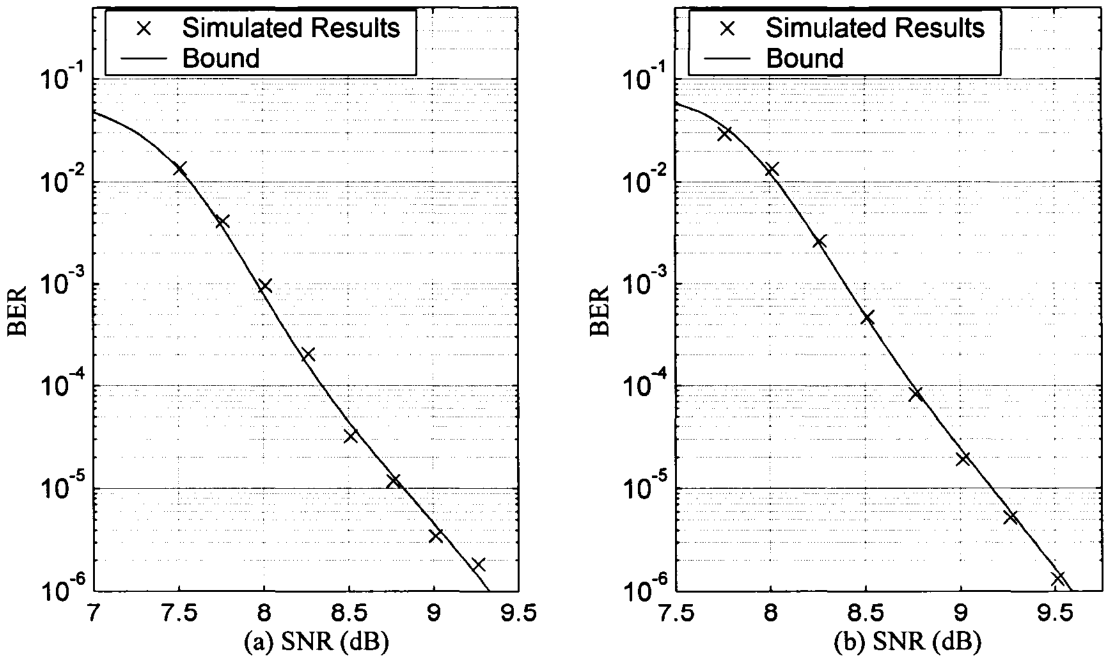

**Fig. 5.19. Comparison of the simulated BER performance and the corresponding approximately evaluated bounds for a rate 8/9 convolutional code after 10 iterations on (a) the PR4 channel; (b) the EPR4 channel.**

## 5.5 Chapter Summary

In Section 5.1, we have provided a motivation for the usefulness of performance analysis techniques and a background on previously proposed methods for turbo-coded MIMO systems. In Section 5.2 we have first described the union bound based result [8] for turbo codes in the AWGN channel setting with the aim of developing BER performance bounds for the considered turbo coded MIMO systems. We have evaluated the performance of both single pass detection and iterative processing at the receiver in uncorrelated and correlated Rayleigh fading channels. In all cases, the bounds on BER performance in the high SNR or error floor region are within 0.5 dB to 0.8 dB of the simulated results.

In Section 5.3, we have developed a new performance analysis technique that approximately evaluates a bound on the proposed coded MIMO system performance in the waterfall region. The new method expresses the bound on BER performance as an integral of the product of two functions. One function uses the properties of the code, while the other function has a closed form expression and encapsulates the noise characteristics. Through comparisons with simulation results, we have observed that the proposed method provides numerical results, which are within 0.2 dB for both uncorrelated and correlated fading channels in single and multi-user scenarios.

Section 5.4 has showed that the second proposed method can also be used to analyze the performance of single head, single track coded magnetic recording channels. As in the wireless MIMO scenario, the BER performance bounds accurately match the simulation results to within 0.1 dB in the waterfall region.

# Chapter 6

# Conclusion

The focus of this dissertation has been turbo-coded uplink transmission over wireless MIMO channels. Its objective has been to exploit the large wireless capacities and potential spectral efficiency increases offered by such channels. This work has been motivated by the use of turbo codes in the 3G (and possibly 4G) wireless standard, where multi-antenna technology has been considered as a means of achieving high data rates required for multimedia applications.

## 6.1 Research Achievements

This dissertation contains several research contributions in the area of coded wireless MIMO systems, which are summarized in the following paragraphs.

Assuming channel state information is only available at the (base-station) receiver, a new front-end MIMO signal detector has been proposed, which is of linear complexity in the number of transmit, receive antennas and the number of users. The detector first produces channel observations on the transmitted symbols and subsequently uses the Gaussian approximation for the co-antenna and multi-user interference to generate soft decisions. In addition, we have derived the symbol error rate expressions for this detector in various scenarios.

Consequently, the proposed signal detector was integrated into a turbo-coded MIMO system with a novel, low complexity iterative receiver. In this receiver, subsequent to turbo decoding, soft decisions on the coded bits were used to update the Gaussian approximation of the transmitted symbols using a symbol-by-symbol, antenna-by-antenna and user-by-user approach in the iterative loop. Due to the decoupled structure of this method, iterative processing complexity increases linearly with the message block length and number of users.

The considered turbo-coded MIMO systems were simulated for currently practical antenna configurations with up to 30 transmit and 120 receive antennas. The achieved coded transmission rates were up to 60 bits per channel use and the proposed MIMO receiver turned out to be robust to the combined effects of spatial correlation and imperfect channel state information. For all considered antenna configurations and a target BER of $10^{-5}$, simulated system performance has been within 1.5 – 1.6 dB of the ergodic capacity limit on an uncorrelated slow frequency non-selective Rayleigh fading channel. Furthermore, the proposed turbo-coded wireless MIMO system outperforms the Turbo-BLAST architecture [80] by 10 dB for the same antenna configurations and transmission rates.

We have also considered certain multi-user scenarios for various antenna configurations in uncorrelated and correlated Rayleigh fading channels. The turbo-coded system was extended to accommodate iterative multi-user MIMO interference cancellation, and the five-user system performance was shown to be within 3.2 dB of the ergodic capacity limit at a BER of $10^{-5}$.

Finally, we have developed two performance analysis techniques that provide accurate bounds on BER performance for the considered turbo-coded MIMO systems. The first technique extends the application of the union bound based method from turbo codes on the AWGN channel [8] to the time-varying MIMO fading channel. The resulting performance bounds were within 0.5 – 0.8 dB of the simulated results in the error floor region. Secondly, we have developed a new performance analysis technique (termed the S-curve method) that expresses the bound on BER performance as an integral of the product of two functions: one that encapsulates the properties of the code and another, which captures the noise characteristics. Numerical results were within 0.1 – 0.5 dB of the simulated performance in the waterfall region for single and multi-user scenarios.

We considered multi-head, multi-track digital magnetic recording systems as an extra application of the developed MIMO signal detector and iterative receiver architecture. The iterative receiver achieved good performance despite strong intertrack and intersymbol interference with up to 20 tracks and 22 heads. Using the S-curve method, analytically approximated BER performance of a single head and single track convolutionally coded magnetic recording system was within 0.1 dB of the simulated results in the waterfall region on traditional PR4 and EPR4 channels.

## 6.2 Directions for Future Work

A number of related topics can be explored as an extension of the presented research on coded wireless MIMO systems, including:

- The wireless MIMO channel can be frequency selective due to delayed signal reflections. In this case, the proposed soft decision MIMO signal detector would need to be either modified for OFDM-based systems or extended to accommodate intersymbol interference for CDMA (or QAM) based systems.
- The coded MIMO systems, presented in this dissertation, were implemented using Matlab on a single PC or on a computing cluster with 17 nodes. One possible direction for future work is to bring the proposed system to real-time operating speeds. This can be accomplished by implementing the detector and iterative receiver on a field programmable gate array.
- The proposed S-curve performance analysis method currently relies on numerically approximating a function that is a property of the turbo code. Future work would be to determine this function analytically through the distance spectrum of the turbo code.

# Appendix A

## A.1 Derivation of the Ergodic MIMO Capacity

We present the derivation of the ergodic MIMO capacity formula developed by Telatar [92] by first considering a fixed channel matrix that is known at the receiver only and then determine the capacity expression for a time varying MIMO channel.

The MIMO channel (which could be spatially correlated) can be decomposed via the singular value decomposition (SVD) $\mathbf{H}_n = \mathbf{U}_n\mathbf{D}_n\mathbf{V}_n^H$, where $(\bullet)^H$ represents the Hermitian operation and $\mathbf{U}_n$, $\mathbf{V}_n$ are unitary matrices, i.e., $\mathbf{U}_n\mathbf{U}_n^H = \mathbf{I}$ and $\mathbf{V}_n\mathbf{V}_n^H = \mathbf{I}$. The matrix $\mathbf{D}_n$ contains the singular values of $\mathbf{H}_n$, which are the square roots of the eigenvalues of $\mathbf{H}_n^H\mathbf{H}_n$. The MIMO channel equation can be written as

$$\mathbf{r}_n = \mathbf{H}_n\mathbf{b}_n + \mathbf{v}_n = \mathbf{U}_n\mathbf{D}_n\mathbf{V}_n^H\mathbf{b}_n + \mathbf{v}_n. \tag{A.1}$$

Since the channel is known at the receiver, we can multiply both sides by $\mathbf{U}_n^H$,

$$\tilde{\mathbf{r}}_n = \mathbf{U}_n^H\mathbf{r}_n = \mathbf{U}_n^H\mathbf{H}_n\mathbf{b}_n + \mathbf{U}_n^H\mathbf{v}_n = \mathbf{D}_n\tilde{\mathbf{b}}_n + \tilde{\mathbf{v}}_n. \tag{A.2}$$

The noise vector $\tilde{\mathbf{v}}_n$ is a rotated version of $\mathbf{v}_n$ and similarly $\tilde{\mathbf{b}}_n$ is a rotated version of $\mathbf{b}_n$. Since $n_R > n_T$, the last $n_R - n_T$ elements of $\tilde{\mathbf{r}}_n$ will not correspond to any elements in $\tilde{\mathbf{b}}_n$. Hence, the scenario with a fixed MIMO channel leads to the case of parallel Gaussian channels and so we can write the capacity expression directly from the formula for the AWGN channel,

$$C = \sum_{j=1}^{n_T} \log_2\left(1 + \frac{(\mathbf{D}_n(j,j))^2 P}{2n_T\sigma^2}\right) = \log_2 \prod_{j=1}^{n_T}\left(1 + \frac{(\mathbf{D}_n(j,j))^2 P}{2n_T\sigma^2}\right), \tag{A.3}$$

where the transmit power $P$ is uniformly distributed on the antennas as channel state information (CSI) is not available at the transmitter. Recall that $(\mathbf{D}_n(j,j))^2$

is the $j$-th eigenvalue of $\mathbf{H}_n^H\mathbf{H}_n$, $j = 1, 2, \ldots, n_T$. The above equation can be written in terms of matrices using the following identity[3] $\det(\mathbf{I}+\mathbf{M}) = \det(\mathbf{I}+\mathbf{V}\boldsymbol{\Lambda}\mathbf{V}^{-1}) = \det(\mathbf{V})\det(\mathbf{I}+\boldsymbol{\Lambda})\det(\mathbf{V}^{-1}) = \det(\mathbf{I}+\boldsymbol{\Lambda}) = \prod_j(1+\boldsymbol{\Lambda}(j,j))$

$$C = \log_2 \prod_{j=1}^{n_T}\left(1+\frac{(\mathbf{D}_n(j,j))^2 P}{2n_T\sigma^2}\right) = \log_2\left(\det\left(\mathbf{I}+\frac{P}{2n_T\sigma^2}\mathbf{H}_n^H\mathbf{H}_n\right)\right). \tag{A.4}$$

Now we consider a time varying channel, where the receiver is assumed to have perfect channel state information. Furthermore, the channel is assumed to be memoryless. We can express the corresponding mutual information at the receiver as

$$\begin{aligned} I(\mathbf{b}_n;(\mathbf{r}_n,\mathbf{H}_n)) &= I(\mathbf{b}_n;\mathbf{H}_n)+I(\mathbf{b}_n;\mathbf{r}_n|\mathbf{H}_n) \\ &= I(\mathbf{b}_n;\mathbf{r}_n|\mathbf{H}_n) \\ &= E\left[I(\mathbf{b}_n;\mathbf{r}_n|\mathbf{H}_n=\mathbf{H}_0)\right], \end{aligned} \tag{A.5}$$

where $\mathbf{H}_0$ is a particular channel realization, $E[\bullet]$ is the expectation over $\mathbf{H}_n$ and in the second line, we used the fact $\mathbf{b}_n$ and $\mathbf{H}_n$ are independent and hence, their mutual information $I(\mathbf{b}_n;\mathbf{H}_n)$ is zero. Hence, the mutual information $I(\mathbf{b}_n;(\mathbf{r}_n,\mathbf{H}_n))$ needs to be averaged over all channel realizations. When CSI is only available at the receiver, $I(\mathbf{b}_n;(\mathbf{r}_n,\mathbf{H}_n))$ is maximized if $\mathbf{b}_n$ is a complex Gaussian random vector with covariance matrix $\mathbf{I}$ [92]. Thus, the ergodic capacity of a slow frequency non-selective Rayleigh fading channel with channel state information available at the receiver only is given by

$$C_{MIMO} = E\left[\log_2\left(\det\left(\mathbf{I}+\frac{P}{2n_T\sigma^2}\mathbf{H}_n^H\mathbf{H}_n\right)\right)\right]. \tag{A.6}$$

## A.2 Ergodic Capacity for Traditional Diversity Systems

We assume that channel state information is available at the receiver only. As in

---

[3] The eigenvalue decomposition of $\mathbf{M}$ is given by $\mathbf{V}\boldsymbol{\Lambda}\mathbf{V}^{-1}$, where the eigenvectors of $\mathbf{M}$ are the columns of the matrix $\mathbf{V}$ and the eigenvalues of $\mathbf{M}$ are the diagonal elements of the diagonal matrix $\boldsymbol{\Lambda}$ [34].

the previous section, we first consider a fixed channel and then extend the result to the time varying case. The same symbol is transmitted from all antennas and the power constraint on the transmitter is still $P$. The received vector is given by

$$\mathbf{r}_n = \mathbf{H}_n \mathbf{b}_n + \mathbf{v}_n, \tag{A.7}$$

where $\mathbf{b}_n = [b_n, b_n, \ldots b_n]^T$ and $b_n$ is the $n$-th transmitted symbol. Let the channel matrix be fixed and the $i$-th row of $\mathbf{H}_n$ has the largest norm, for some $i \in \{1, 2, \ldots, n_R\}$. Thus, the $i$-th receive antenna is selected, resulting in the following equivalent channel,

$$\mathbf{r}_n(i) = \sum_{j=1}^{n_T} \mathbf{H}_n(i,j) b_n + \mathbf{v}_n(i). \tag{A.8}$$

The capacity of this fixed channel is equivalent to the capacity of an additive white Gaussian noise channel with a scaled amplitude, i.e.,

$$C_{AS}^{\text{Fixed}} = \log_2\left(1 + \frac{P}{2n_T\sigma^2}\left\|\sum_{j=1}^{n_T} \mathbf{H}_n(i,j)\right\|^2\right), \tag{A.9}$$

where the power of $b_n$ is $P/n_T$ and the variance of the noise $\mathbf{v}_n(i)$ is $\sigma^2$ in the real and imaginary dimensions. For the case of a time-varying channel, the elements of $\mathbf{H}_n$ are i.i.d. and are realizations of a zero mean complex Gaussian random variable with variance ½ in the real and imaginary dimensions. We further assume the channel changes with each transmission to a new independent realization. The capacity of this channel is given by the expectation of the capacity expression in (A.9),

$$C_{AS} = E\left[\log_2\left(1 + \frac{P}{2n_T\sigma^2}\left\|\sum_{j=1}^{n_T} \mathbf{H}_n(i,j)\right\|^2\right)\right]. \tag{A.10}$$

As in the antenna selection case, we first evaluate the capacity of a EGC system for a fixed channel and then consider a time-varying channel. The elements of the received vector for a fixed channel is given by

$$\mathbf{r}_n(i) = \sum_{j=1}^{n_T} \mathbf{H}_n(i,j) b_n + \mathbf{v}_n(i), \ i = 1, 2, \ldots, n_R. \tag{A.11}$$

We define $\xi_n(i) = \sum_{j=1}^{n_T} \mathbf{H}_n(i,j)$, and filter the received vector in (A.11) by $\psi_n =$

$\left[\xi_n(1)/\|\xi_n(1)\|, \xi_n(2)/\|\xi_n(2)\|, \ldots, \xi_n(n_R)/\|\xi_n(n_R)\|\right]^T$, which results in

$$\psi_n^H \mathbf{r}_n = \bar{r}_n = \sum_{i=1}^{n_R} \|\xi_n(i)\| b_n + \bar{v}_n, \tag{A.12}$$

where $\bar{v}_n = \psi_n^H \mathbf{v}_n$ is a zero mean complex Gaussian random variable with variance $\sigma^2 \sum_{i=1}^{n_R} \|\xi_n(i)\|$ in the real and imaginary dimensions. The capacity of the channel in (A.12) can be expressed in terms of the AWGN channel capacity,

$$C_{EGC}^{\text{Fixed}} = \log_2\left(1 + \frac{P}{2n_T\sigma^2} \sum_{i=1}^{n_R} \|\xi_n(i)\|\right). \tag{A.13}$$

For the case of a time-varying channel, we assume the same channel setup as in the antenna selection case (i.i.d. Rayleigh fading, memoryless channel). The capacity of this channel is given by the expectation of the capacity expression in (A.13),

$$C_{EGC} = E\left[\log_2\left(1 + \frac{P}{2n_T\sigma^2} \sum_{i=1}^{n_R} \|\xi_n(i)\|\right)\right], \tag{A.14}$$

where the expectation is with respect to the channel matrix and $\xi_n(i) = \sum_{j=1}^{n_T} \mathbf{H}_n(i,j)$.

In the MRC case, the received vector is filtered by a vector $\psi_n$, which maximizes the post-combining SNR [93]. Assuming a fixed channel, the result of filtering the received vector given in (A.7) by $\psi_n$ is given by

$$\psi_n^H \mathbf{r}_n = \bar{\bar{r}}_n = \sum_{i=1}^{n_R} \psi_n^*(i)\xi_n(i) b_n + \sum_{i=1}^{n_R} \psi_n^*(i)\mathbf{v}_n(i), \tag{A.15}$$

where $(\bullet)^*$ denotes the complex conjugate operation and $\xi_n(i) = \sum_{j=1}^{n_T} \mathbf{H}_n(i,j)$, $i =$ 1, 2, …, $n_R$. The post combining SNR at the receiver is defined as [93]

$$SNR_{\text{received}} = \frac{P \sum_{i=1}^{n_R} \left|\psi_n^*(i)\xi_n(i)\right|^2}{2\sigma^2 \sum_{i=1}^{n_R} \left|\psi_n^*(i)\right|^2}. \tag{A.16}$$

The $SNR_{\text{received}}$ is maximized by applying the Cauchy-Schwartz inequality, which results in $\psi_n = \left[\xi_n(1), \xi_n(2), \ldots, \xi_n(n_R)\right]^T$. Thus, unlike the EGC technique, the received observations, which are least reliable, (corresponding to the smallest row norm in $\mathbf{H}_n$) have a smaller contribution to the channel observation $\bar{r}_n$ on the transmitted symbol $b_n$. Substituting in (A.15), we have

$$\bar{\bar{r}}_n = \sum_{i=1}^{n_R} \left\| \xi_n(i) \right\|^2 b_n + \bar{\bar{v}}_n, \tag{A.17}$$

where $\bar{\bar{v}}_n = \psi^H \mathbf{v}_n$ is a zero mean complex Gaussian random variable with variance $\sigma^2 \sum_{i=1}^{n_R} \left\| \xi_n(i) \right\|^2$ in the real and imaginary dimensions. Thus, the capacity of a fixed channel using the MRC technique is given by

$$C_{MRC}^{\text{Fixed}} = \log_2\left(1 + \frac{P}{2n_T\sigma^2} \sum_{i=1}^{n_R} \left\| \xi_n(i) \right\|^2\right). \tag{A.18}$$

For the case of a time-varying channel, we assume the same channel setup as in the antenna selection case (i.i.d. Rayleigh fading, memoryless channel). The capacity of this channel is given by the expectation of the capacity expression in (A.18),

$$C_{MRC} = E\left[\log_2\left(1 + \frac{P}{2n_T\sigma^2} \sum_{i=1}^{n_R} \left\| \xi_n(i) \right\|^2\right)\right]. \tag{A.19}$$

where the expectation is with respect to the channel matrix and $\xi_n(i) = \sum_{j=1}^{n_T} \mathbf{H}_n(i,j)$.

## A.3 Ergodic MIMO Capacity for Imperfect CSI Scenarios

Yoo and Goldsmith derived the expression for the ergodic MIMO capacity in case of imperfect channel state information at the receiver only [106]. Here, we provide an alternate (and simpler) method to determine the same expression. When the channel is not perfectly estimated at the receiver, recall from (2.6) that the channel matrix can be expressed as $\mathbf{H}_n = \hat{\mathbf{H}}_n + \varepsilon_n$. Substituting this expression into (A.1) and performing the SVD on $\hat{\mathbf{H}}_n$, we have

$$\mathbf{r}_n = \hat{\mathbf{U}}_n \hat{\mathbf{D}}_n \hat{\mathbf{V}}_n^H \mathbf{b}_n + \varepsilon_n \mathbf{b}_n + \mathbf{v}_n. \tag{A.20}$$

We initially assume the estimated channel matrix $\hat{\mathbf{H}}_n$ is known at the transmitter but the random channel matrix $\varepsilon_n$ is not. Therefore, multiplying throughout by $\hat{\mathbf{U}}_n^H$, we have

$$\tilde{\mathbf{r}}_n = \hat{\mathbf{D}}_n \tilde{\mathbf{b}}_n + \hat{\mathbf{U}}_n^H \varepsilon_n \tilde{\mathbf{b}}_n + \hat{\mathbf{v}}_n . \tag{A.21}$$

In the following, we approximate the sum of the random vectors $\hat{\mathbf{U}}_n^H \varepsilon_n \tilde{\mathbf{b}}_n$ and $\hat{\mathbf{v}}_n$ by a zero mean Gaussian random vector with i.i.d. elements. The covariance matrix of $\hat{\mathbf{v}}_n$ is $\sigma^2 \mathbf{I}$ in the real and imaginary dimensions. The covariance matrix of $\hat{\mathbf{U}}_n^H \varepsilon_n \tilde{\mathbf{b}}_n$ is given by

$$\begin{aligned} E\left[\hat{\mathbf{U}}_n^H \varepsilon_n \tilde{\mathbf{b}}_n \tilde{\mathbf{b}}_n^H \varepsilon_n^H \hat{\mathbf{U}}_n\right] &= \hat{\mathbf{U}}_n^H E\left[\varepsilon_n \tilde{\mathbf{b}}_n \tilde{\mathbf{b}}_n^H \varepsilon_n^H\right] \hat{\mathbf{U}}_n \\ &= P \hat{\mathbf{U}}_n^H E\left[\frac{\varepsilon_n \varepsilon_n^H}{n_T}\right] \hat{\mathbf{U}}_n \\ &= P \sigma_\varepsilon^2 \mathbf{I}, \end{aligned} \tag{A.22}$$

where we used $E\left[\varepsilon_n \tilde{\mathbf{b}}_n \tilde{\mathbf{b}}_n^H \varepsilon_n^H\right] = E\left[E\left[\varepsilon_n \tilde{\mathbf{b}}_n \tilde{\mathbf{b}}_n^H \varepsilon_n^H \middle| \varepsilon_n\right]\right]$, $E\left[\varepsilon_n \tilde{\mathbf{b}}_n \tilde{\mathbf{b}}_n^H \varepsilon_n^H \middle| \varepsilon_n\right] = P/n_T$ and $E\left[\varepsilon_n \varepsilon_n^H\right] = n_T \sigma_\varepsilon^2$. Hence, the variance of the elements of the Gaussian approximation is $\sigma^2 + P\sigma_\varepsilon^2/2$ in the real and imaginary dimensions. Equation (A.21) implies parallel Gaussian channels and thus the capacity formula (assuming the power is uniformly distributed on all transmit antennas) can be expressed as

$$\hat{C} = \sum_{j=1}^{n_T} \log_2 \left(1 + \frac{\left(\hat{\mathbf{D}}_n(j,j)\right)^2 P}{n_T \left(2\sigma^2 + P\sigma_\varepsilon^2\right)}\right). \tag{A.23}$$

Applying a similar methodology as in the Section A.1, the ergodic MIMO capacity with imperfect CSI at the receiver (and no CSI at the transmitter) can be expressed as

$$\hat{C} = E\left[\log_2\left(\det\left(\mathbf{I} + \frac{P}{n_T\left(2\sigma^2 + \sigma_\varepsilon^2 P\right)} \hat{\mathbf{H}}_n^H \hat{\mathbf{H}}_n\right)\right)\right], \tag{A.24}$$

or equivalently

$$\hat{C} = E\left[\log_2\left(\det\left(\mathbf{I} + \frac{P}{2 n_T \sigma^2} \hat{\mathbf{H}}_n^H \hat{\mathbf{H}}_n \frac{2\sigma^2}{2\sigma^2 + \sigma_\varepsilon^2 P}\right)\right)\right]. \tag{A.25}$$

# Appendix B

In this appendix, for completeness, we restate the proofs of Theorems 4.7.1 and 4.7.2 in [85], which are used in the evaluation of the union bound in Section 5.2.1.

*Theorem 4.7.1 in* [85]: The $(u, v)$-th entry of $\mathbf{X}^l$ is equal to $B_{u,v}(l)$, and $\mathbf{X}^0 = \mathbf{I}$, where $\mathbf{X}$ is the state transition matrix.

*Proof of Theorem 4.7.1 in* [85]*:*

Recall that $B_{u,v}(l)$ is the sum of the weights of all walks of length $l$ in the state transition diagram. A walk of zero length implies that $B_{u,v}(0) = 1$ if states $s$ and $t$ are the same and zero otherwise. Similarly a walk corresponding to $l = 1$ results in $B_{u,v}(l)$ being equal to the $(s, t)$-th entry in the state transition matrix $\mathbf{X}$. We can extend this result to any arbitrary $l$ by considering the definition of matrix multiplication, i.e.,

$$\mathbf{X}^l(u,v) = \sum \mathbf{X}(u,i_1)\mathbf{X}(i_1,i_2)\cdots\mathbf{X}(i_{l-1},v) \tag{B.1}$$

where the sum is over all sequences $(i_1, i_2, \ldots, i_{l-1})$, $i_j$ is one of four possible states (considering the state diagram from Fig. 5.1), $j = 1, 2, \ldots, l - 1$. The summand is equal to zero unless there is a walk from state $u$ to $v$. If such a walk exists, then the summand is equal to the sum of the weights of all such walks.

*Theorem 4.7.2 in* [85]*:* We define the generating function as $F_{u,v} = \sum_{l\geq 0} B_{u,v}(l)$ and it can be expressed as

$$F_{u,v} = \frac{(-1)^{s+t}\det(\mathbf{I} - \mathbf{X} : v, u)}{\det(\mathbf{I} - \mathbf{X})} \tag{B.2}$$

where the notation $(\mathbf{C} : t, s)$ denotes the matrix obtained by removing the $v$-th row and the $u$-th column of $\mathbf{C}$.

*Proof of Theorem 4.7.2 in* [85]*:*

Using the result of Theorem 1, $F_{u,v}$ is the $(u,\ v)$-th entry of the matrix $\sum_{l\geq 0}\mathbf{X}^{l}$. The sum of this infinite geometric series is given by $(\mathbf{I}-\mathbf{X})^{-1}$ (as $\mathbf{X}$ is a positive definite matrix). If $\mathbf{C}$ is an invertible matrix, then the $(u,\ v)$-th entry in the inverse matrix is given by the adjoint formula [34]

$$\mathbf{C}^{-1}(u,v)=\frac{(-1)^{u+v}\det(\mathbf{C}:v,u)}{\det(\mathbf{C})} \tag{B.3}$$

and hence, (B.2) follows.

# References

[1] S. M. Alamouti, “A simple transmit diversity technique for wireless communications,” *IEEE J. Select. Areas Commun.*, vol. 16, no. 8, pp. 1451 –1458, Oct. 1998.

[2] S. L. Ariyavisitakul, “Turbo space-time processing to improve wireless channel capacity,” *IEEE Trans. Commun.*, vol. 48, no. 8, pp. 1347 – 1359, Aug. 2000.

[3] AT&T, “Milestones in AT&T history, ” available at www.att.com/history/milestones.html.

[4] L. Bahl, J. Cocke, F. Jelinek and J. Raviv, “Optimal decoding of linear codes for minimizing symbol error rate,” *IEEE Trans. Inform. Theory*, vol. 20, no. 2, pp. 284 – 287, Mar. 1974.

[5] J. Bajcsy and H. Kobayashi, “On obtaining the BCJR algorithm via path counting,” in *Proc. Int. Symp. Inform. Theory and its Appl.*, Honolulu, HI, pp. 192 – 194, Nov. 2000.

[6] J. Bajcsy, C. V. Chong, J. A. Hunziker, D. A. Garr and H. Kobayashi, “Iterative decoding in some existing systems,” *IEEE J. Select. Areas Commun.*, vol. 19, no. 5, pp. 883 – 890, May 2001.

[7] S. Benedetto, E. Biglieri and V. Castellani, *Digital Transmission Theory*, Prentice-Hall, Englewood Cliffs, New Jersey, 1987.

[8] S. Benedetto and G. Montorsi, "Unveiling turbo-codes: Some results on parallel concatenated coding schemes," *IEEE Trans. Inform. Theory*, vol. 42, no. 2, pp. 409 – 428, Mar. 1996.

[9] C. Berrou and A. Glavieux, "Near optimum error correcting coding and decoding: Turbo codes," *IEEE Trans. Commun.*, vol. 44, no. 10, pp. 1261 – 1271, Oct. 1996.

[10] C. Berrou and M. Jézéquel, "Non-binary convolutional codes for turbo coding," *Electron. Lett.*, vol. 35, no. 1, pp. 39 – 40, Jan. 7th, 1999.

[11] V. K. Bhargava, "From Marconi to wireless internet: The wireless (r)evolution," Wireless Networking and Communications Seminar, The University of Texas at Austin, Feb. 17th, 2003, available at http://signal .ece.utexas.edu/seminars/dsp_seminars/03spring/bhargava.html.

[12] K. Binmore, P. Klemperer, "The biggest auction ever: The sale of British 3G telecom licenses," *The Economic Journal*, pp. C74 – C96, March 2002, available at www.paulklemperer.org.

[13] J. Blau, "NTT DoCoMo hits 300 Mbps in 4G research," June 4, 2004, available at www.infoworld.com/article/04/06/04/HNntt4g_1.html.

[14] S. D. Blostein and H. Leib, "Multiple antenna systems: Their role and impact in future wireless access," *IEEE Commun. Mag.*, vol. 41, no. 7, pp. 94 – 101, July 2003.

[15] F. Boixadera and J. Boutros, "Capacity considerations for wireless multiple-input multiple-output channels," in *Proc. Workshop Multiaccess, Mobility and Teletraffic Wireless Commun.*, 10 pages, Venice, Italy, Oct. 1999.

[16] S. ten Brink, "Convergence behavior of iteratively decoded parallel concatenated codes," *IEEE Trans. Commun.*, vol. 49, no. 10, pp. 1727 – 1737, Oct. 2001.

[17] R. M. Buehrer and N. A. Kumar, "The impact of channel estimation error on space-time block codes," in *Proc. IEEE Veh. Tech. Conf.*, pp. 1921 – 1925, Vancouver, Canada, Sept. 2002.

[18] D. Chizhik, F. Rashid-Farrokhi, J. Ling and A. Lozano, "Effect of antenna separation on the capacity of BLAST in correlated channels," *IEEE Commun. Lett.*, vol. 44, no. 11, pp. 337 – 339, Nov. 2000.

[19] D. C. Chu, "Polyphase codes with good periodic correlation characteristics," *IEEE Trans. Inform. Theory*, vol. IT-18, pp. 720 – 724, July 1972.

[20] C. N. Chuah, D. N. C. Tse, J. M. Kahn and R. A. Valenzuela, "Capacity scaling in MIMO wireless systems under correlated fading," *IEEE Trans. Inform. Theory*, vol. 48, no. 3, pp. 637 – 650, Mar. 2002.

[21] M. O. Damen, K. Abed-Meraim and J. C. Belfiore, "A generalized lattice decoder for asymmetrical space-time communication architecture," in *Proc. IEEE Conf. Acoustics, Speech, and Signal Process.*, vol. 5, pp. 2581 – 2584, Istanbul, Turkey, June 2000.

[22] J. Delaney, "3G wireless enters mainstream," Feb. 10, 2005, available at www.3g.co.uk/PR/Feb2005/9112.htm.

[23] D. Divsalar, S. Dolinar, F. Pollara and R. J. McEliece, "Transfer function bounds on the performance of turbo codes," *TDA Progress Report 42–122*, pp. 44 – 55, Aug. 15, 1995.

[24] C. Douillard, M. Jézéquel, C. Berrou, A. Picart, P. Didier and A. Glavieux, "Iterative correction of intersymbol interference: Turbo-equalization," *Eur. Trans. Telecommun.*, vol. 6, no.5, pp. 507 – 511, Sept. – Oct. 1995.

[25] T. M. Duman and E. M. Kurtas, "Performance bounds for high rate codes over partial-response channels," *IEEE Trans. Inform. Theory*, vol. 37, no. 12, pp. 1201 – 1205, Mar. 2001.

[26] G. D. Durgin, *Space-Time Wireless Channels*, Prentice Hall, Upper Saddle River, NJ, 2003.

[27] ETSI EN 301 790, V1.3.1: Digital video broadcasting, "Interaction channel for satellite distribution systems," Mar. 2003.

[28] U. Fincke and M. Pohst, "Improved methods for calculating vectors of short length in a lattice, including a computational complexity," *Math. Comput.* vol. 44, pp. 463 – 471, Apr. 1985.

[29] G. D. Forney, *Concatenated Codes*, MIT Press, Cambridge, MA, 1966.

[30] G. J. Foschini, "Layered space-time architecture for wireless communications in a fading environment when using multi-element antennas," *Bell Labs Tech. J.*, vol. 1, no. 2, pp. 41 – 59, Autumn 1996.

[31] C. Fragouli and R. D. Wesel, "Turbo-encoder design for symbol-interleaved parallel concatenated trellis-coded modulation," *IEEE Trans. Commun.*, vol. 49, no. 3, pp. 425 – 435, Mar. 2001.

[32] R. L. Frank, "Polyphase codes with good nonperiodic correlation characteristics," *IEEE Trans. Inform. Theory*, vol. IT – 9, pp. 43 – 45, Jan. 1963.

1. A. A. Garba, N. Mysore and J. Bajcsy, "Increasing the spectral efficiency in microcell hotspots using M-ary CDMA: Capacity analysis and simulation re-

sults," *Proc. IEEE Broadband Networks Conf.*, pp. 799 – 808, Boston, MA, Oct. 2005.

[33] G. D. Golden, G. J. Foschini, R. A. Valenzuela and P. W. Wolniansky, "Detection algorithm and initial laboratory results using the V-BLAST space-time communication architecture," *Electron. Lett.*, vol. 35, no. 1, pp. 14 – 15, Jan. 1999.

[34] G. H. Golub and C. F. Van Loan, *Matrix Computations*, Johns Hopkins University Press, Baltimore MD, 1996.

[35] E. Guizzo, "Closing in on the perfect code," *IEEE Spectrum*, pp. 36 – 42, March 2004.

[36] N. K. Gupta, "Wireless broadband: 40Mbps in your palm," Jan. 2001, available at http://www.angelfire.com/nd/ramdinchacha/JAN01.html.

[37] J. Gurland, "Distribution of definite and of indefinite quadratic forms," *Ann. Math. Stat.*, pp. 122 – 127, Mar. 1955.

[38] R. W. Hamming, "Error detecting and correcting codes," *Bell Sys. Tech. J.*, vol. 29, pp. 147-160, 1950.

[39] C. Hermosilla and L. Szczecinski, "Exit charts for turbo receivers in MIMO systems," in *Proc. Int. Symp. Sig. Process. and Appl.*, pp. 209 – 212, Paris, France, July 2003.

[40] B. Hassibi and B. M. Hochwald, "High-rate codes that are linear in space and time," *IEEE Trans. Inform. Theory*, vol. 48, no. 7, pp. 1804 – 1824, June 2002.

[41] M. S. C. Ho, S. S. Pietrobon and T. C. Giles. "Interleavers for punctured turbo codes," in *Proc. IEEE Asia-Pacific Conf. on Commun.*, pp. 520 – 524, Singapore, Nov. 1998.

[42] B. Hochwald and S. ten Brink, "Achieving near-capacity on a multiple-antenna channel," *IEEE Trans. Commun.*, vol. 51, no. 3, pp. 389 – 399, Mar. 2003.

[43] W. C. Jakes, *Microwave Mobile Communications*, IEEE Press, New York, 1974.

[44] P. Kabal and S. Pasupathy, "Partial-response signaling," *IEEE Trans. Commun.*, vol. COM-23, no. 9, pp. 921 – 934, Sept. 1975.

[45] Y. Kim, B. J. Jeong, J. Chung, C. Hwang, J. S. Ryu, K. Kim and Y. K. Kim, "Beyond 3G: Vision, requirements and enabling technologies," *IEEE Commun. Mag.*, vol. 41, no. 3, pp. 120 – 124, Mar. 2003.

[46] H. Kobayashi and D. T. Tang, "Application of partial-response channel coding to magnetic recording systems," *IBM J. Res. Develop.*, vol. 14, pp. 368 – 375, July 1970.

[47] E. R. Kretzmer, "Generalization of a technique for binary data transmission," *IEEE Trans. Commun. Technol.*, vol. COM-14, pp. 67 – 68, Feb. 1966.

[48] E. Kurtas, J. G. Proakis and M. Salehi, "Reduced complexity maximum likelihood sequence estimation for multitrack high-density magnetic recording channels," *IEEE Trans. Magnetics*, vol. 35, no. 4, pp. 2187 – 2193, July 1999.

[49] S. Lee, *Spread Spectrum CDMA: IS-95 and IS-2000 for RF Communication*, McGraw Hill, New York, 2002.

[50] B. Lu and X. Wang, "Iterative receivers for multiuser space-time coding systems," *IEEE J. Select. Areas Commun.*, vol. 18, no. 11, pp. 2322 – 2335, Nov. 2000.

[51] X. Ma and L. Ping, "Iterative detection/decoding for two-track partial response channels," *IEEE Commun. Lett.*, vol. 8, no. 7, pp. 464 – 466, July 2004.

[52] L. L. McPheters, S. W. McLaughlin and K. R. Narayanan, "Precoded PRML, serial concatenation, and iterative (turbo) decoding for digital magnetic recording," *IEEE Trans. Magnetics*, vol. 35, no.5, pp. 2325 – 2327, Sept. 1999.

[53] M. Mouly and M.-B. Pautet, *The GSM System for Mobile Communications*, Telecom Publishing, Mercer Island, WA, 1992.

[54] M. E. Muller, "A note on a method for generating points uniformly on n-dimensional spheres," *Commun. ACM*, vol. 2, pp. 19 – 20, 1959.

[55] N. Mysore and J. Bajcsy, "Combined turbo coding and turbo equalization in a wireless system with antenna diversity," in *Proc. IEEE Veh. Tech. Conf.*, pp. 1242 – 1246, Birmingham, AL, May 2002.

[56] N. Mysore, "Combined turbo coding and turbo equalization for wireless systems with antenna diversity," MEng thesis, McGill University, Montreal, Quebec, Jan. 2002.

[57] N. Mysore and J. Bajcsy, "On linear complexity detection with iterative processing for space-time coded systems," *Can. J. Elec. Comp. Eng.*, vol. 29, no. ½, pp. 35 – 41, Jan. – Apr. 2004 (available on IEEE explorer).

[58] N. Mysore and J. Bajcsy, "Performance analysis of a low complexity space-time detector in Rayleigh fading environments," *in Proc. IEEE Can. Conf. on Elec. and Comput. Eng.*, pp. 2271 – 2275, Niagara Falls, Ontario, May 2004.

[59] N. Mysore and J. Bajcsy, "A linear complexity detection method and iterative equalization for coded MIMO systems," *in Proc. IEEE Sensor Array and*

*Multichannel Signal Processing Workshop*, pp. 163 – 167, Barcelona, Spain, July 2004.

[60] N. Mysore and J. Bajcsy, "The impact of channel estimation errors on a linearly complex space-time signal detector in a coded MIMO system," *in Proc. IEEE Military Communications Conference (MILCOM) 2004*, pp. 841 – 847, Monterey, CA, Oct. 2004.

[61] N. Mysore and J. Bajcsy, "The impact of channel estimation errors and co-antenna interference on the performance of a coded MIMO system," *Eurasip J. Appl. Sign. Process.: Special Issue on System-Integration-Oriented Transceiver Designs for Wireless Networks Beyond 3G*, vol. 2005, no. 11, pp. 1680 – 1697, July 2005 (available at www.hindawi.com/journals/asp/ index.html).

[62] N. Mysore and J. Bajcsy, "Reduced complexity signal detection and turbo decoding for multitrack magnetic recording channels," *in Proc. IEEE Int. Conf. Magnetics (INTERMAG)*, pg. EP 01, Nagoya, Japan, Apr. 2005.

[63] N. Mysore and J. Bajcsy, "Reduced complexity signal detection and turbo decoding for multitrack magnetic recording channels," *IEEE Trans. Magnetics*, vol. 41, no. 10, pp. 2974 – 2976, Oct. 2005.

[64] N. Mysore, M. Akçakaya, J. Bajcsy and H. Kobayashi, "A new performance evaluation technique for iteratively decoded magnetic recording systems," *in Proc. IEEE Int. Conf. on Magnetics (INTERMAG)*, pg. GC 05, Nagoya, Japan, Apr. 2005.

[65] N. Mysore, J. Bajcsy, M. Akçakaya and H. Kobayashi, "A new performance evaluation technique for iteratively decoded magnetic recording systems," *IEEE Trans. Magnetics*, vol. 41, no. 10, pp. 2986 – 2988, Oct. 2005.

[66] N. Mysore and J. Bajcsy, " A new performance evaluation technique for turbo-coded MIMO systems with iterative processing," in *Proc. Can. Workshop on Information Theory*, pp. 40 – 45, Montreal, Quebec, June 2005.

[67] N. Mysore and J. Bajcsy, "System and method for data communication over multi-input, multi-output channels," US Patent Pending, Filed on Aug. 2, 2005, US Provisional Patent no. 85827-65, Feb. 2003, Report on Invention, May 2002.

[68] N. Mysore and J. Bajcsy, "On achieving near-capacity transmission in uplink multi-user MIMO systems: Performance analysis and simulation results," in *Proc. IEEE Broadnets Networks Conf.*, pp. 817 – 826, Boston, MA, Oct. 2005.

[69] N. Mysore and J. Bajcsy, "Union bound based performance evaluation of turbo-coded uplink MIMO systems," in *Proc. IEEE Military Communications Conference (MILCOM) 2005*, CDROM, 7 pages, Atlantic City, NJ, Oct. 2005.

[70] N. Mysore, J. Bajcsy, "BER bounding techniques for selected turbo-coded MIMO systems in Rayleigh fading," submitted to *IEEE Trans. Wireless Commun.*, 26 pages, Nov. 2005.

[71] M. Öberg and P. H. Siegel, "Performance analysis of turbo-equalized partial response channels," *IEEE Trans. Commun.*, vol. 49, no. 3, pp. 436 – 444, Mar. 2001.

[72] I. Oppermann and B. S. Vucetic, "Complex spreading sequences with a wide range of correlation properties," *IEEE Trans. Commun.*, vol. 45, no. 3, pp. 365 – 375, Mar. 1997.

[73] A. Papoulis and S. Unnikrishna Pillai, *Probability, Random Variables and Stochastic Processes*, Fourth Edition, McGraw Hill, New York, 2002.

[74] K. I. Pedersen, P. E. Mogensen and B. H. Fleury, "Spatial channel characteristics in outdoor environments and their impact on BS antenna system performance," in *Proc. IEEE Veh. Tech. Conf.*, pp. 719 – 723, Ottawa, Ontario, May 1998.

[75] M. Pettersen, P. H. Lehne, J. Noll, O. Røstbakken, E. Antonsen and R. Eckhoff, "Characterization of the directional wideband radio channel in urban and suburban areas," in *Proc. IEEE Veh. Tech. Conf.*, pp. 1454 – 1459, Amsterdam, Netherlands, Sept. 1999.

[76] J. Proakis, *Digital Communications*, Third Edition, McGraw Hill, New York, 1989.

[77] T. S. Rappaport, *Wireless Communcations: Principles and Practice*, Prentice Hall PTR, Upper Saddle River, NJ, 1996.

[78] W. Rhee and J. M. Cioffi, "On the capacity of multiuser wireless channels with multiple antennas," *IEEE Trans. Inform. Theory*, vol. 49, no. 10, pp. 2580 – 2595, Oct. 2003.

[79] H. Sawaguchi and J. K. Wolf, "Turbo decoding for high-rate concatenated parity-check codes on PRML channels," *IEEE Trans. Magnetics*, vol. 36, no. 5, pp. 2173 – 2175, Sept. 2000.

[80] M. Sellathurai and S. Haykin, "TURBO-BLAST for wireless communications: Theory and experiments," *IEEE Trans. Sig. Process.*, vol. 50, no. 10, pp. 2538 – 2546, Oct. 2002.

[81] C. E. Shannon, "A mathematical theory of communication," *Bell Sys. Tech. J.*, vol. 27, pp. 379-423 and pp. 623-656, July 1948.

[82] J. Shen and A. G. Burr, "Iterative multi-user-antenna detector for MIMO CDMA employing space-time turbo codes," in *Proc. Globecom 2002,* pp. 419 – 423, Taipei, Taiwan, Nov. 2002.

[83] E. Soljanin and C. Georghiades, "Multihead detection for multitrack recording channels," *IEEE Trans. Inform. Theory*, vol. 44, no. 7, pp. 2988 – 2997, Nov. 1998.

[84] T. V. Souvignier, M. Öberg, P. H. Siegel, R. E. Swanson and J. K. Wolf, "Turbo decoding for partial response channels," *IEEE Trans. Commun.*, vol. 48, no. 8, pp. 1297 – 1308, Aug. 2000.

[85] R. P. Stanley, *Enumerative Combinatorics*, Wadsworth & Brooks / Cole Monterey, California, 1986.

[86] L. Staphorst, M. Jamil and L. P. Linde, "Performance of a synchronous balanced QPSK CDMA system using complex spreading sequences in AWGN," in *Proc. IEEE AFRICON*, pp. 215 – 220, Cape Town, South Africa, Sept. 1999.

[87] A. Stefanov and T. Duman, "Turbo-coded modulation for systems with transmit and receive antenna diversity over block fading channels: System model, decoding approaches and practical considerations," *IEEE J. Select. Areas Commun.*, vol. 19, no. 5, pp. 958 – 968, May 2001.

[88] A. Stefanov and T. M. Duman, "Performance bounds for turbo-coded multiple antenna systems," *IEEE J. Select. Areas Commun.*, vol. 23, no. 3, pp. 374 – 381, Apr. 2003.

[89] V. Tarokh, N. Seshadri and A. R. Calderbank, "Space-time codes for high data rate wireless communication: Performance criterion and code construction," *IEEE Trans. Inform. Theory*, vol. 44, no. 2, pp. 744 – 765, Mar. 1998.

[90] V. Tarokh, A. Naquib, N. Seshadri and A. R. Calderbank, "Space-time codes for high data rate wireless communication: Performance criteria in the presence of channel estimation errors, mobility, and multiple paths," *IEEE Trans. Commun.*, vol. 47, no. 2, pp. 199 – 207, Feb. 1999.

[91] V. Tarokh, H. Jafarkhami, and A. R. Calderbank, "Space-time block codes from orthogonal designs," *IEEE Trans. Inform. Theory*, vol. 45, no. 5, pp. 1456 – 1467, July 1999.

[92] İ. E. Telatar, "Capacity of multi-antenna Gaussian channels," *Eur. Trans. Telecommun.*, vol. 10, no. 6, pp. 585 – 595, Nov. – Dec. 1999.

[93] S. Thoen, L. Van de Perre, B. Gyselinckx, and M. Engels, "Performance analysis of combined transmit-SC/receive-MRC," *IEEE Trans. Commun.*, vol. 49, no. 1, pp. 5 – 8, Jan. 2001.

[94] 3Gnewsrooms, "Opera Telecom launches 3G video services," July 27, 2005 available at www.3gnewsroom.com/3g_news/jul_05/news_6097.shtml.

[95] Third Generation Partnership Project (3GPP), www.3gpp.org.

[96] Third Generation Partnership Project (3GPP) Technical Specification Group, *Multiplexing and Channel Coding (FDD)*, TS 25.212 v6.5.0, June 2005.

[97] Third Generation Partnership Project (3GPP) Technical Specification Group, *Radio Access Network; Spreading and Modulation (FDD)*, TS 25.213 v6.3.0, June 2005.

[98] A. M. Tonello, "MIMO MAP equalization and turbo decoding in interleaved space-time coded systems," *IEEE Trans. Commun.*, vol. 51, no. 2, pp. 155 – 160, Feb. 2003.

[99] M. Tüchler, "Convergence prediction for iterative decoding of threefold concatenated systems," in *Proc. IEEE Global Commun. Conf.*, pp. 1358 –1362, Taipei, Taiwan, Nov. 2002.

[100] N. Varnica and A. Kavčić, "Optimized low-density parity-check codes for partial response channels," *IEEE Commun. Lett.*, vol. 7, no. 4, pp. 168 – 170, Apr. 2003.

[101] S. Verdú, *Multiuser Detection*, Cambridge University Press, New York, 1998.

[102] H. Vikalo and B. Hassibi, "Low-complexity iterative detection and decoding of multi-antenna systems employing channel and space-time codes," in *Proc. Asilomar Conf. Signals, Syst. Comp.*, pp. 294 – 298, Pacific Grove, CA, Nov. 2002.

[103] E. W. Weisstein, *CRC Concise Encyclopedia of Mathematics*, Chapman & Hall / CRC, Boca Raton, FL, 2003.

[104] S. B. Wicker, V. K. Bhargava, *Reed-Solomon Codes and Their Applications*, John Wiley & Sons, New York, 1999.

[105] W. Ye and A. M. Haimovich, "Performance of cellular CDMA with cell site antenna arrays, Rayleigh fading and power control error," *IEEE Trans. Commun.*, vol. 48, no. 7, pp. 1151 – 1159, July 2000.

[106] T. Yoo and A. Goldsmith, "Capacity of fading MIMO channels with channel estimation error," in *Proc. IEEE Int. Conf. on Commun.*, pp. 808 – 813, Paris, France, June 2004.

[107] Y. Young-Hwan and S. Hyoung-Kyu, "Influence of channel estimation error on layered space-time receivers," *Electron. Lett.*, vol. 39, no. 13, pp. 1008 – 1010, June 26, 2003.

[108] Z. Zhang, T. M. Duman, E. M. Kurtas, “Achievable information rates and coding for MIMO systems over ISI channels and frequency-selective fading channels,” *IEEE Trans. Commun.*, vol. 52, no. 10, pp. 1698 – 1710, Oct. 2004.